Toluene Total Oxidation over $CuO\text{-}CeO_2/Al_2O_3$: Structural and Kinetic Characterization

Totale oxidatie van tolueen over $CuO\text{-}CeO_2/Al_2O_3$: structurele en kinetische karakterisering

Unmesh Menon

Promotoren: prof. dr. ir. G. B. Marin, dr. V. Galvita
Proefschrift ingediend tot het behalen van de graad van
Doctor in de Ingenieurswetenschappen: Chemische Technologie

Vakgroep Chemische Proceskunde en Technische Chemie
Voorzitter: prof. dr. ir. G. B. Marin
Faculteit Ingenieurswetenschappen en Architectuur
Academiejaar 2012 - 2013

UNIVERSITEIT GENT

ISBN 978-90-8578-569-9
NUR 952
Wettelijk depot: D/2013/10.500/2

EXAMINATION COMMITTEE

Promoters

Prof. dr. ir. Guy B. Marin	Ghent University, Belgium
Dr. Vladimir V. Galvita	Ghent University, Belgium

Other members

Prof. dr. Denis Constales	Ghent University, Belgium
Prof. dr. Dirk Poelman	Ghent University, Belgium
Prof. dr. Chris Hardacre	Queens University, Belfast, UK
Prof. dr. Gregory S. Yablonsky	Saint Louis University, USA
Dr. ir. Yves Schuurman	IRCELYON, France
Dr. Hilde Poelman	Ghent University [Secretary]
Prof. dr. ir. Hendrik Van Landeghem	GhentUniversity [Chairman]

This research was funded by a Concerted Research Action (GOA) of Ghent University and "Long term Methusalem funding by the Flemish government".

Ghent University
Department of Chemical Engineering and Technical Chemistry
Laboratory for Chemical Technology
Technologiepark 918/Krijgslaan 281 S5
9000 Gent
Belgium

UNIVERSITEIT GENT

Dedicated to my parents

Acknowledgement

Working on the PhD has been a wonderful and an overwhelming experience. The topic itself had been a real learning curve. More than that, working on papers, giving seminars, preparing for meetings, staying awake and focused until the birds start singing, has given me unmatchable experiences. There are many individuals who in one way or another contributed and extended their valuable assistance during my tenure as a PhD student for the completion of this study.

First and foremost, my utmost gratitude to my promoters, Guy Marin and Vladimir Galvita for their invaluable assistance, support and guidance during my tenure as a PhD student. Prof. Marin provided me the opportunity to work as a PhD student in the LCT and was a continuous encouragement throughout my PhD tenure. I am very grateful for the insightful comments both in my work and in the thesis, for his support and for many motivating discussions. Vladimir has been my inspiration as I hurdle all the obstacles in the completion of this research work. To work with him was a great pleasure with lots of fun and excitement. Vladimir had been a steady influence throughout my PhD having oriented and supported me with promptness and care and have always been patient and encouraging in times of new ideas and difficulties. He has listened to my ideas and discussions with him frequently led to key insights. Above all Vladimir made me feel like a friend which I appreciate from my heart.

I would like to thank my PhD examination committee for reading my thesis and providing me with useful comments which helped improve the thesis greatly.

In addition I have been privileged to get to know and work with many other great people who became friends over the last several years. I wish to thank Raf Roelant and Veerle Balcaen who helped me during

the initial days of my PhD. Raf helped me with programming and Veerle trained me in operating the TAP machine. More than just colleagues they were good friends too. Thank you both of you!.

I did not have an opportunity to work with Geraldine Heyderickx, Joris Thybaut, and Marie-Françoise Reyniers but I thank them for the friendliness they showed. Special thanks to Geraldine Heyderickx for all the nice discussions during the breaks. All your friendly gestures made me feel at home and not in a foreign country.

I thank Hilde Poelman who gave me lessons on XAS and other characterization techniques. The trips to SOLIEL and ESRF for synchrotronic measurements has been a lot valuable both in terms of gaining new knowledge and making good friends. I thank all those who made those campaigns memorable. To name a few would be Kostas Alexopoulos and Kristof Van der Borght.

I have greatly enjoyed the opportunity to work with Denis Constales whose mathematical knowledge is impressive. I thank him for all the fruitful discussions that we have had. I thank Gregory Yablonsky for all the interesting and useful interactions that we have had. I take this opportunity to thank Roger Van Keer for attending my progress meetings and providing me with useful comments. I would like to thank Vitaliy Bliznuk for the TEM measurements.

This PhD would not have been possible without the support from the technical and administrative staff of LCT. I extend my sincere gratitude towards Andy De Prez who had lended a helping hand with the TAP set-up whenever I was in need. Andy has offered help and advices over telephone even when he was on sick holidays. His sincerity in work is something that I will always admire. I would like to thank Hans Heene, Marcel Vervust, Tom Ravelingen and Michale Lottin for all the timely helps whenever I needed them with the experimental set-up. I would like to extend my thanks Georges Verenghen for all his support with computer related issues. Special thanks to Petra Vereecken,

Kim Verbeeck and Kevin De Wolf for all the administerial support during my stay in the lab.

I am also indebted to my colleagues I had the pleasure to work with. You have been an invaluable support day in, day out during all these years. Special thanks to Ionel, Nima, Evgeniy, Tatyana, Carolina, Gaoping, Will, Luis, Dagmar, Pieter, Paul, Jeroen, Matthias, Panos, Maria, Evelyn, Philippe, Kostas, Kristof. Thanks to all of you! This journey would not have been as enjoyable without you all. I would also like to thank the Indian students in Gent especially in LCT for making me feel at home. Special thanks to Indranil, Prasad, Vinod, Kamal, Nissy, Sukumar, Samir, Rajesh, Pravesh, Tapan, Ark, Amit, Aditya, Chetan and all the others.

I am indebted to all my teachers who have played a great role in shaping my career. Last but not the least, I thank my family for their unconditional support without which this wonderful journey would not have been real.

Ghent, January 2013

Unmesh Menon

Contents

Samenvatting

Vluchtige Organische Stoffen (VOS) vormen een grote groep van op koolstof gebaseerde chemicaliën die gemakkelijk verdampen bij kamertemperatuur. VOS komen vrij bij het verbranden van stoffen zoals benzine, hout, kool of aardgas, en worden beschouwd als gevaarlijke luchtvervuilers. In combinatie met stikstofoxiden vormen ze ozon in de onderste luchtlaag en smog, die bijdragen tot klimaatverandering. VOS komen eveneens vrij uit oplosmiddelen, verf, lijm en andere producten die thuis en op het werk gebruikt en bewaard worden. Vaak gaat het om schadelijke of kankerverwekkende stoffen, die rechtstreeks of onrechtstreeks ernstige gevolgen hebben voor de menselijke gezondheid, zelfs in zeer kleine concentraties.

Vandaag worden verscheidene technieken gebruikt of ontwikkeld om VOS uit de lucht te verwijderen, zoals adsorptie, absorptie, biofiltratie, verbranding en katalytische oxidatie, afhankelijk van de eigenschappen van de VOS, hun concentratie en het gasdebiet. Katalytische oxidatie kan efficiënt en goedkoop toegepast worden binnen een breed bereik aan VOS-concentraties en stroomsnelheden, en vormt daardoor een interessante oplossing voor de eliminatie van VOS. Katalysatoren gebaseerd op edelmetalen en transitiemetalen worden met succes toegepast voor de totale oxidatie of afbraak van VOS. Edelmetaalkatalysatoren zijn weliswaar zeer actief, maar hun hoge kostprijs staat een brede toepassing in de weg. Anderzijds vertonen transitiemetaaloxiden een vergelijkbare activiteit bij hoge temperatuur en laten een hoge katalysatorbelading toe. In the voorbije jaren is dan ook

veel aandacht besteed aan transitiemetaaloxiden voor het verwijderen van VOS, in het bijzonder aan katalysatoren gebaseerd op koper.

Het belangrijkste doel van dit doctoraatsonderzoek is een beter begrip van het werkingsmechanisme van $CuO\text{-}CeO_2/\gamma\text{-}Al_2O_3$ in de totale oxidatie van VOS en van de bijhorende kinetiek. Dit zal bijdragen tot de optimalisatie van de industriële $CuO\text{-}CeO_2/\gamma\text{-}Al_2O_3$ katalysator. Het werk uitgevoerd voor dit doctoraat kadert in lopend onderzoek in het Laboratorium voor Chemische Technologie aan de Gentse Universiteit naar de verwijdering van VOS. Als modelmolecule is tolueen gekozen en de totale oxidatie van deze molecule over de bi-metallische katalysator $CuO\text{-}CeO_2/\gamma\text{-}Al_2O_3$ is bestudeerd met behulp van de krachtige transiënte techniek Temporal Analysis of Products (TAP). Deze laat toe om de chemie van kortlevende tussenproducten te onderzoeken, die normaal gezien het oppervlak niet verlaten, waardoor gedetailleerde reactiepaden en -mechanismen kunnen verduidelijkt worden. Het werkingsprincipe omvat het gebruik van zeer snelle pulskleppen om een zeer klein aantal moleculen (10^{13}-10^{14}/puls) in het vacuüm van de microreactor te injecteren. Een massaspectrometer volgt de moleculen die de reactor verlaten en levert met hoge snelheid informatie over de reactanten, eindproducten en intermediairen.

De katalysator wordt onderworpen aan tolueen pulsexperimenten met en zonder zuurstof en dit in een breed temperatuurgebied (673K-923K). Via isotoopexperimenten met $^{18}O_2$ wordt informatie verkregen over de deelname van de verschillende types zuurstofatomen in de katalysator, zoals oppervlak-roosterzuurstof en geadsorbeerd zuurstof. Tolueen blijkt te interageren met katalytisch zuurstof en hiermee CO_2 en H_2O te vormen, terwijl zuurstof in de voeding de katalysator re-oxideert, in overeenstemming met het mechanisme van Mars en van Krevelen. Zwak gebonden oppervlak-roosterzuurstofatomen met een levensduur van 1s, zijn zeer reactief en komen enkel voor op een volledig geoxideerde katalysator in aanwezigheid van zuurstof. Tolueen pulsexperimenten bij hogere reductiegraad van de katalysator tonen een

daling van de totale-oxidatiesnelheid. Naast de rol van de verschillende zuurstofatomen, werd eveneens een gedetailleerd reactienetwerk voor de totale oxidatie van tolueen opgesteld, door het uitvoeren van isotoopexperimenten met C_6H_5-$^{13}CH_3$ en C_6H_5-CD_3.

Het reactienetwerk van de katalytische totale oxidatie van tolueen omvat de volgende stappen (Figuur 1): adsorptie van tolueen op het katalysatoroppervlak met de methylgroep op O^{2-} en de fenylgroep op Cu^{2+}; gelijktijdige onttrekking van H aan de methyl- en fenylgroep op 4 tot 5 aangrenzende zuurstofplaatsen en de vorming van water; onttrekking van het koolstofatoom aan de methylgroep en tenslotte, afbraak van de aromatische ring. De koolstofhoudende intermediairen tussen tolueen en CO_2 worden aan het oppervlak traag geoxideerd door roosterzuurstof en/of geadsorbeerd zuurstof op een tijdsschaal van ~10s.

De katalytische prestatie van het binaire metaaloxide CuO-CeO_2/Al_2O_3 wordt vergeleken met de overeenkomstige enkelvoudige metaaloxides CuO/Al_2O_3 en CeO_2/Al_2O_3. De reden voor de verbeterde prestatie van de binaire metaaloxidekatalysator in vergelijking met de enkelvoudige metaaloxides wordt onderzocht met behulp van structurele karakteriseringsmethodes, zoals transmissie-elektronenmicrosopie met hoge resolutie (HRTEM) en x-stralenabsorptiespectroscopie (XAS). Op basis van de structurele karakterisering kan de verbeterde prestatie van het binaire metaaloxide toegeschreven worden aan de vorming van een vaste oplossing $Ce_{1-x}Cu_xO_{2-x}$, waarbij Cu^{2+} substitutioneel is ingebouwd in het CeO_2 rooster, die bestaat naast een bulk CuO fase. XAS experimenten tijdens temperatuur-geprogrammeerde reductie van de CuO-CeO_2/Al_2O_3 katalysator wijzen op verbeterde reductie van zowel Ce als Cu in de vaste oplossing. Ceriumoxide geeft evenwel O door aan nabijgelegen koper zodat het in geoxideerde toestand blijft. Wanneer alle beschikbare O^{2-} van ceriumoxide verbruikt is, reduceert het opgeloste Cu^{2+} tot Cu^{1+}.

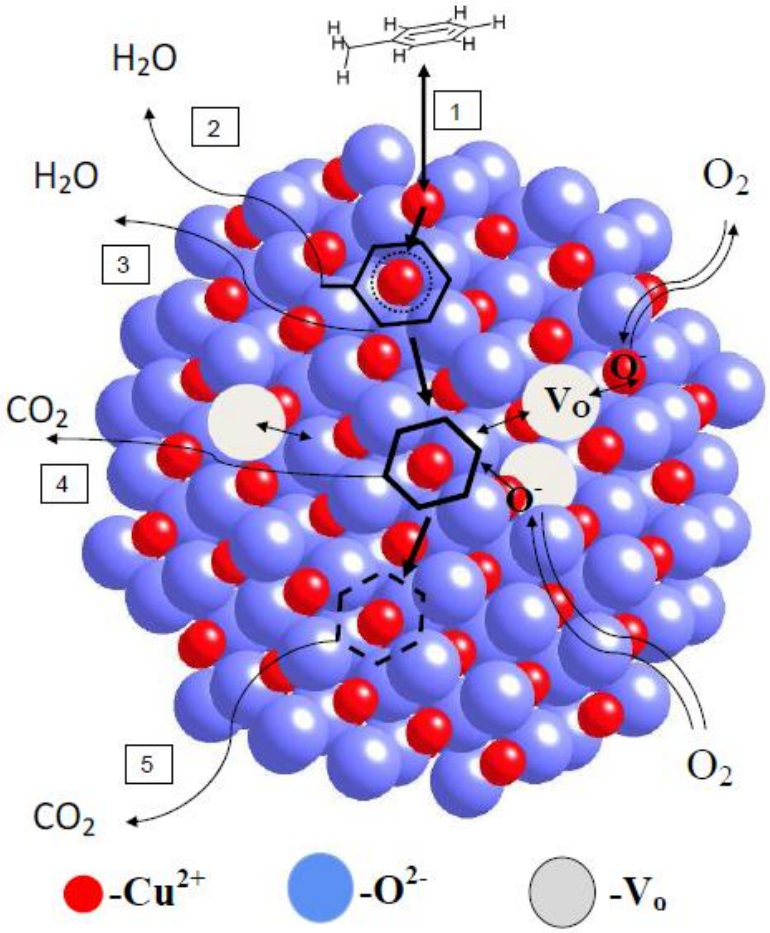

Figuur 1: Reactienetwerk voor de totale oxidatie van tolueen

Twee afzonderlijke roosterplaatsen zijn verantwoordelijk voor oxidatie en reductie (Figuur 2): tolueen wordt geoxideerd op Cu^{2+}-plaatsen in de vaste oplossing, terwijl zuurstof gereduceerd wordt op Ce^{3+}-plaatsen. Bij oxidatie van Ce^{3+} geven deze hun elektronen en zuurstofionen snel door aan Cu-plaatsen in de vaste oplossing. Daarnaast kunnen ook H_2O of CO_2 het gereduceerd Ce^{3+} oxideren. In tegenstelling tot CeO_2 kan gereduceerd CuO/Al_2O_3 niet geoxideerd worden door H_2O of CO_2. De waargenomen verminderde activiteit voor CuO/Al_2O_3 in aanwezigheid van water kan bijgevolg toegeschreven worden aan een competitie tussen H_2O/CO_2 en zuurstof voor dezelfde actieve plaatsen.

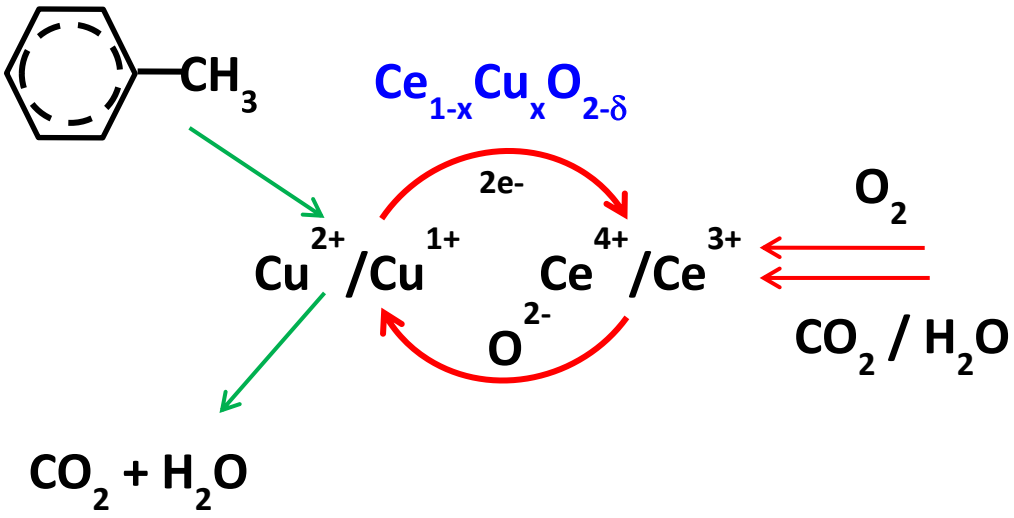

Figuur 2: het algemene redox schema dat de heterogene oxidatiereacties in CuO-CeO_2/Al_2O_3 beschrijft.

Zowel het gedetailleerd reactiemechanisme als de aard en structuur van de actieve plaatsen in CuO-CeO_2/Al_2O_3 voor totale oxidatie van tolueen verschaffen noodzakelijke informatie voor het ontwikkelen van een microkinetisch model. Beperking van het reactienetwerk tot oxidatie en reductie van de katalysator laat toe een kinetisch model op te bouwen dat de experimentele gegevens passend beschrijft. Een enkelvoudige reeks kinetische parameters biedt dan een verklaring voor een breed gebied van temperaturen en toestanden, i.e. reductiegraden van de katalysator. De geschatte kinetische parameters zijn statistisch significant en vertonen een solide fysisch-chemische betekenis. De overeenkomstige snelheidscoëfficiënten worden geschat met behulp van een niet-lineaire kleinste-kwadratenregressie. CuO-CeO_2/Al_2O_3 vertoont een hoge snelheid van watervorming uit tolueen tijdens reductie van de katalysator en een hoog vermogen om zijn initiële activiteit te herstellen door zuurstofactivering en daaropvolgende re-oxidatie van de katalysator. Naast snelheidscoëfficiënten en activeringsenergieën wordt ook de partiële orde van zuurstof significant geschat. De afbraak van de aromatische ring is de snelheidsbepalende stap in het hele proces. De activeringsenergieën van de verschillende processen, inclusief de zuurstofdiffusie vanuit de bulk naar het oppervlak, blijken lineair afhankelijk van de reductiegraad van de

katalysator. De zuurstofdiffusie van bulk naar oppervlak verloopt trager op een gereduceerde katalysator dan op een vooraf geoxideerde, hetgeen correspondeert met een lineaire toename van de overeenkomstige activeringsenergieën met stijgende reductiegraad.

Summary

Volatile Organic Compounds (VOCs) are a large group of carbon-based chemicals that easily evaporate at room temperature. VOCs are released from burning fuel, such as gasoline, wood, coal, or natural gas and are regarded as hazardous air pollutants. When combined with nitrogen oxides, volatile Organic Compounds react to form ground-level ozone, or smog, which contributes to climate change. They are also released from solvents, paints, glues, and other products that are used and stored at home and at work. They are often noxious or carcinogenic, either directly or indirectly, having many severe effects on human health at very low concentrations.

Several techniques are currently employed, or under development, to eliminate VOCs from the air, such as adsorption, absorption, bio-filtration, combustion and catalytic oxidation depending on the characteristics of the VOCs and concentration and waste gas flow rate. Catalytic oxidation can be applied effectively and at lower cost in a wide range of VOCs concentrations and waste gas flow rates, and, therefore, presents an interesting solution for VOCs elimination. Catalysts based on noble metals and transition metals are successfully applied to eliminate VOCs by total oxidation. Noble metal catalysts are very active, but their high cost limits their wide application. Transition metal oxides, on the other hand, have comparable activity at high temperatures. In the past several years, much attention has been paid to transition metal oxides, especially to copper based catalysts in VOCs removal.

The main aim of this PhD research is to gain a better understanding of the mechanism of action of the $CuO\text{-}CeO_2/\gamma\text{-}Al_2O_3$ in VOCs total oxidation and the corresponding kinetics. This will help to optimize the industrial $CuO\text{-}CeO_2/Al_2O_3$ catalyst. The work performed in this PhD is within the framework of the ongoing research activities on the elimination of VOCs at Laboratory for Chemical Technology, Ghent University. Toluene is chosen as the VOC and its total oxidation on bimetallic catalyst $CuO\text{-}CeO_2/Al_2O_3$ was studied by making use of the powerful transient technique Temporal Analysis of products (TAP). This technique allows to examine the chemistry of short-lived intermediates, thereby allowing detailed reaction paths and mechanisms to be elucidated. The principle of operation involves the use of high speed pulse valves to release a very small number of molecules (10^{13}-10^{14}/pulse) into a microreactor that is placed in vacuum. A mass spectrometer monitors the wave of molecules exiting the reactor and stores the information about reactants, products, and intermediates at a fast rate.

The catalyst is subjected to pulse experiments with toluene molecules in the presence and absence of dioxygen at a wide temperature range (673K-923K). The information on the participation of various oxygen species in the catalyst such as surface lattice oxygen and adsorbed oxygen, is obtained by isotopic experiments with $^{18}O_2$. Toluene is found to interact with the catalytic oxygen and form CO_2 and H_2O whereas the dioxygen in the feed helped reoxidize the catalyst which was in accordance with the Mars and van Krevelen mechanism. Weakly bound surface lattice oxygen atoms, the lifetime of which is close to 1 s, are highly reactive and only found over a fully oxidized catalyst and in the presence of dioxygen. Toluene pulse experiments on higher degrees of reduction of the catalyst showed a reduction in the rate of total oxidation. In addition to the role of oxygen species, a detailed reaction network of toluene total oxidation was revealed by conducting isotopic experiments with $C_6H_5\text{-}^{13}CH_3$ and $C_6H_5\text{-}CD_3$.

The reaction network of the catalytic total oxidation of toluene consists of the following sequences (Figure 1): adsorption of toluene on the catalyst surface with the methyl group on O^{2-} and phenyl on Cu^{2+}; the simultaneous abstraction of H from the methyl and the phenyl group on 4-5 adjacent oxygen sites and the formation of water; abstraction of the carbon atom of the methyl group and finally, destruction of the aromatic ring. The carbon containing surface intermediates between toluene and CO_2 are slowly oxidized by the lattice and/or adsorbed oxygen i.e. on a time scale of ~10s.

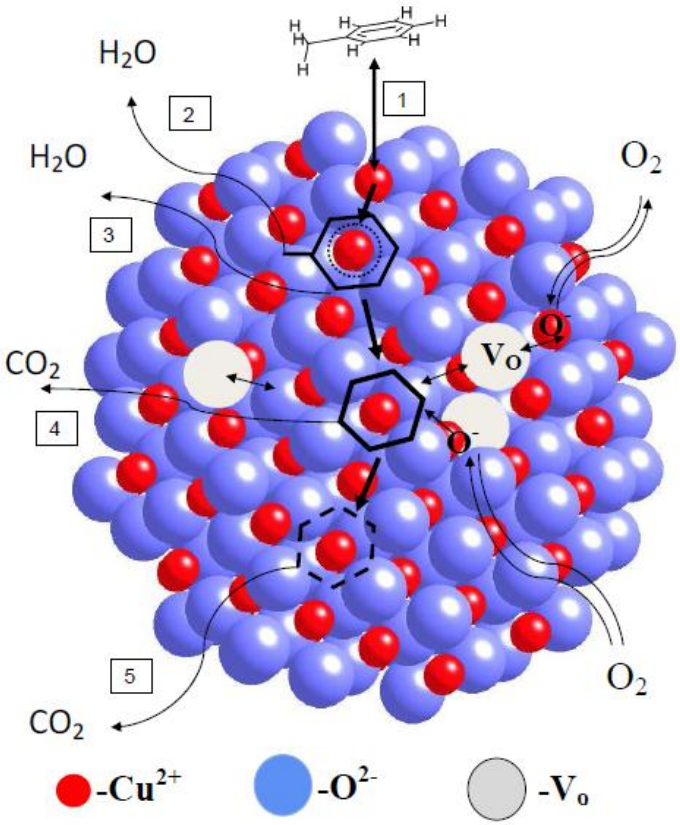

Figure 1: Reaction network for toluene total oxidation

The catalytic performance of the binary metal oxide CuO-CeO_2/Al_2O_3 is compared with corresponding single metal oxides CuO/Al_2O_3 and CeO_2/Al_2O_3. The reason for the improved performance of the binary metal oxide catalyst compared to its single metal oxides is investigated by means of structural characterization methods viz. high resolution transmission electron microscopy

(HRTEM) and X-ray absorption spectroscopy (XAS). Based upon structural characterization, the improved performance of the mixed oxide catalyst can be attributed to the formation of a solid solution $Ce_{1-x}Cu_xO_{2-x}$, i.e. with Cu^{2+} substitutionally incorporated into CeO_2, existing next to a bulk CuO phase. XAS experiments during temperature programmed reduction of the $CuO\text{-}CeO_2/Al_2O_3$ catalyst indicate enhanced reduction of both Ce and Cu inside the solid solution. However, ceria passes O to nearby copper to keep it oxidized. When all the readily available O^{2-} from ceria are consumed, the dissolved Cu^{2+} reduces to Cu^{1+}.

It is found that two separate sites in the catalyst are responsible for oxidation and reduction (Figure 2): toluene is oxidized on the dissolved Cu^{2+} sites in the solid solution, while dioxygen is reduced at the Ce^{3+} sites. Ce sites upon oxidation quickly transfer electrons and oxygen ions to Cu sites. Reduced Ce^{3+} can also be re-oxidized by H_2O or CO_2.

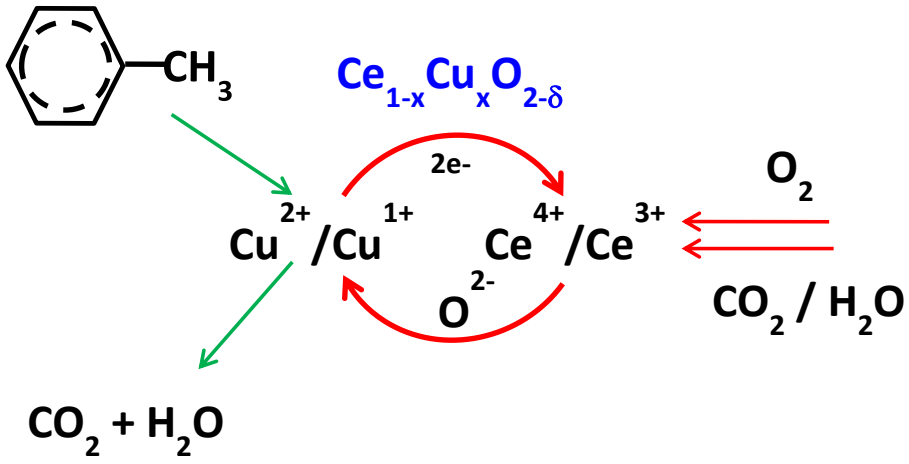

Figure 2: The general redox scheme describing heterogeneous oxidation reactions in $CuO\text{-}CeO_2/Al_2O_3$

In contrast to CeO_2, reduced CuO/Al_2O_3 cannot be re-oxidized by H_2O or CO_2. The observed activity decrease for CuO/Al_2O_3 in the presence of water can be attributed to a competition between H_2O/CO_2 and dioxygen for the same active sites.

The detailed reaction mechanism and the nature and structure of active sites in $CuO\text{-}CeO_2/Al_2O_3$ for the total oxidation of toluene provides necessary information for developing a microkinetic model.

Limiting the reaction network to the reduction and oxidation on the catalyst allows to obtain a kinetic model that describes adequately the experimental data. A single set of kinetic parameters could explain a broad range of temperatures and states, i.e., degrees of reduction of the catalyst. The kinetic parameters were estimated to be statistically significant and to have a sound physico-chemical meaning. The corresponding rate coefficients are estimated by a non-weighted, non-linear least squares regression. The $CuO\text{-}CeO_2/Al_2O_3$ catalyst shows a high rate of water formation from toluene during the reduction of the catalyst and a high ability to restore its initial activity by O_2 activation and subsequent re-oxidation of the catalyst. In addition to the rate coefficients and activation energies, the partial order of dioxygen is also significantly estimated. The rate determining step in the whole process was found to be the destruction of the aromatic ring. A linear dependency of activation energies of the processes including diffusion of oxygen from the bulk to the surface on degree of reduction of the catalyst was found. Bulk to surface oxygen diffusion is found to be slower on reduced catalyst than on a pre-oxidized catalyst and is described by a linear increase of the corresponding activation energies with increasing degree of reduction.

List of Symbols

Roman symbols

A_0	Pre-exponential factor (m^3 mol^{-1} s^{-1}, kg mol^{-1} s^{-1})
$C_{b,A}$	Concentration of catalyst bulk species A (mol kg_c^{-1})
$C_{b,A}^0$	Initial concentration of catalyst bulk species A (mol kg_c^{-1})
Cf_A	Calibration factor of gas A
$C_{g,A}$	Concentration of gas species A (mol m_g^3)
C_{s,A_s}	Concentration of catalyst surface species A (mol kg_c^{-1})
C_{s,A_s}^0	Initial concentration of catalyst surface species A (mol kg_c^{-1})
C_{Z_b}	Concentration of reduced bulk sites in the $Ce_{1-x}Cu_xO_{2-x}$ solid solution of the catalyst (mol kg_c^{-1})
$C_{b,Z_{b_{tot}}}$	Total concentration of Cu and Ce sites in the bulk of the $Ce_{1-x}Cu_xO_{2-x}$ phase of the catalyst (mol kg_c^{-1})
C_{b,Z_bO}	Concentration of available bulk oxygen in the $Ce_{1-x}Cu_xO_{2-x}$ solid solution of the catalyst (mol kg_c^{-1})
$C_{s,Z_{Ce,s}}$	Concentration of reduced Ce sites (mol kg_c^{-1})
$C_{s,Z_{Ce,s_{tot}}}$	Total concentration of Ce sites on the surface of $Ce_{1-x}Cu_xO_{2-x}$ phase of the catalyst (mol kg_c^{-1})
$C_{s,Z_{Ce,s}O}$	Concentration of fully oxidized Ce sites (mol kg_c^{-1})
$C_{s,Z_{Cu,s}}$	Concentration of reduced Cu Sites (mol kg_c^{-1})
$C_{s,Z_{Cu,s_{tot}}}$	Total concentration of Cu sites on the surface of the $Ce_{1-x}Cu_xO_{2-x}$ phase of the catalyst (mol kg_c^{-1})
$C_{s,Z_{Cu,s}O_4}$	Concentration of oxidized Cu sites (mol kg_c^{-1})

$D_{O,b}$	Diffusion coefficient of oxygen atoms from the bulk to the surface ($m^2\ s^{-1}$)
$D^I_{eff,A}$	Effective Knudsen diffusion coefficient of gas component *A* in the inert zone ($m_g^3\ m_r^{-1}\ s^{-1}$)
$D^C_{eff,A}$	Effective Knudsen diffusion coefficient of gas component *A* in the catalytic zone ($m_g^3\ m_r^{-1}\ s^{-1}$)
E_a	Activation energy ($kJ\ mol^{-1}$)
E_a^0	Activation energy at zero degree of reduction of catalyst ($kJ\ mol^{-1}$)
F_A	Experimental outlet flowrate of gas *A* ($mol\ s^{-1}$)
$\hat{F}_A$	Simulated outlet flowrate of gas *A* ($mol\ s^{-1}$)
ΔH_a^0	Standard enthalpy of adsorption
K	Adsorption equilibrium constant
k_n	Rate coefficient of elementary step n ($m^3\ mol^{-1}\ s^{-1}$, $kg\ mol^{-1}\ s^{-1}$)
L_1	Length of the first zone of the reactor from the inlet (m_r)
L_2	Length of the first two zones of the reactor from the inlet (m_r)
L_3	Total length of the three zones of the reactor (m_r)
L_{23}	Excitation from 2nd shell
M_A	Molecular mass of component A ($g\ mol^{-1}$)
M_0	Zeroth moment of responses (Vs)
M_{45}	Excitation from 3rd shell
N_e	Number of experimental conditions (-)
N_g	Number of gases (-)
N_p	Number of pulses per response (-)
$N_{p,A}$	Molar pulsed quantity of gas *A* (mol)
N_{res}	Number of responses (-)
N_t	Number of samples per pulse response (-)
[O]	Number of oxygen atoms consumed from the catalyst during single pulse experiments (-)

$[O]_s$	Number of exchangeable oxygen atoms on the surface of the $Ce_{1-x}Cu_xO_{2-x}$ solid solution of the catalyst (-)
$[O]_b$	Number of exchangeable oxygen atoms in the bulk of the $Ce_{1-x}Cu_xO_{2-x}$ solid solution of the catalyst (-)
$[O]_t$	Total number of exchangeable oxygen atoms in CuO and CeO_2 of the catalyst (-)
$[O]_{tot}$	Total number of exchangeable oxygen atoms in the $Ce_{1-x}Cu_xO_{2-x}$ solid solution of the catalyst (-)
ΔP_A	Pressure decrease of gas A in the feed line (Pa)
P_A	Partial pressures of component A (Pa)
R	Universal gas constant (J mol^{-1} K^{-1})
R^0	Degree of reduction of the $Ce_{1-x}Cu_xO_{2-x}$ solid solution of the catalyst
R_c^0	Degree of reduction of the catalyst
R_A	Extensive production rate of component A (mol s^{-1})
$R_{g,A}$	Specific net production rate of gas species A (mol kg_c^{-1} s^{-1})
R_{s,A_s}	Specific net production rate of adsorbed species A (mol kg_c^{-1} s^{-1})
r	Radius of spherical particles (m)
S	Cross sectional area of the microreactor (m_g^3)
S^0	Sticking coefficient (-)
ΔS_a^0	Standard entropy of adsorption.
t	Time (s)
$\bar{t}$	Time taken for displacement of oxygen from the bulk to surface of the catalyst (s)
T	Temperature (K)
T_0	Room temperature (K)
T_{ref}	Reference temperature (K)
Δt	Sampling time (s)
V	Volume of feed line (m_g^3)
w	Weight applied to responses for regression

$\bar{x}$	Average traveling distance of the oxygen atoms in the lattice of the catalyst (m)
Y	CO_2 yield (mol%)
y	Experimental response sample points (V)
$\hat{y}$	Simulated response sample points (V)
z	Axial coordinate in the reactor (m_r)

Greek symbols

α	Proportionality constant between the change in activation energies with respect to the degree of reduction and degree of reduction (kJ mol^{-1})
ε_I	Bed porosity in the inert zone of the reactor
ε_C	Bed porosity in the catalytic zone of the reactor
$\eta_{CO_2}^{H_2O}$	The ratio between CO_2 yield from toluene pulse with and without H_2O
$\eta_{12CO_2}^{13CO_2}$	The ratio between CO_2 yield from toluene pulse with and without $^{13}CO_2$
θ	X-ray diffraction angle
ρ_B	Density of the catalytic bed ($kg_c\ m^{-3}$)
τ	Tortuosity factor (-)
$\boldsymbol{\tau_p}$	Pulse peak time (s)
ϕ	Objective function to be minimized (-)
χ_{Ce}	The ratio between CO_2 yield from $CuO\text{-}CeO_2/Al_2O_3$ and the sum of CO_2 yields from CuO/Al_2O_3 and CeO_2/Al_2O_3 (-)

Subscripts

b	bulk
c	catalyst
g	gas
I	Inert
p	pulse
r	reactor
ref	reference
s	surface

Abbreviations and acronyms

DOR	Degree of reduction
EDX	Energy dispersive X-ray analysis
EELS	Electron energy loss spectroscopy
HRTEM	High resolution transmission electron microscopy
ICP	Inductive coupled plasma
SAD	Selective area diffraction
STEM	Scanning transmission electron microscopy
TPR	Temperature programmed reduction or reaction
VOC	Volatile organic compound
XANES	X-ray absorption near edge structure
XAS	X-ray absorption spectroscopy
XRD	X-ray diffraction

Chapter 1
Introduction

Air pollution is a problem caused by the emission of certain pollutants that, either alone or by chemical reactions, pose serious negative impacts on environment and human health [1]. Some of the major contributors to air pollution are the volatile organic compounds (VOC). VOCs cover a wide range of compounds that differ in their properties and chemistry, but display similar behavior in the atmosphere. The release of VOC into the atmosphere has widespread environmental implications through their toxic nature and has been linked to stratospheric ozone depletion, formation of ground level ozone (photochemical smog) and aggravation of the global greenhouse effect [2-4]. Moreover, VOCs require special attention due to their high stability and ubiquitous nature. VOC emissions cover a large variety of sources, such as transport and industrial processes as well as household products. Examples of industrial processes that emit VOCs are chemical and pharmaceutical plants, petroleum refineries, automobile manufacturers, food processors, textile manufacturers etc. Among household sources, office supplies, printers, insulating materials, solvents and cleaning products, pressed woods, restaurant and domestic cooking, wood stoves are recognized as major contributors to VOCs emission. The nature of VOCs depends on the process and includes alkanes, alcohols, ketones, aldehydes, aromatics, paraffins, olefins, halogenated hydrocarbons [3].

There are several halogenated and non-halogenated compounds that fall under harmful VOCs. Halogenated, especially chlorinated

VOCs, such as dichloromethane, chloroform, carbon tetrachloride, 1,2-dichloroethane, trichloroethylene, tetrachloroethylene, have widespread applications in industry. These compounds are considered to be toxic and have severe implications in the destruction of the ozone layer [5, 6]. Toluene, benzene, xylene, propylene, formaldehyde, carbon monoxide, phenol, acetone, styrene are among the most common and toxic non-halogenated compounds that are worth to mention. Of the several solvents, benzene, toluene and xylene are widely used in diverse chemical, industrial and commercial processes [7]. These monocyclic hydrocarbons are also generated through processing, combustion and evaporation of gasoline and are constituents of several commercial products such as cleaning fluids, paints and glues [8]. Toluene and propene are recognized as highly polluting molecules due to their high POCP (photochemical ozone creativity potential) [9, 10].

The effects of air pollution on environmental and human health have led to a variety of standards and legislation over the past few decades [2]. According to the Goteborg protocol, the maximum VOC emission level by 2020 in the EU member countries should be reduced by nearly half as compared to the base year 2000 [11]. Therefore, the development of new effective methods for the abatement of VOC is mandatory. The most efficient methods for VOCs destruction are thermal and catalytic oxidation. Catalytic oxidation is becoming most attractive because of its high efficiency and low cost for dilute pollutant concentrations [12]. The next section will discuss more about catalytic oxidation and the type of catalysts used.

1.1 Heterogeneous catalytic oxidation

Heterogeneous catalytic oxidation is a broadly studied and industrially useful process. The main advantages of catalytic combustion compared with other decontamination technologies are high efficiency at a very low pollutants concentration, low energy consumption and low production of harmful by-products, such as dioxins and NO_x [12, 13]. Due to the large variety of VOCs and their complicated nature, the

selection of catalytic materials and the optimization of their formulation for various organic pollutants has been the subject of many studies and is not an easy task. Moreover, the catalytic performances depend on the preparation method, type of precursor, metal loading and particle size, nature of support [14, 15]. The operating conditions used, pollutant concentrations, overall gas flow rate, type of reactor also plays important role on the catalytic performances [12, 13].

Two classes of catalysts, noble metals and transition metal oxides, have been widely explored for oxidation of organic pollutants [12, 13, 15-19]. The noble metal based catalysts have high specific activity, resistance to deactivation and ability to be regenerated, but are more expensive and of lower stability in the presence of chlorine compounds. Transition metal oxides, such as copper, cobalt, manganese, and chromium, are known to be active combustion catalysts [12, 20]. They are less active at lower temperatures but have comparable activity at high temperatures [14]. The transition metal oxides are known for their lower cost, higher thermal stability, higher resistance to steam and higher specific surface area [21, 22]. In the past several years, much attention has been paid to transition metal oxides, especially to copper based catalysts [23-25]. Numerous studies on VOC oxidation have been on CuO catalyst.

1.2 CuO based catalysts in VOC oxidation

CuO based catalysts are considered to be some of the most active metal oxide catalysts available. CuO was reported to be as effective as Pt for the oxidation of n-butanol and methyl mercaptan [26]. Copper oxide on titania is shown to be more active than cobalt, manganese, and iron oxide on the same support [27]. Studies have also revealed CuO/Al_2O_3 to be the most active base metal oxide catalyst for the complete oxidation of ethanol [28, 29]. CuO was the most active transition-metal oxide of those tested for the catalytic total oxidation of toluene with γ-Al_2O_3 as support [30].

CuO catalysts have low activity at low temperatures and in the presence of total oxidation products. Copper promoted by ceria shows better catalytic performance for the complete oxidation of toluene, propane, benzene, and p-xylene as well as improved activity in the presence of the oxidation products CO_2 and water [30-32].

Adding ceria as a promoter to supported copper oxide has shown several advantages for the catalyst performance. Ceria was found to stabilize the dispersion of the active phase of the catalyst [33, 34]. Interactions between the doped ceria and CuO strongly affect their redox property which in turn has influence on the catalytic properties [33, 35, 36]. Tschoppe et al. [37] showed that by variation of the copper loading in a series of $Cu_xCe_{1-x}O_{2-x}$ samples, it was possible to separate the oxidation of the copper component and the cerium oxide support during N_2O temperature-programmed oxidation. Chen et al. [38] suggested a free movement of oxygen atoms from ceria to copper that leads to oxygen vacancies in ceria, significantly enhancing CuO/CeO_2, for NO reduction by CO. Ceria also acts as an oxygen storing phase due to the presence of mixed oxidation states (3+/4+) of cerium [39-42]. Copper doping of CeO_2 can improve the oxygen storage capacity, diffusivity and redox properties, which is attributed to the formation of structural defects [38, 39, 42, 43]. Bera et al. [43] found evidence for the formation of a $Ce_{1-x}Cu_xO_{2-\delta}$ type of solid solution phase in a CuO/CeO_2 catalysts. Higher concentrations of oxygen vacancies in the catalysts can enhance catalytic activity, the vacancies providing sites for dioxygen activation [44].

1.3 Mechanism for VOC oxidation

It is generally accepted that the oxidation of VOCs over transition metal oxide catalysts occurs according to a Mars–van Krevelen type redox cycle [31, 45-48]. Fig. 1.1 illustrates VOC oxidation based on the Mars-van Krevelen mechanism. In the catalyst oxygen species are present in the lattice – surface and bulk – which is in equilibrium with the adsorbed oxygen species – O^-, O_2^-, O_{2ads}.

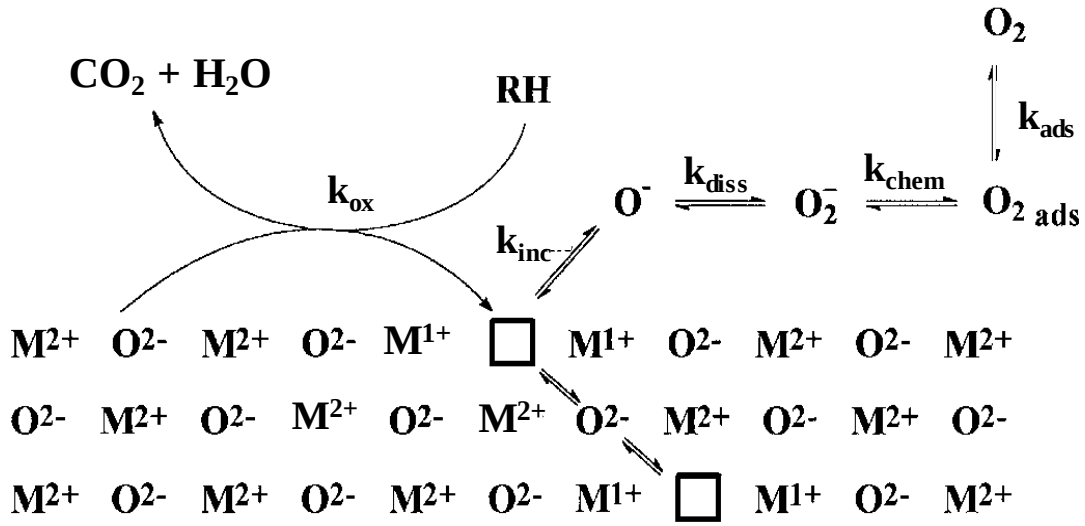

Figure 1.1 Mars-van Krevelen mechanism (modification of figure from [49]

The mechanism consists of at least 2 steps:

(a) $RH+MO \rightarrow M+H_2O+CO_2$
(b) $M + (1/2)O_2 \rightarrow MO$

The hydrocarbon (RH) adsorbs on the catalytic surface and reacts with the surface lattice oxygen to form total oxidation products (H_2O and CO_2), thereby creating a vacancy on the surface. This vacancy is filled by the adsorbed oxygen species or the lattice oxygen diffusing from the bulk. However, the extent of oxygen extraction from the catalyst for the mechanism depends upon the oxygen mobility in the catalyst [12, 50, 51]. The amount of oxygen that takes part in the reaction and its restoration upon reoxidation varies depending on the catalysts and the hydrocarbon. This mechanism has been proven in many systems over a wide range of temperatures [52]. The role of adsorbed oxygen species, whether it reacts with the hydrocarbon in the total oxidation of VOCs, is still a matter of debate.

1.4 Mechanistic studies: the position of TAP reactor

Despite advances in surface science and computational chemistry that provide molecular level insight into surface physics and chemistry, catalyst development in industry is still based on time-consuming trial and error approaches, often leading to incremental improvements in the

process. This can be attributed to a lack of in-depth understanding of reaction mechanisms and kinetics, and of correlations between the physicochemical properties of the catalyst under reaction conditions and its performance. This knowledge is vital in catalyst development program, see Fig 1.2, bridging the identification of promising materials in the primary screening phase and the scale-up of the catalytic process. Progress in this direction is important in strengthening the competitiveness of the chemical industry.

To accelerate the rate of catalyst development an approach of high-throughput catalyst synthesis has been employed, but it ultimately does not offer the required structure-activity relationships for catalyst design. So the focus is on making the catalyst development program more efficient by increasing the quantity and quality of information obtained in each stage. Information that links changes in kinetic properties to changes in the structure of a catalyst sample is very valuable.

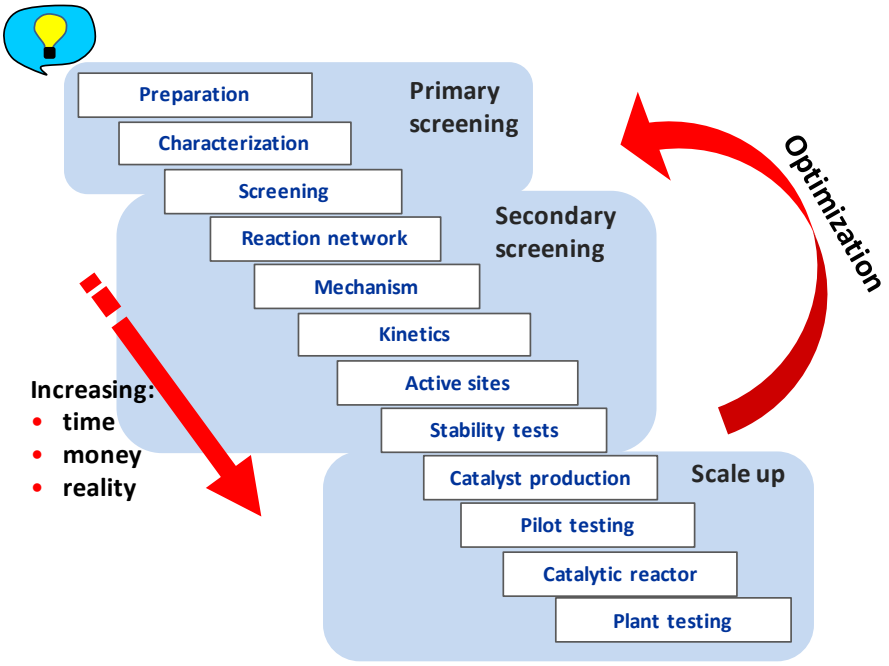

Figure 1.2 stages in a catalyst development program [53]

Understanding how the catalytic activity and selectivity of a substance is related to the composition and structure of the substance is a fundamental problem in the field of catalysis. This understanding

involves finding relationships between kinetic data and structural data. This correlation provides essential information for explaining how catalytic cycles work, and for creating new or improved catalysts.

Traditional steady-state techniques operating at or near ambient pressure have been successfully applied to kinetic studies, but they lack molecular detail due to the low time resolution, in the order of seconds. Steady-state testing provides macrokinetic models, that is, the reaction mechanism with few complex steps that cannot be subdivided further using the experimental data. This provides an integrated description of the reaction system by means of the analysis of the global behavior of the catalyst [54, 55]. These models cannot be confidently applied to predict the reactor performance in a wide range of operating conditions. Substantially improved knowledge of the catalytic events can be obtained by adaptation of spectroscopic techniques in flow reactors, enabling to monitor the catalyst in action (coined as operando spectroscopy).

Surface science techniques, like reactive molecular beam surface scattering which is a ultra high vacuum (UHV) technique, can be used to characterize the structure or composition of technical catalysts. However, direct kinetic testing of technical catalysts in surface science systems is usually impractical [56, 57]. Fundamental knowledge generated using surface science devices cannot be effectively extrapolated to industrial processes. A well known problem is the so-called "pressure gap" [58]. The large differences in pressures, and the difference between model surfaces, viz. single crystals versus commercial catalysts, make it very difficult to compare results from the two experimental regimes. Fig. 1.3 presents the pressure-materials diagram indicating the position of various approaches.

Under reaction conditions, the state of a catalyst can change due to a change in the catalyst surface area, crystal morphology, or surface oxidation state. During reaction, the available number of active sites can change, which can lead to a change in its structure and the specific reactivity. This complicates the determination of the number of active sites on a catalyst and their specific reactivity. An experimental strategy

that would provide means of maintaining the catalyst in a constant state or insignificant change in state, would simplify the determination the number of active sites and the kinetic characteristics of individual sites.

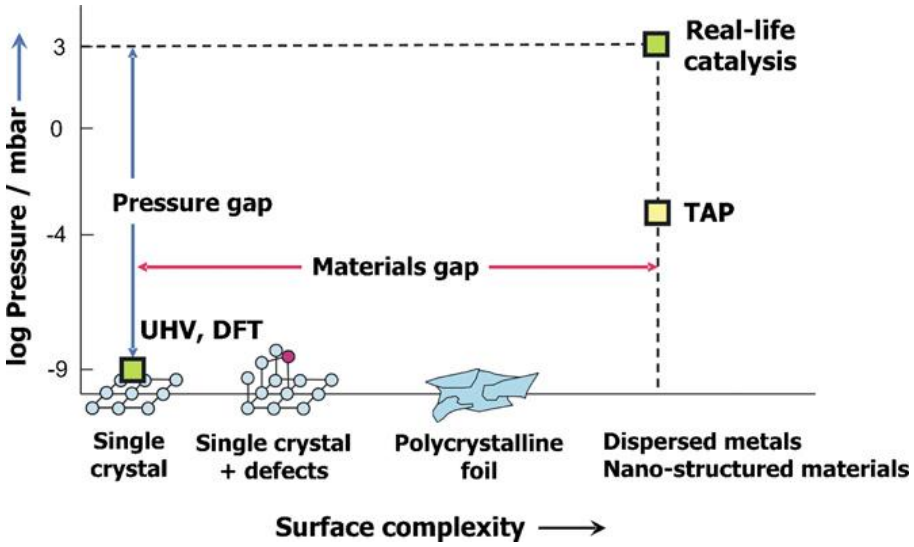

Figure 1.3 Pressure–materials diagram indicating the position of the various approaches to investigate mechanisms and kinetics of heterogeneously catalyzed reactions [53]

Transient methods can provide more mechanistic information about reaction intermediates and pathways of the various elementary steps when compared to steady-state experiments. Transient experiments allow reactions to be analyzed as individual steps, providing a detailed understanding of the functioning of the catalyst. Transients are introduced into a system by perturbation of one or more state variables, (pressure, temperature, composition, flow rate) [59-61]. The Temporal Analysis of Products (TAP) reactor [62-64] belongs to such experimental techniques. The main feature of the TAP technique is its sub-millisecond time resolution, which makes it a powerful approach to study mechanisms, kinetics, and transport phenomena of heterogeneously catalyzed gas–solid reactions at near-to elementary level. In a broader perspective, the main benefits of the TAP technique are with respect to its position in the pressure–materials diagram in Fig. 1.3. Its position in the pressure-materials diagram enables the investigation of model surfaces as well as practical catalysts. Moreover, the peak pressure in the reactor can reach values in the order of 100 Pa,

that is, up to 9 orders of magnitude higher than that applied in UHV techniques. These features bring the TAP reactor at the boundary between traditional steady-state flow techniques and surface science techniques with model surfaces in ultra-high vacuum [53]. In this thesis the TAP reactor has been used as a catalyst evaluation technique for VOCs oxidation research.

1.5 Outline of the thesis

The goal of this PhD is to study the mechanism and kinetics of toluene total oxidation over $CuO\text{-}CeO_2/Al_2O_3$ catalyst besides characterizing it. This PhD research consists of mainly three parts. In the first part of the research, the reaction path analysis of toluene total oxidation over $CuO\text{-}CeO_2/Al_2O_3$ is performed by use of Temporal Analysis of Products reactor (TAP) set-up. An investigation of the role of different oxygen species in the catalyst is performed and a detailed reaction network is unraveled using isotopic experiments.

The second part of the research, deals with an elaborate structural characterization of the Cu and Ce based single and binary metal oxide catalysts. The catalysts were studied by means of transmission electron microscopy and *in situ* X-ray absorption spectroscopy. The nature of active sites in the catalyst is explained and the role of ceria in the binary metal oxide catalyst in the global oxidation of toluene is discovered. Additionally, the participation and influence of total oxidation products towards the reaction is also investigated.

In the third and the final part of the research, the reaction path that was developed in the first part is validated by means of a detailed microkinetic model. Corresponding kinetic parameters are significantly estimated and are tested for their physicochemical meaning.

This thesis is divided into six chapters. Chapter 2 provides a description of the experimental set-up and procedures used. Furthermore, the preparation and the methods for characterization of the Cu and Ce based metal oxide catalysts are presented. The last part of chapter 2 presents the TAP reactor model. Chapter 3 presents the

reaction network for the toluene total oxidation over CuO-CeO_2/Al_2O_3 catalyst. A detailed mechanism of the total oxidation reaction and the role of different oxygen species in the catalyst are elaborated. In Chapter 4 a detailed structural characterization of the metal oxide catalysts using XRD, TEM and XANES is detailed. The role of ceria in CuO-CeO_2/Al_2O_3 is elaborated. A comparison of the activity of binary CuO-CeO_2/Al_2O_3 with the corresponding single metal oxides CuO/Al_2O_3 and CeO_2/Al_2O_3 is presented. The role of oxidation products in toluene total oxidation is also elaborated. Chapter 5 reports the kinetic modeling of toluene total oxidation over CuO-CeO_2/Al_2O_3 catalyst. A reaction scheme with detailed elementary steps for toluene total oxidation is proposed and kinetic parameters are significantly estimated. A kinetic state-by-state investigation of the catalyst is performed. A single set of parameters which can describe the various state of the catalyst is estimated. Finally Chapter 6 presents the most important conclusions from this study.

References

1. R.J. Heinsohn, R.L. Kabel, Sources and Control of Air Pollution, Prentice Hall, Upper Saddle River, NJ 1999.
2. M. Amann, M. Lutz, The revision of the air quality legislation in the European Union related to ground-level ozone, Journal of Hazardous Materials, 78 (2000) 41-62.
3. R. M. Heck, R.J. Farrauto, Catalytic Pollution Control, second ed., Wiley-Interscience, New York, 2002.
4. E.C. Moretti, N. Mukhopadhyay, VOC control: Current practices and future trends, Chem. Eng. Prog, 89 (1983) 20.
5. E.C. Moretti, Practical Solutions for Reducing Volatile Organic Compounds and Hazardous Air Pollutants, CWRT AIChE, New York, 2001.
6. V.J. Feron, J.E.H. Arts, P.J.v. Bladeren, Pollut. Atmos., 134 (1992) 18.
7. WHO, Sources of human and environmental exposure., in: WHO. Benzene. Environmental Health Criteria 150, WHO, Geneva, 1993, pp. 28-31.
8. P. Arlien-Suborg, Solvent Neurotoxicity, CRC Press, Inc., Boca Raton, Florida, 1992.
9. H. Fontane, M. Veillerot, J.C. Gallo, R. Guillermo, in: 8th International Symposium on Transport and Air Pollution, Graz, 1999.
10. E. Rivière, CITEPA Report, in, Paris, 1998.
11. Environmental Fact Sheet No. 19, January 2006, in, Produced by The Swedish NGO Secretariat on Acid Rain, Goteborg, Sweden.
12. J.J. Spivey, Complete catalytic oxidation of volatile organics, Industrial & Engineering Chemistry Research, 26 (1987) 2165–2180.

13. K. Everaert, J. Baeyens, J. Hazard. Mater. B, 109 (2004) 113.
14. P.-O. Larsson, A. Andersson, Complete Oxidation of CO, Ethanol, and Ethyl Acetate over Copper Oxide Supported on Titania and Ceria Modified Titania, Journal of Catalysis, 179 (1998) 72-89.
15. L.F. Liotta, Catalytic oxidation of volatile organic compounds on supported noble metals, Applied Catalysis B: Environmental, 100 403-412.
16. D. Pope, D.S. Walker, R.L. Moss, Atmos. Environ., 12 (1978) 1921.
17. L.F. Liotta, M. Ousmane, G. Di Carlo, G. Pantaleo, G. Deganello, G. MarcÃ¬, L. Retailleau, A. Giroir-Fendler, Total oxidation of propene at low temperature over Co_3O_4-CeO_2 mixed oxides: Role of surface oxygen vacancies and bulk oxygen mobility in the catalytic activity, Applied Catalysis A: General, 347 (2008) 81-88.
18. P. Papaefthimiou, T. Ioannides, X.E. Verykios, Combustion of non-halogenated volatile organic compounds over group VIII metal catalysts, Applied Catalysis B: Environmental, 13 (1997) 175-184.
19. L.F. Liotta, M. Ousmane, G. Di Carlo, G. Pantaleo, G. Deganello, G. Marci, L. Retailleau, A. Giroir-Fendler, Applied Catalysis A: General, 347 (2008) 81.
20. E.M. Cordi, P.J. O'Neill, J.L. Falconer, Transient oxidation of volatile organic compounds on a CuO/Al_2O_3 catalyst, Applied Catalysis B: Environmental, 14 (1997) 23-36.
21. J. Carpentier, J.F. Lamonier, S. Siffert, E.A. Zhilinskaya, A. Aboukaïs, Characterisation of Mg/Al hydrotalcite with interlayer palladium complex for catalytic oxidation of toluene, Applied Catalysis A: General, 234 (2002) 91-101.
22. M.C. Álvarez-Galván, V.A. de la Peña O'Shea, J.L.G. Fierro, P.L. Arias, Alumina-supported manganese- and manganese–palladium oxide catalysts for VOCs combustion, Catalysis Communications, 4 (2003) 223-228.

23. X.-C. Zheng, S.-H. Wu, S.-P. Wang, S.-R. Wang, S.-M. Zhang, W.-P. Huang, The preparation and catalytic behavior of copper–cerium oxide catalysts for low-temperature carbon monoxide oxidation, Applied Catalysis A: General, 283 (2005) 217-223.

24. M.-F. Luo, J.-M. Ma, J.-Q. Lu, Y.-P. Song, Y.-J. Wang, High-surface area CuO–CeO2 catalysts prepared by a surfactant-templated method for low-temperature CO oxidation, Journal of Catalysis, 246 (2007) 52-59.

25. G. Avgouropoulos, Ioannides, T., Matralis, H.K. , Batista, J., Hocevar, S., CuO-CeO2 mixed oxide catalysts for the selective oxidation of carbon monoxide in excess hydrogen, Catalysis Letters, 73 33-40.

26. C.J. Heyes, James G. Irwin, Hilary A. Johnson, R.L. Moss, The catalytic oxidation of organic air pollutants part 1. Single metal oxide catalysts, Journal of Chemical Technology and Biotechnology, 32 (1982) 1025-1033.

27. P.-O. Larsson, A. Andersson, L.R. Wallenberg, B. Svensson, Combustion of CO and Toluene; Characterisation of Copper Oxide Supported on Titania and Activity Comparisons with Supported Cobalt, Iron, and Manganese Oxide, Journal of Catalysis, 163 (1996) 279-293.

28. Y.-F.Y. Yao, Ind. Eng. Chem. Process Des. Dev, 23 (1984) 60.

29. H. Rajesh, U.S. Ozkan, Complete Oxidation of Ethanol, Acetaldehyde, and Ethanol/Methanol Mixtures over Copper Oxide and Copper-Chromium Oxide Catalysts, Industrial & Engineering Chemistry Research, 32 (1993) 1622-1630.

30. C.-H. Wang, S.-S. Lin, C.-L. Chen, H.-S. Weng, Performance of the supported copper oxide catalysts for the catalytic incineration of aromatic hydrocarbons, Chemosphere, 64 (2006) 503-509.

31. P.M. Heynderickx, J.W. Thybaut, H. Poelman, D. Poelman, G.B. Marin, The total oxidation of propane over supported Cu and Ce

oxides: A comparison of single and binary metal oxides, Journal of Catalysis, 272 (2010) 109-120.

32. C.-H. Wang, Al_2O_3-supported transition-metal oxide catalysts for catalytic incineration of toluene, Chemosphere, 55 (2004) 11-17.
33. L. Dong, Y. Hu, M. Shen, T. Jin, J. Wang, W. Ding, Y. Chen, Dispersion Behaviors of Copper Oxide on the Mixed "CeO_2 + γ-Al_2O_3" Support, Chemistry of Materials, 13 (2001) 4227-4232.
34. B. Skarman, T. Nakayama, D. Grandjean, R.E. Benfield, E. Olsson, K. Niihara, L.R. Wallenberg, Chemistry of Materials, 14 (2002) 3686-3699.
35. J. Chen, J. Zhu, Y. Zhan, X. Lin, G. Cai, K. Wei, Q. Zheng, Characterization and catalytic performance of Cu/CeO2 and Cu/MgO-CeO2 catalysts for NO reduction by CO, Applied Catalysis A: General, 363 (2009) 208-215.
36. W. Shan, W. Shen, C. Li, Structural Characteristics and Redox Behaviors of Ce1-xCuxOy Solid Solutions, Chemistry of Materials, 15 (2003) 4761-4767.
37. A. Tschope, J. Markmann, P. Zimmer, R. Birringer, Chadwick, N2O Temperature-Programmed Oxidation and EXAFS Studies on the Dispersion of Copper in Ceria-Supported Nanocatalysts, Chemistry of Materials, 17 (2005) 3935-3943.
38. J. Chen, Y. Zhan, J. Zhu, C. Chen, X. Lin, Q. Zheng, The synergetic mechanism between copper species and ceria in NO abatement over Cu/CeO2 catalysts, Applied Catalysis A: General, 377 (2010) 121-127.
39. P.G. Harrison, I.K. Ball, W. Azelee, W. Daniell, D. Goldfarb, Nature and Surface Redox Properties of Copper(II)-Promoted Cerium(IV) Oxide CO-Oxidation Catalysts, Chemistry of Materials, 12 (2000) 3715-3725.

40. G. Sedmak, S. Hocevar, J. Levec, Kinetics of selective CO oxidation in excess of H_2 over the nanostructured $Cu_{0.1}Ce_{0.9}O_{2-y}$ catalyst, Journal of Catalysis, 213 (2003) 135-150.

41. X. Wang, J.A. Rodriguez, J.C. Hanson, D. Gamarra, A. Martínez-Arias, M. Fernández-Garcia, Unusual Physical and Chemical Properties of Cu in $Ce_{1-x}Cu_xO_2$ Oxides, The Journal of Physical Chemistry B, 109 (2005) 19595-19603.

42. Z. Wu, M. Li, J. Howe, H.M. Meyer, S.H. Overbury, Probing Defect Sites on CeO2 Nanocrystals with Well-Defined Surface Planes by Raman Spectroscopy and O2 Adsorption Langmuir, 26 (2010) 16595-16606.

43. P. Bera, K.R. Priolkar, P.R. Sarode, M.S. Hegde, S. Emura, R. Kumashiro, N.P. Lalla, Structural Investigation of Combustion Synthesized Cu/CeO_2 Catalysts by EXAFS and Other Physical Techniques: Formation of a Ce1-xCuxO2-δ Solid Solution, Chemistry of Materials, 14 (2002) 3591-3601.

44. V. Shapovalov, H. Metiu, Catalysis by doped oxides: CO oxidation by $Au_xCe_{1-x}O_2$, Journal of Catalysis, 245 (2007) 205-214.

45. P. Mars, D.W.v. Krevelen, Oxidations carried out by means of vanadium oxide catalysts, Chemical Engineering Science, 3 (1954) 41-58.

46. C. Doornkamp, V. Ponec, The universal character of the Mars and Van Krevelen mechanism, Journal of Molecular Catalysis A: Chemical, 162 (2000) 19-32.

47. V. Balcaen, R. Roelant, H. Poelman, D. Poelman, G.B. Marin, TAP study on the active oxygen species in the total oxidation of propane over a $CuO–CeO_2/\gamma\text{-}Al_2O_3$ catalyst, Catalysis Today, 157 (2010) 49-54.

48. A.C. Gluhoi, N. Bogdanchikova, B.E. Nieuwenhuys, The effect of different types of additives on the catalytic activity of Au/Al_2O_3 in

propene total oxidation: transition metal oxides and ceria, Journal of Catalysis, 229 (2005) 154-162.

49. J. Haber, W. Turek, Kinetic Studies as a Method to Differentiate between Oxygen Species Involved in the Oxidation of Propene, Journal of Catalysis, 190 (2000) 320-326.
50. C.N. Satterfield, Heterogeneous Catalysis in Industrial Practice 2ed., McGraw-Hill New York, 1991.
51. M. Iwamoto, Y. Yoda, N. Yamazoe, T. Seiyama, J. Phys. Chem., 82 (1978) 2564.
52. B. Grzybowska-Świerkosz, Thirty years in selective oxidation on oxides: What have we learned?, Topics in Catalysis, 11-12 (2000) 23-42.
53. J. Pe´rez-Ramı´rez, E.V. Kondratenko, Evolution, achievements, and perspectives of the TAP technique, Catalysis Today, 121 (2007) 160-169.
54. R.D. Cortright, Dumesic, J.A., Kinetics of heterogeneous catalytic reactions: Analysis of reaction schemes, Advances in Catalysis, 46 (2001) 161-264.
55. Guy B. Marin, G.S. Yablonsky, Kinetics of Chemical Reactions - Decoding Complexity, Wiley-VCH Verlag & Co. KGaA, 2011.
56. R.I. Masel, Principles of Adsorption and Reaction on Solid Surfaces, Wiley, New York, 1996.
57. G.A. Somorjai, Introduction to Surface Chemistry and Catalysis, Wiley, New York 1994.
58. H.P. Bonzel, The role of surface science experiments in understanding heterogeneous catalysis, Surface Science, 68 (1977) 236-258.
59. C.O. Bennett, Experiments and Processes in the Transient Regime for Heterogeneous Catalysis, Advances in Catalysis, 44 (1999) 329-416.

60. T. Engel, Ertl, G., Elementary Steps in the Catalytic Oxidation of Carbon Monoxide on Platinum Metals, Advances in Catalysis, 28 (1979) 1-78.

61. S.L. Shannon, Goodwin Jr., J.G., Characterization of catalytic surfaces by isotopic-transient kinetics during steady-state reaction, Chemical Reviews, 95 (1995) 677-695.

62. J.T. Gleaves, G.S. Yablonskii, P. Phanawadee, Y. Schuurman, TAP-2: An interrogative kinetics approach, Applied Catalysis A: General, 160 (1997) 55-88.

63. J.T. Gleaves, G. Yablonsky, X. Zheng, R. Fushimi, P.L. Mills, Temporal Analysis of Products (TAP) - Recent advances in technology for kinetic analysis of multi-component catalysts, Journal of Molecular Catalysis A: Chemical, 315 (2010) 108-134.

64. J.T. Gleaves, J.R. Ebner, P.L. Mills, A Novel Catalyst Evaluation System For Temporal Analysis of Reaction Products With Submillisecond Time Resolution, Studies in Surface Science and Catalysis, 38 (1988) 633-644.

Chapter 2

Experimental procedures and reactor model

2.1 Introduction

In this chapter a detailed description on all the experimental set-ups, procedures and conditions used in this PhD work will be presented. Section 2.2 will provide a survey on the Temporal Analysis of Products or TAP set-up which was used for performing experiments for studying the catalytic activity. Section 2.3 will discuss the procedure for TAP experiments. A detailed structural characterization of the catalyst is performed by using several techniques including advanced XRD, TEM, as well as time-resolved operando XANES. Catalyst preparation and characterization techniques will be outlined in Section 2.4. Section 2.5 will present the reactant gases and liquids used in this study. Various definitions and calculations are discussed in section 2.6. Sections 2.7 and 2.8 describe the TAP reactor model and kinetic parameter estimation respectively.

2.2 The TAP set-up

All the experiments performed for catalytic activity were carried out in the TAP reactor, which was developed by Gleaves et al [1] and has been recognized as an important transient experimental method for heterogeneous catalytic reaction studies. A TAP pulse response

experiment with its key components is shown in Fig. 2.1. The technique involves injecting a narrow gas pulse (10^{-11}-10^{-8} mol) into an evacuated microreactor (10^{-4} – 10^{-5} Pa). The gas emerging from the outlet of the microreactor, that is, any products and unreacted reactants, are monitored by a quadrupole mass spectrometer.

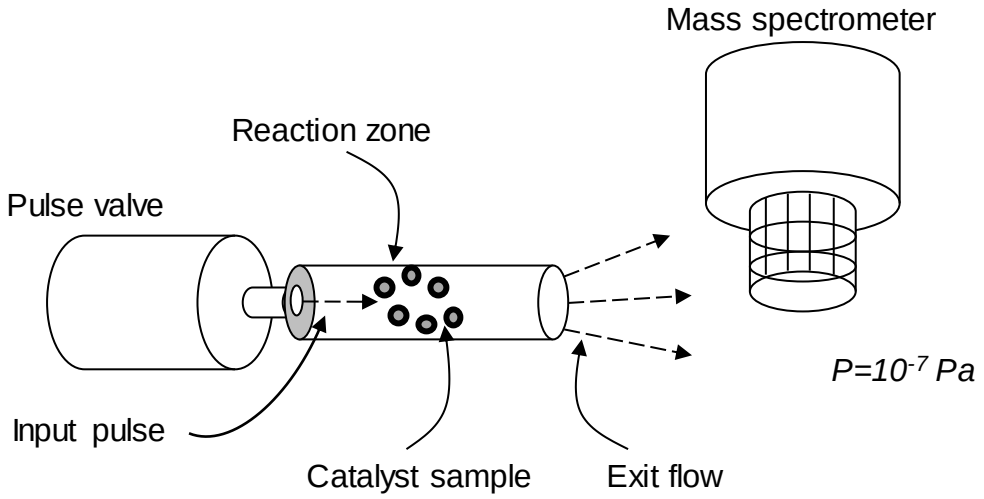

Figure 2.1: Key components of a TAP experiment [2]

One of the important features of the TAP reactor is its sub-millisecond time resolution. Due to its ability to function at sub-millisecond time scale it is possible to identify reaction intermediates with very low time of life, elucidate processes and their occurence in reaction networks, determinate rate coefficients of elementary steps (single-event kinetics), estimate number of active sites and manipulate surface oxidation states of the catalyst. The presence of external mass transfer limitations can be excluded as the TAP reactor operates in high vacuum.

It is possible to control the amount of molecules that are admitted into the reactor. By injecting a very small amount of molecules, it enables us to study the catalytic sequences at a given state of the catalyst. Usually in such experiments the amount of molecules pulsed ($<10^{15}$/pulse) is controlled up to 6 orders lower than the amount of active sites present in the catalyst. The transport of the gas molecules in the reactor are governed by Knudsen diffusion. In the Knudsen diffusion regime, the collision between gas molecules is negligible

compared to the collision of gas molecules with the surface of the reactor bed particles. As a result, the gas phase reactions can be eliminated [3]. In the Knudsen diffusion regime, the transport characteristics of any component are constant with respect to composition. This forms an important feature of TAP pulse response technique, to being able to extract the kinetic information without compromising the effects of transport. TAP experiments also allow the catalytic processes to happen in molecular diffusion regime. By admitting a large amount of molecules (>10^{15}/pulse), potential gas phase effects can be studied. The processes can be studied at different surface coverages of the catalyst.

The use of isotopes can be helpful in the determination of reaction mechanisms. In TAP reactor experiments, only a small amount of expensive isotopes is needed. Fig. 2.2 represents the key advantages of a TAP reactor

Time resolution	Vacuum	Specimen
Millsecond regime	No external mass transfer limitations	From model surfaces to practical catalysts
Diffusion regime	**T-control**	**Reconstruction**
Knudsen or molecular	Very low ΔT_{ad} Pulse sizes 0.1-10 nmol	Minimal alteration of the catalyst surface
Peak pressure	**Use of isotopes**	**Oxidation state**
Up to 100 Pa P_{TAP}/P_{UHV}~10^{6}-10^{9}	Discrimination of amus Small amounts needed	Can be manipulated and probed

Figure 2.2 Key advantages of a TAP reactor (modification of figure from [4])

The main components of a TAP reactor set-up are

- a high vacuum system
- a microreactor
- a fast pulse feed system
- a feed preparation section

- a mass spectrometer
- a computerized control and data acquisition system

2.2.1 High vacuum system

The TAP apparatus comprises three separate vacuum chambers designated as: the reactor chamber, the differential chamber and the detector or analysis chamber. A schematic diagram is presented in Fig. 2.3.

The reactor chamber is pumped by a Varian VHS10 oil diffusion pump and a Varian SD700 mechanical pump and the differential chamber by a Varian VHS6 oil diffusion pump and a Varian SD 700 mechanical pump. The reactor chamber holds the microreactor and the manifold assembly with the pulse valves. The pressure in the reactor chamber, measured by a Balzers IKR020 cold cathode gauge head, amounts to 10^{-4} – 10^{-5} Pa. The differential chamber is placed between the reactor chamber and the analysis chamber, which creates a pre-vacuum for the latter. A pressure of 10^{-6} Pa is attained here. The analysis chamber holds the UTI 100C Mass spectrometer. The vacuum in the detector chamber, which is 10^{-7} Pa, is realized by a Balzers TPU 520 turbo molecular pump.

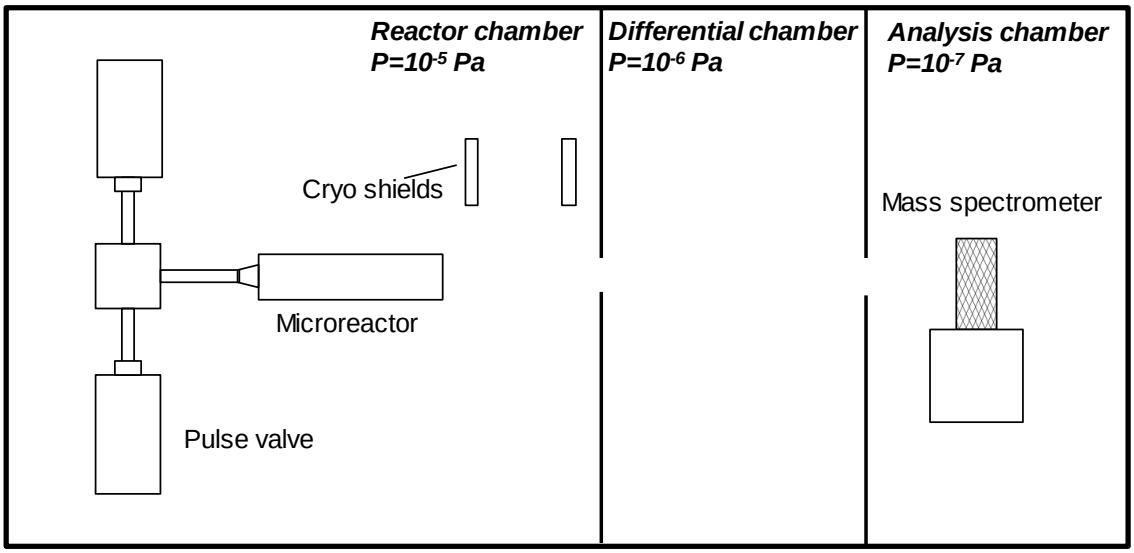

Figure 2.3. Schematic diagram of the TAP reactor depicting the different chambers based on pressure

The chambers are fitted with a liquid nitrogen trap in order to condense the oil vapors reaching the detector from the oil diffusion pumps, which may otherwise hamper the detection of compounds emerging from the outlet of the microreactor. A shutter valve separates the reactor chamber from the differential chamber. This is important while removing the reactor for refilling. In this way the high vacuum inside the differential and the analysis chamber is not lost during catalyst refilling.

2.2.2 Microreactor

The microreactor is shown schematically in Fig. 2.4. and is enclosed in a high-vacuum chamber with a background pressure of the order of 10^{-5} Pa. The microreactor is a hollow cylinder made of quartz material and has typical dimensions of 33 mm bed length length, 4.75 mm inner diameter and 7 mm outer diameter. Quartz material allows exposure of the microreactor to temperatures as high as 1200 K.

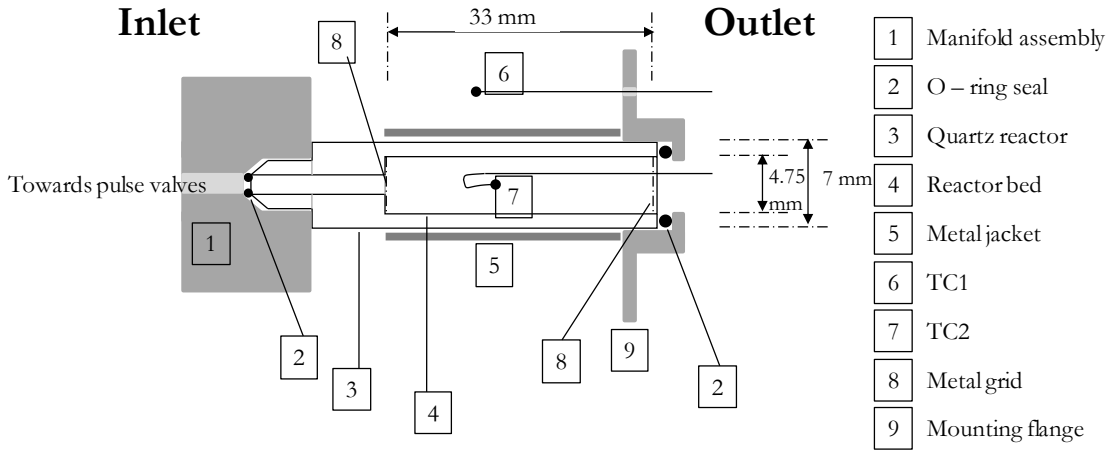

Figure 2.4. Schematic representation of the microreactor

Both the inlet and the outlet of the reactor are sealed by Viton® O-rings which are water cooled. The inlet of the microreactor is connected to the manifold assembly, which holds the high speed pulse valves. The microreactor is placed inside an oven which provides the heating, as high as 1000 K in vacuum. The temperature here is

controlled by a thermocouple TC1 as shown in the Fig. 2.4. The reactor is encased in a stainless steel jacket, which helps improve the heating of the reactor wall. The temperature inside the reactor is measured by the thermocouple TC2. A stainless steel grid is placed at both the ends of the reactor bed, which keeps it intact. The outlet of the reactor is mounted on a metal flange and the gases emerging from the reactor are exposed to a high vacuum at the analysis chamber.

2.2.3 Fast pulse feed system

Fig. 2.5 gives a schematic representation of the fast pulse feed section. It consists of a manifold that connects the pulse valves and the continuous valves to the microreactor. As continuous valves were not used in this PhD research, those will not be explained. For details on continuous valves the PhD dissertation of Glenn Creten can be referred [5]. During operational mode, the temperature of the manifold is set at 348 K by an OMRON™ temperature controller. The dead volume of the intersection of the valves and the microreactor is less than 1 μl. Two sweep valves corresponding to each high speed pulse valve are present which are used to evacuate the feed line of the respective valves before every new feed is injected.

The pulse valves present in the TAP section in Laboratory for Chemical Technology, Ghent university are that from a TAP-2 reactor set-up [6]. These high speed pulse valves are electromagnetically driven by energizing a wire coil with a short current pulse. An intense transient magnetic field is produced due to the current pulse, which attracts a magnetic disk that is attached to the shaft of the valve. During a pulse, the shaft lifts out of the valve seat and allows the required quantity of gas to flow out of the valve. When the magnetic field collapses, a spring located behind the magnetic disc forces the Kalrez® tip back into the valve seat. The typical opening time of a valve for one pulse is between 90 and 150μs.

2.2.4 Mass spectrometer

The TAP reactor set-up uses a UTI 100C quadrupole mass spectrometer (QMS) to detect components leaving the microreactor. The mass spectrometer is situated in the analysis chamber with its axis mounted perpendicular to the line of flight of the product pulse with the ionizer cage centered in the beam. The flow rate of a component is measured as a current which is transformed into a potential (Volts). Absolute calibration of the mass spectrometer for molar flow rates of different gas components is possible and is described in section 2.3.3.1. The mass spectrometer produces analog signals, which are digitized by the data acquisition system, and operates between m/e ratios (Atomic Mass Units (AMU)) of 1 to 300. The spectrometer is tuned to observe a single mass (m/e) for a component of interest. The response at that mass may be monitored at a rate of 10,000 times per second, thus generating the response curve of flow rate vs. time for that component at the outlet of the reactor. The response curves of different components may be measured by performing replicate experiments and tuning the QMS to monitor the appropriate masses.

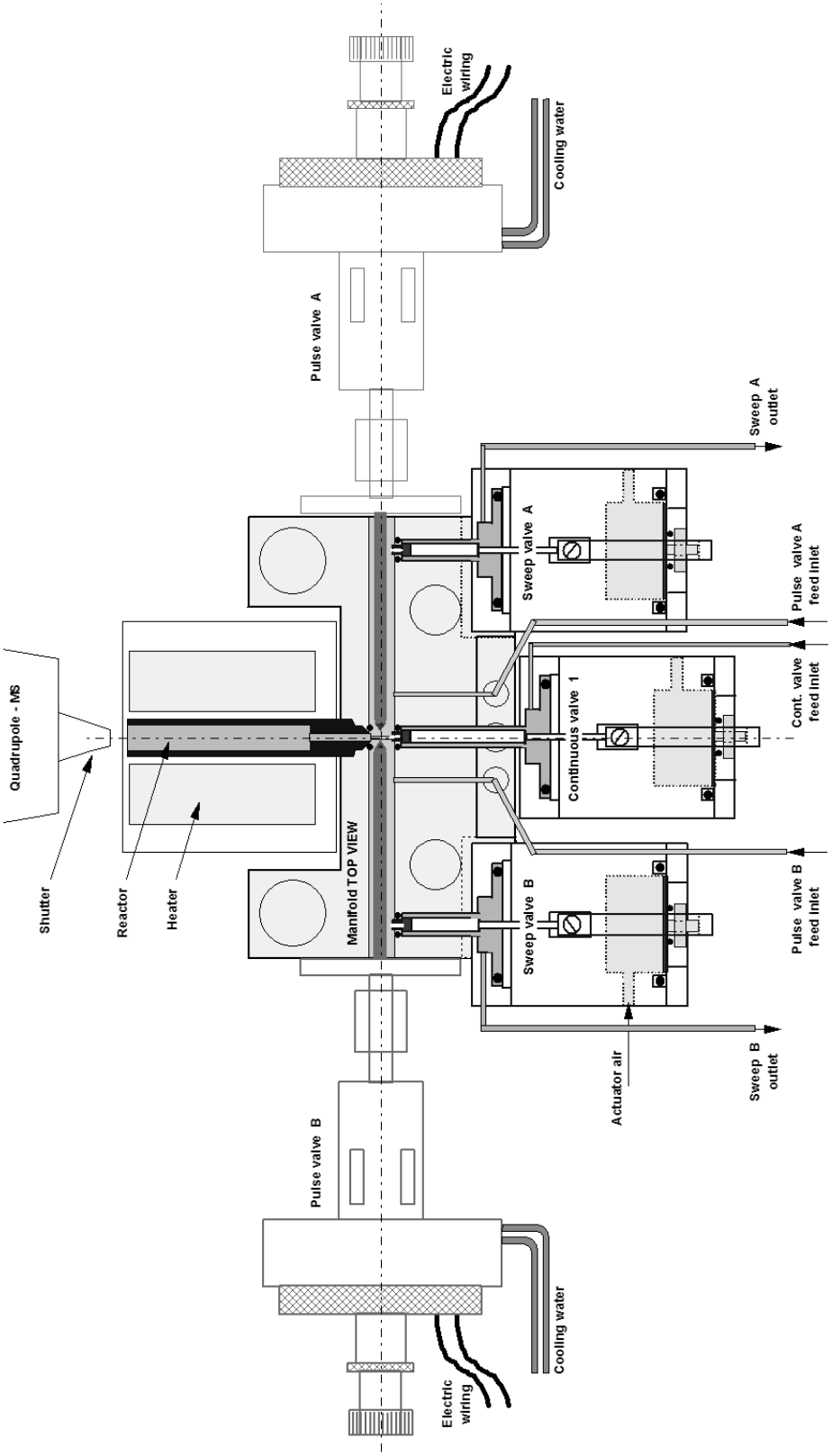

Figure 2.5 : Schematic representation of the manifold assembly with different valves, reactor and oven[7]

2.2.5 Feed preparation section

For preparation of feed for the pulse valves, there are separate gas and liquid feed sections. The feed section is schematically represented in Fig. 2.6 and consists of a number of connections, valves, pressure regulators and pressure and temperature indicators. The gas preparation section is connected to a vacuum system that is kept at approximately 1 Pa by a mechanical Varian SD200 pump. Through this vacuum system, each feed line can be evacuated separately and contamination between gases can be avoided. The feed isolation valves isolate the particular feed from getting contaminated. The feed evacuation and bleed valves are used to evacuate the feed from the lines. Two vessels of 150 cm^3 are present to prepare and store gas reactant mixtures shown as gas mixing A and B in the figure. The procedure for making gas mixtures is discussed in detail in the PhD theses of Balcaen [8] and Dewaele [9]. However, for the preparation of mixtures, the volume of each section of the feed line should be known. The volume of each section of the feed line was determined and is given in Fig. 2.7.

Pressure regulators are used to set the correct pressure downstream in the feed lines. Pressure and temperature indicators are also present in the feed line.

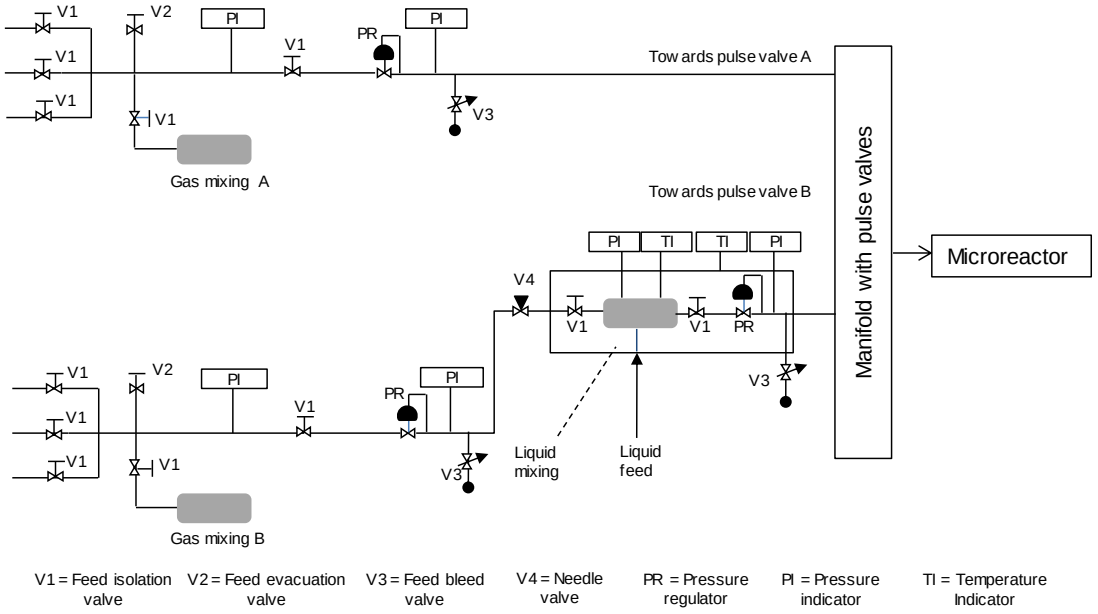

Figure 2.6 Gas and Liquid feeding in TAP

As the experiments performed in this PhD involved feeding toluene, a liquid feed set-up was designed and constructed at the Laboratory for Chemical Technology, Ghent University. It consists of a liquid vaporizing chamber, which is heated to 423K, into which the liquid feed is injected by use of a 500µl Hamilton Gastight ® #1750 syringe. The pressure at the point of injection is held by a Hamilton, high-temperature septum. The vaporizing chamber is also connected with gas bottles, which allows making gas mixtures. The temperature of the feeding lines is maintained at 423K. The manifold assembly containing the pulse valves is kept at 348K, the maximum temperature allowed. The pressure of the feed from the liquid feeding lines to the pulse valves is maintained at 1.1 bar as it was experimentally determined to be the pressure at which the pulse valves function best. The amount of liquid injected into the vaporizing chamber is such that a vapor state is maintained in the manifold assembly.

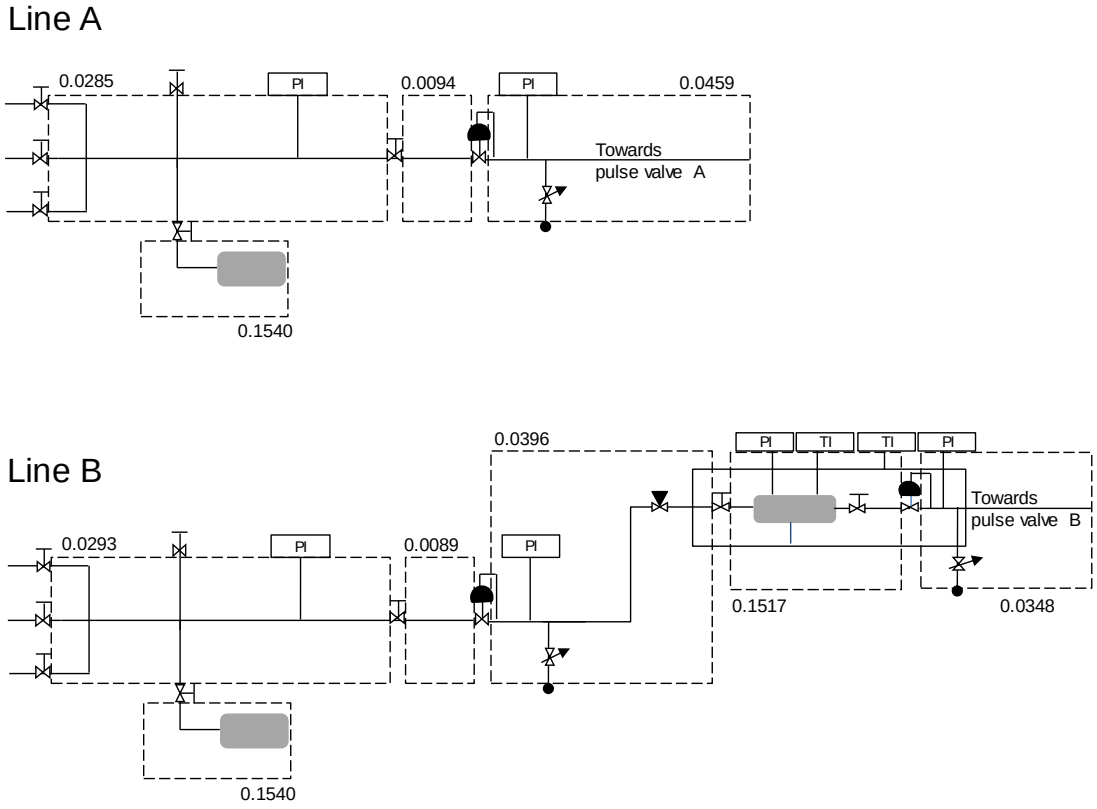

Figure 2.7 Volumes (m^3) of different sections of feed lines A and B

Pulse intensities are determined by monitoring the change in pressure in the known volume of the feed chambers while the valve is pulsing. By varying the feed pressure of the valve driver intensity settings, pulse intensities between 10^{13} and 10^{20} molecules per pulse can be attained. The latter corresponds to an instantaneous reactor pressure of nearly 1 atm.

2.2.6 Computerized control and data acquisition system

The computerized control of the TAP set-up includes following settings: the experimental conditions, the pulse valves, the QMS sensitivity etc. The feed valves and the valves for the vacuum system are manually operated. The control system is discussed in detail in the PhD theses of Creten [5] and Sack [7].

The data acquisition software, TAPPLOT, has two modes of operation: Scan mode and transient mode. In scan mode, a background scan of the detector chamber is performed, where the AMUs corresponding to all the components will be displayed. More on Scan experiments will be discussed in section 2.3.2. In transient mode, the transient experiments are performed. The settings of the pulse generator and the mass spectrometer can be provided in the transient mode. Transient experiments will be discussed in detail in section 2.3.2. The data from the experiment can be stored, plotted and analyzed. Many transformations of the pulse responses can also be done, like normalizing the responses, correcting the baseline, smoothing the curves, averaging several responses to improve the signal to noise ratio. Moreover, mathematical operations like addition, subtraction between pulse responses can be performed. This helps in accounting for the fragmentation of different components on a single AMU.

2.3 Experiments in TAP

2.3.1 Reactor configuration: Thin zone reactor

There are different configurations of TAP microreactor that has been used over the years. The most commonly used microreactor configuration is the three-zone one, see Fig. 2.8a. In this type of configuration, the catalyst particles are sandwiched between two beds filled with inert particles of the same size. The main advantage of three-zone configuration is that it maintains the catalyst under isothermal conditions [10]. However, because of the gas concentration gradient inside the reactor due to diffusional transport, it is a challenge to maintain a uniform surface composition throughout the catalyst bed. A 'thin-zone reactor' configuration was proposed by Shekhtman et al. [11] which allows to neglect the concentration gradients across the catalyst bed, and separate diffusion and chemical reaction. In a thin-zone reactor, the thickness of the catalyst bed is made very small compared to the total length of the reactor, see Fig. 2.8b. In this PhD the TAP experiments are performed in a thin-zone reactor.

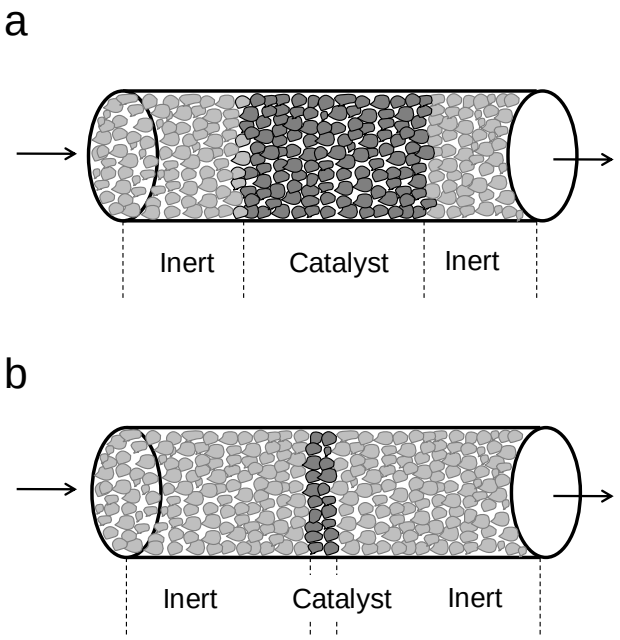

Figure 2.8 (a) Three zone reactor and (b) Thin-zone reactor

2.3.2 Types of experiments

There are three types of transient experiments performed in the TAP reactor.

- Single-pulse experiment
- Multi-pulse experiment
- Alternating-pulse experiment

Before performing these experiments a background scan in the vacuum chamber is done with and without a reactant feed in order to account for the components, residual or inherent, that are present in the chamber. A typical background spectrum without reactant feed is shown in Fig. 2.8.

A background scan with a high frequent reactant pulse train is used to screen a reaction by identifying different reaction products. By setting a complete AMU range the different products can be identified.

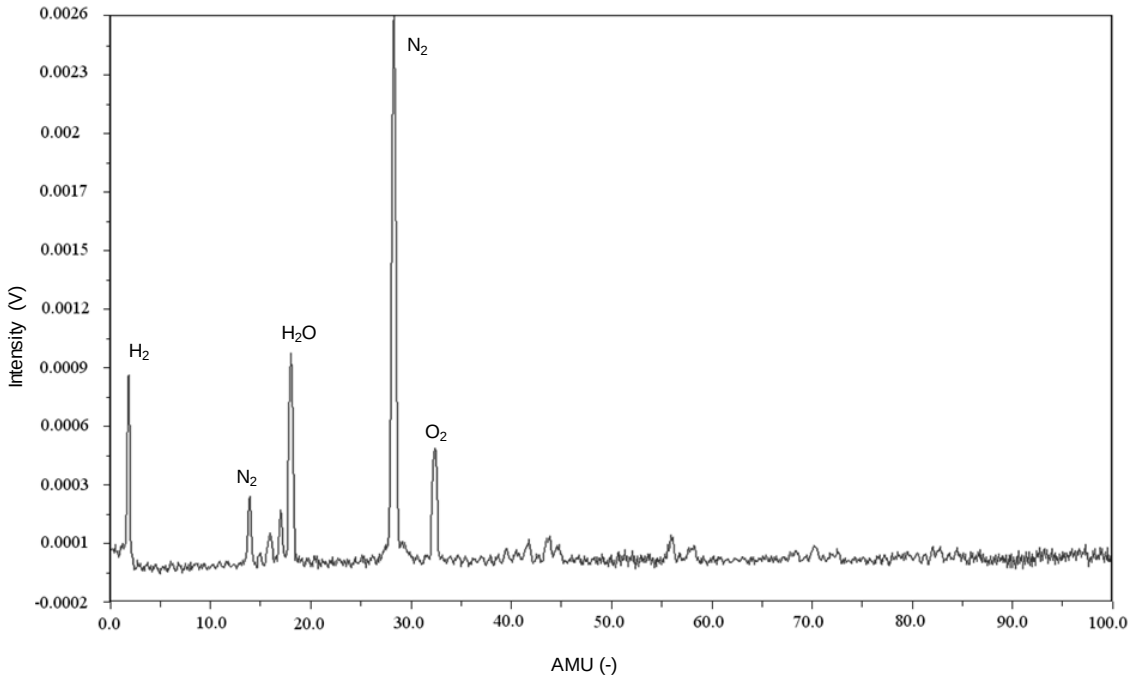

Figure 2.9 Spectrum of components from a background scan without reactant feed

2.3.2.1 Single-pulse experiment

Single-pulse experiments are carried out in order to study the interaction of a gas with the catalyst at a particular state. This is achieved by pulsing an amount of molecules that is sufficiently smaller than the amount of active sites in the catalyst. Typical number of molecules injected in a single-pulse experiment are of the order of 10^{13} molecules/pulse. Pulse openings of 90-110 μs were used for such experiments. These pulse times, which ensure that the flow inside the bed to be of the Knudsen diffusion type, are experimentally determined. In the Knudsen diffusion regime, the shape of the outlet gas responses over inert material does not depend on the pulse intensity. Typically, 20-25 responses of a particular AMU are collected and averaged in order to obtain a better signal to noise ratio. The pulse spacing between the single pulses of a single-pulse experiment is chosen sufficiently large to avoid interference of previous pulse response with the current. If components corresponding to different AMUs have to be measured, each component is measured one pulse after another for the required number of times and then averaged. A single-pulse experiment is also known as a state-defining experiment [12] since the state of the catalyst is not significantly altered during such experiments. Fig. 2.9 shows a typical pulse response measurement during a single-pulse experiment.

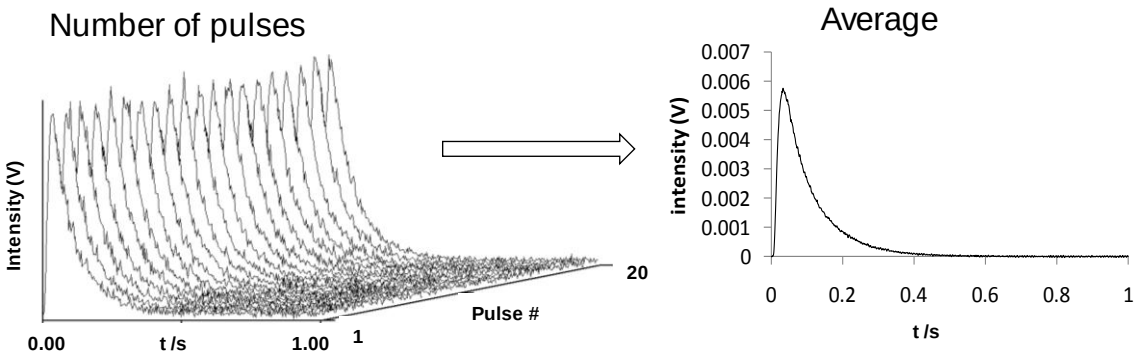

Figure 2.10 Typical pulse response measurement in a single-pulse experiment

2.3.2.2 Multi-pulse experiment

Multi-pulse experiments are carried out in order to change deliberately the state of the catalyst. This is achieved by injecting a higher number of pulses, typically 1000, with the amount of molecules of the order of $>10^{14}$ molecules/pulse. Pulse openings of 115-150 μs are used for such experiments. Multi-pulse experiments are used to study the interaction of a component with the catalyst at different degrees of surface coverage. Therefore, a multi-pulse experiment is also called a state-altering experiment since it alters the catalyst composition in some predetermined fashion. In this way the changes in kinetics can be related to differences in catalyst composition, catalyst structure, catalyst oxidation state, etc [6]. Fig. 2.10 shows a typical pulse response measurement during a multi-pulse experiment.

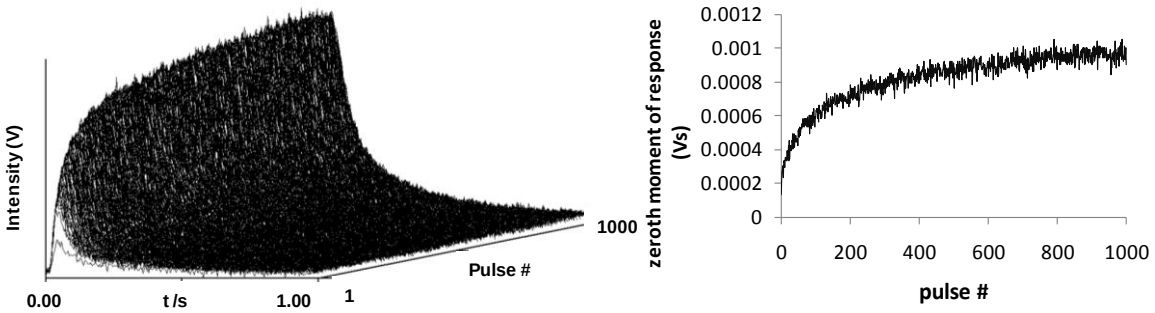

Figure 2.11 Typical pulse response measurement in a multi-pulse experiment

2.3.2.3 Alternating-pulse experiment

Both the reactant pulses are sequentially pulsed from two pulse valves with different time delays (Δt) between the pulses. The time delay between the pulsed reactants can be varied from 0 to several seconds. In general, by varying the time lags between the two pulses, the lifetime and reactivity of the surface species originating from the first, that is, the pump pulse can be determined. As in the case of a single-pulse experiment, a number of pulses responses are collected and averaged to obtain a better signal-to-noise ratio. Fig. 2.12 shows an example of a pulse response measurement during an alternating-pulse experiment [13].

Fig. 2.12a shows the krypton response and Fig. 2.12b the ethane response from an experiment with O_2/Kr as pump and CH_4/Kr as probe. A, B, C, D and E shows different time intervals between pump and probe pulses.
Alternating-pulse experiments, also known as pump-probe experiments are performed at various time lags between two different pulses.

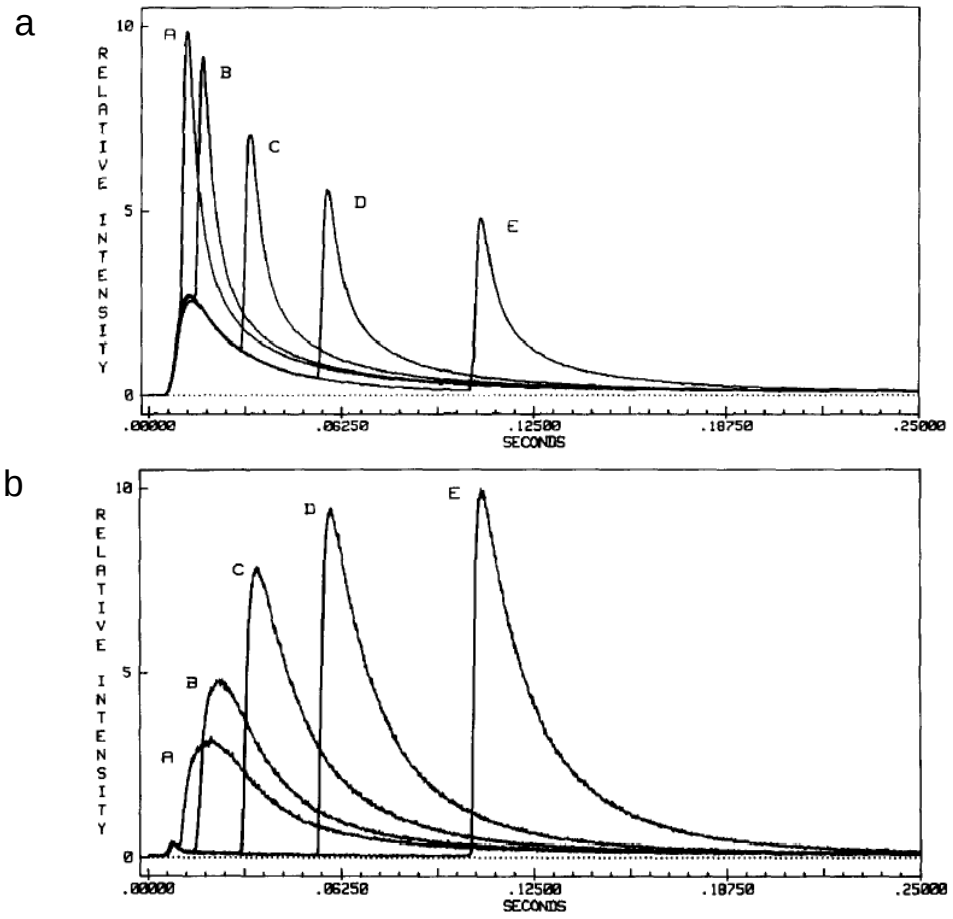

Figure 2.12 Typical pulse response measurement in a alternating-pulse experiment [13]

2.3.3 Standardization methods

2.3.3.1 Determination of the Knudsen diffusion regime

In the Knudsen diffusion regime, the molecules collide only with the solid surface. There is minimal or no collision between gas phase molecules. If the amount of admitted molecules is sufficiently small, the

transport through the reactor is governed by Knudsen diffusion [14]. The amount of molecules that is admitted, is determined by the width (opening) of the pulse valves. The longer the pulse opening, the larger the pulsed quantity. In the Knudsen diffusion regime, the shape of the response is independent of the pulse width. If the pulse width becomes too large, Knudsen diffusion is not the only transport mechanism. The maximum pulse width for Knudsen diffusion can vary slightly with reactor temperature and molecular mass of the gas component.

The maximum pulse width corresponding to Knudsen diffusion is determined experimentally according to the following procedure. Single-pulse experiments with any gas are carried out over inert material at different pulse widths (varying from 75 μs to 120 μs). The resulting pulse responses are area normalized. From a range of pulse responses, those with insignificant change in shape are identified to be Knudsen diffusion governed. The peak of the response will be at similar times. For responses corresponding to non-Knudsen regime, the maximum of the peak occurs at lower times and is higher. Fig. 2.8 shows the influence of increasing pulse width on the area normalized responses.

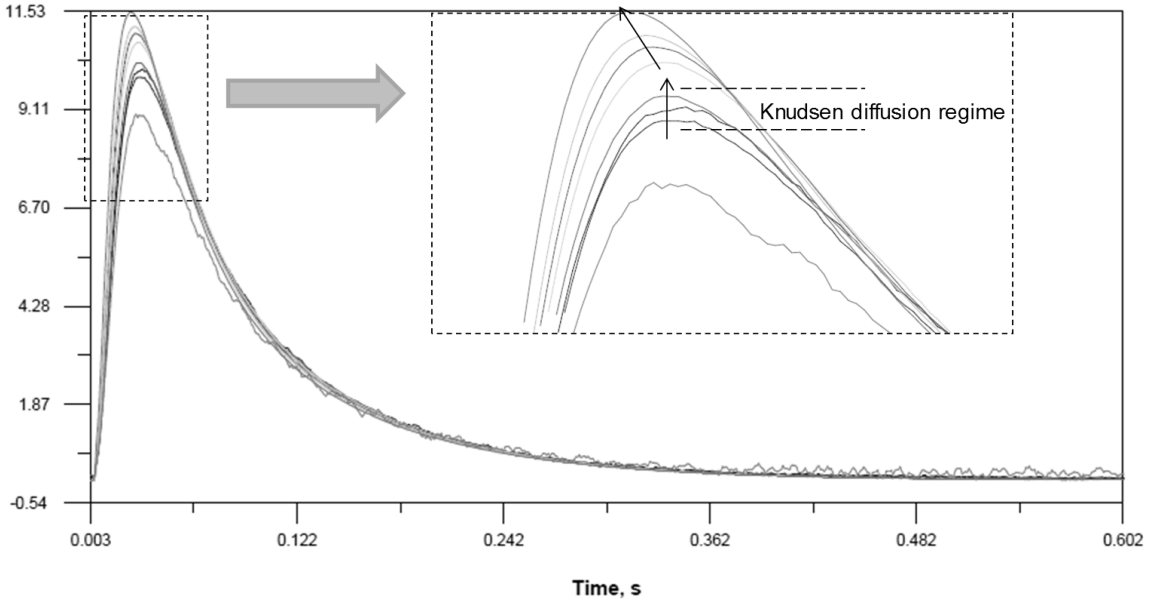

Figure 2.13 Area normalized pulse responses of Ar at 623K vs. increasing pulse widths.

2.3.3.2 Determination of Calibration factor

Quantitative interpretation of pulse responses requires a calibration with respect to the number of molecules in a pulse. As discussed in section 2.4 a TAP pulse response is measured in Volts corresponding to a molar flow rate at the reactor outlet. The area under the pulse response curve corresponds to the number of molecules detected by the mass spectrometer. For inert gases this is equal to amount of molecules pulsed into the reactor. A calibration factor relates the area under the pulse response to the amount of molecules pulsed. The calibration factor has to be determined for each gas reactant and proceeds in the following way.

A high frequent pulse train from a vessel with a known volume in the gas preparation section is injected into a reactor filled with inert particles and the pulse responses are monitored by the mass spectrometer. The pulse train consists of a number of pulses sufficient for a significant change in the pressure inside the vessel, typically 1000 high intensity pulses (>10^{15} molecules/pulse). The resulting pulse responses are averaged and the area under the curve is determined. The change in pressure in the vessel corresponds to the pulsed gas quantity. The absolute calibration factor for the component is then calculated using Eq. 2.1.

$$cf_A = \frac{N_p M_0 R T_0}{\Delta P_A V} \tag{2.1}$$

where cf_A is the absolute calibration factor of gas A (Vs mol^{-1})

M_0, the zeroth moment of the response (Vs)

N_p, the number of pulses (-)

R, the universal gas constant (8.314 J mol^{-1} K^{-1})

T_0, room temperature (K)

ΔP_A, the pressure decrease of gas A in the feed line (Pa)

V, the volume of the feed line (m_g^3)

2.4 Catalysts

2.4.1 Catalysts preparation

A commercial $CuO\text{-}CeO_2/Al_2O_3$ and lab made $CuO\text{-}CeO_2/Al_2O_3$, CuO/Al_2O_3 and CeO_2/Al_2O_3 were used in this work. The commercial mixed metal oxide (11.58wt.%)CuO-(6.36wt.%)$CeO_2/\gamma\text{-}Al_2O_3$ catalyst was synthesized via impregnation of $\gamma\text{-}Al_2O_3$ with $Cu(NO_3)_2$ and $Ce(NO_3)_3$ precursors, dried and calcined above 973 K.
Lab made (9.2wt.%)CuO-(5.2wt.%)$CeO_2/\gamma\text{-}Al_2O_3$, (9.0wt.%)$CuO/\gamma\text{-}Al_2O_3$ and (5.2wt.%)$CeO_2/\gamma\text{-}Al_2O_3$ were synthesized via incipient wetness impregnation/co-impregnation of $\gamma\text{-}Al_2O_3$ (Merk) with $Cu(NO_3)_2.2.5H_2O$ (Sigma-Aldrich) and/or $Ce(NO_3)_4.9H_2O$ (Fluka) precursors, followed by drying at 357 K for 8h and calcination in air at 973 K for 8h. After grinding, powder with a grain diameter of 75-100 μm was used for catalyst characterization. Grains of diameter 250 – 500 μm were used for the TAP experiments to determine catalytic activity.

2.4.2 Catalyst characterization

The bulk chemical composition of the tested catalysts was determined by means of inductively coupled plasma atomic emission spectrometry (ICP-AES) (IRIS Advantage system, Thermo Jarrell Ash). N_2 physisorption at 77 K was applied to determine the BET specific surface area using a Gemini V (Micromeritics) set-up. BET values with their 95% confidence intervals were obtained by regression of the experimental data in the range $0.05 < p/p0 < 0.30$ with the BET equation. The BET surface area of the commercial catalyst is around 156 m^2/g. The BET surface area of all the three lab made catalysts amounts to 170 ± 10 m^2/g. Crystallographic analyses for the tested catalysts were performed after air exposure ('ex situ') by means of X-ray diffraction (XRD) measurements in θ–2θ mode using a Bruker-AXS D8 Discover apparatus with lynx eye detector covering 3° and 192 channels over the range 15–85° with a step of 0.04°. The surface composition followed from XPS measurements using a Perkin Elmer PHI ESCA 5500 system

equipped with a monochromatic 450 Watt Al Kα source and showing a base pressure below 1×10^{-7}Pa. Detailed windows of Cu2p, Cu LMM, Ce3d, O1s and Al2p were recorded with pass energy 58.7 eV and step 0.13 eV. The Al2p photoemission line at 74.0 eV served as binding energy reference.

Transmission electron microscopy (TEM) specimens were prepared by applying simple immersion of a carbon-support film on a nickel grid into the catalyst powder followed by careful shaking off the excess powder. Catalyst particles which had adhered to the carbon film were investigated by means of various TEM modes: Conventional and high resolution TEM (HRTEM), electron diffraction, scanning transmission electron microscope (STEM), Energy dispersive X-ray (EDX) analysis and electron energy loss spectroscopy (EELS). A microscope JEOL JEM2200FS-Cscorrected, operated at 200 kV and equipped with Schottky-type FEG, EDX JEOL JED-2300D and JEOL in-column omega filter, was used. Secondary X-ray fluorescence from the analytical specimen holder was eliminated by means of a beryllium retainer. However, Ni peaks were detected in the EDX spectra due to secondary fluorescence from the Ni support grid. EEL spectra were obtained in STEM spot mode using an electron probe of 1.0 nm and objective aperture angular size of 6 mrad. The latter allows obtaining an optimal signal-to-noise ratio of Cu L and Ce M core-loss peaks.

Operando X-ray absorption spectroscopy (XAS) measurements were performed on all three catalysts at the SAMBA beam line of the 2.75 GeV synchrotron SOLEIL (Saint-Aubin, France) with a top-up X-ray beam of 400 mA [15]. X-ray absorption near edge structure (XANES) spectra were measured in transmission at the Cu K edge (8979 eV) and the Ce LIII edge (5723 eV) during TPR and isothermal reoxidation experiments explained in chapter 4. In addition, reference spectra for the Cu oxidation states were recorded from CuO, Cu_2O and Cu powder pellets and foil, while CeO_2 and CeF_3 pelletized powders served as references for the Ce^{4+} and Ce^{3+} oxidation states. The optics alignment was performed using a Cu and Cr foil respectively and the same foils served as reference sample between the second and third

ionization chamber. An oscillating monochromator setup [16] allowed recording Quick XAS spectra with a time resolution of 1s. The operando experiments were performed in a microreactor consisting of a thermally insulated frame with an X-ray passage of 2 mm diameter, bearing a quartz capillary of 0.8 mm outer diameter and 10 μm wall thickness. The gas composition at the reactor outlet was monitored with mass spectrometry (MS), while simultaneously recording the XAS spectra. The raw data were transformed to general spectral format and analyzed using Athena software [17]. In addition, a white line analysis was performed for Ce and Cu, based on the energy position of the first peak after the edge and compared to the ones of the reference materials. This analysis is based upon a shift in energy position of the white line with oxidation state [18-21].

The effect of thermal-reduction of the catalyst was investigated by *in situ* XRD in a He stream from 300K to 1073K. It was found that Cu^{2+} species were partly reduced to Cu^{+} at 873K and to Cu^{0} at 1073K. This thermal-reduction behavior of copper oxide is also reported in literature. A more detailed characterization of the catalysts has been reported elsewhere.

2.5 Reactant gases and liquids

The gases and liquids used for experiments in this PhD work together with their purity and supplier are listed in table 2.1.

Gases/Liquids	Purity	Supplier
C_7H_8	99.9%	Sigma Aldrich
$^{16}O_2$	99.9995%	Alphagaz™, Air Liquide
CO	99.97%	Alphagaz™, Air Liquide
CO_2	99.5%	Alphagaz™, Air Liquide
H_2O	deionized	
$^{18}O_2$	97%, chemical purity 99.8 %	Cambridge Isotope Laboratories Inc.
$^{13}CO_2$	99%, <1% 18O	Cambridge Isotope Laboratories Inc.
$^{12}C_6H_5$-$13CH_3$	99 atom% 13C	Isotec ™
C_6H_5-CD_3	99 atom% D	Isotec ™
Ar	99.999%	Alphagaz™ , Air Liquide
Kr	99.998%	Alphagaz™, Air liquide
H_2	99.99%	Alphagaz™ , Air Liquide

Table 2.1 Gases and liquids used for experiments

2.6 Definitions and calculations

2.6.1 Degree of catalyst reduction

The degree of reduction is defined as follows: the ratio of the number of oxygen atoms consumed from the catalyst during the reaction to the total number of exchangeable atoms. In this thesis the degree of catalyst reduction has been defined in two ways: degree of reduction with respect to the whole catalyst, R_c^0 (section 3.2.3.1) and that with respect to the most active part of the catalyst R^0 (section 5.2.2). The reader is referred to the corresponding sections for the definitions.

2.6.2 Promoting effect of ceria

The promoting or inhibiting effect of ceria in CuO-CeO_2/Al_2O_3 is expressed as $\boldsymbol{\chi_{Ce}}$, the ratio between the CO_2 yield from CuO-CeO_2/Al_2O_3 and the sum of CO_2 yields from CuO/Al_2O_3 and CeO_2/Al_2O_3

$$\boldsymbol{\chi_{Ce}} = \frac{\boldsymbol{Y_{CuO-CeO_2/Al_2O_3}}}{\left(\boldsymbol{Y_{CuO/Al_2O_3}} + \boldsymbol{Y_{CeO_2/Al_2O_3}}\right)} \tag{2.11}$$

where **Y** is the yield of CO_2 for toluene pulse experiments in the feed, the subscript indicating the catalyst used.

2.6.3 Promoting/inhibiting effect of oxidation products in feed

The ratio between the CO_2 yields from toluene pulse experiments with and without H_2O and $^{13}CO_2$ in the feed is denoted by $\eta_{12CO_2}^{H_2O}$ and $\eta_{12CO_2}^{13CO_2}$ respectively. The superscript denotes the co-feed and the subscript the product monitored.

$$\boldsymbol{\eta_{12CO_2}^{H_2O}} = \frac{\mathbf{Y_{(C_7H_8/O_2/H_2O)}}}{\mathbf{Y_{(C_7H_8/O_2)}}} \tag{2.12}$$

$$\boldsymbol{\eta_{12CO_2}^{13CO_2}} = \frac{\mathbf{Y_{(C_7H_8/O_2/^{13}CO_2)}}}{\mathbf{Y_{(C_7H_8/O_2)}}} \tag{2.13}$$

where Y is the yield of the $^{12}CO_2$ product, the subscript being the feed used.

2.7 TAP reactor model

A detailed description of the TAP reactor model can be found in Gleaves et al. [2, 6]. As a "thin-zone" TAP reactor configuration was used in this study, the reactor model for other configurations will not be presented. Interested readers are referred to Gleaves et al. [2, 6]. A thin-zone TAP reactor is shown in Fig. 2.14. The reactor consists of a reactive zone interposed between two inert zones.

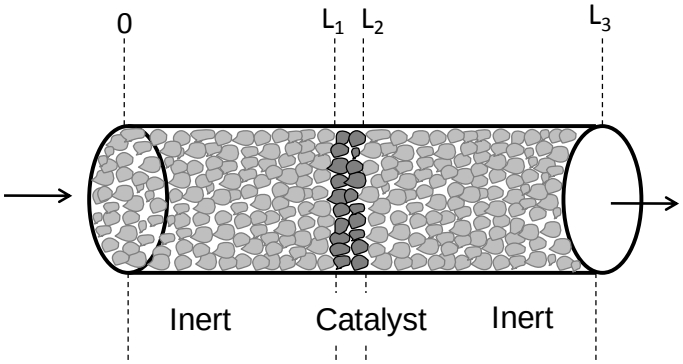

Figure 2.14 Schematic representation of a "thin-zone" TAP reactor

2.7.1 Inert zones

In the inert zones, $0 < z < L_1$ and $L_2 < z < L_3$, the continuity equation for gas components in the Knudsen diffusion regime is given in Eq. 2.14.

$$\varepsilon_I \frac{\partial C_{g,A}}{\partial t} = D^I_{eff,A} \frac{\partial^2 C_{g,A}}{\partial z^2} \tag{2.14}$$

where, $C_{g,A}$ is the concentration of gas species A, $D^I_{eff,i}$ is the effective Knudsen diffusivity of gas component A in the inert zone, ε_I is the bed porosity in the inert zone, z is the axial position in the reactor and t is the time.

The effective Knudsen diffusion coefficient $D_{eff,A}$ of a component A through a bed of uniform spheres can be expressed as in Eq. 2.15 [22].

$$D_{eff,A} = \frac{4\bar{r}\epsilon_b}{3\tau}\sqrt{\frac{2RT}{\pi M_A}} \tag{2.15}$$

where ϵ_b is the bed porosity, τ is the tortuosity factor, R is the universal gas constant, T is the absolute temperature, M_A is the molecular mass of A and $\bar{r}$ is the mean pore radius as given in Eq. 2.16.

$$\bar{r} = \frac{2}{3}\frac{\epsilon_b}{1-\epsilon_b}r \tag{2.16}$$

where r is the radius of the spherical particles.

Eq. 2.14 can be generalized where the Knudsen diffusion coefficient of any gas component can be derived from a known Knudsen diffusion coefficient of a reference gas component at a reference temperature, see Eq. 2.17.

$$D_{eff,A} = D_{eff,ref}\sqrt{\frac{T}{T_{ref}}}\sqrt{\frac{M_r}{M_A}} \tag{2.17}$$

2.7.2 Catalyst zone

In the catalyst zone, $L_1 < z < L_2$, besides the diffusion one must also account for the adsorption, reaction and desorption. These additional phenomena occur at the active sites of the catalyst. The continuity equation takes the form as in Eq. 2.18 - 2.20.

$$\varepsilon_C \frac{\partial C_{g,A}}{\partial t} = D^C_{eff,A}\frac{\partial^2 C_{g,A}}{\partial z^2} + \rho_B R_{g,A} \tag{2.18}$$

$$\frac{\partial C_{s,A_S}}{\partial t} = R_{s,A_S} \tag{2.19}$$

$$\frac{\partial C_{b,A}}{\partial t} = R_{b,A} \tag{2.20}$$

where, C_{s,A_S} is the concentration of surface species A, $D^C_{eff,A}$ is the effective Knudsen diffusivity of gas component A in the catalytic zone, ε_C is the catalytic bed porosity, ρ_B is the density of catalytic bed and $R_{g,A}$, R_{s,A_S} and $R_{b,A}$ are the specific net production rate of gas species A , adsorbed species A^* and bulk species A respectively.

2.7.3 Initial, boundary and transmission conditions

The initial gas concentrations are assumed to be zero and the surface concentrations are assumed to be known. The initial conditions are given in Eq. 2.21 - 2.23.

$$C_{g,A} = 0 \qquad t = 0, \quad 0 < z < L_3 \tag{2.21}$$

$$C_{s,A_s} = C_{s,A_s}^0 \qquad t = 0, \quad L_1 < z < L_2 \tag{2.22}$$

$$C_{b,A} = C_{b,A}^0 \qquad t = 0, \quad L_1 < z < L_2 \tag{2.23}$$

The boundary conditions are given in Eq. 2.24 and 2.25.

$$-SD_{eff,A}\left(\frac{\partial C_{g,A}}{\partial z}\right) = \frac{N_{p,A}}{{\tau_p}^2} te^{\left(-\frac{t}{\tau_p}\right)} \qquad t \geq 0, \quad z = 0 \tag{2.24}$$

$$C_{g,A} = 0 \qquad z = L_3 \tag{2.25}$$

where $N_{p,A}$ is the molar pulsed quantity of gas A, τ_p is the pulse peak time and S is the cross sectional area of the microreactor.

As there are three zones, there are transmission condition between the zones. Eq. 2.26-2.29 express the continuity in concentration and flux profiles.

$$C_{g,A}|_{z=L_{1-}} = C_{g,A}|_{z=L_{1+}} \tag{2.26}$$

$$D_{eff,A}^I \frac{\partial C_{g,A}}{\partial z}|_{z=L_{1-}} = D_{eff,A}^C \frac{\partial C_{g,A}}{\partial z}|_{z=L_{1+}} \tag{2.27}$$

$$C_{g,A}|_{z=L_{2-}} = C_{g,A}|_{z=L_{2+}} \tag{2.28}$$

$$D_{eff,A}^C \frac{\partial C_{g,A}}{\partial z}|_{z=L_{2-}} = D_{eff,A}^I \frac{\partial C_{g,A}}{\partial z}|_{z=L_{2+}} \tag{2.29}$$

In order to obtain the equivalent of experimental responses, a reaction model or reaction network is developed from which the specific

net production rates of the gas and the surface species $R_{g,A}$ and R_{s,A^*} are inserted in the reactor model. A reaction network is a collection of elementary processes with several kinetically relevant steps. The rate coefficients of these kinetically relevant steps influence the calculated responses.

In modeling, the partial differential equations Eq. 2.14-2.29 are solved by integrating in the time domain using the method of lines. The numerical calculation of pulse responses using method of lines is detailed in Roelant 2011 [23]. A computer program TAPFIT has been developed in Laboratory for Chemical Technology which is used for calculating TAP pulse responses using the model described above. Simulation using method of lines is applicable to both state defining and state altering experiments. The resulting ordinary differential equations are integrated by using the Livermore solver for ordinary differential equations (LSODE) from ODEPACK [24].

2.8 Determination and validation of kinetic parameters

Kinetic parameters corresponding to the kinetic model are estimated by means of weighted nonlinear least-squares (NLSQ) regression. The regression is performed using the Levenberg-Marquardt algorithm [25, 26] as implemented in the Orthogonal Distance Regression PACKage (ODRPACK) [27]. ODRPACK was used in its ordinary least squares mode.

The regression algorithm is used for the minimization of the objective function Φ as described in Eq. 2.30.

$$\Phi = \sum_{i=1}^{N_{res}} \sum_{j=1}^{N_e} \sum_{k=1}^{N_p} \sum_{l=1}^{N_t} w_{i,j}\left(y_{i,j,k,l} - \hat{y}_{i,j,k,l}\right)^2 \quad (2.30)$$

where $y_{i,j,k,l}$ and $\hat{y}_{i,j,k,l}$ are the experimental and simulated response sample points respectively, see Eq. 2.31 and 2.32, corresponding to the response *j* followed by the mass-spectrometer. $w_{i,j}$ represent the weights applied to different responses during regression calculated as the inverse of the average of the error variances of the sample points in the responses. N_{res}, N_e, N_p and N_t are the number of responses, the

number of experimental conditions, the number of pulses per response and the number of samples per pulse response respectively.

$$y_{i,j,k,l} = \sum_{A=1}^{N_g} cf_A F_{A,j,k,l} \tag{2.31}$$

$$\hat{y}_{i,j,k,l} = \sum_{A=1}^{N_g} cf_A \hat{F}_{A,j,k,l} \tag{2.32}$$

where $F_{A,j,k,l} = -D_{eff,A,j} S \frac{\partial C_{g,A,k,l}}{\partial z}$ and $\hat{F}_{A,j,k,l} = -D_{eff,A,j} S \frac{\partial \hat{C}_{g,A,k,l}}{\partial z}$ are the experimental and simulated outlet flow rates of gas A respectively and cf_A is the calibration coefficient of gas A. The least square regression analysis is applied to responses, y, electric potential expressed in volts [23]. The mass spectrometer collects the experimental time series $y_{i,j,k,l}$ consisting of N_t samples with sampling time Δt. The total collection time of an experimental response consisting of N_t samples is equal to $N_t \Delta t$.

For the regression of data at different temperatures, the Arrhenius dependence of the rate coefficients on temperature was reparameterized as in Eq. (2.33). This reduces the strong correlation between the activation energy E_a and the pre-exponential factor A_0.

$$k = A_0^{'} \exp\left[\frac{E_a}{R}\left(\frac{1}{T} - \frac{1}{T_{ref}}\right)\right] \tag{2.33}$$

where $A_0' = A_0 \exp\left[\frac{E_a}{RT_{ref}}\right]$, T_{ref} is the reference temperature taken as the average of all the studied temperatures.

The rate coefficients of some reaction steps can be dependent on the degree of reduction of the catalyst, R^0. Eq. (2.33) is modified for such rate coefficients by introducing the parameter α, see Eq. (2.34), which accounts for the assumed linear dependence of activation energies with R^0.

$$k = A_0^{''} \exp\left[\frac{(E_a + \alpha R^0)}{R}\left(\frac{1}{T} - \frac{1}{T_{ref}}\right)\right] \tag{2.34}$$

where $A_0'' = A_0 \exp\left[\frac{(E_a+\alpha R^0)}{RT_{ref}}\right]$.

The significance of regression will be characterized by means of the known *F* test in which higher *F* values are desirable. A *t* test is performed for the significance of individual parameter estimates. An analysis of correlation coefficients has to be performed and the correlations between different parameters should be sufficiently low. The obtained parameter values are further interpreted from a physicochemical point of view.

For any reversible step in the reaction mechanism, the adsorption equilibrium constant is $K = e^{\Delta S_a^0/R}\, e^{-\Delta H_a^0/RT}$ where $\Delta H_a^0$is the standard enthalpy of adsorption and ΔS_a^0 is the standard entropy of adsorption. Boudart et. al. [28, 29] provided guidelines to determine the physical meaning of the reported equilibrium constants as follows:

$$41.9 \leq -\Delta S_a^0 \leq S_g \tag{2.35}$$

$$-\Delta S_a^0 \leq 51.1 - 1.4\Delta H_a^0 \tag{2.36}$$

where S_g is the entropy of the gas component. The upper limit in Eq. 2.35 suggests the fact that there is an entropy loss upon adsorption. However, the value should remain greater than 41.9 J mol^{-1} K^{-1}. The upper limit in Eq. 2.36 corresponds to a tightly bound molecule with a larger $-\Delta H_a^0$ and $-\Delta S_a^0$ values. The relation presents a linear relationship between $-\Delta H_a^0$ and $-\Delta S_a^0$ observed by Everett for physical adsorption [28].

References

1 J.T. Gleaves, J.R. Ebner, P.L. Mills, A Novel Catalyst Evaluation System For Temporal Analysis of Reaction Products With Submillisecond Time Resolution, Studies in Surface Science and Catalysis, 38 (1988) 633-644.

2 J.T. Gleaves, G. Yablonsky, X. Zheng, R. Fushimi, P.L. Mills, Temporal Analysis of Products (TAP) - Recent advances in technology for kinetic analysis of multi-component catalysts, Journal of Molecular Catalysis A: Chemical, 315 (2010) 108-134.

3 M. Rothaemel, M. Baerns, Modeling and Simulation of Transient Adsorption and Reaction in Vacuum Using the Temporal Analysis of Products Reactor, Industrial & Engineering Chemistry Research, 35 (1996) 1556-1565.

4 J. Perez-Ramirez, E.V. Kondratenko, Evolution, achievements, and perspectives of the TAP technique, Catalysis Today, 121 (2007) 160-169.

5 G. Creten, TAP-studie : Reactiemechanismen en transiënte kinetiek van katalytische oxidatiereacties, in: Laboratory for Chemical Technology, Ghent University, Ghent, 1995.

6 J.T. Gleaves, G.S. Yablonskii, P. Phanawadee, Y. Schuurman, TAP-2: An interrogative kinetics approach, Applied Catalysis A: General, 160 (1997) 55-88.

7 I. Sack, A Kinetic Study of the Reduction and the Reoxidation of Vanadia-Based Catalysts by Temporal Analysis of Products, in: Laboratory for Chemical Technology, Ghent University, Ghent, 2006.

8 V. Balcaen, The total oxidation of propane over metal oxide catalysts: transient kinetics and monolith reactors, in: Laboratory for Chemical Technology, Ghent University, Ghent, 2011.

9 O. Dewaele, Gebruik van de TAP-reactor voor de kinetische studie van complexe reacties, in: Laboratory for Chemical Technology, Ghent University, Ghent, 1998.

10 G.S. Yablonsky, M. Olea, G.B. Marin, Temporal Analysis of Products: basic principles, applications, and theory, Journal of Catalysis, 216 (2003) 120-134.

11 S.O. Shekhtman, G.S. Yablonsky, S. Chen, J.T. Gleaves, Thin-zone TAP-reactor : theory and application, Chemical Engineering Science, 54 (1999) 4371-4378.

12 J.T. Gleaves, G.S. Yablonskii, P. Phanawadee, Y. Schuurman, G.F. Froment, K.C. Waugh, "State-Defining" TAP pulse response experiments, in: Studies in Surface Science and Catalysis, Elsevier, 1997, pp. 333-340.

13 D.J. Statman, J.T. Gleaves, D. McNamara, P.L. Mills, G. Fornasari, J.R.H. Ross, TAP reactor investigation of methane coupling over samarium oxide catalysts, Applied Catalysis, 77 (1991) 45-53.

14 J.P. Huinink, A quantitative analysis of transient kinetic experiments : the oxidation of CO by O_2/NO on Pt, in: Department of Chemical Engineering and Chemistry, Eindhoven University of Technology, Eindhoven, 1995.

15 V. Briois, E. Fonda, S. Belin, L. Barthe, C.L. Fontaine, F. Langlois, M. Ribbens, F. Villain, SAMBA: The 4-40 keV X-ray absorption spectroscopy beamline at SOLEIL, UVX 2010, (2011) 41 - 47.

16 R. Frahm, New method for time dependent x - ray absorption studies Review of Scientific Instruments, 60 (1989).

17 B. Ravel, M. Newville, ATHENA,ARTEMIS,HEPHAESTUS: data analysis for X-ray absorption spectroscopy using IFEFFIT, Journal of Synchrotron Radiation, 12 (2005) 537-541.

18 M. Olea, H. Poelman, M. Capron, S. Cristol, Combining XAS with on-line GC catalytic studies for in situ characterization of Volatile

Organic Compounds (VOCs) elimination over a $CuO\text{-}CeO_2/Al_2O_3$ catalyst, in, 2007.

19 J. Wong, F.W. Lytle, R.P. Messmer, D.H. Maylotte, K-edge absorption spectra of selected vanadium compounds, Physical Review B, 30 (1984) 5596-5610.

20 T. Ressler, J. Wienold, R.E. Jentoft, T. Neisius, Bulk Structural Investigation of the Reduction of MoO_3 with Propene and the Oxidation of MoO_2 with Oxygen, Journal of Catalysis, 210 (2002) 67-83.

21 G. Silversmit, H. Poelman, I. Sack, G. Buyle, G. Marin, R. De Gryse, An in-situ Reduction/Oxidation XAS Study on the EL10V8 VO_x/TiO_2(Anatase) Powder Catalyst Catalysis Letters, 107 (2006) 61-71.

22 D.G. Huizenga, D.M. Smith, Knudesen diffusion in random assemblages of uniform spheres, AIChE Journal, 32 (1986) 1-6.

23 R. Roelant, Mathematical determination of reaction networks from transient kinetic experiments, in: Laboratory for chemical technology, Ghent University, Ghent, 2011.

24 A.C. Hindmarsh, ODEPACK - A Systematized Collection of ODE Solvers, in: R.S.S.e. al. (Ed.) Scientific Computing, North-Holland, Amsterdam, 1983, pp. 55-64.

25 K. Levenberg, A method for the solution of certain non-linear problems in least-squares, Quarterly of Applied Mathematics, 2 (1944) 164-168.

26 D.W. Marquardt, An algorithm for least-squares estimation of nonlinear parameters, Journal of the Society for Industrial and Applied Mathematics, 11 (1963) 431-441.

27 P.T. Boggs, Byrd, R.H., Schnabel, R.B., A stable and efficient algorithm for nonlinear orthogonal distance regression., SIAM Journal on Scientific and Statistical Computation, 8 (1987) 1052-1078.

28 D.H. Everett, Thermodynamics of adsorption. Part I.—General considerations, Trans. Faraday Soc., 46 (1950) 453-459.

29 M. Boudart, D.E. Mears, M.A. Vannice, Ind. Chim. Belge, 32 (1967) 281.

Chapter 3

Reaction network for the total oxidation of toluene over $CuO\text{-}CeO_2/Al_2O_3$

This chapter has been published as "Unmesh Menon, Vladimir V. Galvita, and Guy B. Marin, Reaction network for the total oxidation of toluene over $CuO\text{-}CeO_2/Al_2O_3$, Journal of Catalysis 283 (1) (2011) 1-9"

Abstract

The total oxidation of toluene was studied over a $CuO–CeO_2/\gamma\text{-}Al_2O_3$ catalyst in a Temporal Analysis of Products (TAP) setup in the temperature range 673–923 K in the presence and absence of dioxygen and at various degrees of reduction of the catalyst. The reaction rate significantly decreases over a mildly reduced catalyst. Under vacuum and at high-temperature, mild reduction also occurs in the absence of toluene.

In the presence of dioxygen, the catalyst activity is determined by weakly bound surface lattice oxygen atoms and adsorbed oxygen species, the lifetime of which is close to 1 s. The weakly bound oxygen is highly reactive and is only found over a fully oxidized catalyst.

The formation of products containing ^{18}O during the isotope-exchange experiments with $^{18}O_2$ indicates that both lattice and adsorbed

oxygen are involved in (a) reoxidation of mildly reduced copper oxide and (b) abstraction of hydrogen atoms and scission of C–C bonds.

Isotopic labeling with C_6H_5–$^{13}CH_3$ and C_6H_5–CD_3 indicates the following reaction paths: adsorption of toluene on the active site, containing Cu^{2+} with 4–5 adjacent surface lattice oxygen atoms; the simultaneous abstraction of H from the methyl and the phenyl group followed by the abstraction of the methyl carbon and next the destruction of the aromatic ring.

3.1 Introduction

The catalytic total oxidation of volatile organic compounds (VOCs) is generally considered to be an effective method for reducing the emission of pollutants in the environment [1, 2]. The main advantages of catalytic combustion compared with other decontamination technologies are high efficiency at a very low pollutants concentration, low energy consumption and low production of secondary pollutants, for example, NO_x. Conventional catalysts based on noble metals supported on Al_2O_3 are successfully used to eliminate VOCs by total oxidation. Noble metal catalysts are very active, but they are costly and have low stability in the presence of chlorine compounds [1, 3]. Transition metal oxides, such as copper, cobalt, manganese, and chromium, are known to be active combustion catalysts [1, 4]. They are less active at lower temperatures but have comparable activity at high temperatures and have high catalyst loading capabilities. CuO was reported to be as effective as Pt for the incineration of n-butanol and methyl mercaptan [3]. Larsson and Andersson found excellent performance for the incineration of CO, ethyl acetate and ethanol over CuO_x/Al_2O_3 [5, 6]. Rajesh and Ozkan reported that CuO/Al_2O_3 was even more active than Pt/Al_2O_3 for the complete oxidation of ethanol [7]. CuO was the most active transition-metal oxide of those tested for the catalytic incineration of toluene with γ-Al_2O_3 as support [8]. Copper promoted by ceria is known to show better catalytic performance for the

complete oxidation of benzene, toluene and *p*-xylene than copper only [5, 8-10].

It is generally accepted that the oxidation of VOCs (toluene, propane) over transition metal oxide catalysts occurs according to a Mars-van Krevelen type redox cycle and proceeds through nucleophilic attack of the lattice oxygen of the oxides [11-18]. This mechanism includes two steps: the first step consists of reactant oxidation using the catalyst lattice oxygen, which will be replaced, in the second step, by atoms originating from dioxygen. However, the first step in the oxidation process is not an elementary step and the actual mechanism involves many consecutive and/or parallel steps [11, 19-22]. Toluene adsorption with the aromatic ring parallel to the exposed metal oxide planes leads to the destruction of the molecule and the formation of total oxidation products. Perpendicular end-on adsorption of toluene on oxygen containing sites leads to abstraction of H-atoms from the methyl group and an adsorbed complex through a strong C-O bond. This complex is considered to be the benzaldehyde and/or other selective-products precursor or further oxidized to carbon oxides [11, 19-22]. On the other hand, according to the Mars-van Krevelen mechanism the dioxygen is only required to re-oxidize the reduced surface metal centers. Dioxygen molecules are activated through an interaction with the surface of the catalyst. This activation proceeds first through a dissociative adsorption, which includes coordination, electron transfer and dissociation, followed by incorporation into the lattice. Consequently, two possible states of oxygen are available on the surface of the catalyst. Adsorbed dioxygen species are also reported to be active in hydrocarbon oxidation catalysis [10, 11, 14, 23-26]. The role and nature of the respective oxygen active species (for example, adsorbed oxygen species acting as electrophilic oxygen and lattice "nucleophilic" oxygen) in catalytic combustion is not fully clarified. Other aspects, for example, the nature of the active sites and the mechanism for C-H and C-C bond activation, are still incompletely explained.

The elucidation of the above issues should aid in better understanding the mechanism of action of the oxide catalysts. Transient

response techniques with millisecond time scale provide a powerful tool for the investigation of the reaction steps and the possible catalyst surface transformations during reaction [27]. The Temporal Analysis of Products (TAP) has been recognized as an important transient experimental method for heterogeneous catalytic reaction studies. A TAP pulse response experiment consists of injecting a very small amount of gas, typically 10^{13}-10^{14} molecules per pulse, into a tubular fixed bed reactor that is kept under vacuum. The pressure rise in the micro-reactor is small and the transport in the reactor, which is driven by a gas concentration gradient, is dominated by Knudsen diffusion. Well defined Knudsen diffusion is used as a tool for measuring chemical reaction rates and obtaining kinetic parameters [27-29]. The time-dependent exit flow rate of each gas is detected by a mass spectrometer. In this study, a TAP reactor is applied as a unique transient tool to investigate the reaction network and kinetics for the catalytic total oxidation of toluene using a commercial CuO-CeO_2/γ-Al_2O_3 catalyst.

3.2 Experimental

3.2.1 Catalyst preparation and characterization

The (11.58wt.%)CuO-(6.36wt.%)CeO_2/γ-Al_2O_3 catalyst is a commercial mixed metal oxide, which was synthesized via impregnation of γ-Al_2O_3 with $Cu(NO_3)_2$ and $Ce(NO_3)_3$ precursors, dried and calcined above 973 K. The bulk chemical composition of the tested catalysts was determined by means of inductively coupled plasma atomic emission spectrometry (ICP-AES) (IRIS Advantage system, Thermo Jarrell Ash). N_2 physisorption at 77 K was applied to determine the BET specific surface area using a Gemini V (Micromeritics) automated system. BET values with their 95% confidence intervals were obtained by regression of the experimental data in the range $0.05 < p/p^0 < 0.30$ with the linear BET equation. The BET surface area of the catalyst is around 156 m^2/g. Crystallographic analysis for the tested catalysts were performed by means of X-ray diffraction (XRD) measurements in θ–2θ mode using a Bruker-AXS D8 Discover apparatus with lynx eye detector covering 3°

and 192 channels over the range 15–85° with a step of 0.04°. XRD analysis shows that alumina and ceria are an order of magnitude smaller than CuO and have a diameter of about 5 nm. The effect of thermal-reduction of the catalyst was investigated by insitu XRD in a He stream from 300K to 1073K. It was found that Cu^{2+} species were partly reduced to Cu^{+} at 873K and to Cu^{0} at 1073K. This thermal-reduction behavior of copper oxide is also reported in literature [23]. A more detailed characterization of the catalysts has been reported elsewhere [30, 31].

3.2.2 Experimental set-up

The TAP reactor setup used in this work is described in section 2.2. The TAP experiments are carried out in a micro-reactor which is placed in vacuum (10^{-4}–10^{-5} Pa) with a very small amount of reactant molecules (10^{-11}–10^{-9} mol). The micro-reactor is made of quartz and is of the size 33 mm bed-length and 4.75 mm inner diameter. The entrance of the reactor is connected with two high-speed pulse valves via a small volume. Molecules are pulsed into the micro-reactor by means of two pulse valves, and the products and the unreacted reactants coming out of the reactor are monitored by a UTI 100C quadruple mass spectrometer. The number of molecules admitted during pulse experiments amounts to 10^{13}–10^{14} molecules/pulse with a pulse time from 90 to 150 μs.

To feed toluene, a liquid feed setup was designed and constructed at the Laboratory for Chemical Technology, Ghent University. It consists of a liquid vaporizing chamber, which is heated to 423 K, into which the liquid feed is injected by use of a 500 lL Hamilton Gastight ® #1750 syringe. The pressure at the point of injection is held by a Hamilton, high-temperature septum. The vaporizing chamber is also connected with gas bottles, which allows making gas mixtures. The temperature of the feeding lines is maintained at 423 K. The manifold assembly containing the pulse valves is kept at 348 K, the maximum temperature allowed. The pressure of the feed from the liquid feeding

lines to the pulse valves is maintained at 1.1 bar as it was experimentally determined to be the pressure at which the pulse valves function best. The amount of liquid injected into the vaporizing chamber is such that a vapor state is maintained at the temperature and pressure in the manifold assembly.

Four types of experiments were carried out as follows: single-pulse, multi-pulse, and alternating-pulse experiments [27,28] and a variation in the latter. Single-pulse experiments were carried out to study the interaction of a gas with the catalyst at a particular state, by pulsing an amount of molecules of the order of 10^{13} molecules/pulse, at pulse times between 90 and 110 ls. These pulse times, which ensure the flow inside the bed to be of the Knudsen diffusion type, are experimentally determined. In the Knudsen diffusion regime, the shape of the outlet gas responses over inert material does not depend on the pulse intensity. The state of the catalyst remains unaltered during a single-pulse experiment as the number of molecules pulsed is 5–6 orders of magnitude less than the number of active sites in the catalyst. Typically, 20–25 responses of a particular AMU are collected and averaged in order to obtain a better signal to noise ratio. If components corresponding to different AMUs have to be measured, each AMU is measured one after another pulse for the required number of times and averaged. Multi-pulse experiments were carried out to change the state of the catalyst by pulsing an amount of molecules of the order of 10^{14} molecules/pulse, at pulse times between 115 and 150 μs and collecting about 1000 responses. Multi-pulse experiments were used to obtain different states of the catalyst. Alternating-pulse experiments were carried out with various time lags between the two different pulses. Information on the lifetime and reactivity of the adsorbed species can be obtained by varying the time lags between the two pulses. The species created during the first pulse (pump pulse) can be probed with a suitable reactant during the second pulse (probe pulse). In the present work, next to "classical" alternating-pulse experiments, the total data acquisition time between two alternating-pulses was also varied.

3.2.3 Catalyst testing

Experiments were carried out over 10 mg of $CuO–CeO_2/Al_2O_3$ catalyst. The catalyst was packed in between two inert zones of quartz particles of the same size ($250<d_p<500$ μm). Typically, reaction mixtures were prepared with Ar as one of the components, so that the inlet amount of the components can be determined from the Ar response. In experiments where there are components with AMUs coinciding with the fragments of Ar, Kr was used instead of Ar. The experiments carried out after reoxidising the catalyst were conducted within 10 s of stopping the reoxidation. A temperature range of 673–923 K was covered. Blank measurements were taken with toluene and dioxygen over quartz particles of the same size. No oxidation products or decomposition of toluene was observed. When required, the reoxidation of the catalyst was performed by conducting dioxygen multi-pulse experiments until the outlet oxygen response was steady.

For experiments that are carried out over an oxidised catalyst, the catalyst is pretreated with high-intensity pulses of dioxygen. After reoxidation by a dioxygen multi-pulse experiment, if the catalyst stayed more than 10 s under vacuum at reaction temperatures, an extra oxygen uptake was seen from another dioxygen pulse. The oxygen uptake increases with increasing time interval between the dioxygen multi-pulse experiments and with reaction temperature. This effect was due to thermal reduction at high temperature and in vacuum. Therefore, to ensure an oxidized catalyst state, toluene or toluene/dioxygen was pulsed not later than 10 s after the reoxidation by dioxygen multi-pulse experiment.

For the quantification of each component of toluene total oxidation, the MS is focused to different AMUs, the selection of which was based on an analysis of the mass spectra of the individual components. $H_2{}^{16}O$ was monitored at 18, $H_2{}^{18}O$ at 20, DHO at 19, D_2O at 20, $C^{16}O_2$ at 44, $C^{16}O^{18}O$ at 46, $C^{18}O_2$ at 48, $^{13}CO_2$ at 45, O_2 at 32, C_7H_8 at 91, C_6H_5-$^{13}CH_3$ at 92, C_6H_5-CD_3 at 94, Ar at 40, and Kr at 84 AMU. When there was an unavoidable interference by the

fragmentation peaks of other gases, a correction was applied to remove their contributions, for example, $H_2{}^{18}O$ is monitored at 20 AMU, subtracting the contribution of Ar, that is, not more than 4% of the peak at 40 AMU.

In order to determine the catalyst activity towards partial oxidation, experiments were performed to find out probable partial oxidation products like benzaldehyde monitored at AMU 77 and 78, CO at 28, H_2 at 2 and benzene at 78. Experiments were performed at fully oxidized state as well as at different degrees of reduction of the catalyst. No such products were observed.

Several single-pulse experiments were performed by pulsing C_7H_8 with and without dioxygen in the feed, at various degrees of reduction of the catalyst and at various temperatures to study the effect of degree of reduction on toluene oxidation and to elucidate the reduction power of toluene. Typically, a stoichiometric ratio of dioxygen to toluene, that is, 9:1, was used in the mixture $C_7H_8/O_2/Ar$, when experiments were conducted in the presence of dioxygen. The degree of reduction was set by multi-pulse experiments with either C_7H_8/Ar or CO/Ar. The latter allowed a higher reduction of the catalyst. Note that there was no progressive deactivation of the catalyst observed for toluene pulse experiments in the presence or absence of dioxygen.

To study the effect of partial pressure of dioxygen in the reaction mixture, feeds with different ratios of components in the reaction mixture $C_7H_8/O_2/Ar$ were applied. The concentration of C_7H_8 was kept constant and that of O_2 and Ar was varied. Ratios of C_7H_8/O_2=1:9, 1:5, 1:1, 1:0 were used. Single-pulse experiments were performed with various feed mixtures on oxidized catalyst at temperatures varying from 673K to 923K. The partial reaction order of dioxygen, *n*, was calculated based on Eq. 3.1:

$$ln(R_{CO_2}) = ln\,k + n\,ln(P_{O_2}) + ln(P_{C_7H_8}) \tag{3.1}$$

where $[CO_2]$ is the extensive molar production of CO_2 (mol) and $[O_2]$ and $[C_7H_8]$ are the amount of dioxygen and toluene in the reaction mixture (mol).

To study the interaction of dioxygen with the catalyst, oxygen isotopic exchange experiments were performed by pulsing mixtures of $C_7H_8/^{18}O_2/Ar$ over an $^{16}O_2$ pre-treated catalyst and monitoring $C^{16}O_2$, $C^{18}O_2$, $C^{16}O^{18}O$ and $H_2{}^{16}O$, $H_2{}^{18}O$ formed. $C_7H_8/^{18}O_2/Ar$ was pulsed at high pulse intensities, ~10^{14} molecules/ pulse, as the sensitivity of the mass spectrometer is not high enough to measure H_2O at lower reactant pulse intensities. $^{18}O_2$ (97%, chemical purity 99.8 %) from Cambridge Isotopes Laboratories Inc. was used for the oxygen isotopic experiments.

To investigate the lifetime of adsorbed oxygen species and their effect on the oxidation of toluene, alternating-pulse experiments were performed with oxygen and toluene, at ~10^{14} molecules/pulse with varying time lags for the toluene pulse. Moreover, to study the adsorption and lifetime of toluene or intermediates between toluene and CO_2 on the surface of the catalyst, alternating-pulse experiments with oxygen and toluene were performed by varying the total data acquisition time and keeping the time lags between the dioxygen and toluene pulses constant. The sequence was repeated 25 times for signal-averaging.

The activation of C-H and C-C bonds in toluene was investigated by pulsing isotopes of toluene, viz. C_6H_5-$^{13}CH_3$ (Isotec ™, 99 atom% ^{13}C) and C_6H_5-CD_3 (Isotec ™, 99 atom% D). Experiments with C_6H_5-$^{13}CH_3/Ar$ were performed at a pulse intensity of ~10^{13} molecules/pulse, which enables Knudsen diffusion regime, whereas experiments with C_6H_5-CD_3 were performed at a pulse intensity of ~10^{14} molecules/pulse, in order to monitor the water responses.

3.2.3.1 Degree of reduction

The degree of reduction is defined according to Eq. 3.2

$$R_c^0 = \frac{[O]}{[O]_t} \tag{3.2}$$

where [*O*] represents the number of oxygen atoms consumed from the catalyst during reaction and $[O]_t$ is the total number of exchangeable

oxygen atoms in CuO and CeO_2 [33, 34] of the catalyst according to Eq. 3.3 and Eq. 3.4.

$$CuO \rightarrow Cu + \frac{1}{2}O_2 \tag{3.3}$$

$$CeO_2 \rightarrow \frac{1}{2}Ce_2O_3 + \frac{1}{4}O_2 \tag{3.4}$$

The theoretical number of exchangeable O atoms in the CuO and CeO_2 for the 10 mg CuO(11.58 wt%)-CeO_2(6.36 wt%)/Al_2O_3 catalyst was calculated to be 9.85 10^{18}, that is, 5 to 6 orders of magnitude higher than the number of molecules admitted in a single pulse.

3.2.3.1.1 C_7H_8/Ar feed

The O_2 pretreated catalyst was titrated with C_7H_8/Ar to obtain different degrees of reduction and single-pulse experiments with the same mixture were performed at these states of the catalyst. The same number of reactant pulses was sent at all temperatures to study the dependence on temperature. The outlet CO_2 was monitored. The number of oxygen atoms consumed from the catalyst due to the formation of CO_2 and H_2O was calculated from the CO_2 response.

$$C_7H_8 + 9O_2 \rightarrow 7CO_2 + 4H_2O \tag{3.5}$$

The amount of H_2O calculated according to Eq. 3.5, from the CO_2 monitored at the outlet is given by Eq. 3.6:

$$[H_2O]_{out} = \left(\frac{4}{7}\right)[CO_2]_{out} \tag{3.6}$$

The total amount of O consumed from the catalyst by a C_7H_8/Ar pulse is given in Eq. 3.7:

$$[O] = 2[CO_2]_{out} + [H_2O]_{out} = \left(\frac{18}{7}\right)[CO_2]_{out} \tag{3.7}$$

3.2.3.1.2 C_7H_8/O_2/Ar feed

CO/Ar was used to reduce the catalyst to different degrees and single-pulse experiments with C_7H_8/O_2/Ar were performed at these

states of the catalyst. The outlet CO_2 response was used for determining the number of O atoms removed from the catalyst during the titration with CO/Ar.

$$CO + \frac{1}{2}O_2 \rightarrow CO_2 \tag{3.8}$$

The total amount of O consumed from the catalyst by CO/Ar pulses is calculated as in Eq. 3.9:

$$[O] = [CO_2]_{out} \tag{3.9}$$

The total amount of O consumed from the catalyst by $C_7H_8/O_2/Ar$ pulses is calculated as in Eq. 3.10:

$$[O] = \frac{18}{7}[CO_2] - 2([O_2]_{in} - [O_2]_{out}) \tag{3.10}$$

The total amount of O_2 consumed by the catalyst during $C_7H_8/O_2/Ar$ or O_2/Ar pulses is calculated as in Eq. 3.11:

$$[O_2] = [O_2]_{in} - [O_2]_{out} \tag{3.11}$$

3.3 Results

3.3.1 Toluene conversion to CO_2 in the presence and absence of dioxygen

The outlet molar flow rate of C_7H_8 and CO_2 obtained by performing single-pulse experiments, pulsing C_7H_8/Ar and $C_7H_8/O_2/Ar$ at 823K over oxidized catalyst is presented in Figs. 3.1a and b, respectively. The amount of C_7H_8 in the feed mixture was kept the same in both the experiments. A ratio of 1:9 for C_7H_8/O_2 was taken in the latter case.

The behavior of toluene oxidation observed from Fig. 3.1a suggests that the reaction is carried out according to a Mars-van Krevelen mechanism [35] Lattice oxygen atoms from the surface of the catalyst are consumed by the C_7H_8 pulse and oxygen vacancies are created. These vacancies are filled by the oxygen atoms that diffuse from

the bulk of the catalyst to the surface. The observed shift in the CO_2 peak and the long residence time can be attributed to the diffusion of oxygen from the bulk and the sequence of reactions for the breakage of C-H and C-C bonds in C_7H_8. However, the addition of dioxygen to the reaction mixture increases the reaction rate. The dioxygen present in the feed re-oxidizes the catalyst surface. On the other hand the adsorbed oxygen can also participate in the reaction. A shift of 55ms was observed when toluene was pulsed with dioxygen in the feed, and 80ms when toluene was pulsed alone. From Figs. 1a and b, it can be seen that the CO_2 response does not become flat at 1s. The signal of CO_2 was detected until 2s (not shown in the figure). The normalized carbon dioxide responses, corresponding to the single-pulse experiment with toluene, and with a mixture of toluene and dioxygen, show that the peak and the tail of the CO_2 response were broader in the former case. In the experiment with a mixture of toluene and dioxygen, the latter regenerates the catalyst thereby increasing the CO_2 production rate. Whereas, in the experiment with toluene alone, the vacant sites at the surface have to be replenished by oxygen atoms diffusing from the bulk.

As an increase in the conversion of toluene to CO_2 was observed in the presence of dioxygen, the effect of partial pressure of dioxygen in the feed mixture was investigated. Reactions were performed with different ratios of C_7H_8/O_2 over the fully oxidized catalyst at different temperatures. The results are summarized in Fig. 3.2. The conversion of toluene to CO_2 for a C_7H_8/O_2 ratio of 1:9 was nearly 1.5 times that of a ratio 1:0 at 923K. The difference in yield of CO_2 between different feed mixtures decreased with increasing reaction temperature. This shows that the influence of partial pressure of dioxygen in the reaction mixture is more important at lower temperatures. The apparent activation energy for the reaction was found to be decreasing with the increasing partial pressure of dioxygen in the feed mixture: 49, 51, 59 and 68 kJ/mol for C_7H_8/O_2 ratios of 1:9, 1:5, 1:1 and 1:0.

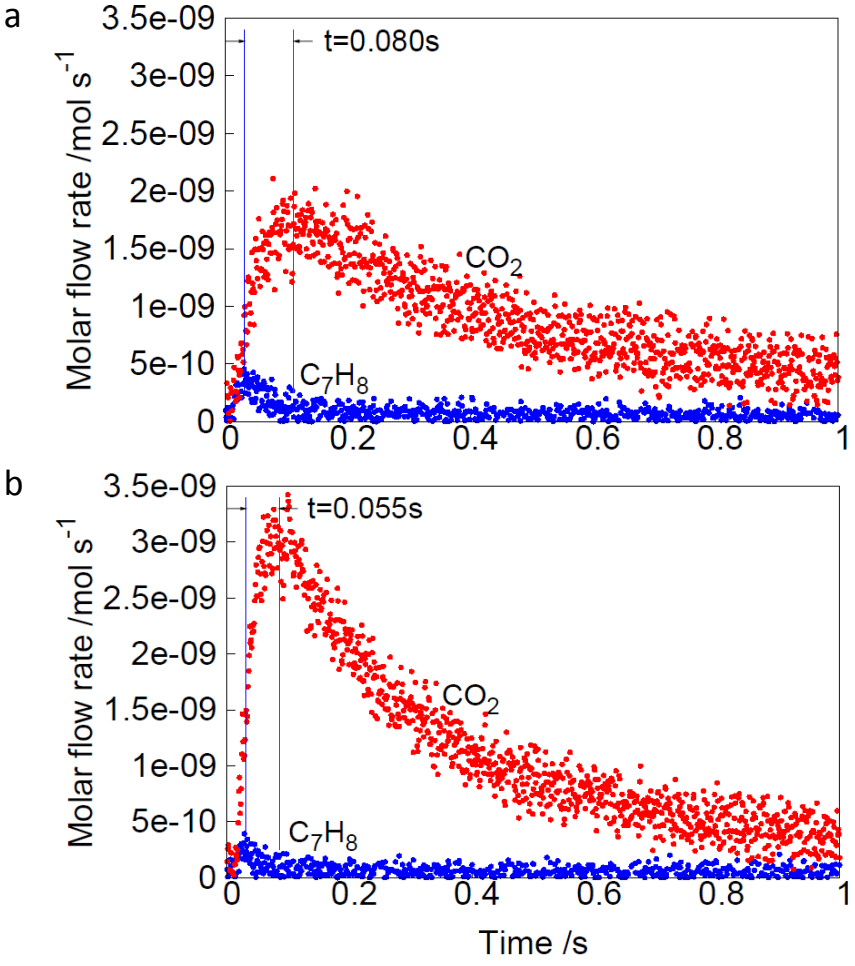

Figure 3.1 Outlet molar flow rate of CO_2 and C_7H_8 versus time to single-pulse experiment with (a) C_7H_8/Ar and (b) C_7H_8/O_2/Ar over oxidized catalyst at T = 823 K.

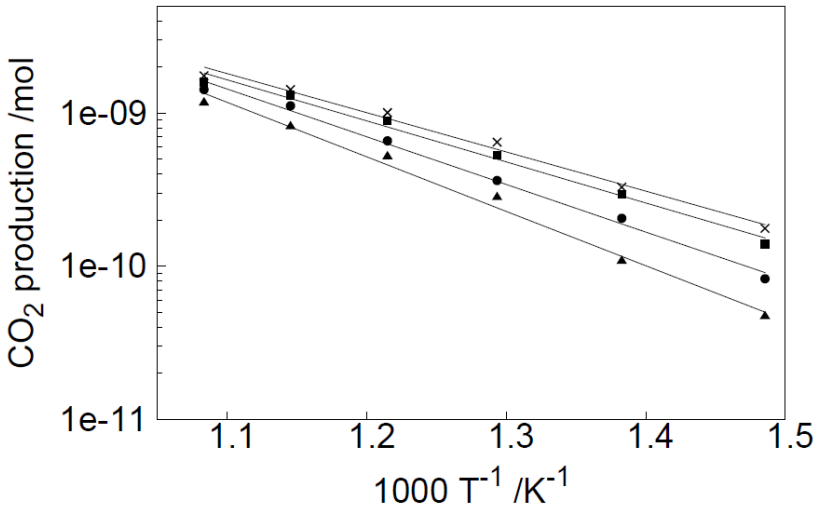

Figure 3.2 CO_2 production versus reciprocal temperature during the total oxidation of toluene for C_7H_8/O_2 molar ratios: (×) 1:9, (■) 1:5, (●) 1:1, (▲) 1:0.

Fig. 3.3 shows the partial reaction order of dioxygen in the reaction mixture with respect to temperature. The order of dioxygen decreases with increasing temperature of reaction from 0.34 at 673K to 0.089 at 923K. This behavior is again in good agreement with a Mars-van Krevelen mechanism. At low reaction temperature the diffusion of oxygen from the catalyst bulk to the surface is a slow process and a competition in the regeneration of the vacant sites of the catalyst between bulk oxygen and gas phase dioxygen is observed. At high temperatures the oxygen mobility in the metal oxides increases and the role of dioxygen is less pronounced.

The CO_2 yields from single-pulse experiments of $C_7H_8/O_2/Ar$ and C_7H_8/Ar in the feed at different degrees of reduction of the catalyst and at temperatures varying from 723K to 923K are depicted in Figs. 3.4a and b, respectively. The effect of the degree of reduction of the catalyst and elucidation of the reduction power of toluene is studied.

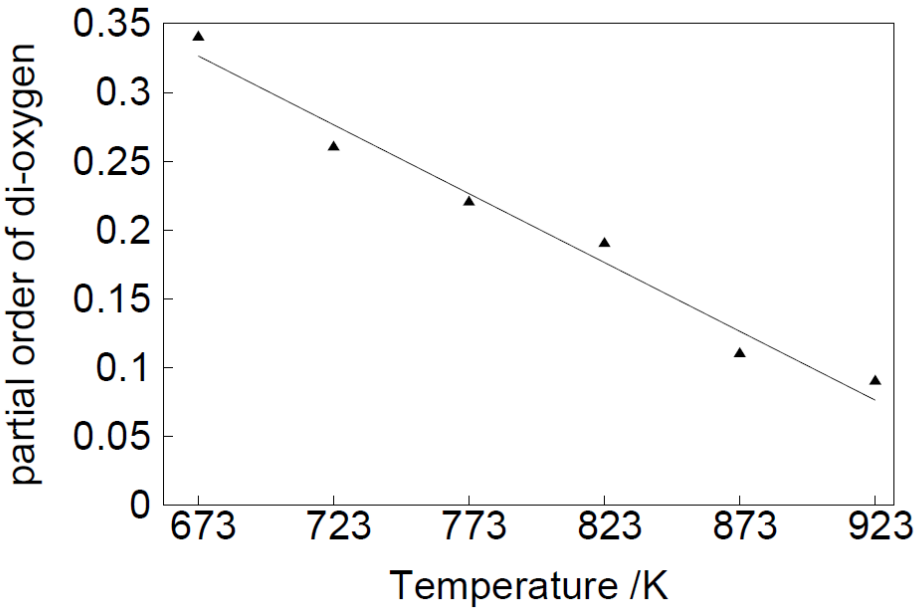

Figure 3.3 Partial reaction order of dioxygen versus temperature.

Fig. 3.4a shows that the CO_2 yield decreases with increasing degree of reduction of the catalyst at all temperatures. The extent to which the catalyst could be reduced was close to 80% at 923K and dropped to 50% and 40% at 823K, 723K respectively, with an equal number of CO

pulses used for catalyst reduction. When a mixture of toluene and dioxygen was pulsed over the completely reduced catalyst, no CO_2 and O_2 was observed initially at the reactor outlet. The dioxygen was used for the catalyst re-oxidation only. CO_2 was observed to increase at the outlet along with O_2 as the catalyst was partially re-oxidized

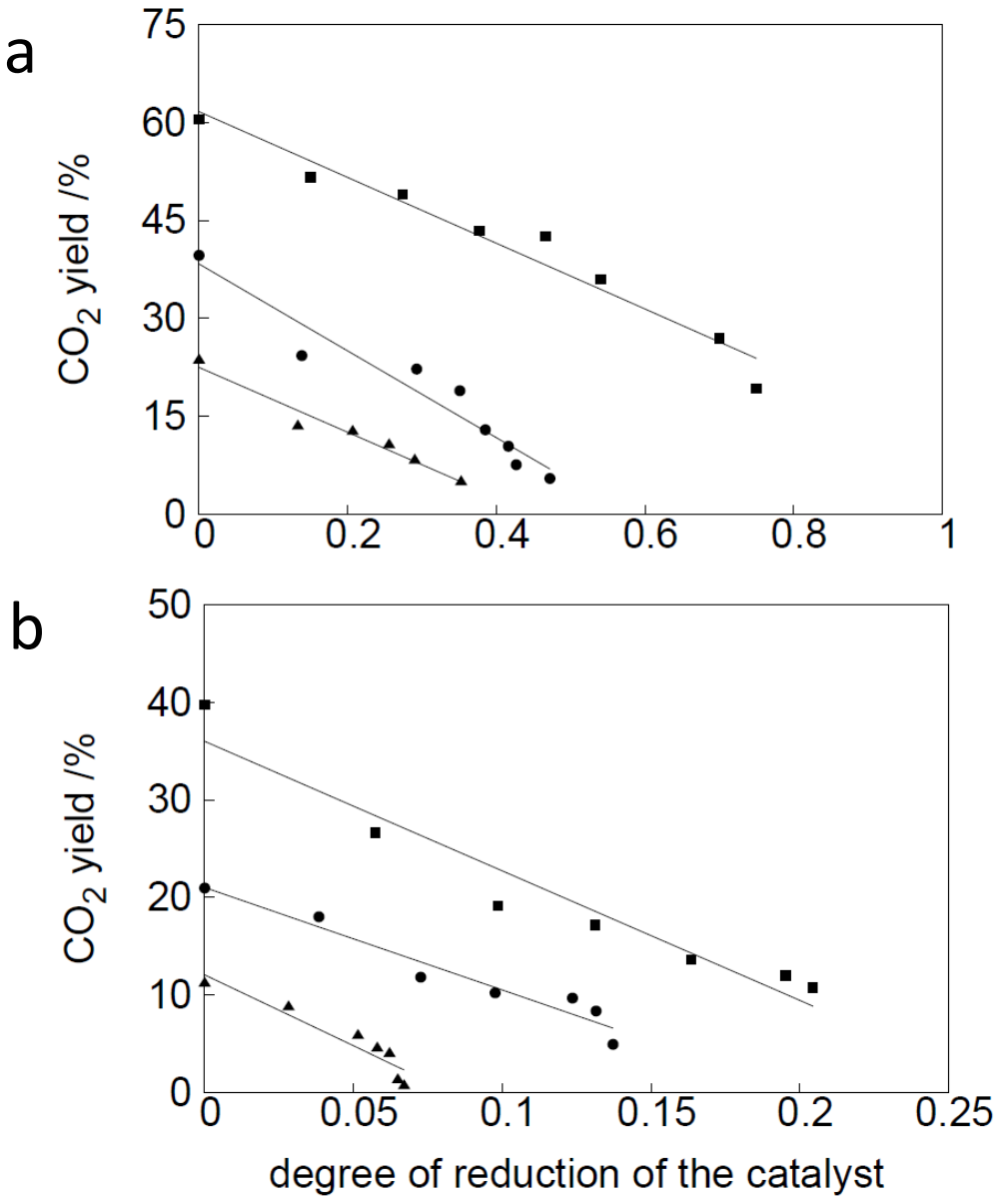

Figure 3.4 CO_2 yield versus degree of reduction of the catalyst at (▲)*T*=723K, (●)*T*=823K and (■)*T*=923K to single pulse experiments with (a) $C_7H_8/O_2/Ar$ as feed, catalyst reduced by CO; and (b) C_7H_8/Ar as feed, catalyst reduced by toluene.

Comparing Figs. 3.4a and b shows that toluene conversion and CO_2 formation are favored by the presence of dioxygen in the feed, at the same degrees of reduction of the catalyst. The extent to which the catalyst could be reduced was observed to be smaller with toluene than when reduced with CO. The reducing power of toluene is much lower compared to CO due to the high C-H and C-C dissociation energy. The extent to which the catalyst could be reduced by pulsing toluene was 20%, 14% and 7% at 923K, 823K and 723K respectively.

Thus, the catalyst degree of reduction has a strong effect on the total oxidation of toluene. A small increase in catalyst degree of reduction decreases the CO_2 formation significantly, when pulsed without dioxygen in the feed. The catalyst activity is determined by weakly bound oxygen atoms in the lattice and is only found over a fully oxidized catalyst and in the presence of dioxygen. When feeding $C_7H_8/O_2/Ar$ over the reduced catalyst, the dioxygen interacts with the catalyst and then with toluene in the form of lattice oxygen. The presence of toluene on the catalyst surface decreases the rate of regeneration of the reduced catalyst by dioxygen. Furthermore, the catalytic activity of a fully oxidized catalyst is different for reaction of toluene with and without dioxygen (see Fig 3.4a and 3.4b). The CO_2 yield is close to two times higher for experiments with dioxygen in the feed over a pre-oxidized catalyst. This difference can be explained by taking into account the thermal reduction of copper oxide at high temperature and in vacuum, see Section 2.1, and the fact that the dioxygen of the mixed pulse reaches the catalyst surface before toluene due to its low molecular mass compared to toluene. It can be concluded that the difference between the initial activity of the catalyst for toluene oxidation experiments with and without dioxygen can be attributed to the fast re-oxidation of mildly reduced copper oxide, due to thermal reduction, by O_2. The degree of reduction of the catalyst due to thermal reduction during 10s is not more than 1%. The loss of oxygen atoms due to thermal reduction is estimated from the cumulative oxygen uptake after 10s exposure of the fully oxidized catalyst to vacuum and

high temperature. A similar reduction behaviour of the catalyst was observed during propane oxidation [23].

To obtain information about the effect of toluene on the consumption of dioxygen by the reduced catalyst, additional experiments were performed. CO pulses were used for catalyst reduction. Dioxygen or a mixture of dioxygen and toluene was pulsed over the fully reduced catalyst. The amount of consumed dioxygen was calculated according to Eq. 3.10. The amount of consumed dioxygen was 10% lower in the presence of toluene. This reflects the inhibition of catalyst re-oxidation by dioxygen due to competition between dioxygen and toluene for the active sites.

3.3.2 Oxygen isotopic exchange

To obtain more information about the participation of lattice and adsorbed oxygen in the reaction, the catalyst was pretreated with $^{16}O_2$ and was pulsed with a mixture of isotopically labeled oxygen $^{18}O_2$, toluene and Ar with a $C_7H_8/^{18}O_2$ ratio of 1:9. The molar outlet flow rate of $H_2{}^{16}O$, $H_2{}^{18}O$ and $C^{16}O_2$, $C^{18}O_2$, $C^{16}O^{18}O$ from the first pulse response are shown in Figs. 5 and 6. The peak time of the H_2O response was 30 ms lower than that of CO_2. This difference cannot be explained by differences in molecular mass and, hence, indicates that H_2O is formed before CO_2. The preferential formation of ^{16}O containing products supports the Mars-van Krevelen mechanism for the total oxidation of toluene. More than 90% of the total water formed is constituted of $H_2{}^{16}O$, see Fig. 3.5. However, the presence of 10% of $H_2{}^{18}O$ could indicate that adsorbed oxygen is also participating in the total oxidation process. The fraction of CO_2 containing either one or two ^{18}O was 18% of the total CO_2 formed. The amount of ^{18}O in CO_2 was almost twice as high as the amount in water. Note that the shape of the $C^{16}O_2$ response in Fig. 3.6 is different from the same response in Fig. 3.1b. This is a consequence of being out of the Knudsen regime. To obtain information about the participation of lattice and adsorbed oxygen in the reaction, we used only the response from the first pulse,

thereby excluding memory effects of carbonaceous species on the catalytic surface originating from the series of high intensity pulses.

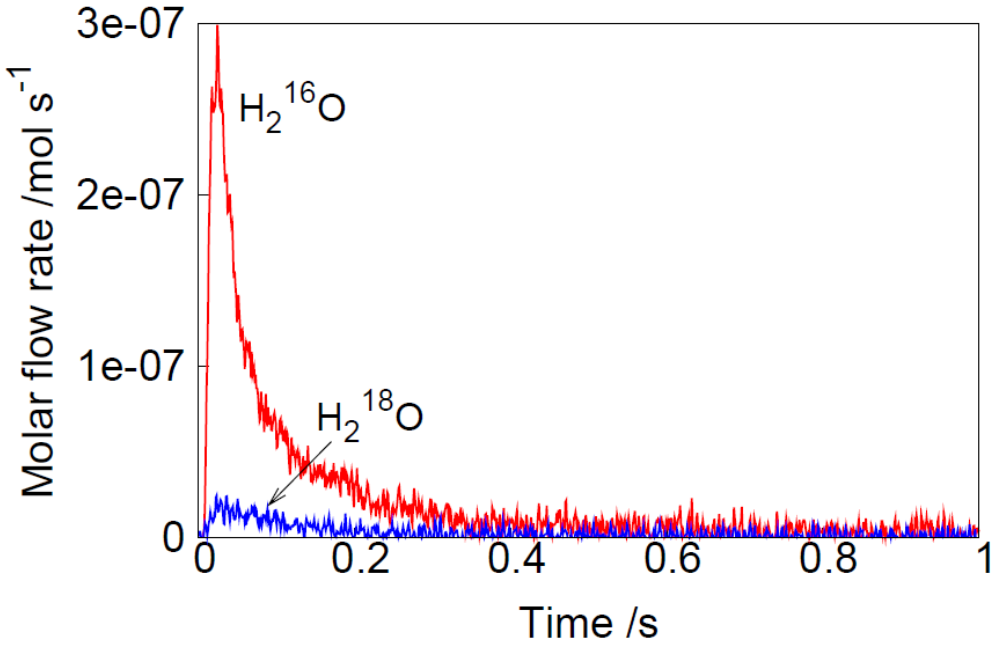

Figure 3.5 $H_2{}^{16}O$ and $H_2{}^{18}O$ production rate versus time to the first pulse of a single pulse experiment with C_7H_8/$^{18}O_2$/Ar over $^{16}O_2$ pretreated catalyst at T=823 K.

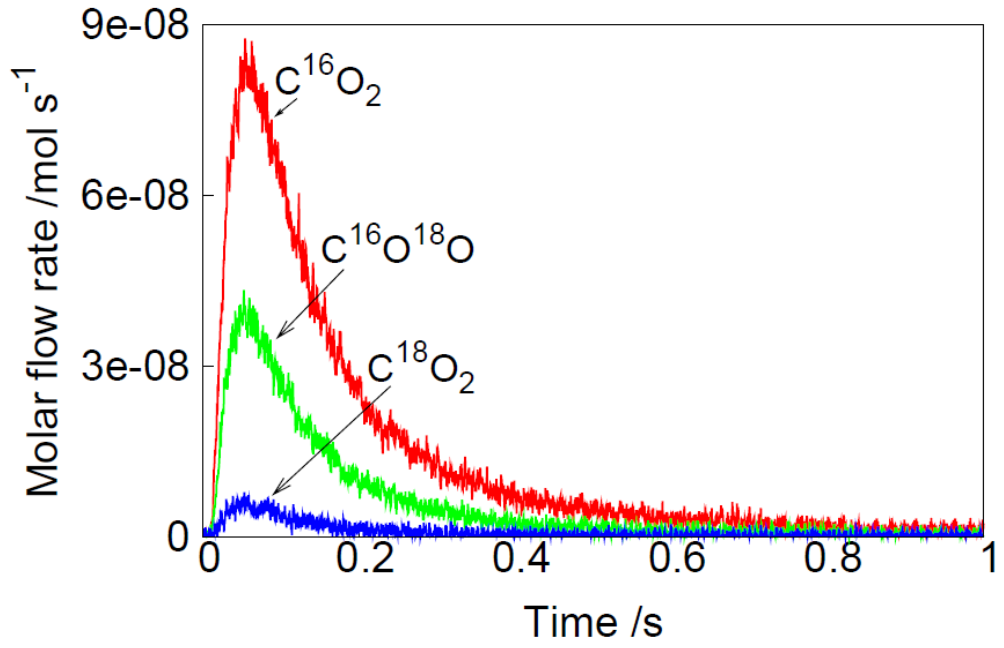

Figure 3.6 $C^{16}O_2$, $C^{16}O^{18}O$ and $C^{18}O_2$ production rate versus time from the first pulse of a single pulse experiment with C_7H_8/$^{18}O_2$/Ar over $^{16}O_2$ pretreated catalyst at T=823 K..

The nature of these isotopic oxygen products can be explained by a set of heterogeneous processes. On the fully oxidized catalyst oxygen

can only weakly and reversibly adsorb [11, 36, 37]. If the catalyst is not fully oxidized, oxygen that is adsorbed on the surface can be incorporated into the lattice. Taking into account the thermal reduction of copper oxide at high temperature and in vacuum, see Section 2.1, and the fact that the dioxygen of the mixed pulse reaches the catalyst surface before toluene due to its low molecular mass compared to toluene, we can conclude that the formation of $H_2{}^{18}O$ during oxygen isotopic experiment can be attributed to the following sequence of processes: (i) fast re-oxidation of mildly reduced copper oxide by $^{18}O_2$; (ii) abstraction of hydrogen by the adsorbed oxygen species and the labeled oxygen incorporated into the lattice. As the formation of water precedes that of carbon dioxide, see Figs. 3.5 and 3.6, the oxygen vacancy that is generated due to the formation of water is refilled either by the dioxygen in the feed mixture or via diffusion from the bulk of the catalyst. Therefore the amount of ^{18}O available in the lattice of the catalyst for carbon dioxide formation will be higher, which results in the formation of a higher fraction of ^{18}O in the carbon dioxide, as has been observed.

Fig. 3.7 shows the amount of carbon dioxide formation vs. time during a multi-pulse experiment with $C_7H_8/^{18}O_2/Ar$ on a $^{16}O_2$ pretreated catalyst. The formation of the ^{18}O containing products increases with time. The amount of $C^{16}O_2$ drops significantly initially due to the fast consumption of surface ^{16}O species. The amount of $C^{16}O^{18}O$ reaches quickly a maximum and then slowly decreases. This long tail is due to the slow diffusion of ^{16}O from the bulk to the surface of the fully oxidized catalyst, which mainly contains ^{18}O, and $C^{18}O_2$ being the main reaction product. The total amount of ^{16}O in the products after the multi-pulse experiment is 50% of the total amount of exchangeable ^{16}O in the catalyst.

In order to understand the role of secondary isotopic exchange in the products distribution, the following experiments were performed. A mixture of $C_7H_8/^{16}O_2/C^{18}O_2$ was pulsed to the catalyst and the amount of $C^{16}O^{18}O$ was monitored at the outlet. The amount of $C^{16}O^{18}O$ at the outlet was 30% of the total amount of CO_2 which confirmed an exchange of lattice ^{16}O with ^{18}O from $C^{18}O_2$. When $^{18}O_2$ was pulsed over

a fully oxidized catalyst, 17% of oxygen containing ^{16}O was found in the total oxygen at the outlet. It has been reported in literature that O from $CuO\text{-}CeO_2/Al_2O_3$, and CeO_2/Al_2O_3 catalyst is exchanged with CO_2 [23, 28].

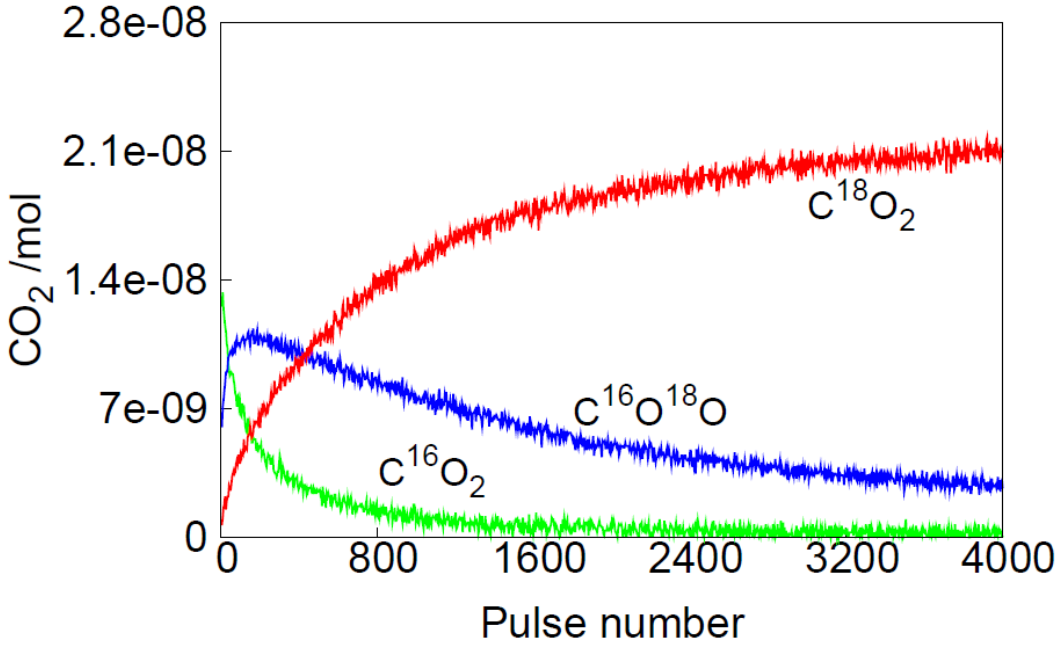

Figure 3.7 $C^{16}O_2$, $C^{16}O^{18}O$ and $C^{18}O_2$ production versus pulse number to multi-pulse experiment with $C_7H_8/^{18}O_2/Ar$ over $^{16}O_2$ pretreated $CuO\text{-}CeO_2/Al_2O_3$ catalyst at T=823 K. $C_7H_8/^{18}O_2$=1:9.

There are three classes of exchange mechanisms known [38, 39]. The first is the equilibration reaction, which requires no participation of oxygen atoms from the solid. The second mechanism constitutes a simple hetero-exchange involving only one surface oxygen atom and the third reaction mechanism involves the exchange of two oxygen atoms of the solid simultaneously (complex hetero-exchange). The first mechanism can be excluded under TAP conditions as collisions between gas-phase molecules can be neglected in the Knudsen diffusion regime. Further, the TAP data do not allow discrimination of isotope exchange between the redox process and secondary isotope exchange of surface oxygen with carbon dioxide and/or dioxygen.

3.3.3 Lifetime of active surface oxygen species

As described in the previous section, two types of oxygen can be present on the catalyst surface: lattice and adsorbed oxygen species. The catalyst activity is determined by weakly bound oxygen in the lattice. The presence of adsorbed oxygen species and weakly bound oxygen in the lattice and their role in the oxidation of toluene was studied by performing alternating-pulse experiments in which the dioxygen was used as pump molecule and toluene as probe molecule. The time lag of the toluene pulse, after the injection of dioxygen pulse, was varied whereas the time from the injection of the toluene pulse to the next dioxygen pulse, that is, the data acquisition time of the toluene response, was kept constant at 20 s. This was done to ensure that toluene stays over the catalyst for the same amount of time for the experiments with different time lag of toluene pulse - thereby providing a similar catalytic state for the dioxygen pulse in all the experiments.

As seen in Fig. 3.8, the formation of carbon dioxide was observed after both the dioxygen and toluene pulse. The amount of CO_2 formed from the toluene pulse decreased with increasing time lag of the toluene pulse. This can be attributed to the low lifetime of active surface oxygen species from the preceding dioxygen pulse. Assuming first order kinetics, the lifetime of the weakly bound oxygen in the lattice and the adsorbed oxygen species was calculated to be of the order of 1s.

The formation of CO_2 as response to the dioxygen pulse indicates that adsorbed oxygen from the gas phase and/or the oxygen incorporated into the lattice reacts with remaining carbon ad-species strongly adsorbed on the catalyst during the toluene pulse. The amount of CO_2 was nearly constant for all the experiments with different time lags of the toluene pulse. This was due to the constant data acquisition time of the toluene response.

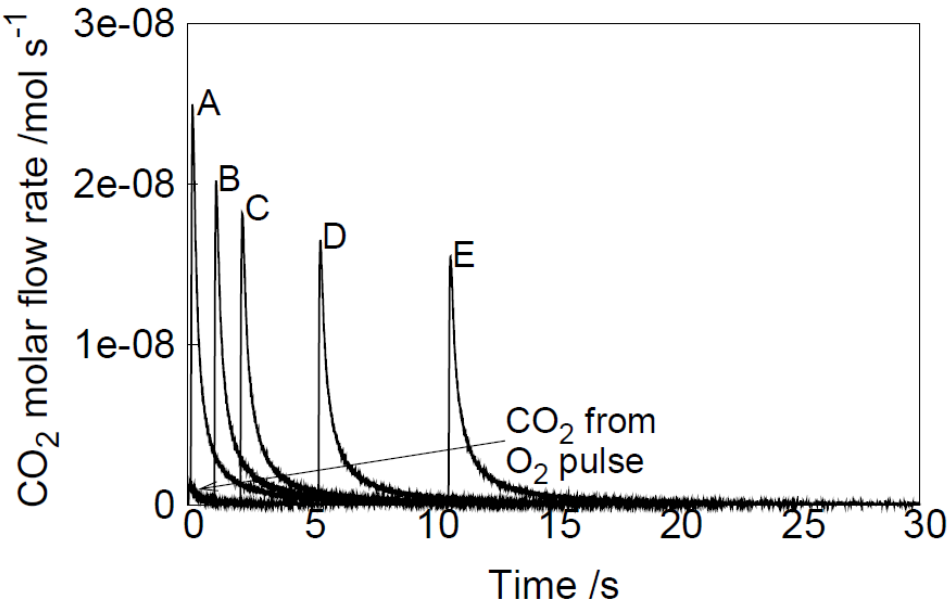

Figure 3.8 CO_2 production rate versus time during O_2 and C_7H_8 alternating-pulse experiment with different time lags of C_7H_8 pulse: (A)0.1s, (B)1s, (C)2s, (D)5s, (E)10s at T=823 K.

The adsorption and lifetime of toluene on the catalyst surface was studied by varying the data acquisition time of the response from the toluene pulse, i.e., allowing toluene to stay on the catalytic surface for varying amounts of time and probing carbon dioxide formation from the di-oxygen pulse. The time lag of the toluene pulse was kept constant at 0.3 s. Total data acquisition times - oxygen and toluene combined - of 2 s, 5 s, 10 s and 20 s were used and CO_2 was monitored. The results for an average of 25 pulse responses for each total data acquisition time are shown in Figure 9. CO_2 obtained during the di-oxygen pulse is higher when the total data acquisition time was lower. The amount of CO_2 during the di-oxygen pulse decreases with increase in the total data acquisition time. The amount of CO_2 during the di-oxygen pulse was almost five times lower at total data acquisition time 20 s than at 2 s. The lifetime of the adsorbed toluene species was calculated to be ~10 s. More CO_2 was produced during the toluene pulse. The intensity of this CO_2 response was high at low total data acquisition time. This was due to the long lifetime of toluene on the catalyst surface. In the process of collecting 25 pulse responses at low total data acquisition time, species intermediate between toluene and CO_2 accumulate on the catalytic surface, thereby increasing the amount of CO_2 produced.

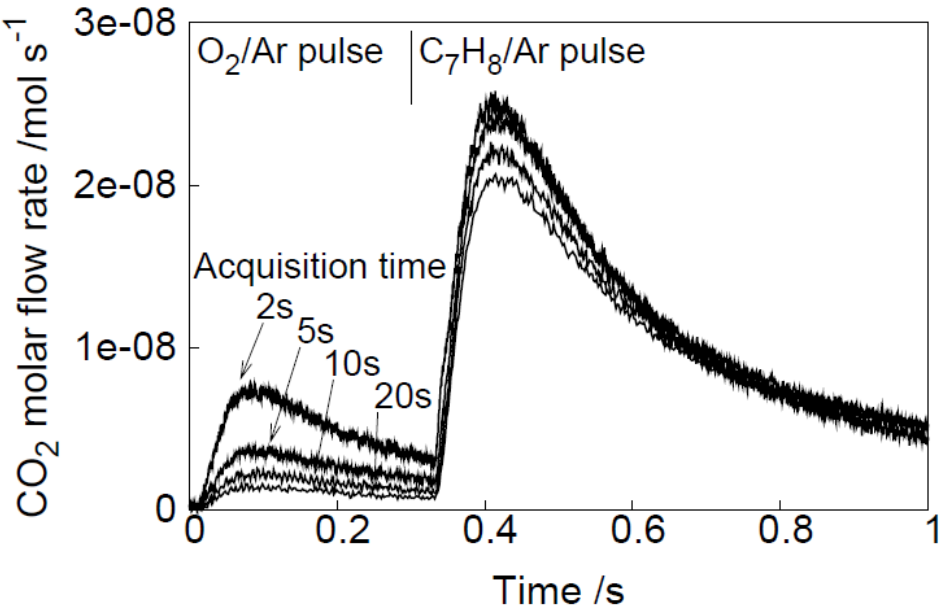

Figure 3.9 CO_2 production rate versus time during O_2 and C_7H_8 alternating-pulse experiment with total data acquisition time 2s, 5s, 10s and 20s at T=823 K. C_7H_8 pulsed at constant time lag = 0.3s.

3.3.4 Carbon and hydrogen labeling

In order to obtain insight in the sequence according to which the various bonds in toluene are broken during the oxidation, pulse experiments were performed with labeled toluene, C_6H_5- CD_3 and C_6H_5-$^{13}CH_3$ on O_2 pretreated catalyst. During experiments with C_6H_5-CD_3/Kr, reaction products H_2O, DHO, D_2O were monitored in order to understand the activation of C-H bonds during the oxidation reaction. $^{12}CO_2$ and $^{13}CO_2$ were monitored when C_6H_5-$^{13}CH_3$/Ar was pulsed in order to obtain information on the activation of C-C bonds during the oxidation reaction.

Fig. 3.10 shows the molar outlet flow rates of H_2O, DHO, D_2O while performing experiments with C_6H_5-CD_3/Kr. H_2O, DHO and D_2O are formed due to the breakage of C-H and C-D bonds thereby initiating the reaction between the departed H and D from C_6H_5- CD_3 and O from the catalyst. The H_2O, DHO and D_2O responses show peaks at the same time which means that these products are formed nearly at the same time. This can be due to the simultaneous abstraction

of hydrogen from the methyl and the phenyl group and/or the long lifetime of hydroxyl groups on the catalyst surface.

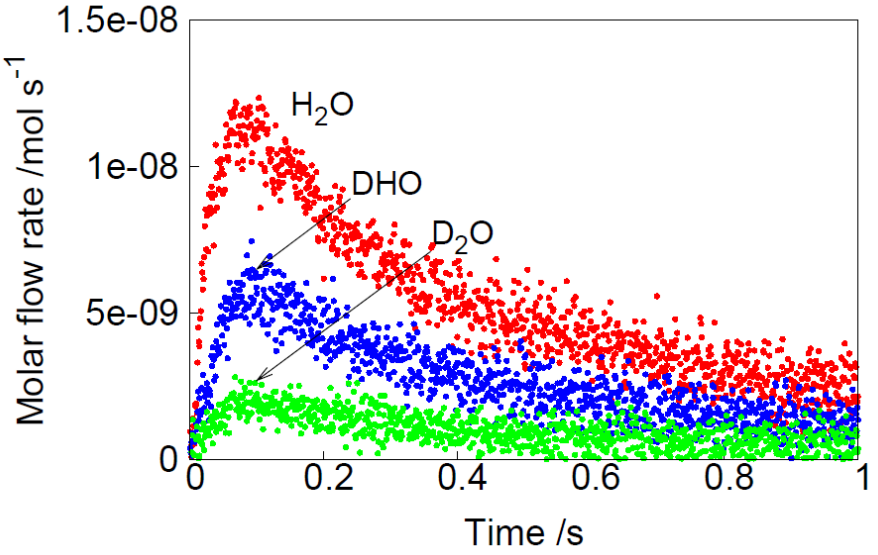

Figure 3.10 H_2O, DHO and D_2O production rate versus time to experiment with C_6H_5-CD_3/O_2/Kr at T=823 K. High intensity pulses of reactants.

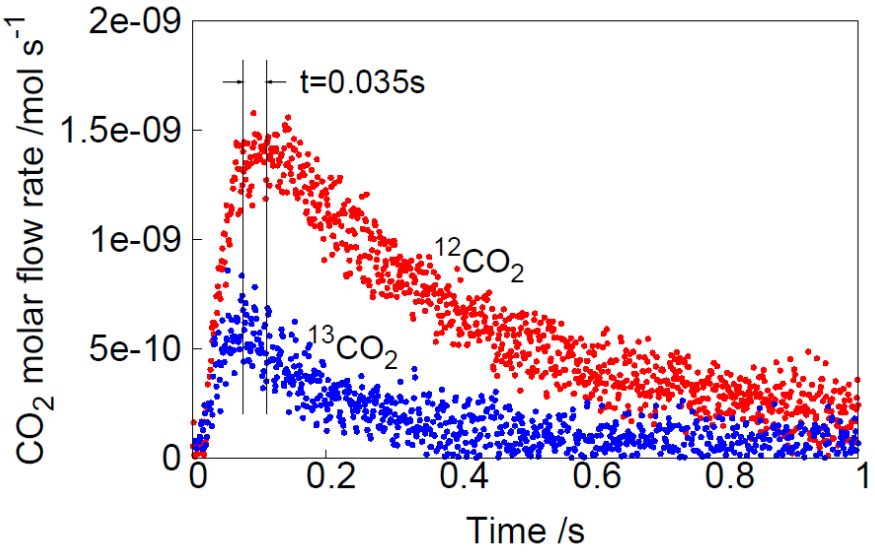

Figure 3.11 $^{13}CO_2$ and $^{12}CO_2$ production rate versus time to single pulse experiment with C6H5-13CH3/O2/Ar at T=873 K.

Moreover, the distribution of deuterium in the isotopomers was far from that expected for a binomial distribution. This can be explained by a set of heterogeneous processes. Surface hydroxyl species would be produced by hydrogen abstraction from toluene on Cu^{2+}-O^{2-} or Ce^{4+}-O^{2-} sites. The hydroxyl groups are stable on the catalyst surface.

However, recombination of these surface hydroxyl groups leads to H_2O formation, followed by desorption from the metal oxide surface. In water formation, only the neighboring hydroxyl groups participate, leading to the formation of the observed isotopic distribution.

Fig. 3.11 shows the molar outlet flow rates of $^{12}CO_2$ and $^{13}CO_2$ while performing experiments with C_6H_5-$^{13}CH_3$/Ar. The $^{13}CO_2$ response reaches a maximum 35 ms before $^{12}CO_2$ which indicates an abstraction of the carbon atom of the methyl group prior to those in the phenyl group.

3.4 General discussion

The results of this study show that the total oxidation of toluene over the CuO-CeO_2/Al_2O_3 catalyst is carried out by a classical redox, that is, Mars-van Krevelen mechanism. However, adsorbed oxygen can also participate in the reaction. Active surface oxygen species with a lifetime of the order of 1 s, will contribute to a higher catalytic activity, but only if dioxygen is present in the feed and the catalyst is fully oxidized. A lifetime of weakly bound oxygen species as low as 10 ms was reported by Balcaen et al. [23] for the total oxidation of propane over the same catalyst. In the study of Balcaen et al., CO_2 was formed only upon the propane pulse - during an alternating-pulse experiment with dioxygen and propane - indicating that the catalyst surface did not contain carbon containing species which can interact with surface oxygen species [23]. In contrast with propane, in toluene total oxidation the surface of the catalyst contains species, intermediate between toluene and CO_2, even 20 seconds after the toluene pulse. Clearly, the interaction of propane with the catalyst is much weaker compared to toluene.

The relative position and width of the H_2O and CO_2 responses, compare for example, Figs. 5 and 6, can be attributed to one or both of the following factors: (i) the strong interaction of CO_2 with the catalyst; (ii) the slow oxygen diffusion from the bulk to the surface which provides oxygen for reaction. During a pulse experiment with carbon

monoxide over the oxidized catalyst at the same temperature, the CO_2 response was much narrower compared to the response from a C_7H_8 pulse. This suggests that the broadening of the CO_2 response in toluene oxidation was not mainly due to the slow desorption of CO_2.

The importance of oxygen diffusion from the bulk to the surface can be assessed by applying the Einstein relation:

$$\bar{t} = \frac{\bar{x}^2}{D_b} \tag{3.11}$$

where $\bar{t}$ is the time taken for displacement of oxygen from the bulk to surface (s), $\bar{x}$ is the average traveling distance of the oxygen atoms (m), and D_b is the diffusion coefficient of oxygen (m^2s^{-1}).

Four oxygen atoms are required to form water and fourteen to form CO_2 for each toluene molecule. The latter is surrounded by 4-5 adjacent oxygen sites which is sufficient for water formation. The rest of the required oxygen atoms have to diffuse from 4-5 lattice planes beneath the surface. Therefore, the distance from which the eighteen oxygen atoms are extracted from the oxide bulk is approximately equal to 1nm. For a fully oxidized catalyst a value of 10^{-15} m^2s^{-1} [40, 41] can be assumed for the diffusion coefficient at 823K which leads to a time scale for diffusion of the order of 10^{-3}s, indicating no diffusion limitation of the formation the CO_2 in this case. However, it is well documented that the diffusion coefficient strongly decreases with increasing degree of reduction [37]. Hence, diffusion could indeed be limiting at the investigated degrees of reduction. This is reflected in the strong decrease of the reaction rate of toluene oxidation in Fig. 3.4. This decrease of the diffusion rate with increasing degree of reduction is reported to be caused by an increase of the lattice oxygen bond strength from 40 to 80kJ/mol at a degree of reduction of 1-2% to 240 kJ/mol at a degree of reduction of 10% [37]. Fig. 3.2 indeed indicates an increase of the activation energy with increasing degree of reduction. Obviously the water formation will be less limited by diffusion compared to CO_2 formation, explaining the appearance of H_2O prior to that of CO_2.

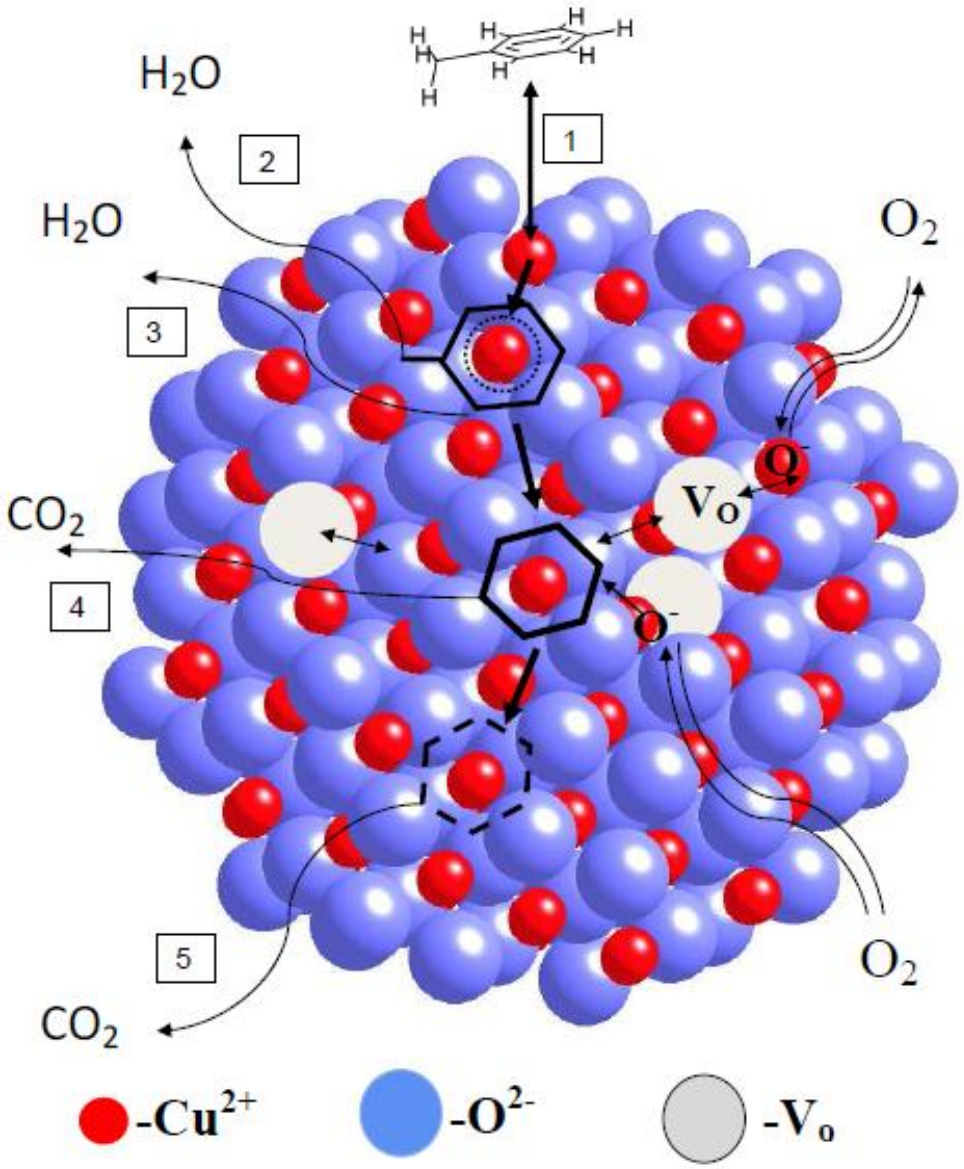

Figure 3.12 Reaction network for the total oxidation of toluene.

Finally, elementary steps in the catalytic cycle, which are thought to be relevant, are shown in Fig. 3.12. According to literature, the first step constitutes the adsorption of toluene with the methyl group on O^{2-} and phenyl on Cu^{2+} [20, 22, 42]. The second and third steps are the simultaneous H-abstraction on 4-5 adjacent oxygen sites from the methyl and phenyl groups and the formation of water. As seen from Fig. 3.11, $^{13}CO_2$ forms before $^{12}CO_2$ upon pulsing C_6H_5-$^{13}CH_3$ over the catalyst. Thus, the abstraction of the carbon atom in the methyl group takes place in the fourth step followed by the carbon atoms in the

phenyl group in the fifth step. The carbon atoms react with O from the lattice/surface of the catalyst forming C-O bonds giving rise to alkoxides. These alkoxides are further oxidized, giving rise to carbonyl compounds and carboxylate species [19, 20]. This route leads to the formation of carbon dioxide and intermediates between toluene and CO_2 on the catalyst surface. The intermediates are then oxidized by the lattice and/or surface oxygen.

3.5 Conclusions

The catalytic cycle for the total oxidation of toluene on CuO-CeO_2/Al_2O_3 can be summarized as follows.

Dioxygen ensures the re-oxidation of the reduced catalyst according to the well-known Mars-van Krevelen mechanism. Weakly bound surface lattice oxygen atoms and adsorbed oxygen species, the lifetime of which is close to 1s, are highly reactive and only found over a fully oxidized catalyst and in the presence of dioxygen. The total oxidation rate significantly decreases over a mildly reduced catalyst.

The reaction network of the catalytic total oxidation of toluene consists of the following sequence: adsorption of toluene on the catalyst surface; the simultaneous abstraction of H from the methyl and the phenyl group; abstraction of the carbon atom of the methyl group and finally, destruction of the aromatic ring. The carbon containing surface intermediates between toluene and CO_2 are slowly oxidized by the lattice and/or adsorbed oxygen that is, on a time scale of ~10s. Water, however, is formed twice as fast. The latter can be attributed to the less stringent requirements for the incorporation of the lattice and/or adsorbed oxygen, in particular related to diffusion.

References

1. J.J. Spivey, Industrial & Engineering Chemistry Research 26 (1987) 2165–2180.
2. L.F. Liotta, Applied Catalysis B: Environmental 100 (2010) 403-412.
3. C.J. Heyes, James G. Irwin, Hilary A. Johnson, R.L. Moss, The catalytic oxidation of organic air pollutants part 1. Single metal oxide catalysts, Journal of Chemical Technology and Biotechnology, 32 (1982) 1025-1033.
4. E.M. Cordi, P.J. O'Neill, and J.L. Falconer, Applied Catalysis B: Environmental 14 (1997) 23-36.
5. P.-O. Larsson, and A. Andersson, Journal of Catalysis 179 (1998) 72-89.
6. P.-O. Larsson, and A. Andersson, Applied Catalysis B: Environmental 24 (2000) 175-192.
7. H. Rajesh, U.S. Ozkan, Complete Oxidation of Ethanol, Acetaldehyde, and Ethanol/Methanol Mixtures over Copper Oxide and Copper-Chromium Oxide Catalysts, Industrial & Engineering Chemistry Research, 32 (1993) 1622-1630.
8. C.-H. Wang, S.-S. Lin, C.-L. Chen, and H.-S. Weng, Chemosphere 64 (2006) 503-509.
9. P.M. Heynderickx, J.W. Thybaut, H. Poelman, D. Poelman, and G.B. Marin, Journal of Catalysis 272 (2010) 109-120.
10. S. Scirè, P.M. Riccobene, and C. Crisafulli, Applied Catalysis B: Environmental 101 (2010) 109-117.
11. B. Grzybowska-Świerkosz, Topics in Catalysis 11-12 (2000) 23-42.
12. S. Minicò, S. Scirè, C. Crisafulli, R. Maggiore, and S. Galvagno, Applied Catalysis B: Environmental 28 (2000) 245-251.

13. S. Scirè, S. Minicò, C. Crisafulli, and S. Galvagno, Catalysis Communications 2 (2001) 229-232.

14. N. Bahlawane, Applied Catalysis B: Environmental 67 (2006) 168-176.

15. A. Bampenrat, V. Meeyoo, B. Kitiyanan, P. Rangsunvigit, and T. Rirksomboon, Catalysis Communications 9 (2008) 2349-2352.

16. B. Solsona, T. García, G.J. Hutchings, S.H. Taylor, and M. Makkee, Applied Catalysis A: General 365 (2009) 222-230.

17. M. Baldi, E. Finocchio, F. Milella, and G. Busca, Applied Catalysis B: Environmental 16 (1998) 43-51.

18. V.P. Santos, M.F.R. Pereira, J.J.M. Órfão, and J.L. Figueiredo, Applied Catalysis B: Environmental 99 (2010) 353-363.

19. S. Lars, and T. Andersson, Journal of Catalysis 98 (1986) 138-149.

20. E. Finocchio, G. Busca, V. Lorenzelli, and R.J. Willey, Journal of Catalysis 151 (1995) 204-215.

21. B. Irigoyen, A. Juan, S. Larrondo, and N. Amadeo, Journal of Catalysis 201 (2001) 169-182.

22. B. Irigoyen, A. Juan, S. Larrondo, and N. Amadeo, Surface Science 523 (2003) 252-266.

23. V. Balcaen, R. Roelant, H. Poelman, D. Poelman, and G.B. Marin, Catalysis Today 157 (2010) 49.

24. F. Konietzni, H.W. Zanthoff, and W.F. Maier, Journal of Catalysis 188 (1999) 154-164.

25. G.I. Panov, K.A. Dubkov, and E.V. Starokon, Catalysis Today 117 (2006) 148-155.

26. M. Machida, Y. Murata, K. Kishikawa, D. Zhang, K. Ikeue, Chemistry of Materials 20 (2008) 4489-4494.

27. J.T. Gleaves, G. Yablonsky, X. Zheng, R. Fushimi, and P.L. Mills, Journal of Molecular Catalysis A: Chemical 315 (2010) 108-134.

28. G.S. Yablonsky, M. Olea, and G.B. Marin, Journal of Catalysis 216 (2003) 120-134.

29. J. Pérez-Ramírez, and E.V. Kondratenko, Catalysis Today 121 (2007) 160-169.

30. G. Silversmit, H. Poelman, V. Balcaen, P.M. Heynderickx, M. Olea, S. Nikitenko, W. Bras, P.F. Smet, D. Poelman, R. De Gryse, M.-F. Reniers, and G.B. Marin, Journal of Physics and Chemistry of Solids 70 (2009) 1274-1284.

31. K. Alexopoulos, M. Anilkumar, M.-F. Reyniers, H. Poelman, S. Cristol, V. Balcaen, P.M. Heynderickx, D. Poelman, and G.B. Marin, Applied Catalysis B: Environmental 97 (2010) 381-388.

32. J.T. Gleaves, J.R. Ebner, P.L. Mills, and J.W. Ward, Studies in Surface Science and Catalysis Volume 38 (1988) 633-644.

33. V. Perrichon, A. Laachir, G. Bergeret, R. Frety, L. Tournayan, and O. Touret, Journal of the Chemical Society, Faraday Transactions 90 (1994) 773-781.

34. P. Fornasiero, G. Balducci, R. Di Monte, J. Kaspar, V. Sergo, G. Gubitosa, A. Ferrero, and M. Graziani, Journal of Catalysis 164 (1996) 173-183.

35. P. Mars, and D.W.v. Krevelen, Chemical Engineering Science 3 (1954) 41-58.

36. J. Haber, and W. Turek, Journal of Catalysis 190 (2000) 320-326.

37. V.A. Sadykov, S.F. Tikhov, N.N. Bulgakov, and A.P. Gerasev, Catalysis Today 144 (2009) 324-333.

38. A. Bueno-López, K. Krishna, and M. Makkee, Applied Catalysis A: General 342 (2008) 144-149.

39. J.S.J. Hargreaves, and I.M. Mellor, Isotopes in heterogeneous catalysis. Imperial College Press, 2006.

40. P. Trocellier, International Congress Copper '06'. WILEY VCH, 2006.

41. J. Li, S.Q. Wang, J.W. Mayer, and K.N. Tu, Physical Review B 39 (1989) 12367.

42. X. Tang, Y. Xu, and W. Shen, Chemical Engineering Journal 144 (2008) 175-180.

Chapter 4

Nature of the active sites for the total oxidation of toluene by $CuO\text{-}CeO_2/Al_2O_3$

This chapter has been published as "Unmesh Menon, Hilde Poelman, Vitaliy Bliznuk, Vladimir V. Galvita, Dirk Poelman, and Guy B. Marin, Nature of the active sites for the total oxidation of toluene by $CuO\text{-}CeO_2/Al_2O_3$, Journal of Catalysis 295 (2012) 91-103"

Abstract

The binary metal oxide, $CuO\text{-}CeO_2/\gamma\text{-}Al_2O_3$, has been compared with the single oxide components $CuO/\gamma\text{-}Al_2O_3$ and $CeO_2/\gamma\text{-}Al_2O_3$ for toluene total oxidation. The nature of the active sites was determined by means of several spectroscopic techniques, while the transient response technique TAP (Temporal Analysis of Products) was used to investigate the catalytic performance.

The improved performance of the $CuO\text{-}CeO_2/\gamma\text{-}Al_2O_3$ catalyst compared to $CuO/\gamma\text{-}Al_2O_3$ is attributed to the formation of a $Ce_{1-x}Cu_xO_{2-x}$ solid solution with a crystallite size of 6 nm. Within this phase, oxidation of toluene occurs at Cu^{2+} sites and reduction of oxygen at Ce^{3+} sites. Similar to Wacker chemistry, two redox couples, Ce^{4+}/Ce^{3+} and Cu^{2+}/Cu^{1+}, are operational. Apart from the solid solution, a copper

oxide phase with a crystallite size of 100 nm shows significantly lower catalytic activity.

X-ray absorption near-edge structure (XANES) experiments at the copper and cerium edge indicate that Ce^{4+} is reduced at lower temperature than Cu^{2+}. Upon reoxidation with CO_2 or H_2O, Ce^{3+} is partly reoxidized, while Cu^0 is not. This explains an activity increase in the CuO-CeO_2/γ-Al_2O_3 in the presence of H_2O or CO_2. CuO/γ-Al_2O_3 shows loss of activity in the presence of H_2O as site blocking is not compensated by an increase in the reoxidation rate.

4.1 Introduction

Catalytic total oxidation is the most promising approach for the abatement of volatile organic compounds (VOCs) owing to its high efficiency and low operating temperature [1, 2]. Two groups of catalytic materials can be applied: (i) noble metal catalysts (mainly Pt and Pd) and (ii) transition metal oxide-based catalysts [3-10]. Although the former usually have higher activities toward oxidation reactions [11-15], the high cost of noble metals limits their wide application. Among the transition metal oxides, the copper oxide catalysts are known to be active combustion catalysts [13, 14, 16, 17]. CuO was reported to be as effective as Pt for the combustion of n-butanol and methyl mercaptan [18]. Moreover, CuO/Al_2O_3 has shown excellent performance for the total oxidation of CO, ethyl acetate, ethanol [11, 16, 19], propane, and toluene [14, 20].

However, a pure copper-based catalyst is less active and stable in the presence of water vapor and/or carbon dioxide [17, 21]. Copper promoted by ceria shows better catalytic performance for the complete oxidation of toluene, propane, benzene, and *p*-xylene as well as improved activity in the presence of the oxidation products CO_2 and water [14, 22-24].

Adding ceria as a promoter to supported copper oxide has shown several advantages for the catalyst performance:(a) ceria stabilizes the dispersion of the active phase [25, 26]; (b) metal oxide/ceria interactions

strongly affect their redox and, as a consequence, catalytic properties [25, 27-30]; (c) ceria also acts as an oxygen storing phase due to the presence of mixed oxidation states (3+/4+) of cerium [31, 34]; (d) copper doping of CeO_2 can improve the oxygen storage capacity, diffusivity and redox properties, which is attributed to the formation of structural defects [29, 32, 33, 35]. Higher concentrations of oxygen vacancies in the catalysts can enhance catalytic activity, the vacancies providing sites for dioxygen activation [27]. How copper and cerium interact with each other and how such interactions promote catalytic activity is still a matter of debate**.**

The central issues addressed in this study are: (1) the nature of the active sites of the CuO – CeO_2 catalyst, (2) participation of CeO_2 in the oxidation of reduced copper, (3) the role of CeO_2 in the enhancement of catalytic activity in the presence of water and carbon dioxide. The elucidation of the above questions should provide a better understanding of the nature of the active sites and the role of ceria in the binary metal oxide catalyst CuO-CeO_2/γ-Al_2O_3. The bimetallic catalyst has been investigated in comparison to monometallic CuO or CeO_2 supported on the same γ-Al_2O_3. The structure of the catalysts was investigated by use of high resolution transmission electron microscopy (HRTEM), selected area electron diffraction (SAED) electron energy loss spectroscopy (EELS), energy dispersive X-ray analysis (EDX), X-ray diffraction (XRD) and *in situ* X-ray absorption spectroscopy (XAS). A transient response technique, Temporal Analysis of Products (TAP) [36, 37] was used to investigate the catalytic activity and inhibiting/promoting effect of water and carbon dioxide on the catalyst behavior. The high time resolution of the TAP technique allows detection of short or long lived reaction intermediates, which helps to formulate the reaction mechanism.

4.2 Experimental

4.2.1 Catalysts preparation

Three catalysts were investigated in this work: (11 wt.%)CuO-(6 wt.%)$CeO_2/\gamma\text{-}Al_2O_3$, (11 wt.%)$CuO/\gamma\text{-}Al_2O_3$ and (6 wt.%)$CeO_2/\gamma\text{-}Al_2O_3$, denoted hereafter as $CuO\text{-}CeO_2/Al_2O_3$, CuO/Al_2O_3 and CeO_2/Al_2O_3. All the three were synthesized via incipient wetness impregnation/co-impregnation of $\gamma\text{-}Al_2O_3$ (Merk) with $Cu(NO_3)_2{\cdot}2.5H_2O$ (Sigma-Aldrich) and/or $Ce(NO_3)_4{\cdot}9H_2O$ (Fluka) precursors, followed by drying at 357 K for 8h and calcination in air at 973 K for 8 h. After grinding, powder with a grain diameter of 75-100 μm was used for catalyst characterization. Grains of diameter 250–500 μm were used for the TAP experiments to determine catalytic activity.

4.2.2 Catalyst characterization

The bulk chemical composition of the tested catalysts was determined by means of inductively coupled plasma atomic emission spectrometry (ICP-AES) (IRIS Advantage system, Thermo Jarrell Ash). The samples were mineralized by fusion with sodium peroxide and sodium hydroxide. $CuO\text{-}CeO_2/Al_2O_3$ contains 11 wt% CuO and 6 wt% CeO_2, while CuO/Al_2O_3 and CeO_2/Al_2O_3 contain 11 wt.%. CuO and 6 wt.% CeO_2 respectively.

N_2 physisorption at 77 K was applied to determine the BET specific surface area using a Gemini V (Micromeritics) set-up. BET values with their 95% confidence intervals were obtained by regression of the experimental data in the range $0.05 < p/p^0 < 0.30$ with the BET equation. The BET surface area of all three catalysts amounts to 170 ± 10 m^2/g. Crystallographic analyses for the tested catalysts were performed after air exposure ("ex situ") by means of XRD measurements in θ–2θ mode using a Bruker-AXS D8 Discover apparatus with lynx eye detector covering 3° and 192 channels over the range 15–85° with a step of 0.04°. Peak positions and widths were

determined by fitting a Gaussian function to the diffraction after background removal.

The surface composition followed from XPS measurements using a Perkin Elmer PHI ESCA 5500 system equipped with a monochromatic 450 W Al Kα source and showing a base pressure below 1×10^{-7} Pa. Detailed windows of Cu2p, Cu LMM, Ce3d, O1s, and Al2p were recorded with pass energy 58.7 eV and step 0.13 eV. The Al2p photoemission line at 74.0 eV served as binding energy reference.

TEM specimens were prepared by applying simple immersion of a carbon-support film on a nickel grid into the catalyst powder followed by careful shaking off the excess powder. Catalyst particles which had adhered to the carbon film were investigated by means of various TEM modes: Conventional and high-resolution (HR) TEM, electron diffraction, STEM, EDX, and electron energy loss spectroscopy (EELS). A microscope JEOL JEM2200FS-Cs-corrected, operated at 200 kV and equipped with Schottky-type FEG, EDX JEOL JED-2300D and JEOL in-column omega filter, was used. Secondary X-ray fluorescence from the analytical specimen holder was eliminated by means of a beryllium retainer. However, Ni-peaks were detected in the EDX spectra due to secondary fluorescence from the Ni support grid. EEL spectra were obtained in STEM spot mode using an electron probe of 1.0 nm and objective aperture angular size of 6 mrad. The latter allows obtaining an optimal signal-to-noise ratio of Cu L and Ce M core-loss peaks.

In situ XAS measurements were performed on all three catalysts at the SAMBA beam line of the 2.75 GeV synchrotron SOLEIL (Saint-Aubin, France) with a top-up X-ray beam of 400 mA [38]. XANES spectra were measured in transmission at the Cu K edge (8979 eV) and the Ce L_{III} edge (5723 eV) during H_2-TPR (flow rate 20 ml/min of 5% H_2/He, ramping rate 10 K/min, max. temperature 773 K) and isothermal reoxidation experiments with CO_2 (flow rate 20 ml/min of 20% CO_2/He, temperature 950 K) and water vapor (2% H_2O/He, temperature 923 K). The reoxidation temperature was chosen fixed and high in order to enhance the oxidizing effect of CO_2 and H_2O.

In addition, reference spectra for the Cu oxidation states were recorded from CuO, Cu_2O, and Cu powder pellets and foil, while CeO_2 and CeF_3 pelletized powders served as references for the Ce 4+ and 3+ oxidation states. The optics alignment was performed using a Cu foil for the Cu K edge and a Cr foil for the Ce L_{III} edge. As no pure Ce reference was available, the Cr foil was chosen as aligning material for Ce L_{III} as its K edge energy (5989 eV) is close to the one of Ce L_{III} (5723 eV). The same foils served as energy reference sample between the second and third ionization chamber. An oscillating monochromator set-up [39] allowed recording Quick XAS spectra with a time resolution of 1 s. The *in situ* experiments were performed in a microreactor consisting of a thermally insulated frame with a X-ray passage of 2 mm diameter, bearing a quartz capillary of 0.8 mm outer diameter and 10 μm wall thickness. The gas composition at the reactor outlet was monitored with mass spectrometry (MS), while simultaneously recording the XAS spectra. The raw data were transformed to general spectral format and analyzed using Athena software [40]. The position of the Ce and Cu white line, that is, the first maximum after the absorption edge, was used in a qualitative way to evaluate the condition of the catalyst during reduction or oxidation and more specifically the temperature at which reduction started. This analysis is based upon a shift in energy position of the white line, which for some elements is linear with oxidation state, though not quite for Cu and Ce [41, 42]. As an alternative, the relative energy position of the white line for the catalyst at the end of a reduction was compared to the ones of the reference materials, so as to give a qualitative indication of the average oxidation state, that is, below 1+.

4.2.3 Experimental TAP set-up, procedures and conditions

The Temporal Analysis of Products (TAP) reactor set-up used in this work is described in section 2.2. The TAP experiments are performed in a microreactor which is placed in vacuum (10^{-4} – 10^{-5} Pa). The microreactor is made of quartz and measures 33 mm bed-length and 4.75 mm inner diameter. The entrance of the reactor is connected

with two high-speed pulse valves via a small volume. An extremely narrow pulse of gas molecules (~10^{14} molecules) is injected into one end of the microreactor by means of the two pulse valves and the products and the unreacted reactants continuously evacuated at the other end are monitored by a UTI 100C quadrupole mass spectrometer. The low amount of gas molecules relative to the amount of catalyst ensures a constant state of the latter.

For the quantitative interpretation of the pulse responses, an absolute calibration factor was determined for each component. The measured response is an electric voltage corresponding to a molar flow rate at the reactor outlet. The area under the pulse response curve corresponds to the number of molecules detected by the mass spectrometer. The calibration factor relates the area under the pulse response to the amount of molecules pulsed. The calibration factor has to be determined for each gas reactant and is obtained in the following way. A high-frequency pulse train from a vessel with a known volume in the gas preparation section is injected into a reactor filled with inert particles and the pulse responses are monitored by the mass spectrometer. The resulting pulse responses are averaged and the area under the curve is determined. The change in pressure in the vessel then corresponds to the pulsed gas quantity.

To feed toluene, a liquid feed set-up was designed and constructed. It consists of a liquid vaporizing chamber, which is heated to 423 K, into which the liquid feed is injected by use of a 500 μL Hamilton Gastight® #1750 syringe through the high-temperature septum. The vaporizing chamber is also connected to gas bottles, which allows making gas-vapor mixtures. The temperature of the feeding lines coming from the vaporizing chamber is maintained at 423 K. The manifold assembly containing the pulse valves is kept at 348 K. The pressure of the feed from the liquid feeding lines to the pulse valves is maintained at 1.1 bar as it was experimentally determined to be the pressure at which the pulse valves function best. The amount of liquid injected into the vaporizing chamber is such that a vapor state is maintained at the given temperature and pressure in the manifold assembly.

Experiments were performed over 10 mg of catalyst, viz. $CuO\text{-}CeO_2/Al_2O_3$, CuO/Al_2O_3 and CeO_2/Al_2O_3. The catalyst was packed in between two inert zones of quartz particles of the same size. All the experiments in this work are collected over O_2 pretreated catalysts. Catalysts are pretreated by injecting a number of high intensity dioxygen pulses (~10^{15} molecules/pulse) until the outlet oxygen responses are stable. Pulse experiments consist of a pulse train with a number of pulses that are injected into the reactor using one pulse valve. The response corresponding to a single pulse is monitored at a fixed AMU. When pulse responses corresponding to different AMUs have to be measured, the responses are measured sequentially 25 times and averaged in order to obtain a better signal-to-noise ratio. The theoretical number of exchangeable O atoms in CuO and CeO_2 was calculated according to reduction of CuO to Cu, $CuO \rightarrow Cu + \frac{1}{2}O_2$, and of CeO_2 to Ce_2O_3, $CeO_2 \rightarrow \frac{1}{2}Ce_2O_3 + \frac{1}{4}O_2$. The 10 mg of $CuO\text{-}CeO_2/Al_2O_3$, CuO/Al_2O_3, and CeO_2/Al_2O_3 then contain 9.38×10^{18}, 8.33×10^{18} and 1.05×10^{18} of O atoms respectively, that is, ~5 orders of magnitude higher than the number of molecules admitted in a pulse. It is assumed that with 75-100 pulses of reactant molecules, corresponding to 3-4 AMUs measured, the state of the catalyst does not change significantly. All reaction mixtures are prepared with Ar as one of the components, so that the admitted amount of the components can be determined from the Ar response. A temperature range of 723 K – 873 K is covered.

To study the activity of the three catalysts toward toluene total oxidation, experiments were performed over pre-treated catalysts by pulsing toluene (Tol) with and without dioxygen in the feed. Typically, a stoichiometric ratio of dioxygen to toluene, that is,. 9:1, was used in the mixture $Tol/O_2/Ar$, when experiments were conducted in the presence of dioxygen.

The promoting or inhibiting effect of ceria in $CuO\text{-}CeO_2/Al_2O_3$ is expressed as χ_{Ce}, the ratio between the CO_2 yield from CuO-

CeO_2/Al_2O_3 and the sum of CO_2 yields from CuO/Al_2O_3 and CeO_2/Al_2O_3

$$\boldsymbol{\chi_{Ce}} = \frac{\boldsymbol{Y_{CuO-CeO_2/Al_2O_3}}}{\left(\boldsymbol{Y_{CuO/Al_2O_3}} + \boldsymbol{Y_{CeO_2/Al_2O_3}}\right)} \qquad \text{Eq. (4.1)}$$

where $\boldsymbol{Y}$ is the yield of CO_2 for toluene pulse experiments in the feed, the subscript indicating the catalyst used. A value of $\boldsymbol{\chi_{Ce}} > 1$ suggests a promoting effect in the catalytic activity with the addition of CeO_2 to CuO, whereas a value less than one indicates an inhibition effect.

Pulse experiments by co-feeding H_2O or CO_2 along with $Tol/O_2/Ar$ ($Tol : (H_2O/CO_2) = 1:1.6$) were performed in order to study the influence of total oxidation products on the oxidation of toluene. The same amount of toluene was used in the experiments with and without oxidation products in the feed. Labeled $^{13}CO_2$ was used as CO_2 co-feed to distinguish the product $^{12}CO_2$ from the co-feed, whereas normal H_2O was used, since water could not be monitored as product due to the low sensitivity of the mass spectrometer towards it.

The ratio between CO_2 yield from toluene pulse experiments with and without H_2O and $^{13}CO_2$ in the feed is denoted by $\eta_{12CO_2}^{H_2O}$ and $\eta_{12CO_2}^{13CO_2}$ respectively. The superscript denotes the co-feed and the subscript the product monitored.

$$\eta_{12CO_2}^{H_2O} = \frac{\mathrm{Y_{(C_7H_8/O_2/H_2O)}}}{\mathrm{Y_{(C_7H_8/O_2)}}} \qquad \text{Eq. (4.2)}$$

$$\eta_{12CO_2}^{13CO_2} = \frac{\mathrm{Y_{(C_7H_8/O_2/^{13}CO_2)}}}{\mathrm{Y_{(C_7H_8/O_2)}}} \qquad \text{Eq. (4.3)}$$

where Y is the yield of $^{12}CO_2$ product, the subscript being the feed used. If $\eta_{12CO_2}^{H_2O}$ or $\eta_{12CO_2}^{13CO_2} > 1$, addition of H_2O or $^{13}CO_2$ has a promoting effect on the catalytic activity. The error bars in the yields ($\boldsymbol{Y}$), χ_{Ce}, and η were calculated according to the standard deviation of the experimental data.

Blank measurements were conducted with toluene and dioxygen over quartz particles of the same size under normal experimental

conditions. No oxidation products or decomposition of toluene was observed.

4.3. Results

4.3.1 Structural characterization

The XRD patterns for the as received and reduced CuO-CeO_2/Al_2O_3 catalyst (inset of Fig. 4.1) contain sharp CuO and Cu diffraction lines corresponding to CuO and Cu crystallites of ~100 nm for as received and reduced catalyst respectively. The CuO loading of 11 wt% thus leads to crystallization of a bulk CuO phase [11] (see A.1, Appendix A). Based on the width of the diffraction peaks, both the CeO_2 promoter and the γ-Al_2O_3 are nano-crystalline before and after reduction (range 4-8 nm) [43]. For the applied temperature range, 723 K – 873 K, $CeAlO_3$ is never observed. The lattice parameter of the CeO_2 unit cell is obtained from the position of its (200) diffraction peak (Table 1). The value of 0.5395 nm for the as received catalyst lies below the bulk value of 0.5411 nm [44] and also below the value of 0.5401 nm as determined for CeO_2/Al_2O_3. This smaller CeO_2 lattice parameter value points towards Cu incorporation into the CeO_2 crystallites, because Cu^{2+} ions are smaller than Ce^{4+} ions [44, 45]. The XRD peaks of CeO_2 are further analyzed by drawing a Williamson-Hall plot (main part of Fig. 4.1). From the slope and intercept of the linear fits to the data points, the contribution of size and microstrain to the broadening of the XRD peak is determined (Table 4.1). The crystallite sizes for CeO_2 from the Williamson-Hall plot are larger than the ones determined directly through the Scherrer equation from the peak width, but remain within the same range [46]. Moreover, the CeO_2 strain values found from the Williamson-Hall plot are larger than the literature values for pure CeO_2 [44, 47], which can originate from Cu incorporation, just like the smaller CeO_2 lattice parameter does. After reduction, an increase of the lattice parameter to 0.5407 nm is observed, which was accounted for by the partial reduction of CeO_2, since Ce^{3+} is larger than Ce^{4+} [48]. The strain on the other hand is relieved by reduction (Table 4.1).

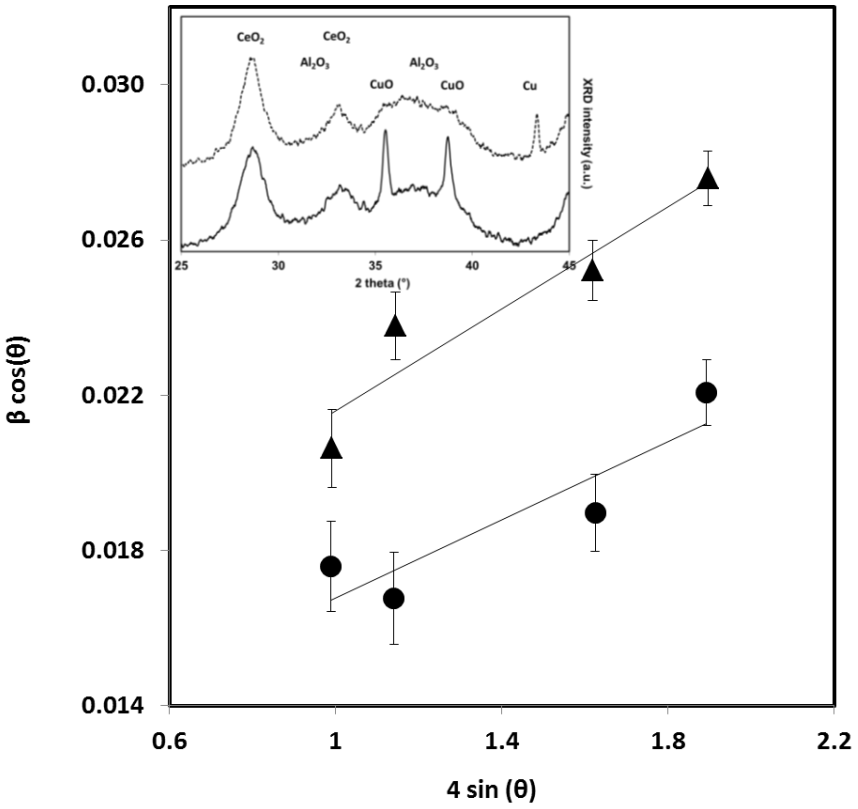

Figure 4.1 Williamson-Hall plot to separate size and strain contributions to the broadening of the diffraction peaks of CeO_2. β = integral width of the peak, θ = diffraction peak position; ▲: catalyst as received; ● : catalyst after reduction at 723 K in a XANES experiment; Straight lines: linear trend lines; error on x-values ~0.002. Inset: XRD pattern for as received (solid line) and reduced catalyst (dotted line)

sample	lattice parameter a (nm)	crystallite size (volume weighted, nm)	microstrain (10^{-3})
as received	0.5395 ± 0.0016	9 ± 1	6.6 ± 0.3
reduced	0.5407 ± 0.0003	12 ± 1	5.0 ± 0.3

Table 4.1: Crystallographic data for CeO_2 crystallites, following from analysis of their diffraction peaks; lattice parameter a from (100) diffraction; crystallite size and microstrain from Williamson-Hall plot (Figure 4.1).

X-ray photoelectron spectra of the $CuO\text{-}CeO_2/\gamma\text{-}Al_2O_3$ catalyst are measured following exposure to air, that is, ex situ, before (labeled 'as received') and after reduction (labeled 'reduced'). The Ce3d signal is very weak, allowing no further line analysis (not shown). For Cu, both the Cu LMM Auger line, with kinetic energy around 915 eV, and the $Cu2p_{3/2}$ photoemission line, with maximum around 934 eV, were recorded. The latter displays a satellite feature at higher binding energy, which is characteristic of Cu^{2+} (not shown). The intensity ratio I_{sat}/I_{main} amounts to 0.37 for the as received catalyst that is, somewhat below the literature value of 0.52 for fully oxidized CuO [11, 16]. As reduced copper species Cu^{1+} and Cu^0 are known not to exhibit such feature, the I_{sat}/I_{main} intensity ratio can be used to evaluate the presence of reduced copper [49]. The lower value found here indicates that part of the as received sample surface is reduced, due to the X-ray irradiation during the XPS measurement.

Identification of the Cu oxidation state cannot be performed solely based on the $Cu2p_{3/2}$ binding energy, because of coinciding photoline positions for Cu^{1+} or Cu^0. A combined evaluation of photoemission and Auger line position is required to discriminate between the 3 possible states. The distinction between oxidation states is adequately made using a Wagner diagram or chemical state plot, see Fig. 4.2, which displays the binding energy of the main Cu photoemission line, the kinetic energy of the main Auger line as well as the Auger parameter α', that is, the sum of $Cu2p_{3/2}$ binding energy and Cu LMM kinetic energy; to be read along the lines with slope -1 [50-52]. In Fig. 4.2, the chemical states for copper before and after reduction, are compared to reference chemical states for the three bulk phases, CuO, Cu_2O and Cu, as well as two chemical states obtained for dispersed Cu^{2+} and Cu^{1+} species [47, 52]. The catalyst as received presents a close to fully oxidized Cu^{2+} state, since it is situated near the 2+ chemical state line with slope -3, passing near the points of bulk CuO and dispersed Cu^{2+}.

Although the oxidation state of Cu in the as received catalyst is found to be 2+, its position on the 2+ chemical state line lies below the point for bulk CuO (lower value of α'). This shows that its electronic

properties are different from those of bulk CuO, either through particle size or because of a different support interaction [47]. Espinós et al. have described how an increasing deposition of CuO onto a ZrO_2 or SiO_2 support leads to a continuous upward shift of the chemical state due to the change in aggregation state from dispersed to more bulk-like [53]. Hence, the present intermediate position between bulk CuO and dispersed Cu^{2+} points to CuO-CeO_2/γ-Al_2O_3 containing a mixture of both phases. Indeed, the presence of small-sized Cu^{2+} will bring down the value of the Auger parameter α' due to the smaller particle size and in addition through an enhanced interaction with the surrounding phase. After reduction, the chemical state shifts towards the 0 chemical state line (Fig. 4.2).

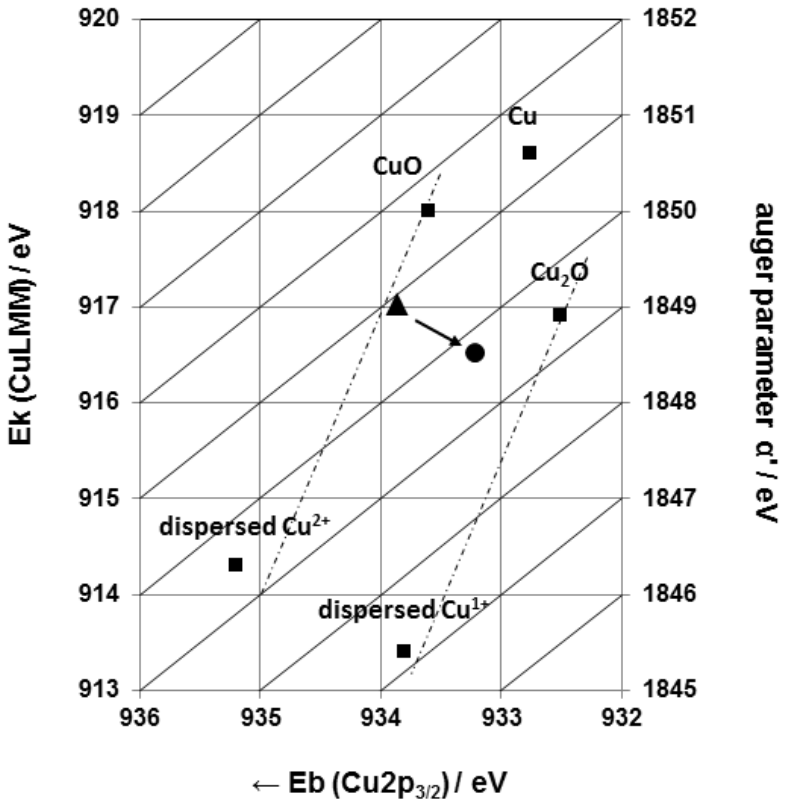

Figure 4.2 Wagner chemical state plot of the Cu XPS results for the catalyst ▲: as received, and ●: after reduction at 723 K in a XANES experiment ; ■ : reference values for Cu compounds and dispersed Cu from [49, 54]; full lines with slope -1: points of equal Auger parameter value; dot-dash lines with slope -3: dot-dash lines: chemical state lines connecting points with the same oxidation state (2+ and 1+ line displayed)

TEM observation of dehydrated CeO_2/Al_2O_3 reveals finely dispersed, randomly oriented crystals from both crystal phases, see Fig. 4.3a. Ceria crystals are visible as darker areas on the alumina agglomerate due to much stronger electron scattering by the heavy Ce atoms than by Al. Selected area electron diffraction (SAED), inset of Fig. 4.3, taken from within the circled area of the figure, consists of ring shaped patterns from the alumina and a discrete number of spots lying on the circles corresponding to ceria. This implies random orientation of a large number of alumina crystals and of few ceria crystallites. A rotational average of the SAED intensity pattern (not shown), confirms the presence of the two crystal phases: gamma-alumina and ceria. EDX spectra taken from the same area as the SAED show the elemental presence of cerium, oxygen and aluminum in the observed frame (not shown). A TEM particle size analysis indicates that the γ-Al_2O_3 support is present as a matrix of ~4 nm crystalline particles with ~6 nm CeO_2 nano-crystallites dispersed among the Al_2O_3. Unlike the case of supported ceria, copper oxide in CuO/Al_2O_3 is formed as relatively large monocrystals, with a mean crystallite size of about 100 nm, see Fig. 4.3b. No copper was detected by EDX within finely dispersed alumina areas. The crystallite sizes for CuO and CeO_2 are in agreement with XRD results (Fig. 4.1) [14].

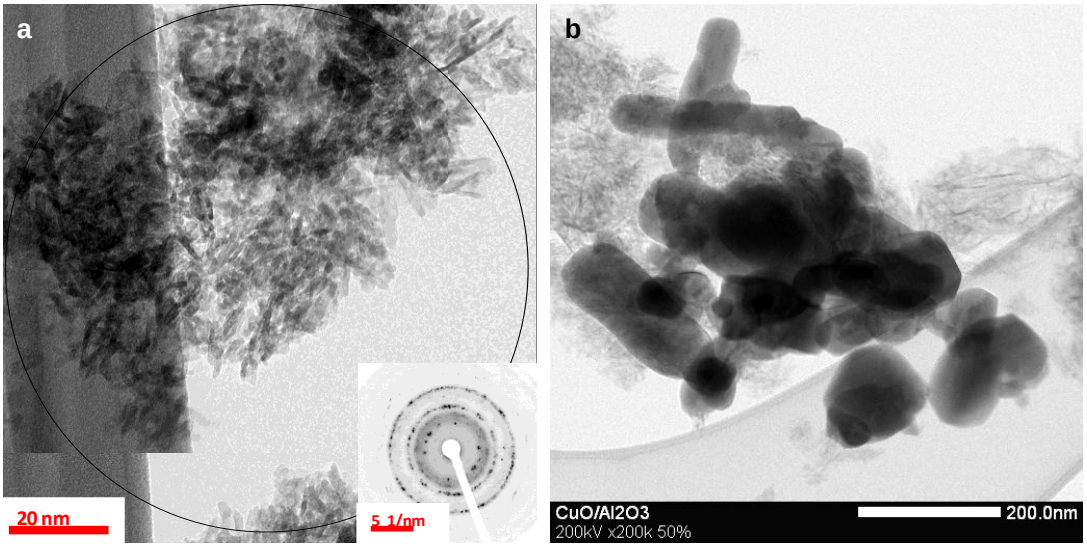

Figure 4.3(a) TEM BF image and SAED taken from the area within the circle of CeO_2/γ-Al_2O_3 particles, (b) TEM BF image of CuO/γ-Al_2O_3 particles.

Two different morphologies were observed on $CuO\text{-}CeO_2/Al_2O_3$. The first type is similar to CeO_2/Al_2O_3, characterized by nano-crystals of ceria (6 nm) which are agglomerated into clusters with estimated diameter of 100 nm, see Fig. 4.4a and b. Electron diffraction taken from areas (sad1) and (sad2) of Fig. 4.4b, exhibit elongated diffraction spots, which fit with the ceria lattice. This elongation implies that the agglomerates consist of ceria nano-crystals which possess a preferential spatial orientation. The second morphology is similar to the one of CuO/Al_2O_3, as described in the previous paragraph (Fig. 4.4b, sad3). Electron diffraction taken from the CuO particle, marked (sad3) on Fig. 4.4b, exhibits a spot pattern, typical for monocrystals and in contrast with the ring pattern of polycrystals.

The EDX line scan in Fig. 4.4c confirms the existence of large CuO monocrystals. The line scan passing through these large entities shows a strong signal of Cu, whereas no Ce was observed. The only other signal observed is a weak one from Al, originating from the alumina matrix. On the other hand, the line scan passing through two CeO_2 clusters shows a considerable Cu signal in addition to the Ce intensity (Fig. 4.4d). Similar observations were made for CeO_2 clusters nowhere near CuO monocrystals, which implies that this Cu intensity cannot be accounted for by electron scattering or secondary X-rays but originates from genuine Cu presence within the CeO_2 clusters. Cu was observed with EDX in all investigated CeO_2 clusters, leading to the conclusion that in this $CuO\text{-}CeO_2/Al_2O_3$ catalyst, Cu is always present in the ceria clusters. Based upon EDX, the average atomic ratio of Ce to Cu within the ceria clusters is 2:1, and the amount of copper in these CeO_2 particles is estimated to less than 15 ± 5 at% of the total amount of copper. Most of the copper in the catalyst is hence located in the CuO bulk monocrystals. Hence, two types of Cu species are present in the $CuO\text{-}CeO_2/Al_2O_3$ catalyst: large CuO monocrystals, labeled CuO, and Cu inside the ceria clusters. Fig. 4.4e shows a high resolution TEM image taken from a CeO_2 cluster within $CuO\text{-}CeO_2/Al_2O_3$, displaying crystalline nano-particles. A fast Fourier transform of this HRTEM image Fig. 4.4f does not reveal any other crystalline component than

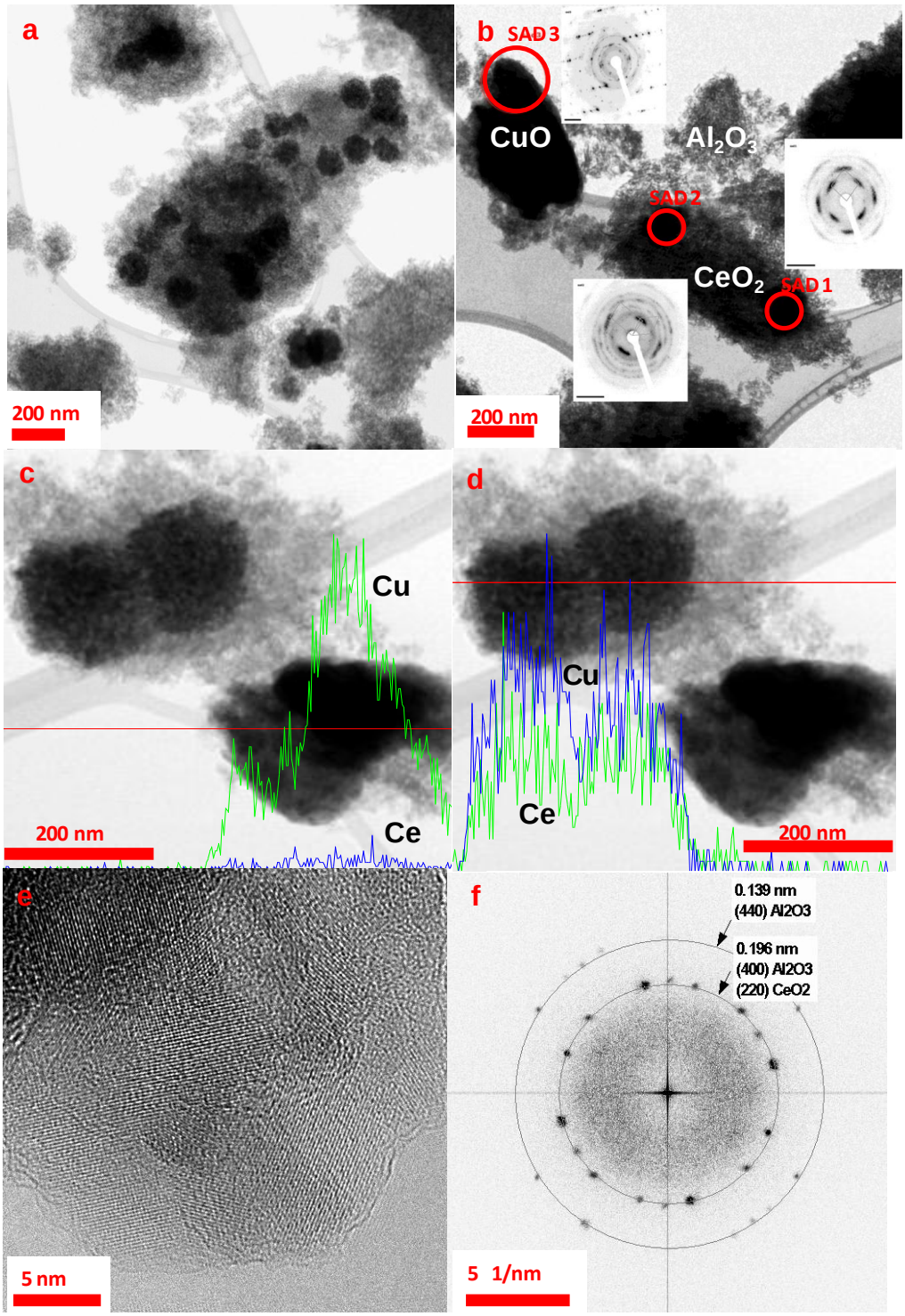

Figure 4.4 TEM BF image of $CuO\text{-}CeO_2/Al_2O_3$ specimen exhibiting (a) nanocrystals of Ce agglomerated into a cluster of estimated diameter 100nm; (b) two types of Cu-containing particles: Cu-rich single crystal (sad3) and dispersed Ce-rich (sad1 and sad2); (c) elemental line-scan of Cu-rich single crystal; (d) elemental line-scan of solid solution $Ce_{1-x}Cu_xO_{2-x}$ area; (e) HRTEM image of solid solution area in $CeO_2\text{-}CuO/Al_2O_3$; (f) FFT of the HRTEM image (e) with lattice parameters for CeO_2 and Al_2O_3.

CeO_2 and Al_2O_3, and in particular no CuO. The latter indicates that the Cu inside CeO_2 is not (nano-) crystalline.

Fig. 4.5a and b show electron energy loss spectra, taken in STEM mode from copper free CeO_2/Al_2O_3 and from CeO_2 with Cu in CuO-CeO_2/Al_2O_3, similar to those shown in Fig. 4.3a and Fig. 4.4a (sad1 and 2), respectively, both in finely dispersed morphology. The EEL spectrum from copper free CeO_2/Al_2O_3 in Fig. 4.5a exhibits clear Ce M_{45} lines from 3d core level excitation. The EEL spectrum from a polycrystalline CeO_2 cluster with dissolved Cu^{2+} in the CuO-CeO_2/Al_2O_3 specimen, see Fig. 4.5b, shows both Ce M_{45} as well as Cu L_{23} white lines, which are broad and weak. In pure CuO or Cu_2O, electrons are drawn away from the copper atom, leading to the presence of empty states in the Cu 3d-band and observation in EELS of sharp L_2 and L_3 white lines caused by the electron transition p → d [54]. For metallic copper on the other hand, the Cu 3d-band is completely filled and the probability of Cu 2p → 3d transitions is reduced so that no sharp L_{23} peaks are observed. For the present CuO-CeO_2/Al_2O_3 sample, Cu^0 is not likely to be present in the catalyst as prepared since full oxidation is expected after the sample pretreatment at 973 K in air. Indeed, no metallic copper was detected by means of SAED. Hence, the L_{23} lines must originate from Cu^{2+}. The weak intensity of the lines points towards small particle size and/or high degree of interaction of the Cu^{2+} with the adjacent atoms in the CuO-CeO_2/Al_2O_3 catalyst. Such enhanced interaction is compatible with Cu being incorporated into the ceria lattice. Substitution of Ce^{4+} with Cu^{2+} will be accompanied by oxygen vacancies to balance charges with the higher valence of Ce^{4+} [31, 33, 35, 55, 56], which in turn influences the Cu L_{23} intensity. Thus, according to the XRD, EDX, SAED, EELS and HRTEM results, it is proposed that Cu^{2+} within CeO_2 is present substitutionally inside the CeO_2 lattice. The incorporation of Cu^{2+} into CeO_2 will be accompanied by defect formation along the following route [57]:

$$x\,CuO + (1-x)CeO_2 \leftrightarrow x\,Cu_{Ce}^{2+} + x\,V_{Ö} + (1-x)\,Ce_{Ce}^{4+} + (2-x)O_O^{2-} \qquad \text{Eq. (4.4)}$$

where the subscript indicates the lattice position. Hence, in addition to the large CuO monocrystals, a $Ce_{1-x}Cu_xO_{2-x}$ solid solution is proposed to be present in the $CuO\text{-}CeO_2/Al_2O_3$ catalyst, with an average x-value of 0.33, based on EDX results. The latter gives rise to an a-typical catalyst picture as drawn in Fig. 4.6. The solid solution will go unnoticed in XRD patterns, as it presents only peaks of the CeO_2 host, but it induces peak shifts due to lattice deformation, which is evidenced from the Williamson-Hall plot. In XPS, the solid solution introduces a shift of the Cu Auger parameter as compared to bulk CuO. Based upon the present structural characterization of the $CuO\text{-}CeO_2/Al_2O_3$ catalyst, the 100 nm monocrystals of CuO, considered as spherical particles, will present a very low dispersion of only 1%. The EDX result of 85 at% of the total Cu amount in bulk CuO will thus present $1.23 \cdot 10^{-2}$ mol/kg_{cat} of surface Cu. The 15 at% dissolved Cu^{2+}, on the other hand, are fully dispersed so that this Cu fraction yields a surface Cu contribution of $4.3 \cdot 10^{-2}$ mol/kg_{cat}.

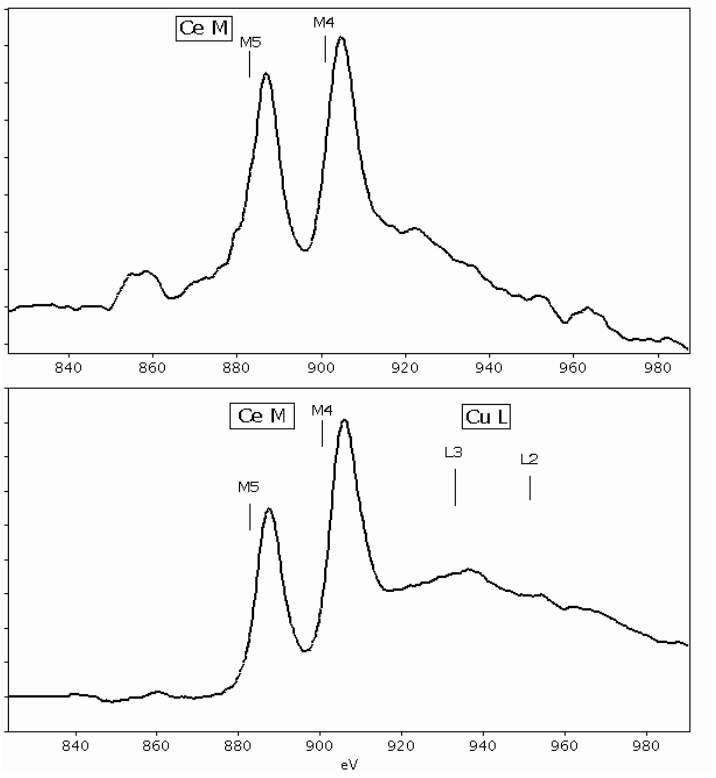

Figure 4.5. Electron energy loss spectra (EELS) taken from (a) copper free CeO_2/Al_2O_3 and (b) $Ce_{1-x}Cu_xO_{2-x}$ solid solution area in $CuO\text{-}CeO_2/Al_2O_3$

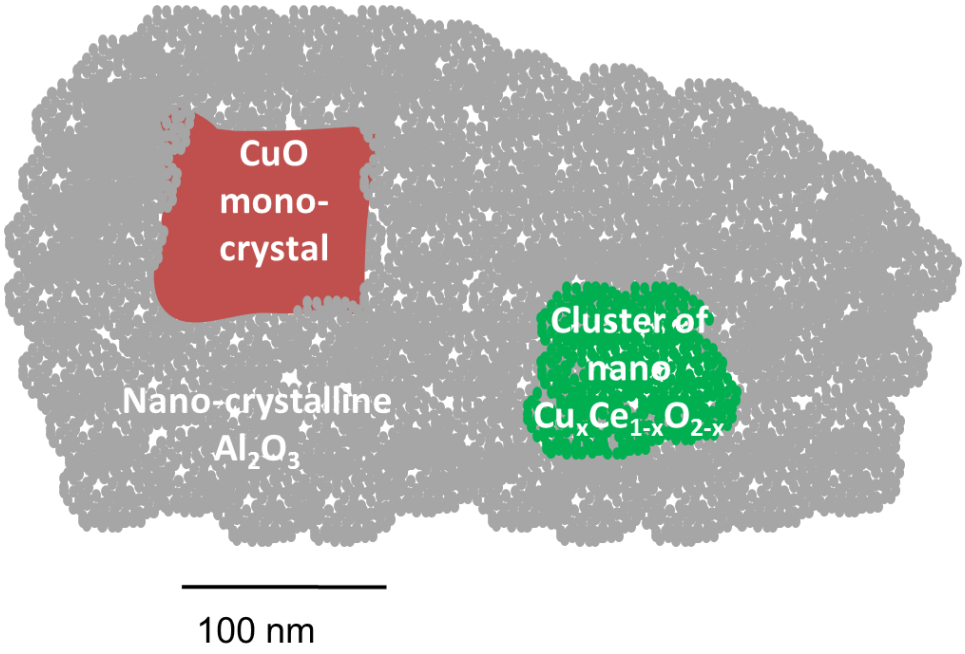

Figure 4.6 Schematic picture of CuO-CeO_2/Al_2O_3, based upon ICP composition, XRD patterns, STEM, EDX line scans and EELS.

4.3.2 *In situ* XANES

The reduction of the catalyst by hydrocarbons has been reported before with either propane, propene and toluene as reductant [20, 58]. A detailed reaction path for the corresponding production of CO_2 and H_2O with toluene as reductant was presented [20]. In this work H_2 was selected as reductant in order to investigate the possible synergy between copper and ceria with respect to the reducibility of the catalyst.

By repeating the experiment at both the Cu K and Ce L_{III} absorption edge, hydrogen was found to reduce both Cu and Ce. The white line position as a function of temperature is shown in Fig. 4.7a and b. At the Ce edge, the white line position at low temperature (~300 K) is close to that of reference CeO_2, pointing to a near 4+ oxidation state. Upon increasing temperature, the white line position remains constant till 450 K and then drops off, followed by a slower decrease from 550 K on. This downward shift of the white line energy relative to the position for CeO_2 corresponds to an average reduction of CeO_2. At

the end point, the average oxidation state of Ce lies closer to Ce^{3+} than to Ce^{4+} based on comparison with the reference Ce^{3+} position.

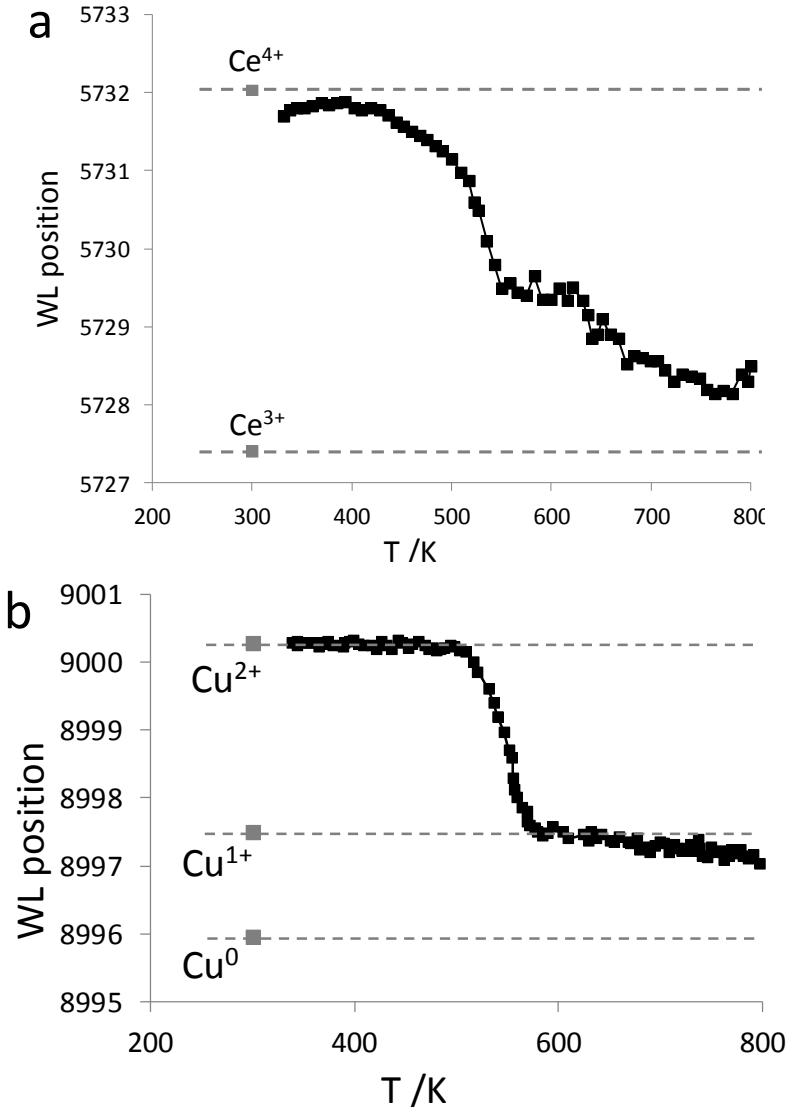

Figure 4.7 White line energy position vs. temperature during hydrogen reduction of CuO-CeO_2/Al_2O_3; (a) Ce L_{III} edge; (b) Cu K edge. The time between 2 data points is 100 s.

At the Cu edge, a similar profile for the white line is found, see Fig. 4.7b. After the first region where CuO remains fully oxidized, reduction sets in at 480 K to reach a slowly decreasing state from 540 K on. As XAS probes the bulk of a sample, the absorption spectrum presents an average signal of all Cu present in the catalyst, that is, of both CuO and dissolved Cu^{2+} phases. Comparison with Fig. 4.7a shows that this overall reduction of CuO phases occurs at similar temperatures as for CeO_2. During the reduction process, Cu goes through and beyond a 1+ state

(see Cu K XANES spectra in A.2, Fig. A.2, Appendix A). At the end of the reduction experiment, the average state of Cu has not reached the Cu metal state but rather lies in between 0 and 1+. It is therefore indicated as Cu^{1+}, although the presence of some Cu^{0} cannot be excluded after reduction.

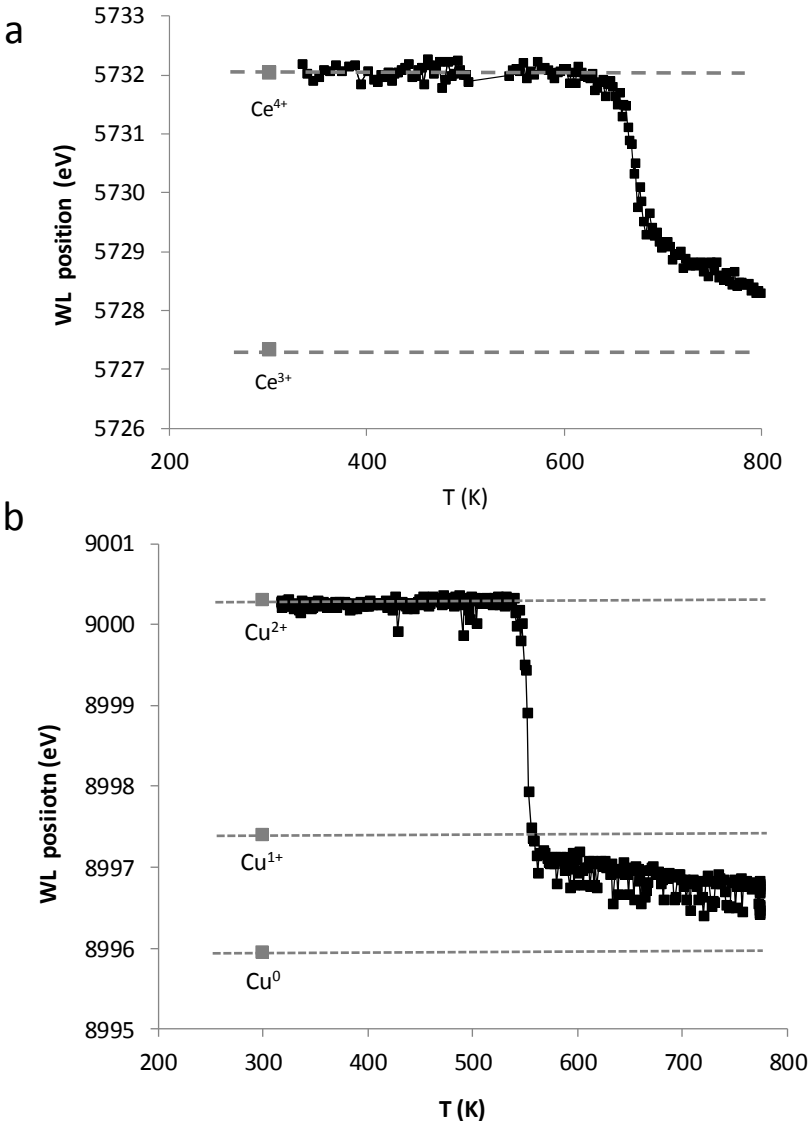

Figure 4.8 White line energy position vs. temperature during hydrogen reduction of (a) CeO_2/Al_2O_3, followed at the Ce L_{III} edge; (b) CuO/Al_2O_3, followed at the Cu K edge.

For comparison, *in situ* XANES during H_2-TPR was equally performed on the single metal oxides CeO_2/Al_2O_3 (Ce L_{III} edge) and CuO/Al_2O_3 (Cu K edge) respectively. The white line energy is plotted versus temperature in both cases, see Fig. 4.8a and b. In Fig. 4.8a, the

onset of reduction of CeO_2/Al_2O_3 is at about 625 K, followed by a sharp downward shift of the white line position. From 700 K onwards, reduction continues slowly. These reduction temperatures are more than 200 K above those registered for Ce in $CuO\text{-}CeO_2/Al_2O_3$, indicating that the combination of Cu and Ce has a beneficial effect upon the Ce reducibility. From the white line analysis for CuO/Al_2O_3 (Fig. 4.8b), the onset of reduction lies at 545 K, with a fast transition to the slower varying part. This onset is slightly higher than that for Cu in the $CuO\text{-}CeO_2/Al_2O_3$, which could be related to the absence of $Ce_{1-x}Cu_xO_{2-x}$ solid solution in CuO/Al_2O_3. However, the main part of the reduction occurs in the same temperature region as in the $CuO\text{-}CeO_2/Al_2O_3$ catalyst, as it is governed by reduction of the CuO single crystals.

The lower reduction temperatures in the binary metal oxide catalyst $CuO\text{-}CeO_2/Al_2O_3$ can only be accounted for by interaction between Cu and Ce in the solid solution. For nano-sized ceria supported on alumina, quite different results have been reported in literature regarding reduction with H_2: no reduction below 773 K [11], two reduction peaks at 873 and 1073 K [59] or a large H_2-reduction peak at 623 K accompanied by a small peak at 873 K [60]. The major part of Ce^{4+} to Ce^{3+} reduction for the $CuO\text{-}CeO_2/Al_2O_3$ catalyst in the present experiment occurs between 400 and 500 K, that is, well below any of the reported temperatures. This can be explained by interaction of Ce with the incorporated Cu^{2+}, introducing an enhanced reducibility for Ce^{4+}. The reduction of Ce^{4+} can have a two-fold origin: either Ce^{4+} is reduced by direct interaction with the hydrogen gas, and/or it supplies O to incorporated, reduced Cu to reoxidize it, thereby being reduced itself. From the reduction of the single oxide catalysts, both options appear as possible, although the single oxides show considerably higher reduction temperatures. Hence, the interaction between Cu and Ce in the solid solution assures enhanced reducibility for both compounds. This allows to have an effective redox cycle at typical industrial total oxidation temperatures.

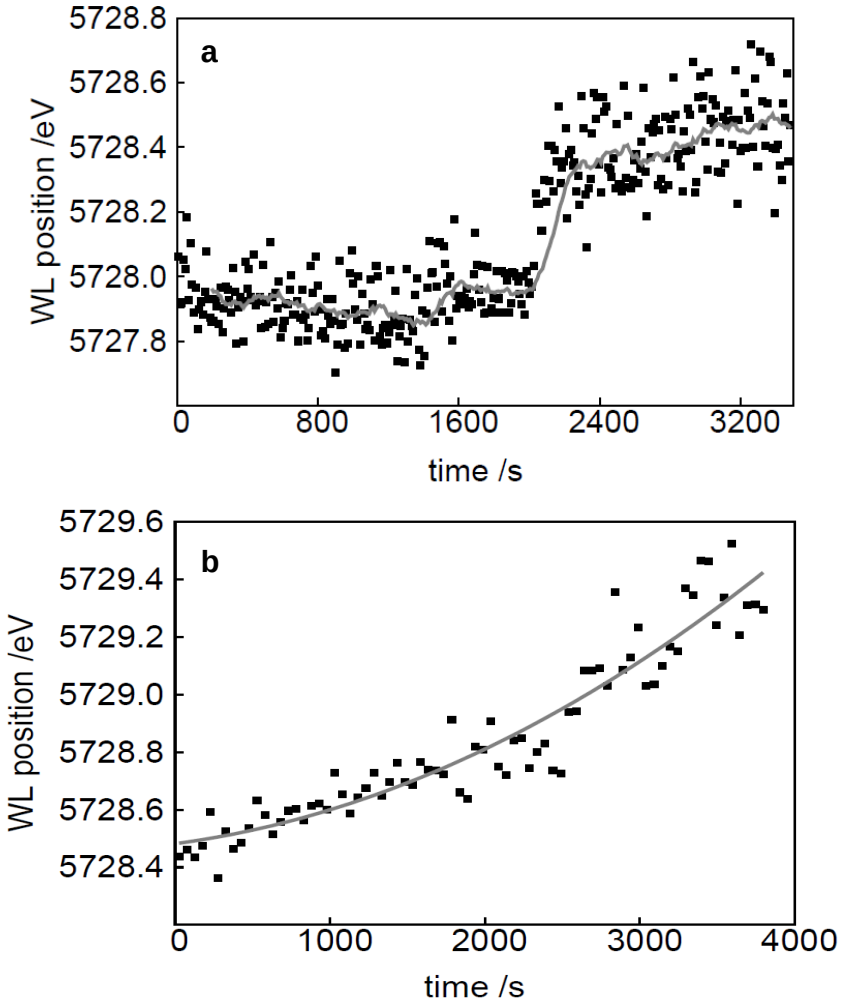

Figure 4.9 White line energy position of the Ce L_{III} edge vs. time during reoxidation of CuO-CeO_2/Al_2O_3 at 950K with (a) CO_2; (b) water vapor.

In order to verify if Ce^{4+} and Cu^{2+} in the solid solution also interact upon oxidation, a reoxidation experiment was set up using CO_2 and H_2O, as these are toluene total oxidation reaction products. While O_2 is known to induce very fast reoxidation for both elements [58], CO_2 and H_2O induce a slower reoxidation. The Ce L_{III} XANES spectra for water reoxidation are displayed in A.2, Fig. A.3, Appendix A. Isothermal reoxidation of the CuO-CeO_2/Al_2O_3 catalyst with either CO_2 or water vapor shows a clear but partial effect at the Ce L_{III} edge, see Fig. 4.9a and b, while the Cu K edge is not notably affected (not shown). This indicates that both oxidants can replenish part of the oxygen vacancies of ceria, but not of Cu, which allows to separate the role of CeO_2 in

reoxidation. However, if CeO_2 passes O to nearby dissolved Cu^{2+}, this would hardly show up in the Cu XANES, since the large CuO monocrystals will remain in reduced state dominating the overall XANES pattern.

4.3.3 Catalytic performance

Results obtained from Tol/Ar pulse experiments over single and binary metal oxide catalysts are summarized in Fig. 4.10a, where the CO_2 yield obtained from the first pulses over $CuO\text{-}CeO_2/Al_2O_3$, CuO/Al_2O_3 and CeO_2/Al_2O_3 is plotted as a function of reaction temperature. The reaction proceeds according to a redox Mars-van Krevelen mechanism [20, 61]. Lattice oxygen atoms from the surface of the catalyst are consumed by the Tol/Ar pulse and oxygen vacancies are created. These vacancies are filled by oxygen atoms that diffuse from the bulk of the catalyst to the surface. As observed in Fig. 4.10a the binary metal oxide catalyst $CuO\text{-}CeO_2/Al_2O_3$ shows higher activity compared to the single metal oxides. Furthermore, the CO_2 yield obtained from $CuO\text{-}CeO_2/Al_2O_3$ is higher than the sum of the individual yields obtained from CuO/Al_2O_3 and CeO_2/Al_2O_3. This is represented as $\boldsymbol{\chi_{Ce}}$. The value of $\boldsymbol{\chi_{Ce}}$ decreases from 3 to 1 with an increase in temperature from 773 K to 873 K corresponding to a more pronounced promoting effect of the $Ce_{1-x}Cu_xO_{2-x}$ solid solution at lower temperature.

As expected, an increase in the CO_2 yield was observed when toluene pulse experiments were performed in the presence of dioxygen. The results are summarized in Fig. 4.10b. The promoting effect of ceria was not as high as that observed in the experiments with Tol/Ar alone. The value of $\boldsymbol{\chi_{Ce}}$ varies from 1.5 to 1. The presence of dioxygen in the gas phase now keeps the catalysts in a oxidized state by reoxidizing the surface and the role of oxygen mobility from the bulk of the metal oxides is less pronounced [20].

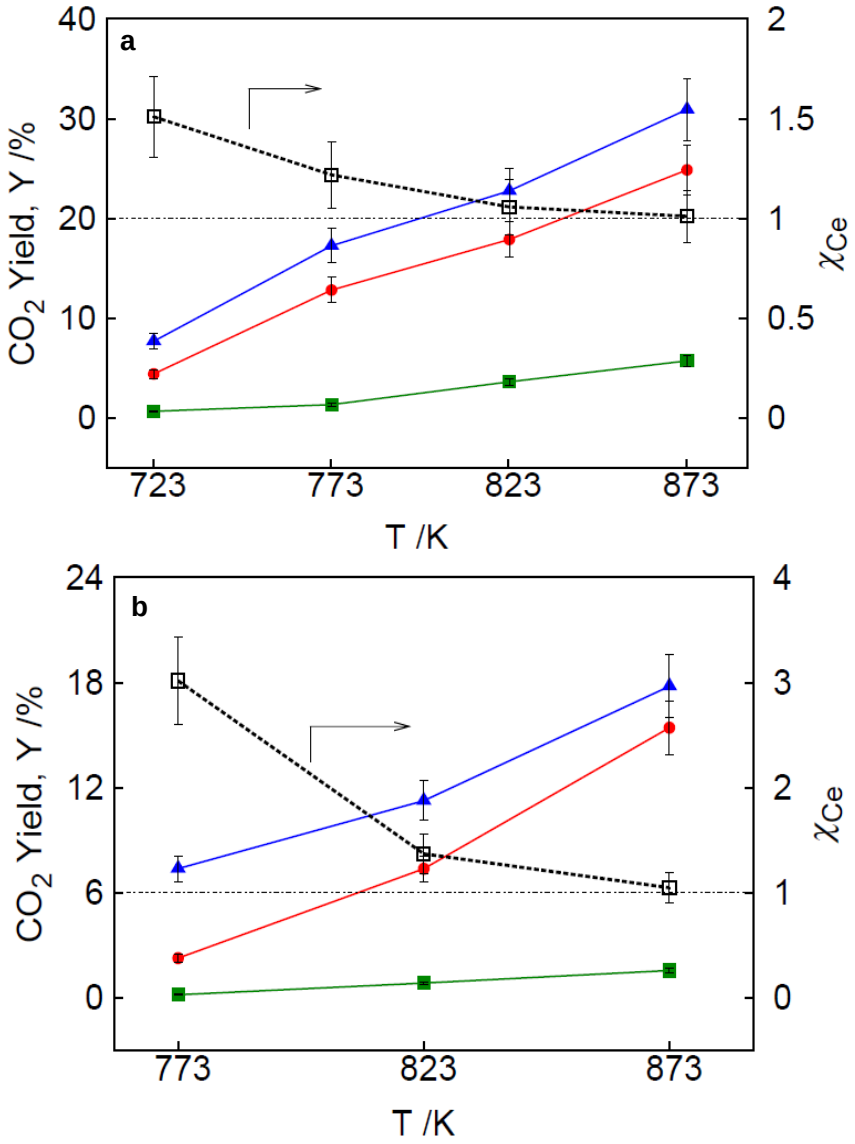

Figure 4.10 CO_2 yield (left y-axis) and χ_{Ce} (Eq. 4.1) (□) vs temperature for pulse experiments with (a) Tol/Ar and (b) Tol/O_2/Ar over CuO-CeO_2/Al_2O_3 (▲), CuO/Al_2O_3 (●), CeO_2 /Al_2O_3 (■)

4.3.4 Effect of H_2O or CO_2 on toluene total oxidation

The oxidation of VOCs is reported to be inhibited by the presence of H_2O and CO_2 [17, 21, 23, 62-64]. The effect of H_2O for toluene total oxidation over CuO-CeO_2/Al_2O_3, CuO/Al_2O_3 and CeO_2/Al_2O_3 is shown in Fig. 4.11. The presence of H_2O in the feed has no effect at lowest or higher temperature but increases the CO_2 yield over CuO-CeO_2/Al_2O_3 at 723 and 773 K. In contrast, there is an inhibition of CuO/Al_2O_3 activity in the presence of water, at the same

medium range temperatures. In the case of CeO_2/Al_2O_3, the presence of H_2O in the feed has no effect on the CO_2 yield at any temperature.

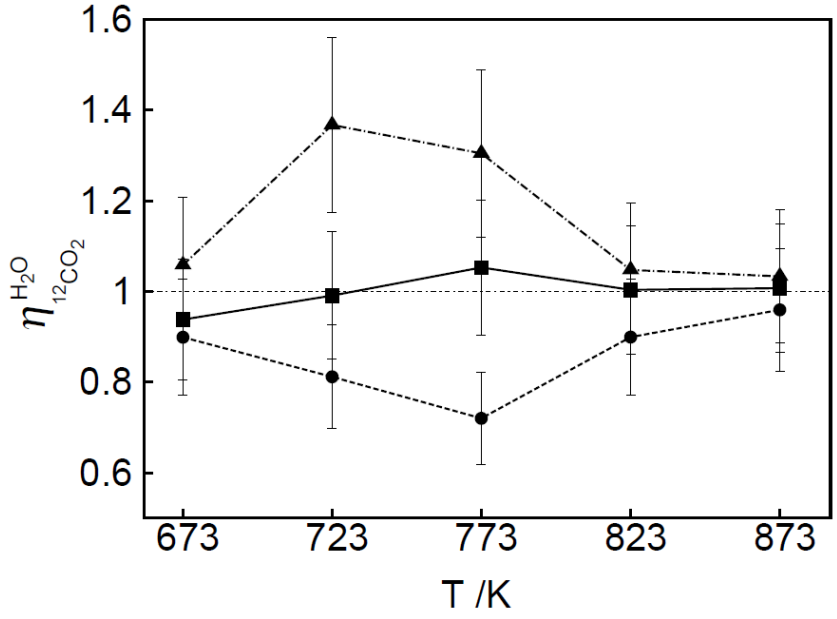

Figure 4.11 $\boldsymbol{\eta^{H_2O}_{CO_2}}$ (Eq. 4.2) as a function of temperature for pulse experiments with Tol/O_2/Ar and Tol/O_2/H_2O/Ar over CuO-CeO_2/Al_2O_3 (▲), CuO/Al_2O_3 (●),CeO_2 /Al_2O_3 (■)

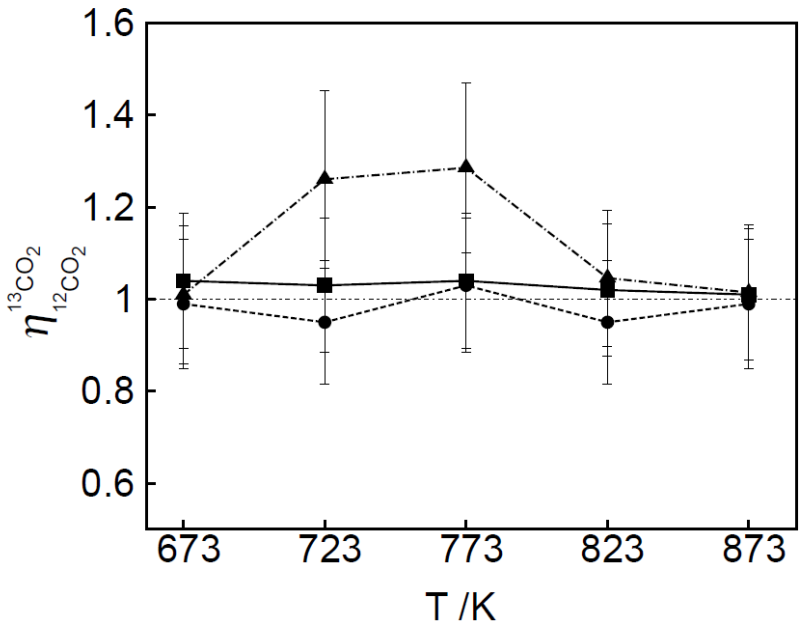

Figure 4.12 $\eta^{13CO_2}_{12CO_2}$ (Eq. 4.3) as a function of temperature for pulse experiments with C_7H_8/O_2/Ar and C_7H_8/O_2/CO_2/Ar over CuO-CeO_2/Al_2O_3 (▲),CuO/Al_2O_3 (●),CeO_2 /Al_2O_3 (■)

The effect of carbon dioxide on the toluene total oxidation over CuO-CeO_2/Al_2O_3, CuO/Al_2O_3 and CeO_2/Al_2O_3 is shown in Fig. 4.12.

The $^{13}CO_2$ co-feed has a less pronounced effect upon toluene total oxidation over $CuO\text{-}CeO_2/Al_2O_3$ than water, although the $^{12}CO_2$ yield appears increased for the medium range temperatures 723 and 773 K. For CuO/Al_2O_3 and CeO_2/Al_2O_3 the presence of $^{13}CO_2$ does not have any effect on catalytic activity.

Catalyst	C_7H_8/O_2 (kJ mol^{-1})	$C_7H_8/O_2/H_2O$ (kJ mol^{-1})	$C_7H_8/O_2/CO_2$ (kJ mol^{-1})
$CuO\text{-}CeO_2/Al_2O_3$	59 ±12	53 ± 15	54 ±18
CuO/Al_2O_3	60 ±14	62 ±11	58 ± 17
CeO_2/Al_2O_3	75 ±8	85 ±16	73 ±9

Table 4.2. The apparent activation energies with 95% confidence intervals for toluene total oxidation in the presence and absence of H_2O and CO_2 over $CuO\text{-}CeO_2/Al_2O_3$, CuO/Al_2O_3 and CeO_2/Al_2O_3.

The apparent activation energies for toluene total oxidation in the presence and absence of H_2O and CO_2 were calculated over all three catalysts based on the Arrhenius relation and are given in Table 4.2. The apparent activation energy slightly decreases for $CuO\text{-}CeO_2/Al_2O_3$ with both co-feeds, while it increases for CuO/Al_2O_3 and CeO_2/Al_2O_3 in the presence of H_2O. The estimated values are in line with the value 50±5 kJ mol^{-1}, obtained in our earlier work [20].

The results of catalytic activity tests show that the $Ce_{1-x}Cu_xO_{2-x}$ solid solution has a beneficial effect on the catalytic performance of $CuO\text{-}CeO_2/Al_2O_3$ for toluene total oxidation, which is even more pronounced in the presence of H_2O and CO_2.

4.4 Discussion

The activity of $CuO\text{-}CeO_2/Al_2O_3$ is determined by the interplay of three distinct features:

- reduction of Cu^{2+}
- oxygen mobility
- oxidation of Ce^{3+}

The Mars-van Krevelen mechanism was shown to allow to describe both the total oxidation of propane [65] and toluene [20] on this catalyst. The most critical properties were found to be the reducibility of the active phase and the mobility of the lattice oxygen atoms, rather than the reoxidation of the active phase [20, 58]. The present experimental work allows to elucidate further on each of these features. XANES during H_2-TPR was applied to yield element-specific reduction characteristics. For the reoxidation, CO_2 and water were chosen as they only oxidize Ce^{3+} and proceed slower than O_2.

4.4.1 Reduction of Cu^{2+}

Based on the catalyst characterization by XRD, XPS, TEM, EELS and EDX (Figs. 4.1-4.5), a picture of $CuO\text{-}CeO_2/Al_2O_3$ can be drawn (Fig. 4.6). The $\gamma\text{-}Al_2O_3$ support presents a matrix of nano-sized crystalline particles (~4 nm). TEM results (Fig. 4.4) show that CuO is present in two phases: CuO as a monocrystal of about 100 nm and dissolved Cu^{2+} within the CeO_2 nano-crystallites (6 nm). The latter is proposed to be incorporated substitutionally into the CeO_2 lattice, giving rise to a $Ce_{1-x}Cu_xO_{2-x}$ solid solution [57, 66].

In H_2-TPR of $CuO\text{-}CeO_2/Al_2O_3$ followed by *in situ* XANES (Fig. 4.7), both Cu^{2+} and Ce^{4+} are reduced by hydrogen, showing that both elements are reducible. . A similar result was found for CO/O_2 redox processes over $CuO\text{-}CeO_2$ [67], where both the CuO particles and the support were found to reduce simultaneously. The conclusions reached from the H_2-TPR XANES experiments, were confirmed previously in propane reduction and TPR experiments on the same $CuO\text{-}CeO_2/Al_2O_3$ catalyst [48, 62]. The similarity of results from propane and hydrogen reduction experiments leads to conclude that this reduction mechanism is characteristic for this catalyst, and in particular for the solid solution phase $Ce_{1-x}Cu_xO_{2-x}$, and holds also for toluene oxidation. It has been shown in literature that Cu from $Ce_{1-x}Cu_xO_{2-x}$ can segregate from the solution upon reduction to Cu^0 with hydrogen [66]. With the present catalyst, no evidence for this kind of behavior was found, indicating that

the reduced oxidation state of Cu is 1+. After reoxidation, the same XANES spectrum was retrieved as before.

XANES during H_2-TPR shows that CuO-CeO_2/Al_2O_3 is reduced at lower temperature than CuO/Al_2O_3 and CeO_2/Al_2O_3 (Figs. 4.7, 4.8). Since the presence of the $Ce_{1-x}Cu_xO_{2-x}$ solid solution is the main difference between CuO-CeO_2/Al_2O_3 and the latter, this phase accounts for the improved reducibility of the binary metal oxide catalyst. This is in agreement with reported reduction of Cu^{2+} ions incorporated into the CeO_2 lattice occurring at lower temperature than for CuO [30, 68]. Likewise, reduction of CeO_2 was seen to proceed at lower temperature when substituted with Cu^{2+} ions [14, 30, 35, 68]. A similar low temperature reduction was observed in solid solution $Ce_{0.8}Cu_{0.2}O_{2-x}$ as well as for mixed oxides CuO/CeO_2 [66].

The above leads to the conclusion that there are two different types of active species on CuO-CeO_2/Al_2O_3: monocrystal CuO and the solid solution $Ce_{1-x}Cu_xO_{2-x}$, that is, CeO_2 with incorporated Cu^{2+} accompanied by oxygen vacancies, where reducibility can be assured by both Cu and Ce at typical total oxidation temperatures. It is this solid solution which explains that "The addition of ceria to the copper oxide catalyst results in a close interaction between these two oxide phases, leading to an increased catalytic activity", as concluded by Balcaen et al. [69], based on kinetic modeling of the total oxidation of propane.

The bulk CuO phase in CuO-CeO_2/Al_2O_3 has the same structure as CuO/Al_2O_3, that is, large bulk CuO particles on the alumina support and no CeO_2 nearby, so that the bulk CuO behavior in CuO-CeO_2/Al_2O_3 can be judged from CuO/Al_2O_3 without CeO_2 promoter. H_2 reduction of the single oxide CuO/Al_2O_3 (Fig. 4.8b) shows that bulk CuO is reduced at a higher temperature than in CuO-CeO_2/Al_2O_3, indicating that the CuO phase will only be active at higher reaction temperature. The latter picture combined with the XANES white line analysis as function of temperature allows to rigorously reinterpret the TPR pattern for this CuO-CeO_2/Al_2O_3 catalyst, consisting of two distinct H_2 consumption peaks [14]: the first peak represents reduction

of the $Ce_{1-x}Cu_xO_{2-x}$ solid solution, while the second peak corresponds to the reduction of the CuO monocrystals.

During catalysis, two redox couples, Ce^{4+}/Ce^{3+} and Cu^{2+}/Cu^{0+}, co-exist within the $Ce_{1-x}Cu_xO_{2-x}$ solid solution. The partial reduction of Ce^{4+} to Ce^{3+} occurs before the Cu reduction is apparent in XANES and is either due to direct interaction with the reducing gas, or to Ce^{4+} passing O to incorporated Cu^{+} or Cu^{0} ions. The latter seems more likely as first reduction of Cu^{2+} in XANES appears around 500 K, that is, when most of the readily available O from Ce^{4+} is already consumed (see Fig. 4.7a and b). The higher activity of CuO-CeO_2/Al_2O_3 (Fig. 4.10) can then be rationalized by the presence of the solid solution $Ce_{1-x}Cu_xO_{2-x}$, in particular at lower reaction temperature.

Ideally, the catalyst should consist of nothing but solid solution $Ce_{1-x}Cu_xO_{2-x}$, which is active at low temperature. The bulk CuO phase on the other hand will only participate in the reaction at higher temperature, based on the activity and reducibility of CuO/Al_2O_3. The reason for the existence of these monocrystals is most likely a CuO overloading of the catalyst during synthesis. Indeed, CeO_2 can incorporate only a limited amount of Cu^{2+} into its lattice and any excess loading will segregate during preparation into a separate bulk CuO phase with growing size as the loading increases [55, 70]. If such bulk CuO particles are present, they can be removed from the sample after synthesis by a catalyst treatment with nitric acid [45].

4.4.2 Oxygen mobility

Next to reducibility the mobility of lattice O atoms can be a rate-determining factor, certainly for the case of toluene oxidation [20, 24, 71]. Four oxygen atoms are required to form water and fourteen to form CO_2 for each toluene molecule. Toluene adsorbed on Cu^{2+} is surrounded by six adjacent oxygen atoms which is sufficient for water formation. The remainder of the required oxygen atoms is obtained by diffusion from the bulk as described by the Mars-van Krevelen mechanism.

Additional elements incorporated in a metal oxide weaken the bond between the metal and the oxygen atoms, making the latter more reactive and mobile [27]. This effect will even be stronger if the added element has a lower valence than the cation it replaces, because it creates an electron deficit in its neighborhood. For some elements, the incorporation is then accompanied by the creation of a nearby vacancy. Bera et al. [72] showed that in Cu/CeO_2 catalysts, Cu^{2+} can be incorporated into the support with creation of a nearby O vacancy. The resulting $Ce_{1-x}Cu_xO_{2-x}$ solid solution presents a lowered Cu redox potential, hence enhanced reducibility, due to the $Cu^{2+} – O^{2-} – Ce^{4+}$ connection. The vacancy is then considered as a bridge for the transfer of O from Ce to Cu [73]. On the other hand, Dow et al. [74] showed that well-dispersed Cu can connect to CeO_2 through a so-called nested oxygen ion (NOI), presenting a weakened Cu=O bond, that allows easy reduction. Wang et al. [75, 76] called the O connecting Cu and Ce an interfacial active center (IAC), presenting a higher activity for CO oxidation. EXAFS on $Ce_{1-x}Cu_xO_2$ with x = 5, 10 and 20% and DFT results for a $Ce_{0.75}Cu_{0.25}O_2$ catalyst of Wang et al. [35] show the structure and chemical environment of Cu dissolved in CeO_2: there are six oxygen atoms around the incorporated Cu^{2+}, the nearest in the first shell at a distance of 1.92-1.95 Å. The rearrangement of the CeO_2 lattice around Cu^{2+} induces vacancies and distortion, which lead to weak Fourier transformed signal from the medium range shells [35]. In a similar manner, the Cu^{2+} of $Ce_{1-x}Cu_xO_{2-x}$ in the present catalyst will weaken the surface oxygen bonds of the solid solution, making them more reactive and thereby easier to remove [27]. Previous EXAFS analysis of the Cu K edge signal of the present $CuO\text{-}CeO_2/Al_2O_3$ catalyst resulted in a first shell Cu-O with 2 + 2 O at an average distance of 1.938 Å, and 2 more oxygen atoms in a second shell at 2.822 Å [35]. These values lie close to those for bulk CuO, 1.955 Å and 2.874 Å respectively [35]. However, since the obtained distances are average values for the two Cu phases present in the catalyst, they do not allow for a conclusion on the surrounding shells of Cu^{2+} in the $Ce_{1-x}Cu_xO_{2-x}$ solid solution.

4.4.3 Oxidation of Ce^{3+}

Of course the reoxidation of the active phase, even if not critical at typical total oxidation conditions, should also be provided by an optimal catalyst. For propane oxidation it was shown that as much as 50% of the active sites were reduced at steady state [14]. O_2 is the major reactant for this step but in the presence of H_2O or CO_2 the reoxidation of CuO-CeO_2/Al_2O_3 is enhanced because of the contribution of these components to the reoxidation of Ce^{3+} (Fig. 4.9).

The above discussion can be summarized schematically represented by Fig. 4.13. The role of Ce^{4+} in the reaction mechanism is similar to that of Cu^{2+} in the well-known Wacker process for the oxidation of ethene to acetaldehyde catalyzed by $PdCl_2$–$CuCl_2$ [77, 78]. $PdCl_2$ and $CuCl_2$ are both required because Pd^0 reduced by ethene is reoxidized by Cu^{2+} in order to regenerate Pd^{2+}, that is, contact between the Pd^0 and Cu^{2+} is essential to close the catalytic cycle. The constituent formal reactions of the complete toluene oxidation cycle on Cu and Ce active sites in the solid solution are described by the following equations:

$$Tol + Cu^{2+} \rightarrow Cu^{1+} + CO_2 + H_2O \qquad \text{Eq. (4.5)}$$

$$Ce^{4+} + Cu^{1+} \rightarrow Ce^{3+} + Cu^{2+} \qquad \text{Eq. (4.6)}$$

$$Ce^{3+} + \tfrac{1}{2}O_2 \rightarrow Ce^{4+} \qquad \text{Eq. (4.7)}$$

and/or

$$Ce^{3+} + H_2O/CO_2 \rightarrow Ce^{4+} + H_2/CO \qquad \text{Eq. (4.8)}$$

The equations indicate Cu^{1+} as most probable lowest valence. This is in line with the observations in XANES and Williamson-Hall plot from XRD, where the overall valence state of the H_2 reduced CuO-CeO_2/Al_2O_3 catalyst was found to lie in between 1+ and 0, with the Cu K XANES spectra in A.2, Fig. A.2, Appendix A. The actual valence state of Cu in the solid solution will depend on the rate of reduction of CuO and Cu_2O, as well as on the rate of reoxidation of reduced Cu by CeO_2. A previous publication reported that propane oxidation proceeds more easily over CuO than for Cu_2O, giving rise to accumulation of Cu^{1+} at intermediate temperatures [58].

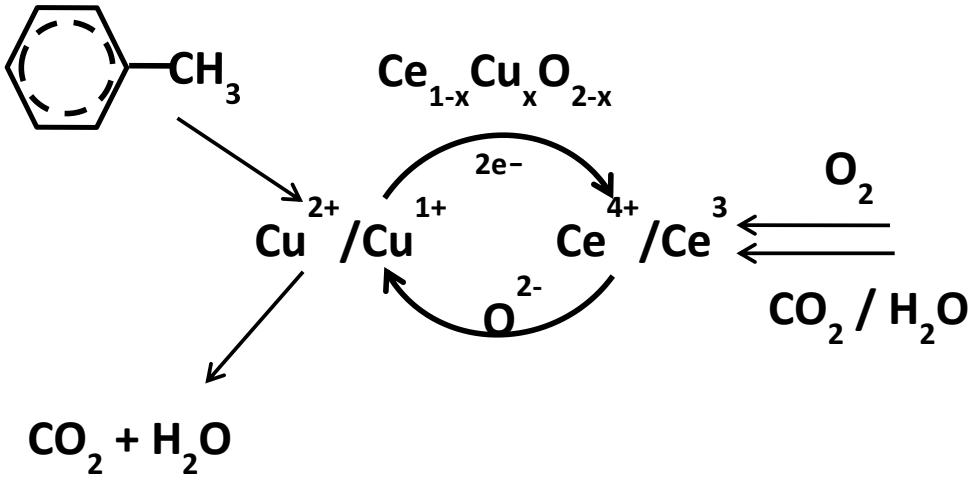

Figure 4.13 The general redox scheme describing heterogeneous oxidation reactions in CuO-CeO_2/Al_2O_3. The reoxidation of the copper can proceed by two parallel paths: directly from the gaseous phase or by diffusion of oxygen in the $Ce_{1-x}Cu_xO_{2-x}$ solid solution.

Oxidation of the toluene and reduction of oxygen occur at different sites of the solid solution $Ce_{1-x}Cu_xO_{2-x}$ between which electrons and oxide ions are transferred. Oxidation of toluene occurs on Cu sites (Eq. 4.5), not on Ce as CeO_2/Al_2O_3 shows no activity for reduction of toluene (Fig. 4.10a). Reduction of oxygen on the other hand proceeds on Ce sites (Eq. 4.7).

Reduced Ce^{3+} can be reoxidized by H_2O or CO_2 (Eq. 4.8), see Fig. 4.9a and b, and Fig. A.3, Appendix A, as well as [67, 79-81]. The addition of H_2O or CO_2 to the feed thus opens a new route for Ce reoxidation, (Eq. 4.8). These reoxidized sites can then act as oxygen supplier at the toluene oxidation site, that is, for reoxidation of nearby reduced Cu^0 (Eq. 4.6). Indeed, the addition of CeO_2 leads to a redox couple (Eq. 4.6), where Ce^{4+} can reoxidize reduced Cu [82].

The toluene oxidation cycle over CuO/Al_2O_3, that is, without promoter, can be represented by the following formal equations:

$$Tol + Cu^{2+} \rightarrow Cu^{1+} + CO_2 + H_2O \qquad \text{Eq. (4.9)}$$

$$Cu^{1+} + ½O_2 \rightarrow Cu^{2+} \qquad \text{Eq.(4.10)}$$

In contrast to CeO_2, reduced Cu/Al_2O_3 cannot be reoxidized by H_2O or CO_2 [65, 83, 84]. The observed activity decrease in the presence

of water, see Fig. 4.11, can be attributed to a competition between H_2O/CO_2 and dioxygen for the same active sites.

4.5 Conclusions

The catalytic activity for toluene total oxidation over a binary mixture of copper and cerium oxide supported on Al_2O_3 has been investigated in comparison to that of single metal oxide materials CuO/Al_2O_3 and CeO_2/Al_2O_3. Based upon structural characterization, the improved performance of the mixed oxide catalyst can be attributed to the formation of a solid solution $Ce_{1-x}Cu_xO_{2-x}$, that is, with Cu^{2+} substitutionally incorporated into CeO_2, existing next to a bulk CuO phase. The average atomic ratio of Ce to Cu in this solid solution is 2:1, yielding an x-value of ~0.33. Temperature programmed reduction of the $CuO\text{-}CeO_2/Al_2O_3$ catalyst during *in situ* XANES experiments indicates enhanced reduction of both Ce and Cu inside the solid solution. At the lowest reduction temperatures, Ce^{4+} reduces first, passing O to nearby Cu, thus keeping it oxidized. When the readily available O^{2-} from Ce^{4+} are consumed, the dissolved Cu^{2+} is reduced. At higher temperatures, the bulk CuO phase is equally reduced.

Enhanced activity in toluene total oxidation is due to the Cu^{2+} incorporation in the solid solution, which weakens the adjacent O bonds and is accompanied by O vacancies. Toluene is oxidized on the dissolved Cu^{2+} sites in the solid solution, while dioxygen is reduced at the Ce sites. The transfer of electrons and oxygen ions between Ce and Cu ensures the fast regeneration of available sites.

In the mixed oxide catalyst, Ce^{3+} is able to be reoxidized by H_2O and/or CO_2. As a result, an enhancement of catalytic activity with H_2O or CO_2 in the feed is observed over the $CuO\text{-}CeO_2/Al_2O_3$ catalyst, because the oxygen in the solid solution is replenished and simultaneously the surface is freed from adsorbed products occupying sites. Compared with this binary oxide catalyst, the activity of a single copper oxide catalyst is inhibited in the presence of water in the feed, due to competition for active sites.

References

1. J.J. Spivey, Industrial & Engineering Chemistry Research 26 (1987) 2165-2180.
2. L.F. Liotta, Applied Catalysis B: Environmental 100 (2010) 403-412.
3. K. Everaert, and J. Baeyens, Journal of Hazardous Materials 109 (2004) 113-139.
4. J.N. Armor, Applied Catalysis B: Environmental 1 (1992) 221-256.
5. J. Carpentier, J.F. Lamonier, S. Siffert, E.A. Zhilinskaya, and A. Aboukaïs, Applied Catalysis A: General 234 (2002) 91-101.
6. M. Paulis, H. Peyrard, and M. Montes, Journal of Catalysis 199 (2001) 30-40.
7. S. Fujita, K. Suzuki, M. Ohkawa, T. Mori, Y. Iida, Y. Miwa, H. Masuda, and S. Shimada, Chemistry of Materials 15 (2002) 255-263.
8. E. N. Ntainjua, and S. Taylor, Topics in Catalysis 52 (2009) 528-541.
9. T. Takeguchi, S. Aoyama, J. Ueda, R. Kikuchi, and K. Eguchi, Topics in Catalysis 23 (2003) 159-162.
10. H. Einaga, S. Hyodo, and Y. Teraoka, Topics in Catalysis 53 (2010) 629-634.
11. P.-O. Larsson, and A. Andersson, Applied Catalysis B: Environmental 24 (2000) 175-192.
12. C. Hettige, K.R.R. Mahanama, and D.P. Dissanayake, Chemosphere 43 (2001) 1079-1083.
13. D. Delimaris, and T. Ioannides, Applied Catalysis B: Environmental 89 (2009) 295-302.
14. P.M. Heynderickx, J.W. Thybaut, H. Poelman, D. Poelman, and G.B. Marin, Journal of Catalysis 272 (2010) 109-120.
15. S. Saqer, D. Kondarides, and X. Verykios, Topics in Catalysis 52 (2009) 517-527.

16. P.-O. Larsson, and A. Andersson, Journal of Catalysis 179 (1998) 72-89.

17. S.M. Saqer, D.I. Kondarides, and X.E. Verykios, Applied Catalysis B: Environmental 103 (2011) 275-286.

18. J.G.I. Christopher, J. Heyes, H.A. Johnson, and R.L. Moss, Journal of Chemical Technology and Biotechnology 32 (1982) 1025-1033.

19. H. Rajesh, and U.S. Ozkan, Industrial & Engineering Chemistry Research 32 (1993) 1622-1630.

20. U. Menon, V.V. Galvita, and G.B. Marin, Journal of Catalysis 283 (2011) 1-9.

21. M.P. Heyndericx, J.W. Thybaut, H. Poelman, D. Poelman, and G.B. Marin, Applied Catalysis B: Environmental 95 (2010) 26-38.

22. C.-H. Wang, Chemosphere 55 (2004) 11-17.

23. C.-H. Wang, S.-S. Lin, C.-L. Chen, and H.-S. Weng, Chemosphere 64 (2006) 503-509.

24. X. Tang, Y. Xu, and W. Shen, Chemical Engineering Journal 144 (2008) 175-180.

25. L. Dong, Y. Hu, M. Shen, T. Jin, J. Wang, W. Ding, and Y. Chen, Chemistry of Materials 13 (2001) 4227-4232.

26. B. Skarman, T. Nakayama, D. Grandjean, R.E. Benfield, E. Olsson, K. Niihara, and L.R. Wallenberg, Chemistry of Materials 14 (2002) 3686-3699.

27. V. Shapovalov, and H. Metiu, Journal of Catalysis 245 (2007) 205-214.

28. A. Tschope, J. Markmann, P. Zimmer, R. Birringer, and Chadwick, Chemistry of Materials 17 (2005) 3935-3943.

29. J. Chen, Y. Zhan, J. Zhu, C. Chen, X. Lin, and Q. Zheng, Applied Catalysis A: General 377 (2010) 121-127.

30. W. Shan, W. Shen, and C. Li, Chemistry of Materials 15 (2003) 4761-4767.

31. X. Wang, J.A. Rodriguez, J.C. Hanson, D. Gamarra, A. Martínez-Arias, and M. Fernández-Garcia, The Journal of Physical Chemistry B 109 (2005) 19595-19603.

32. P.G. Harrison, I.K. Ball, W. Azelee, W. Daniell, and D. Goldfarb, Chemistry of Materials 12 (2000) 3715-3725.

33. Z. Wu, M. Li, J. Howe, H.M. Meyer, and S.H. Overbury, Langmuir 26 (2010) 16595-16606.

34. G. Sedmak, S. Hocevar, and J. Levec, Journal of Catalysis 213 (2003) 135-150.

35. P. Bera, K.R. Priolkar, P.R. Sarode, M.S. Hegde, S. Emura, R. Kumashiro, and N.P. Lalla, Chemistry of Materials 14 (2002) 3591-3601.

36. J.T. Gleaves, G. Yablonsky, X. Zheng, R. Fushimi, and P.L. Mills, Journal of Molecular Catalysis A: Chemical 315 (2010) 108-134.

37. G.S. Yablonsky, M. Olea, and G.B. Marin, Journal of Catalysis 216 (2003) 120-134.

38. V. Briois, E. Fonda, S. Belin, L. Barthe, C.L. Fontaine, F. Langlois, M. Ribbens, and F. Villain, UVX 2010 (2011) 41 - 47.

39. R. Frahm, Review of Scientific Instruments 60 (1989).

40. B. Ravel, and M. Newville, Journal of Synchrotron Radiation 12 (2005) 537-541.

41. G. Silversmit, H. Poelman, I. Sack, G. Buyle, G. Marin, and R. De Gryse, Catalysis Letters 107 (2006) 61-71.

41. T. Ressler, J. Wienold, R.E. Jentoft, and T. Neisius, Journal of Catalysis 210 (2002) 67-83.

42. J. Wong, F.W. Lytle, R.P. Messmer, and D.H. Maylotte, Physical Review B 30 (1984) 5596-5610.

44. M. Olea, H. Poelman, M. Capron, and S. Cristol. 2007. Combining XAS with on-line GC catalytic studies for in situ characterization of Volatile Organic Compounds (VOCs) elimination over a CuO-CeO_2/Al_2O_3 catalyst.

43. P. Scherrer, Nachr Ges Wiss Göttingen 26 (1918) 98-100.

44. V.P. Pakharukova, E.M. Moroz, V.V. Kriventsov, D.A. Zyuzin, G.R. Kosmambetova, and P.E. Strizhak, Applied Catalysis A: General 365 (2009) 159-164.

45. M.-F. Luo, Y.-P. Song, J.-Q. Lu, X.-Y. Wang, and Z.-Y. Pu, The Journal of Physical Chemistry C 111 (2007) 12686-12692.

46. G. Silversmit, H. Poelman, V. Balcaen, P.M. Heynderickx, M. Olea, S. Nikitenko, W. Bras, P.F. Smet, D. Poelman, R. De Gryse, M.-F. Reniers, and G.B. Marin, Journal of Physics and Chemistry of Solids 70 (2009) 1274-1284.

47. A. Martínez-Arias, A.B. Hungria, M. Fernández-Garcia, J.C. Conesa, and G. Munuera, The Journal of Physical Chemistry B 108 (2004) 17983-17991.

48. A. Martínez-Arias, D. Gamarra, M. Fernández-Garcia, X.Q. Wang, J.C. Hanson, and J.A. Rodriguez, Journal of Catalysis 240 (2006) 1-7.

49. B.R. Strohmeier, D.E. Levden, R.S. Field, and D.M. Hercules, Journal of Catalysis 94 (1985) 514-530.

50. C.D. Wagner, Analytical Chemistry 47 (1975) 1201-1203.

51. M. Giuliano, Journal of Electron Spectroscopy and Related Phenomena 95 (1998) 95-144.

52. W. Gruenert, N.W. Hayes, R.W. Joyner, E.S. Shpiro, M.R.H. Siddiqui, and G.N. Baeva, The Journal of Physical Chemistry 98 (1994) 10832-10846.

53. J.P. Espinós, J. Morales, A. Barranco, A. Caballero, J.P. Holgado, and A.R. González-Elipe, The Journal of Physical Chemistry B 106 (2002) 6921-6929.

54. R.D. Leapman, L.A. Grunes, and P.L. Fejes, Physical Review B 26 (1982) 614.

55. B. Skarman, D. Grandjean, R.E. Benfield, A. Hinz, A. Andersson, and L.R. Wallenberg, Journal of Catalysis 211 (2002) 119-133.

56. D. Gamarra, G. Munuera, A.B. Hungría, M. Fernández-García, J.C. Conesa, P.A. Midgley, X.Q. Wang, J.C. Hanson, J.A. Rodríguez, and A. Martínez-Arias, The Journal of Physical Chemistry C 111 (2007) 11026-11038.

57. A. Trovarelli, Catalysis by Ceria and Related Materials. Imperial college press, 2002.

58. K. Alexopoulos, M. Anilkumar, M.-F. Reyniers, H. Poelman, S. Cristol, V. Balcaen, P.M. Heynderickx, D. Poelman, and G.B. Marin, Applied Catalysis B: Environmental 97 (2010) 381-388.

59. J.Z. Shyu, W.H. Weber, and H.S. Gandhi, The Journal of Physical Chemistry 92 (1988) 4964-4970.

60. M. Ferrandon, B. Ferrand, E. Björnbom, F. Klingstedt, A.K. Neyestanaki, H. Karhu, and I.J. Väyrynen, Journal of Catalysis 202 (2001) 354-366.

61. P. Mars, and D.W. van Krevelen, Chemical Engineering Science 3 (1954) 41-59.

62. P. Gélin, and M. Primet, Applied Catalysis B: Environmental 39 (2002) 1-37.

63. D. Delimaris, and T. Ioannides, Applied Catalysis B: Environmental 84 (2008) 303-312.

64. J.C. van Giezen, F.R. van den Berg, J.L. Kleinen, A.J. van Dillen, and J.W. Geus, Catalysis Today 47 (1999) 287-293.

65. V. Balcaen, R. Roelant, H. Poelman, D. Poelman, and G.B. Marin, Catalysis Today 157 (2010) 49-54.

66. J. Ciston, R. Si, J. A. Rodriguez, J. C. Harison, A. Martinez- Aroas, M. Fernandez – Garcia, Y. Zhu, J. Phys. Chem. C 115 (2011) 13851-13859.

67. A. Martinez-Arias, M. Fernandez-Garcia, O. Galvez, J.M. Coronado, J.A. Anderson, J.C. Conesa, J. Soria, G. Munuera, J. Catal. 195 (2000) 207–216.

68. A. Gupta, U.V. Waghmare, and M.S. Hegde, Chemistry of Materials 22 (2010) 5184-5198.

69. V. Balcaen, H. Poelman, D. Poelman, and G.B. Marin, Journal of Catalysis 283 (2011) 75-88.

70. W. Liu, and M. Flytzanistephanopoulos, Journal of Catalysis 153 (1995) 317-332.

71. B. Irigoyen, A. Juan, S. Larrondo, and N. Amadeo, Surface Science 523 (2003) 252-266.

72. P. Bera, S. Mitra, S. Sampath, and M.S. Hegde, Chemical Communications (2001) 927-928.

73. J. Chen, J. Zhu, Y. Zhan, X. Lin, G. Cai, K. Wei, and Q. Zheng, Applied Catalysis A: General 363 (2009) 208-215.

74. W.-P. Dow, Y.-P. Wang, and T.-J. Huang, Applied Catalysis A: General 190 (2000) 25-34.

75. J.B. Wang, W.-H. Shih, and T.-J. Huang, Applied Catalysis A: General 203 (2000) 191-199.

76. J.B. Wang, S.-C. Lin, and T.-J. Huang, Applied Catalysis A: General 232 (2002) 107-120.

77. Jacobs P.A., Ertl G. , Knözinger H. , Schüth F. , and W. J., Handbook of Heterogeneous Catalysis. Wiley–VCH, Weinheim, 2008.

78. M. Okamoto, and Y. Taniguchi, Journal of Catalysis 261 (2009) 195-200.

79. M. Turco, G. Bagnasco, C. Cammarano, L. Micoli, M. Lenarda, E. Moretti, L. Storaro, and A. Talon, Applied Catalysis B: Environmental 102 (2011) 387-394.

80. Y. Men, H. Gnaser, R. Zapf, V. Hessel, C. Ziegler, and G. Kolb, Applied Catalysis A: General 277 (2004) 83-90.

81. R.H. Nibbelke, M.A.J. Campman, J.H.B.J. Hoebink, and G.B. Marin, Journal of Catalysis 171 (1997) 358-373.

82. J.-Y. Luo, M. Meng, J.-S. Yao, X.-G. Li, Y.-Q. Zha, X. Wang, and T.-Y. Zhang, Applied Catalysis B: Environmental 87 (2009) 92-103.

83. V. Galvita, and K. Sundmacher, Applied Catalysis A: General 289 (2005) 121-127.

84. T. Staudt, Y. Lykhach, N. Tsud, T. Skála, K.C. Prince, V. Matolín, and J. Libuda, Journal of Catalysis 275 (2010) 181-185.

Chapter 5

Microkinetics for toluene total oxidation over $CuO\text{-}CeO_2/Al_2O_3$

Abstract

The microkinetics of total oxidation of toluene over a $CuO\text{-}CeO_2/Al_2O_3$ catalyst are studied by means of Temporal Analysis of Products. The validation of the mechanism of toluene total oxidation where oxidation and reduction occurs at different sites is performed by kinetic modeling. The interaction of reactants and products with the catalytic support is taken into account while modeling.

A single set of kinetic parameters that can explain the experimental data over a wide range of temperatures and degrees of catalytic reduction are significantly estimated. The abstraction of H atoms and formation of water is the fastest process. The CO_2 formation occurs through three kinetically significant steps. The rate determining step in the whole process was found to be the destruction of the aromatic ring. A linear dependency of activation energies of the processes including transport of oxygen from the bulk to the surface on degree of reduction of the catalyst was found.

5.1 Introduction

Catalytic total oxidation is considered to be one of the most efficient methods for the abatement of volatile organic compounds (VOCs), which are recognized as major contributors to air pollution [1, 2]. Catalysts based on noble metals (Pt, Pd) are widely used to eliminate VOCs because of their high specific activity, resistance to deactivation and ability to be regenerated [2]. Transition-metal oxide catalysts, based on copper, cobalt, manganese and chromium, are also widely explored for VOC incineration and are known to be active combustion catalysts [1, 3]. CuO was reported as effective as Pt for the combustion of n-butanol and methyl mercaptan [4] and for the total oxidation of ethanol [5]. CuO supported on Al_2O_3 had excellent performance for the conversion of CO, ethyl acetate and ethanol [6, 7] and was found to be the most active transition-metal oxide of those tested for the catalytic combustion of toluene [8].

Addition of ceria as a promoter to supported copper oxide results in better catalytic performance for the complete oxidation of toluene, propane, benzene, and *p*-xylene [6, 8-10]. Based on structural characterization [10-15], the improved performance of the mixed oxide catalyst, compared with the single metal oxide, can be attributed to the formation of a solid solution $Ce_{1-x}Cu_xO_{2-x}$, i.e., with Cu^{2+} substitutionally incorporated into CeO_2. The solid solution $Ce_{1-x}Cu_xO_{2-x}$ has an increased oxygen storage capacity in comparison with CuO due to the mixed oxidation states of Ce (3+ /4+) [16-18] and improvement in redox properties of the catalyst due to the metal oxide/ceria interactions [19-21].

The accepted mechanism of oxidation of VOCs over transition-metal oxide catalysts was established to follow the Mars-van Krevelen type redox cycles [13, 22-25]. The first step is the reactant oxidation process using catalyst lattice oxygen, which will be replaced in the second step by dioxygen. It was found in [23] that the catalytic reduction during the total oxidation of toluene over $CuO\text{-}CeO_2/\gamma\text{-}Al_2O_3$ proceeds through the following sequence of processes: adsorption of toluene on

the catalyst surface; simultaneous abstraction of H from the methyl and the phenyl group; abstraction of the methyl carbon atom; followed by destruction of the aromatic ring. The oxygen species that is involved in the oxidation of toluene is the weakly bound lattice oxygen [23, 25]. The catalytic oxidation is satisfied by the dioxygen in the feed when present, which regenerates the reduced surface sites of the catalyst. In the absence of dioxygen the surface sites are regenerated by the oxygen diffusing from the bulk of the catalyst. However, a detailed microkinetic model for the total oxidation of toluene has not yet been developed.

Modeling of the transient phenomena allows obtaining valuable kinetic coefficients which often could not be determined from the steady state experiments. The experimental data obtained in a TAP reactor can be used to build a kinetic model based on elementary step mechanism. In this work we employ a microkinetic model for toluene total oxidation over $CuO\text{-}CeO_2/Al_2O_3$. This model relies on kinetic and catalyst descriptors. The interaction of reactants and products with the support is taken into consideration in the model.

5.2 Procedures

5.2.1 Catalyst

A commercial (11.6wt.%)CuO-(6.4wt.%)$CeO_2/\gamma\text{-}Al_2O_3$ catalyst was used in this study. Preparation of the catalyst is given in section 2.4.1. A detailed characterization of the catalyst by means of X-ray diffraction (XRD), high resolution transmission electron microscopy (HRTEM), X-ray absorption spectroscopy (XAS), etc. is described in chapter 2. The reader is also referred to [10-12].

5.2.2 TAP reactor set-up, procedures and conditions

The reader is referred to sections 2.2 and 2.3 for detailed description of the TAP reactor set-up and the types of experiments that were conducted for obtaining the experimental data for the microkinetic modeling.

The experimental data used for modeling in this work were collected over the temperature range 723K – 873K. The experimental data involving reaction was collected from a "thin-zone" TAP reactor configuration [26], where 10 mg of $CuO\text{-}CeO_2/Al_2O_3$ catalyst ($250<d_p<500\mu m$) was packed between two inert zones in the microreactor. The inert zones, which were packed with quartz particles of the same size, ensured Knudsen diffusion in the catalyst bed and uniformity in temperature of the gases travelling in and out of the catalyst bed. Separate experimental data on a thin-zone reactor filled with Al_2O_3 were collected to study the adsorption and desorption of toluene and CO_2 on Al_2O_3.

The experiments have been performed with toluene/oxygen mixture (molar ratio=1:9) over oxidized catalyst and toluene over oxidized and partially reduced catalyst. For experiments over preoxidized catalyst, an oxidized state of the catalyst was ensured by performing multi-pulse experiments with dioxygen prior to the single pulse experiments with toluene or toluene/oxygen. Different degrees of reduction of the catalyst were attained by performing multi-pulse experiments with toluene.

Active sites responsible for the activity of the catalyst are present in the $Ce_{1-x}Cu_xO_{2-x}$ phase and CuO monocrystals [10]. However, the main part of Cu dispersion in the catalyst is from the $Ce_{1-x}Cu_xO_{2-x}$ phase, which yields a contribution of 78% towards the total Cu on the surface. This amounts to 0.044 mol/kg_{cat}. The rest of the surface Cu contribution from the less disperse CuO single crystals are active only at $T > 873$ K [10]. Hence, in the present reaction conditions, the $Cu_{1-x}Ce_xO_{2-x}$ solid solution in the catalyst is assumed to be the only active phase towards total activity. As it was found that the oxygen atoms in Al_2O_3 are not available for reaction [23], and that the bulk CuO phase is not contributing towards the total activity under present reaction conditions, only the oxygen atoms related to $Cu_{1-x}Ce_xO_{2-x}$ are accounted for reaction. Therefore, unlike in chapter 3, the degree of reduction of the catalyst is determined in terms of the oxygen removed from the

$Cu_{1-x}Ce_xO_{2-x}$ phase and the exchangeable oxygen atoms in it. The degree of reduction, R^0 is calculated as follows:

$$R^0 = \frac{[O]}{[O]_{tot}} \tag{5.1}$$

where $[O]$ is the number of oxygen atoms consumed from the $Cu_{1-x}Ce_xO_{2-x}$ solid solution during the reaction and $[O]_{tot}$, the total number of exchangeable oxygen atoms in Cu-Ce solid solution involved in Eq. 5.2 and 5.3

$$CuO \rightarrow \frac{1}{2}Cu_2O + \frac{1}{2}O \tag{5.2}$$

$$CeO_2 \rightarrow \frac{1}{2}Ce_2O_3 + \frac{1}{2}O \tag{5.3}$$

Eq. 5.2 represents the reduction of Cu^{2+} to Cu^{1+} and Eq. 5.3 that of Ce^{4+} to Ce^{3+}. The total number of exchangeable oxygen atoms in the $Cu_{1-x}Ce_xO_{2-x}$ phase for a 10 mg catalyst was calculated to be $1.76\ \ 10^{18}$.

Sixteen sets of experimental data were used in this study which corresponds to four different temperatures with seven initial oxidation states of the catalyst. It should be mentioned that even after reoxidation, the catalyst is mildly reduced due to thermal reduction [23, 27]. The presence of dioxygen in the feed is assumed to nullify the effect of thermal reduction (see section 3.1). Hence, the experimental data collected by pulsing toluene/oxygen over the preoxidized catalyst were assumed to be collected over a fully oxidized catalyst, i.e., at $R^0 = 0$. Toluene pulsed over the catalyst without di-oxygen in the feed reacts with a thermally reduced catalyst, that is, at $R^0 = 0.0014$, 0.0028, 0.0042 and 0.0056 at 723 K, 773 K, 823 K and 873 K respectively. The catalyst was also deeply reduced by toluene multi-pulse experiments in order to study reaction at higher degrees of reduction at 723 K – 873 K. Initial degrees of reduction, $R^0 = 0.279$ and 0.419 were used for such experiments.

5.2.3 TAP modeling equations

5.2.3.1 Reactor model

A detailed description of the TAP reactor model can be found in section 2.7.

5.2.3.2 Determination and validation of kinetic parameters

The reader is referred to section 2.8 for a detailed explanation of determination of kinetic parameters.

It should be stressed that the rate coefficients of some reaction steps were dependent on the degree of reduction of the catalyst, R^0, see section 5.4. The activation energies of such steps are assumed to be linearly dependent on the degree of reduction of the catalyst, R^0, as given in Eq. 5.4.

$$E_a = E_a^0 + \alpha R^0 \tag{5.4}$$

where parameter α is the proportionality constant between the change in activation energy and degree of reduction. The reader is referred to Eq. 2.34.

The methods by which the significance of the kinetic parameters are determined is explained in section 2.8.

5.3 Active sites and oxygen species

The structure and the chemical environment of the mixed oxide solid solution is studied by means of EXAFS and DFT for a $Ce_{1-x}Cu_xO_{2-x}$ catalyst [20] and the results show dissolved Cu in CeO_2 with six oxygen atoms around the incorporated Cu^{2+}, the nearest three in the first shell at a distance of 1.96 Å and three in the second shell at a distance 2.9 Å. Not all the oxygen participate in the reaction. According to the global stoichiometry of toluene total oxidation, four of these surface oxygen atoms are required to form water from the adsorbed toluene molecule. Moreover, water formed from the methyl and the phenyl group of the toluene molecule had response peaks at the same time [23]. Hence, it is

assumed that four oxygen atoms surrounding the Cu^{2+} are simultaneously available for reaction. An oxidized Cu active site is hence represented as $Z_{Cu,s}O_4$. The oxygen atoms required for the formation of CO_2 are obtained by diffusion from the bulk. Nevertheless, active sites with one to six simultaneously available oxygen atoms have also been tested. It was the $Z_{Cu,s}O_4$ form that provided significant kinetic parameters while modeling and the best fit between experimental and calculated responses based on Eq. 5.4-16. Therefore, $Z_{Cu,s}O_4$ was considered as the most appropriate structure of the active site.

A reduced Cu site is represented as $Z_{Cu,s}$. A reduced Ce site is represented as $Z_{Ce,s}$ and an oxidized Ce site as $Z_{Ce,s}O$.

Other than the active sites in Cu and Ce, the catalyst also has its oxygen reservoir in the catalyst bulk. These are termed as Z_bO. No distinction is made between oxygen related to Cu and Ce in the bulk. These are weakly bound oxygen atoms in the bulk that take part in the reaction after diffusion towards the surface. Z_bO, upon transfer of oxygen to the surface for reaction reduces to Z_b. As important is the oxygen transfer from Ce to Cu through Z_bO. A reduced Z_b accepts the oxygen from Ce and converts into Z_bO, which can transfer its oxygen to the Cu site for reaction. This reaction will be discussed in section 5.3.2.

The following site balances apply in the present work.

$$C_{s,Z_{Cu,s}O_4} + C_{s,Z_{Cu,s}} = C_{s,Z_{Cu,s_{tot}}} \tag{5.5}$$

$$C_{s,Z_{Ce,s}O} + C_{s,Z_{Ce,s}} = C_{s,Z_{Ce,s_{tot}}} \tag{5.6}$$

$$C_{b,Z_bO} + C_{b,Z_b} = C_{b,Z_{b_{tot}}} \tag{5.7}$$

where $C_{s,Z_{Cu,s_{tot}}}$ is the total concentration of Cu sites on the surface of the $Ce_{1-x}Cu_xO_{2-x}$ phase of the catalyst which is 0.044 mol/kg_{cat}, $C_{s,Z_{Ce,s_{tot}}}$ is the total concentration of Ce sites on the surface of $Ce_{1-x}Cu_xO_{2-x}$ phase of the catalyst which is 0.088 mol/kg_{cat} and $C_{b,Z_{b_{tot}}}$ is the total concentration of Cu and Ce sites in the bulk of the $Ce_{1-x}Cu_xO_{2-x}$ phase of the catalyst which is equal to 0.5226 mol/kg_{cat}. However, the number

of exchangeable oxygen atoms from these sites depend on Eqs. 5.2 and 5.3.

A thermal reduction in a preoxidized state of the catalyst means that the pulse experiments with toluene in the presence and absence of oxygen are not executed over a completely oxidized, but a mildly reduced catalyst [23, 27]. It was shown in Fig. 3.4 in chapter 3 that the catalyst is active until a certain degree of reduction depending upon the reaction temperature. At reaction conditions applied in this chapter (723 K – 873 K) the catalyst was seen to be active until R_C^0 = 0.075 (i.e., R^0= 0.419), see Fig 3.4b. Nonetheless, for the reaction to take place, the surface Cu sites should be oxidized. Therefore, at $R^0 \leq 0.419$ the surface sites are considered to be oxidized, thereby attributing the reduced state of the catalyst, solely, to the bulk of the catalyst.

The change in the concentration of the oxidized and reduced sites in the bulk C_{b,Z_bO} and C_{b,Z_b}, depending upon the degree of reduction, R^0 can be expressed as in Eq. 5.8 and 5.9.

$$C_{b,Z_bO} = C_{b,Z_{b_{tot}}} - R^0[O_{tot}] \tag{5.8}$$

$$C_{b,Z_b} = R^0[O_{tot}] \tag{5.9}$$

The initial concentration of the oxidized and reduced sites in the bulk and the surface at various degrees of reduction, R^0 is given in Table 5.1.

The catalyst contains non-reactive sites, the majority of which are Al_2O_3. These are represented as Y_S. C_7H_8, CO_2 and O_2 adsorb reversibly on Al_2O_3. The concentration of sites for adsorption of compounds on Al_2O_3 was calculated to be 1.65 mol/kg_{cat}.

R^0	C^0_{b,Z_bO} (mol kg_{cat}^{-1})	C^0_{b,Z_b} (mol kg_{cat}^{-1})	$C^0_{s,Z_{Cu,s}O_4}$ (mol kg_{cat}^{-1})	$C^0_{s,Z_{Cu,s}}$ (mol kg_{cat}^{-1})	$C^0_{s,Z_{Ce,s}O}$ (mol kg_{cat}^{-1})	$C^0_{s,Z_{Ce,s}}$ (mol kg_{cat}^{-1})
0	0.2613	0				
0.014[a]	0.2571	0.0042				
0.028[b]	0.2531	0.0082				
0.042[c]	0.2451	0.0162	0.44	0	0.88	0
0.056[d]	0.2371	0.0242				
0.279	0.1808	0.0805				
0.419	0.1405	0.1208				

Table 5.1. Initial concentrations of Z_bO, Z_b, $Z_{Cu,s}O_4$, $Z_{Cu,s}$, $Z_{Ce,s}O$ and $Z_{Ce,s}$ at various degrees of reduction of the catalyst.
* due to thermal reduction. a) 723 K, b) 773 K, c) 823 K, and d) 873 K respectively

5.4 Reaction network

In [10] it was stated that the complex catalytic process of toluene total oxidation over the multi-component CuO-CeO_2/Al_2O_3 can be represented by the following formal equations similar to the classical Mars-van Krevelen mechanism:

$$Tol + Cu^{2+} \rightarrow Cu^{1+} + CO_2 + H_2O \quad (5.10)$$

$$Ce^{4+} + Cu^{1+} \rightarrow Ce^{3+} + Cu^{2+} \quad (5.11)$$

$$Ce^{3+} + ½O_2 \rightarrow Ce^{4+} \quad (5.12)$$

In the reaction presented in Eq. 5.10, toluene is oxidized over Cu^{2+}. This is a purely Cu-part of this catalytic process. Reoxidation of the Ce form, represented by Eq. 5.12, is a purely Ce-part of the process. Finally, the reaction presented in Eq. 5.11 is the "oxidation-reduction" process between oxidized Ce^{4+} and reduced Cu^{1+}. This reaction closes the catalytic cycle.

The reactions represented by Eq 5.10-5.12 are complex as well. In [23], the reaction of toluene interaction with the catalyst is explained in detail. The complex reaction consists of four steps at least. The first step is the adsorption of toluene on active sites. The second and the third steps involve reaction of adsorbed toluene with surface lattice oxygen, with abstraction of H and C atoms to form H_2O and CO_2. In the fourth

step, an interaction of dioxygen with the catalyst, including an oxygen exchange process between the catalyst surface and bulk, takes place.

Eq. 5.10 will be further developed into a more detailed scheme. This will be detailed in section 5.4.1. Eq. 5.11-5.12 be explained in detail in section 5.4.2.

Fig. 5.1 and Table 5.2 presents the detailed reaction network for the total oxidation of toluene over $CuO\text{-}CeO_2/Al_2O_3$. Fig. 5.1(a) shows the reduction of the catalyst by the formation of H_2O and CO_2. Fig. 5.1(b) shows the reoxidation of the catalyst by dioxygen through the Ce part. Steps R1-R26 in Table 5.2 present the elementary steps on the reactive part of the catalyst.

Elementary reactions R1-R26 are combined to obtain the reactions paths designated by Greek symbols α, β, γ, δ, ε, ζ and η, taking into account the stoichiometric numbers σ_i. These reaction paths are combined by using stoichiometric numbers, $\sigma_{\alpha\alpha}$, to obtain global reaction $\alpha\alpha$.

The role of non-reactive sites on reversible adsorption of different gas species will also be taken into account. Table 5.3 presents the elementary steps of reversible adsorption of C_7H_8, O_2 and CO_2 on the support (Al_2O_3).

As water was not detected by the mass spectrometer as a response during the single pulse experiment, the reaction steps involved in the adsorption of water on the catalytic surface were omitted. The single pulse responses of C_7H_8, O_2, and CO_2 could be adequately described without such elementary steps.

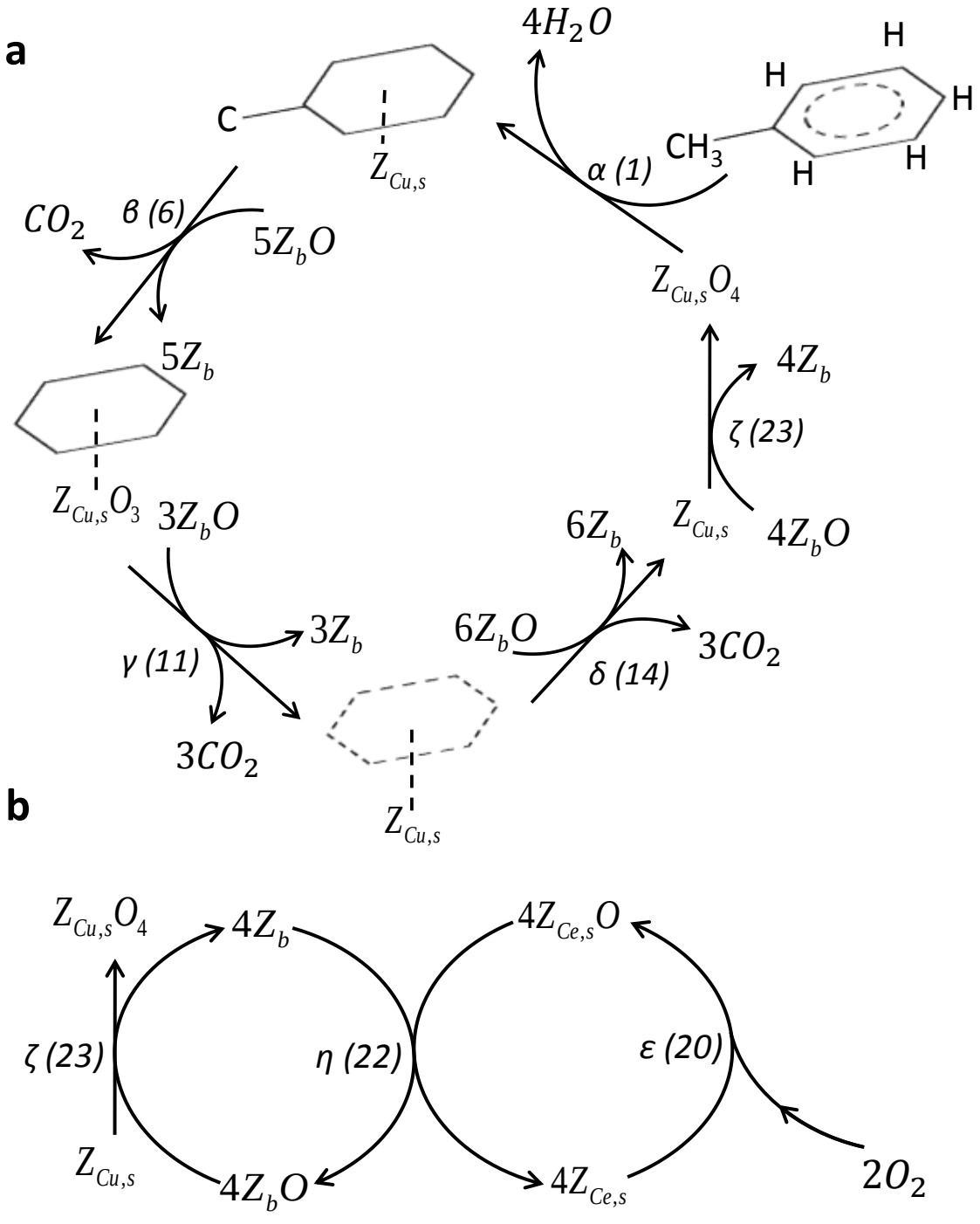

Fig. 5.1. Set of reaction schemes: (a) reaction network for the reduction of CuO-CeO_2/Al_2O_3 with toluene; (b) reaction network for the oxidation of CuO-CeO_2/Al_2O_3 with O_2. The steps are identical to those of Table 2. Only kinetically significant steps are presented. In each of the steps presented in catalyst reduction, oxidation of the catalyst takes place in parallel.

	Elementary steps	σ_α	σ_β	σ_γ	σ_δ	σ_ε	σ_η	σ_ζ	
reduction	$\boldsymbol{C_6H_5CH_3 + Z_{Cu,s}O_4 \rightarrow (C_6H_5Z_{Cu,s}O_4)CH_3}$	1	0	0	0	0	0	0	(R1)
	$(C_6H_5Z_{Cu,s}O_4)CH_3 \rightarrow H_2O + (C_6H_5Z_{Cu,s}O_3)CH$	1	0	0	0	0	0	0	(R2)
	$(C_6H_5Z_{Cu,s}O_3)CH \rightarrow H_2O + (C_6H_4Z_{Cu,s}O_2)C$	1	0	0	0	0	0	0	(R3)
	$(C_6H_4Z_{Cu,s}O_2)C \rightarrow H_2O + (C_6H_2Z_{Cu,s}O)C$	1	0	0	0	0	0	0	(R4)
	$(C_6H_2Z_{Cu,s}O)CH \rightarrow H_2O + (C_6Z_{Cu,s})C$	1	0	0	0	0	0	0	(R5)
	$\boldsymbol{(C_6Z_{Cu,s})C + Z_bO \rightarrow (C_6Z_{Cu,s}O)C + Z_b}$	0	1	0	0	0	0	0	(R6)
	$(C_6Z_{Cu,s}O)C + Z_bO \rightarrow (C_6Z_{Cu,s}O_2)C + Z_b$	0	1	0	0	0	0	0	(R7)
	$(C_6Z_{Cu,s}O_2)C + Z_bO \rightarrow (C_6Z_{Cu,s}O_3)C + Z_b$	0	1	0	0	0	0	0	(R8)
	$(C_6Z_{Cu,s}O_3)C + Z_bO \rightarrow (C_6Z_{Cu,s}O_4)C + Z_b$	0	1	0	0	0	0	0	(R9)
	$(C_6Z_{Cu,s}O_4)C + Z_bO \rightarrow CO_2 + C_6Z_{Cu,s}O_3 + Z_b$	0	1	0	0	0	0	0	(R10)
	$\boldsymbol{C_6Z_{Cu,s}O_3 + Z_bO \rightarrow CO_2 + C_5Z_{Cu,s}O_2 + Z_b}$	0	0	1	0	0	0	0	(R11)
	$C_5Z_{Cu,s}O_2 + Z_bO \rightarrow CO_2 + C_4Z_{Cu,s}O + Z_b$	0	0	1	0	0	0	0	(R12)
	$C_4Z_{Cu,s}O + Z_bO \rightarrow CO_2 + C_3Z_{Cu,s} + Z_b$	0	0	1	0	0	0	0	(R13)
	$\boldsymbol{C_3Z_{Cu,s} + Z_bO \rightarrow C_3Z_{Cu,s}O + Z_b}$	0	0	0	1	0	0	0	(R14)
	$C_3Z_{Cu,s}O + Z_bO \rightarrow CO_2 + C_2Z_{Cu,s} + Z_b$	0	0	0	1	0	0	0	(R15)
	$C_2Z_{Cu,s} + Z_bO \rightarrow C_2Z_{Cu,s}O + Z_b$	0	0	0	1	0	0	0	(R16)
	$C_2Z_{Cu,s}O + Z_bO \rightarrow CO_2 + CZ_{Cu,s} + Z_b$	0	0	0	1	0	0	0	(R17)
	$CZ_{Cu,s} + Z_bO \rightarrow CZ_{Cu,s}O + Z_b$	0	0	0	1	0	0	0	(R18)
	$CZ_{Cu,s}O + Z_bO \rightarrow CO_2 + Z_{Cu,s} + Z_b$	0	0	0	1	0	0	0	(R19)
oxidation	$\boldsymbol{O_2 + Z_{Ce,s} \rightarrow O_2Z_{Ce,s}}$	0	0	0	0	1	0	0	(R20)
	$O_2Z_{Ce,s} + Z_{Ce,s} \rightarrow 2Z_{Ce,s}O$	0	0	0	0	1	0	0	(R21)
	$\boldsymbol{Z_{Ce,s}O + Z_b \rightarrow Z_{Ce,s} + Z_bO}$	0	0	0	0	0	1	0	(R22)
	$\boldsymbol{Z_{Cu,s} + Z_bO \rightarrow Z_{Cu,s}O + Z_b}$	0	0	0	0	0	0	1	(R23)
	$Z_{Cu,s}O + Z_bO \rightarrow Z_{Cu,s}O_2 + Z_b$	0	0	0	0	0	0	1	(R24)
	$Z_{Cu,s}O_2 + Z_bO \rightarrow Z_{Cu,s}O_3 + Z_b$	0	0	0	0	0	0	1	(R25)
	$Z_{Cu,s}O_3 + Z_bO \rightarrow Z_{Cu,s}O_4 + Z_b$	0	0	0	0	0	0	1	(R26)
					$\sigma_{\alpha\alpha}$				
	$C_6H_5CH_3 + Z_{Cu,s}O_4 \rightarrow (C_6Z_{Cu,s})C + 4H_2O$				1				(α)
	$(C_6Z_{Cu,s})C + 5Z_bO \rightarrow CO_2 + C_6Z_{Cu,s}O_3 + 5Z_b$				1				(β)
	$C_6Z_{Cu,s}O_3 + 3Z_bO \rightarrow 3CO_2 + C_3Z_{Cu,s} + 3Z_b$				1				(γ)
	$C_3Z_{Cu,s} + 6Z_bO \rightarrow 3CO_2 + Z_{Cu,s} + 6Z_b$				1				(δ)
	$O_2 + 2Z_{Ce,s} \rightarrow 2Z_{Ce,s}O$				9				(ε)
	$Z_{Ce,s}O + Z_b \rightarrow Z_{Ce,s} + Z_bO$				18				(η)
	$Z_{Cu,s} + 4Z_bO \rightarrow Z_{Cu,s}O_4 + 4Z_b$				1				(ζ)
	$C_6H_5CH_3 + 9O_2 \rightarrow 4H_2O + 7CO_2$								(αα)

Table 5.2. Elementary reactions considered during the total oxidation of toluene over $CuO\text{-}CeO_2/Al_2O_3$. Reactions (R1) – (R19) represents reduction of the catalyst and reactions (R20)-(R27) represents reoxidation of the catalyst. The overall reaction is represented as (αα). The reaction paths for reduction is represented as (α), (β), (γ), and (δ) and that of reoxidation is represented as (ε) and (η). The corresponding scheme is represented in Fig. 1. Kinetically significant steps are represented in bold.

Elementary steps	
$C_7H_8 + Y_s \leftrightarrows (C_7H_8)Y_s$	(R27)
$O_2 + Y_s \leftrightarrows (O_2)Y_s$	(R28)
$CO_2 + Y_s \leftrightarrows (CO_2)Y_s$	(R29)

Table 5.3. Steps corresponding to the adsorption and desorption of toluene and CO_2 on Al_2O_3.

5.4.1 Reduction of the catalyst by toluene

The catalyst reduction is schematically presented in Fig. 5.1a. The detailed elementary steps corresponding to the reduction of the catalyst are presented in Table 5.2, viz. steps R1-R19.

Reduction of the catalyst by toluene involves formation of H_2O and CO_2. Steps R1-R5 describe water formation and steps R6-R19 describe CO_2 formation.

5.4.1.1Toluene adsorption and water formation

The reaction path for water formation from toluene can be represented as

$$C_7H_8+Z_{Cu,s}O_4 \rightarrow (C_6Z_{Cu,s})C+ 4H_2O \quad (5.13)$$

In the detailed mechanism, this process is described by five elementary steps, see steps R1-R5, Table 5.2. In step 1, C_7H_8 adsorbs on the oxidized metal surface active site $Z_{Cu,s}O_4$ and forms the adsorbed species (C_7H_8) $Z_{Cu,s}O_4$. The adsorbed species (C_7H_8) $Z_{Cu,s}O_4$ decomposes to form water. At least four elementary steps can be distinguished. In each of these steps two H atoms depart from the toluene molecule to react with the adjacent O atom and leave the catalytic surface as H_2O. The O atom for the first H_2O molecule is readily available at the oxidized Cu site, $Z_{Cu,s}O_4$. Assuming a faster oxygen consumption from the active sites than oxygen bulk-surface exchange, one can consider that in the next three steps the

intermediates,$(C_6H_5Z_{Cu,s}O_3)CH$,$(C_6H_4Z_{Cu,s}O_2)C$ and $(C_6H_2Z_{Cu,s}O)C$ consume O atoms from the partially oxidized Cu sites.

The reaction path for water formation is represented as step α in Table 5.2. A reversible adsorption of water on the catalyst surface was not considered in the model due to the unavailability of H_2O response. The mass spectrometer was not sensitive towards measuring H_2O response during single pulse experiments.

5.4.1.2 CO_2 formation – exchange with bulk oxygen

The global reaction for CO_2 formation can be represented as

$$(C_6Z_{Cu,s})C+14Z_bO \rightarrow 7CO_2 + Z_{Cu,s} + 14Z_b \quad (5.14)$$

This process consists of fourteen elementary steps viz. R6-R19, where in each step one O atom from the bulk takes part in the reaction. Steps R6-R9 in Table 5.2 describe the reoxidation of the reduced sites which have carbon containing species after H-abstraction over them. The carbon containing surface species react with the bulk lattice oxygen, Z_bO, to quickly regenerate to $(C_6Z_{Cu,s}O_4)C$. This $(C_6Z_{Cu,s}O_4)C$ is converted to CO_2 in ten elementary steps namely R10 - R19 in Table 5.2. Each of these steps consumes one oxygen atom from the bulk, Z_bO. These steps relate to the different structural fragments of the transformed toluene, methyl and phenyl groups respectively. Removal of the carbon atom in the methyl group takes place first to form CO_2 (steps R10-R12) followed by the breakage of the aromatic ring (steps R13-R19). Steps R6-R13 are combined into one reaction path which is represented as β in Table 5.2. Steps R14-R19 are combined into two reaction paths namely γ and δ in Table 5.2. Two steps in the reaction path were necessary and adequate to explain all the complex processes occurring during the CO_2 formation from the destruction of the aromatic ring. The abstraction of carbon atoms from the phenyl as well as the methyl group and formation of CO_2 results in reduced sites, Z_b and $Z_{Cu,s}$.

In Fig. 5.1a, only the reaction paths, that is steps α, β, γ, δ and η, are represented. In each of these steps, bulk oxygen Z_bO takes part in the reaction thereby getting converted into Z_b. This process along with the reoxidation of the catalyst with dioxygen takes place in parallel to steps including CO_2 formation. This will be explained in more detail in section 5.4.2.

5.4.2 Reoxidation of the catalyst by dioxygen

The reoxidation process is schematically represented in Fig. 5.1b. The detailed elementary steps corresponding to the oxidation of the catalyst are presented in Table 5.2, viz. steps R20-R26. The gas phase oxygen adsorbs on the reduced surface Ce site $Z_{Ce,s}$, oxidizing it into $Z_{Ce,s}O$, the oxidized Ce site. This takes place in two elementary steps, that is R20 and R21. In the first step dioxygen adsorbs on $Z_{Ce,s}$ to form the adsorbed species $O_2Z_{Ce,s}$. This adsorbed species reacts with an adjacent $Z_{Ce,s}$ in the next step to form another $Z_{Ce,s}O$. Steps R20 and R21 are combined into reaction path ε in Table 5.2.

$Z_{Ce,s}O$ exchanges oxygen with the reduced bulk lattice, Z_b as shown in step R22, thereby oxidizing them into Z_bO.

The bulk lattice oxygen diffuses to the surface and oxidizes the reduced $Z_{Cu,s}$ site thereby taking part in the steps corresponding to reduction of the catalyst as described in section 5.4.1. Four O atoms are required to reoxidize $Z_{Cu,s}$ into $Z_{Cu,s}O_4$. Steps R23-R26 represent the elementary steps corresponding to the oxidation of the reduced surface Cu sites by bulk oxygen. These steps are combined into reaction path η in Table 5.2.

5.5 Net rates of production

The specified rate coefficients of reactions steps in Table 5.2 will be estimated by multiresponse regression, applying Eq. 5.15 – 5.31 for the net production rates. A pseudo-steady state assumption has been applied on $\left(C_6H_5Z_{Cu,s}O_4\right)CH_3$, $\left(C_6Z_{Cu,s}O\right)C$, $C_5Z_{Cu,s}O_2$, $C_3Z_{Cu,s}O$, $O_2Z_{Ce,s}$,

and $Z_{Cu,s}O$. The concentration of oxidized and reduced bulk sites changes during reaction and is taken care of according to Eq. 5.8 and 5.9.

Gas species

$$R_{g,C_6H_5CH_3} = -k_1 C_{g,C_6H_5CH_3} C_{s,Z_{Cu,s}O_4} - k_{27^+} C_{g,C_6H_5CH_3} C_{s,Y_s} - k_{27^-} C_{s,(C_6H_5CH_3)Y_s} \quad (5.15)$$

$$R_{g,O_2} = -k_{20} C_{g,O_2} C_{s,Z_{Ce,s}} - k_{28^+} C_{g,O_2} C_{s,Y_s} + k_{28^-} C_{s,(O_2)Y_s} \quad (5.16)$$

$$R_{g,CO_2} = k_6 C_{s,(C_6Z_{Cu,s})C} C_{s,Z_bO} + k_{11} C_{s,C_6Z_{Cu,s}O_3} C_{b,Z_bO} + k_{14} C_{s,C_3Z_{Cu,s}} C_{b,Z_bO} - k_{29^+} C_{g,CO_2} C_{s,Y_s} + k_{29^-} C_{s,(CO_2)Y_s} \quad (5.17)$$

$$R_{g,H_2O} = k_1 C_{g,C_6H_5CH_3} C_{s,Z_{Cu,s}O_4} \quad (5.18)$$

Surface species

$$R_{s,(C_6Z_{Cu,s})C} = k_1 C_{g,C_6H_5CH_3} C_{s,Z_{Cu,s}O_4} - k_6 C_{s,(C_6Z_{Cu,s})C} C_{b,Z_bO} \quad (5.19)$$

$$R_{s,C_6Z_{Cu,s}O_3} = k_6 C_{s,(C_6Z_{Cu,s})C} C_{b,Z_bO} - k_{11} C_{s,C_6Z_{Cu,s}O_3} C_{b,Z_bO} \quad (5.20)$$

$$R_{s,C_3Z_{Cu,s}} = k_{11} C_{s,C_6Z_{Cu,s}O_3} C_{b,Z_bO} - k_{14} C_{s,C_3Z_{Cu,s}} C_{b,Z_bO} \quad (5.21)$$

$$R_{s,Z_{Cu,s}O_4} = -k_1 C_{g,C_6H_5CH_3} C_{s,Z_{Cu,s}O_4} + k_{23} C_{s,Z_{Cu,s}} C_{b,Z_bO} \quad (5.22)$$

$$R_{s,Z_{Cu,s}} = k_{14} C_{s,C_3Z_{Cu,s}} C_{b,Z_bO} - k_{23} C_{s,Z_{Cu,s}} C_{b,Z_bO} \quad (5.23)$$

$$R_{s,Z_{Ce,s}O} = k_{20} C_{g,O_2} C_{s,Z_{Ce,s}} - k_{22} C_{s,Z_{Ce,s}O} C_{b,Z_b} \quad (5.24)$$

$$R_{s,Z_{Ce,s}} = -k_{20} C_{g,O_2} C_{s,Z_{Ce,s}} + k_{22} C_{s,Z_{Ce,s}O} C_{b,Z_b} \quad (5.25)$$

Bulk species

$$R_{b,Z_bO} = -k_6 C_{s,(C_6Z_{Cu,s})C} C_{b,Z_bO} - k_{11} C_{s,C_6Z_{Cu,s}O_3} C_{b,Z_bO} - k_{14} C_{s,C_3Z_{Cu,s}} C_{b,Z_bO} + k_{22} C_{s,Z_{Ce,s}O} C_{b,Z_b} - k_{23} C_{s,Z_{Cu,s}} C_{b,Z_bO} \quad (5.26)$$

$$R_{s,Z_b} = k_6 C_{s,(C_6Z_{Cu,s})C} C_{b,Z_bO} + k_{11} C_{s,C_6Z_{Cu,s}O_3} C_{b,Z_bO} + k_{14} C_{s,C_3Z_{Cu,s}} C_{b,Z_bO} - k_{22} C_{s,Z_{Ce,s}} C_{b,Z_b} + k_{23} C_{s,Z_{Cu,s}} C_{b,Z_bO} \quad (5.27)$$

Surface species on support

$$R_{s,Y_s} = -k_{27^+} C_{g,C_6H_5CH_3} C_{s,Y_s} + k_{27^-} C_{s,(C_6H_5CH_3)Y_s} - k_{28^+} C_{g,O_2} C_{s,Y_s} + k_{28^-} C_{s,(O_2)Y_s} - k_{29^+} C_{g,CO_2} C_{s,Y_s} + k_{29^-} C_{s,(CO_2)Y_s} \quad (5.28)$$

$$R_{s,(C_6H_5CH_3)Y_s} = k_{27^+} C_{g,C_6H_5CH_3} C_{s,Y_s} - k_{27^-} C_{s,(C_6H_5CH_3)Y_s} \quad (5.29)$$

$$R_{s,(\boldsymbol{O_2})\boldsymbol{Y_s}} = k_{28^+} C_{\boldsymbol{g},\boldsymbol{O_2}} C_{\boldsymbol{s},\boldsymbol{Y_s}} - k_{28^-} C_{s,(\boldsymbol{O_2})\boldsymbol{Y_s}} \quad (5.30)$$

$$R_{s,(\boldsymbol{CO_2})\boldsymbol{Y_s}} = k_{29^+} C_{\boldsymbol{g},\boldsymbol{CO_2}} C_{\boldsymbol{s},\boldsymbol{Y_s}} - k_{29^-} C_{s,(\boldsymbol{CO_2})\boldsymbol{Y_s}} \quad (5.31)$$

5.6 Regression of experimental data on support

As toluene and CO_2 are known to interact with Al_2O_3 [28-31], adsorption behavior of C_7H_8, O_2 and CO_2 on Al_2O_3 was seen as a prerequisite for successful kinetic analysis of toluene total oxidation on $CuO\text{-}CeO_2/Al_2O_3$. Prior to modeling the total oxidation reaction on $CuO\text{-}CeO_2/Al_2O_3$, regression was performed over the experimental data collected over non-reactive support, Al_2O_3. Rate coefficients for adsorption and desorption and the activation energies for the desorption process were estimated. The kinetic parameters estimated along with their 95% confidence interval are presented in Table 5.4. Adsorption and desorption coefficients of both toluene and CO_2 were significantly estimated and these parameters must be taken into account while modeling the reaction over $CuO\text{-}CeO_2/Al_2O_3$ as adsorption of toluene and CO_2 significantly affects the shape and size of outlet responses. Toluene adsorbs on the support with a rate coefficient of 0.041 $m^3mol^{-1}s^{-1}$. The corresponding desorption rate coefficient was estimated to be 32.8 s^{-1} with an activation energy of desorption as 65 ± 9 kJ mol^{-1}. This is in good agreement with activation energies obtained for desorption of toluene from Al_2O_3 at ambient pressure during TPD experiments with values of 54 ± 5 kJ mol-1 [32]. CO_2 adsorption and desorption rate coefficients were estimated to be 0.033 m^3 mol^{-1} s^{-1} and 53.7 s^{-1} respectively with an activation energy of desorption as 10 $kJmol^{-1}$. A weak adsorption of CO_2 over pure γ-Al_2O_3 is reported in literature [33]. Fig. 5.2 shows the fit between experimental and simulated responses calculated with the set of parameter estimates given in Table 5.4 by the integration of Eq. 2.14–2.29 with the corresponding net production rates Eq. 5.28–5.31.

The rate coefficients were also validated by means of the Boudart criteria, see Eq. 2.35 and 2.36. The parameter estimates that are obtained here are taken into account for modeling of single pulse experimental

data involving reaction. Results of parameter estimation with experimental data involving reaction are discussed in section 5.7.

	Reaction step	Rate coefficient (forward) at 798 K	Rate coefficient (reverse) at 798 K	Activation Energy (reverse)	F (10^5)	ρ_{max}
R27	$C_7H_8 + Y_s \leftrightarrows (C_7H_8)Y_s$	(4.1 ± 2.1) 10^{-2}	32.85 ± 8.45	64.76 ± 9.32	0.15	0.92
R28	$O_2 + Y_s \leftrightarrows (O_2)Y_s$	(9.9 ± 1.3) 10^{-3}	13.12 ± 2.48	9.78 ± 9.03	2.13	0.69
R29	$CO_2 + Y_s \leftrightarrows (CO_2)Y_s$	(3.3 ± 0.2) 10^{-2}	53.68 ± 3.14	9.65 ± 2.42	0.11	0.89

Table 5.4. Estimates for the rate coefficients at 798 K and activation energies with their 95% confidence intervals, for steps R27, R28 and R29 of Table 5.3, obtained by non-isothermal regression of single pulse experiments with feeds toluene and CO_2.

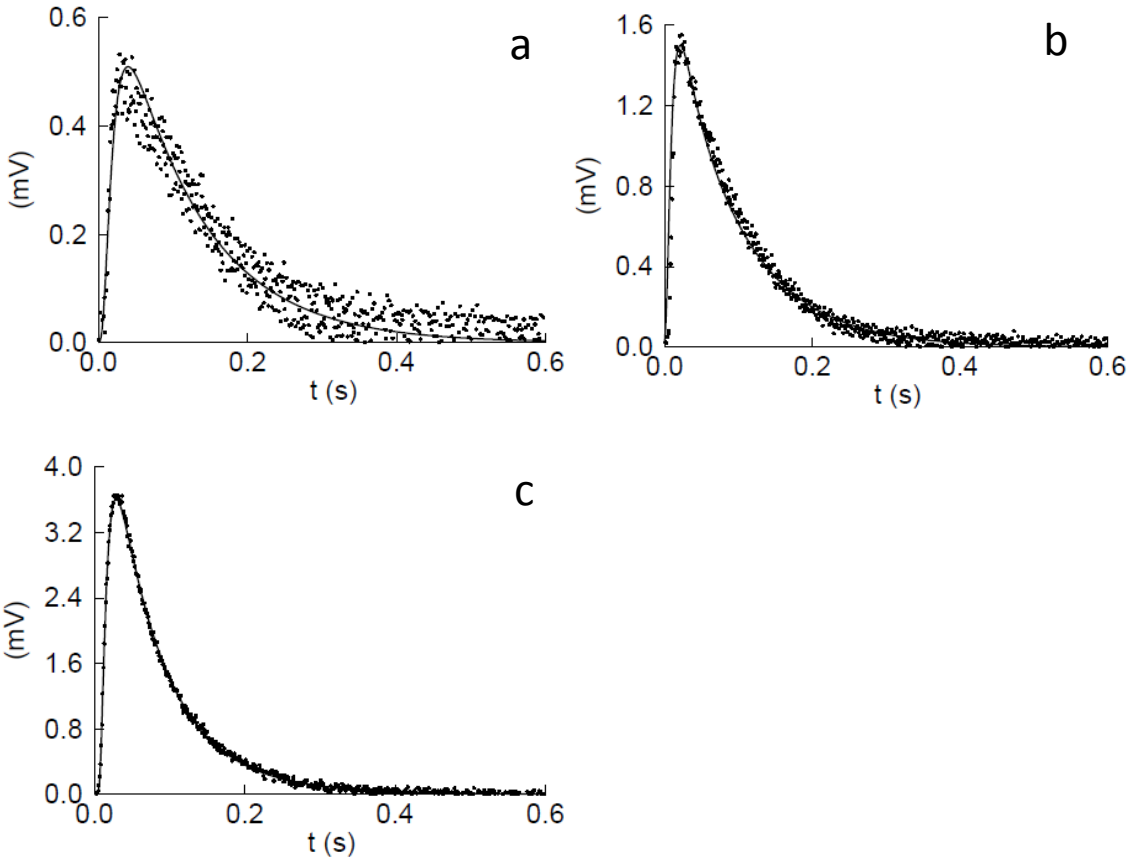

Fig. 5.2. TAP single pulse responses of (a) toluene corresponding to feed: toluene, (b) CO_2 corresponding to feed: CO_2 and (c) O_2 corresponding to feed: O_2 at T=823 K over Al_2O_3. Full lines represent responses calculated by integration of Eq. 2.14-2.29 and with corresponding net production rates Eq. 5.28-5.31 and the parameters estimated given in Table 5.4.

5.7 Regression of toluene single pulse data over CuO-CeO_2/Al_2O_3 with and without O_2 at various degrees of reduction

The reaction scheme for the oxidation of toluene over CuO-CeO_2/Al_2O_3 in the presence and absence of oxygen is presented in Table 5.2. Non-isothermal regression of the experimental data of toluene total oxidation collected over fully and partially reduced catalyst was performed. Sixteen sets of experimental data were used which corresponds to four different temperatures and seven initial states of the catalyst. C_7H_8/O_2 (1:9) single pulse experimental data over catalytic state $R^0 = 0$ and C_7H_8 single pulse experimental data over catalytic states $R^0 =$ 0.014, 0.028, 0.042, 0.056, 0.279 and 0.419 were used for non-isothermal regression. The average temperature of 798 K was used as T_r in Eq. 5.20 and 5.21.

The rate coefficients and activation energies corresponding to the adsorption and desorption of reactants and products on the support were also estimated together with those corresponding to reactions. The estimates reported in Table 5.4 were used as initial guess values for such parameters.

The broad range of temperatures, 723 K – 873 K, and the broad range of initial catalytic states, $0 \leq R^0 \leq 0.419$ can be well explained by a single mechanism and corresponding set of kinetic parameters values. Table 5.5 presents estimates of kinetic parameters at average temperature, 798 K. The experimental and calculated responses, based on estimated parameters and integration of Eq. 2.14-2.29 with corresponding net production rates Eq. 5.15-5.27, of C_7H_8, O_2 and CO_2 at 723K, 773K, 823K and 873K obtained by feeding C_7H_8/O_2 are plotted in Fig. 5.3. A good correspondence between the calculated responses and the experimental ones was obtained. Fig. 5.4a presents the experimental and calculated responses of CO_2 by feeding toluene at a thermally reduced state of the catalyst. Experimental and calculated responses of CO_2 with toluene fed at $R^0 = 0.279$ and 0.419 are

presented in Fig. 5.4b and c respectively. Satisfactory fits between the calculated and the experimental responses are obtained.

	Reaction step	Rate coefficient at 798 K	Activation energy at R^0=0 (kJ mol^{-1})
	<u>On reactive sites</u>		
R1	$C_6H_5CH_3 + Z_{Cu,s}O_4 \rightarrow (C_6H_5Z_{Cu,s}O_4)CH_3$	25.0 ± 1.0[a]	-§
R6	$(C_6Z_{Cu,s})C + Z_bO \rightarrow (C_6Z_{Cu,s}O)C + Z_b$	202.5 ± 14.8[b]	50.8 ± 2.3
R11	$C_6Z_{Cu,s}O_3 + Z_bO \rightarrow CO_2 + C_5Z_{Cu,s}O_2 + Z_b$	5.5 ± 0.1[b]	72.6 ± 2.2
R14	$C_3Z_{Cu,s} + Z_bO \rightarrow C_3Z_{Cu,s}O + Z_b$	94.9 ± 31.5[b]	86.4 ± 28.2
R23	$Z_{Ce,s}O + Z_b \rightarrow Z_{Ce,s} + Z_bO$	525.7 ± 88.2[b]	-§
R24	$Z_{Cu,s} + Z_bO \rightarrow Z_{Cu,s}O + Z_b$	202.5 ± 14.8[b]	50.8 ± 2.3
R20	$O_2 + Z_{Ce,s} \rightarrow O_2Z_{Ce,s}$	38.3 ± 2.5[a]	-§
			$\propto$ (kJ mol^{-1}) = 52.5 ± 1.2
	<u>On support</u>		
R27	$C_6H_5CH_3 + Y_s \rightarrow (C_6H_5CH_3)Y_s$	(3.7 ± 2.7) 10^{-2} [a]	-§
	$(C_6H_5CH_3)Y_s \rightarrow C_6H_5CH_3 + Y_s$	31.1 ± 23.3 [c]	65.2 ± 51.6
R28	$O_2 + Y_s \rightarrow (O_2)Y_s$	(6.0 ± 1.5) 10^{-2} [a]	-§
	$(O_2)Y_s \rightarrow O_2 + Y_s$	16.4 ± 2.5 [c]	14.2 ± 7.7
R29	$CO_2 + Y_s \rightarrow (CO_2)Y_s$	(3.3 ± 2.8) 10^{-2} [a]	-§
	$(CO_2)Y_s \rightarrow CO_2 + Y_s$	51.9 ± 37.7 [c]	10.1 ± 9.9
		F (10^4) =2.36	ρ_{max} = 0.90

Table 5.5. Estimates for the rate coefficients at 798K (k), activation energies at R^0=0 (E_a^0), and factor (a) corresponding to the linear dependence of activation energies on degree of reduction, for the steps in toluene total oxidation in the presence and absence of dioxygen, see Fig. 5.1 and Table 5.2 and 5.3, with their 95% confidence intervals obtained by non-isothermal multiresponse regression of single pulse experiments between 723 K and 873 K, over preoxidized and partially reduced catalyst.

[a] m^3 mol^{-1} s^{-1}, [b] kg mol^{-1} s^{-1}, [c] s^{-1}

§ cannot be estimated with significant values at 95% confidence intervals.

It was discussed in section 5.3 that $Z_{Cu,s}O_4$ was considered as the most appropriate structure of active site. Toluene adsorbs on the $Z_{Cu,s}O_4$ sites. This is presented in step R1, Table 5.2. The adsorbed

species, $(C_6H_5Z_{Cu,s}O_4)CH_3$, utilize oxygen from the fully oxidized $Z_{Cu,s}O_4$ sites for the hydrocarbon activation and subsequent abstraction of H atoms (R2-R5) leaving behind carbon containing $(C_6Z_{Cu,s})C$ species on the catalytic surface. The rate coefficient corresponding to the formation of H_2O was very high. Hence, its value was not relevant to describe the experimental data. Considering a quasi-instantaneous formation of H_2O from $(C_6H_5Z_{Cu,s}O_4)CH_3$ a pseudo steady state was assumed on $(C_6H_5Z_{Cu,s}O_4)CH_3$. The elementary steps R1-R5 are combined into one step, α. The rate coefficient at average temperature of step R1, i.e., adsorption of toluene on the catalytic surface is estimated to be 25.0 $m^3\ mol^{-1}\ s^{-1}$. There is no available information in literature regarding the toluene adsorption on such catalytic surface. However, this value is about one order higher than that obtained for adsorption of propane on the same catalyst [9]. This is reasonable since the adsorption of aromatics is stronger than that of paraffins and assuming a Polanyi or Bronsted type of relation between the thermodynamic and kinetic behavior [34].

Not all collisions between the gas phase molecules and the catalytic surface result in chemisorption for reaction. The sticking coefficient, S^0, gives the fraction of molecular collisions that result in chemisorption and subsequent catalytic reaction. It can be calculated from the adsorption coefficient, k_{ads} according to the relation, Eq. 5.32.

$$S^0 = k_{ads}\, C_{Z_{Cu,s}O_4} \sqrt{\frac{2\,\pi M_i}{RT}} \tag{5.32}$$

At the reference temperature, the sticking coefficient for C_7H_8 on $Z_{Cu,s}O_4$sites was calculated to be of the order of 10^{-6}.

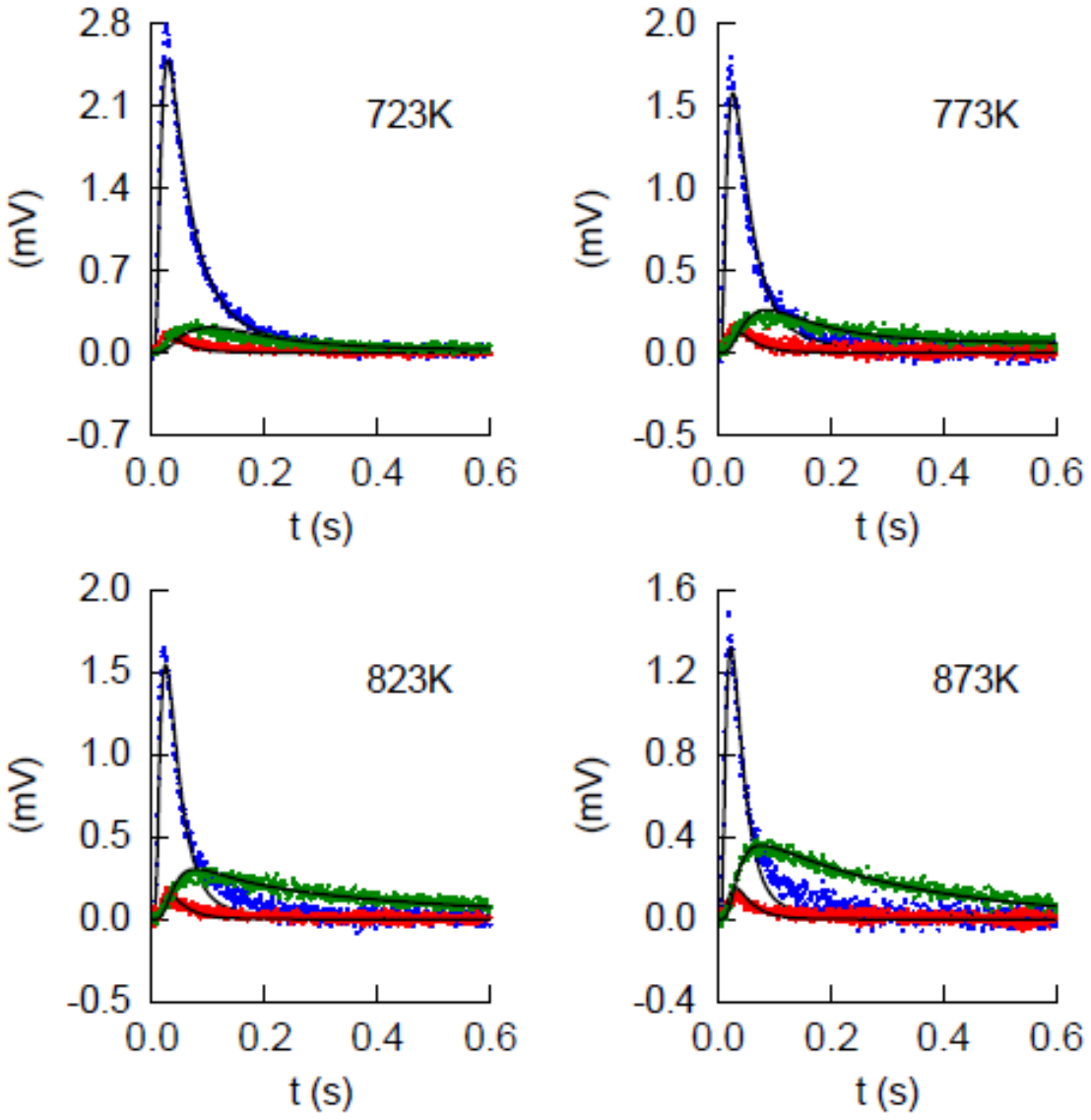

Fig. 5.3. TAP single pulse responses of CO_2 (●), toluene (●) and O_2 (●) corresponding to feed: toluene/O_2 at T=723 K – 873 K. Full lines represent responses calculated by integration of Eq. 2.14-2.29 and with corresponding net production rates Eq. 5.15-5.30 and the parameter estimated given in Table 5.4.

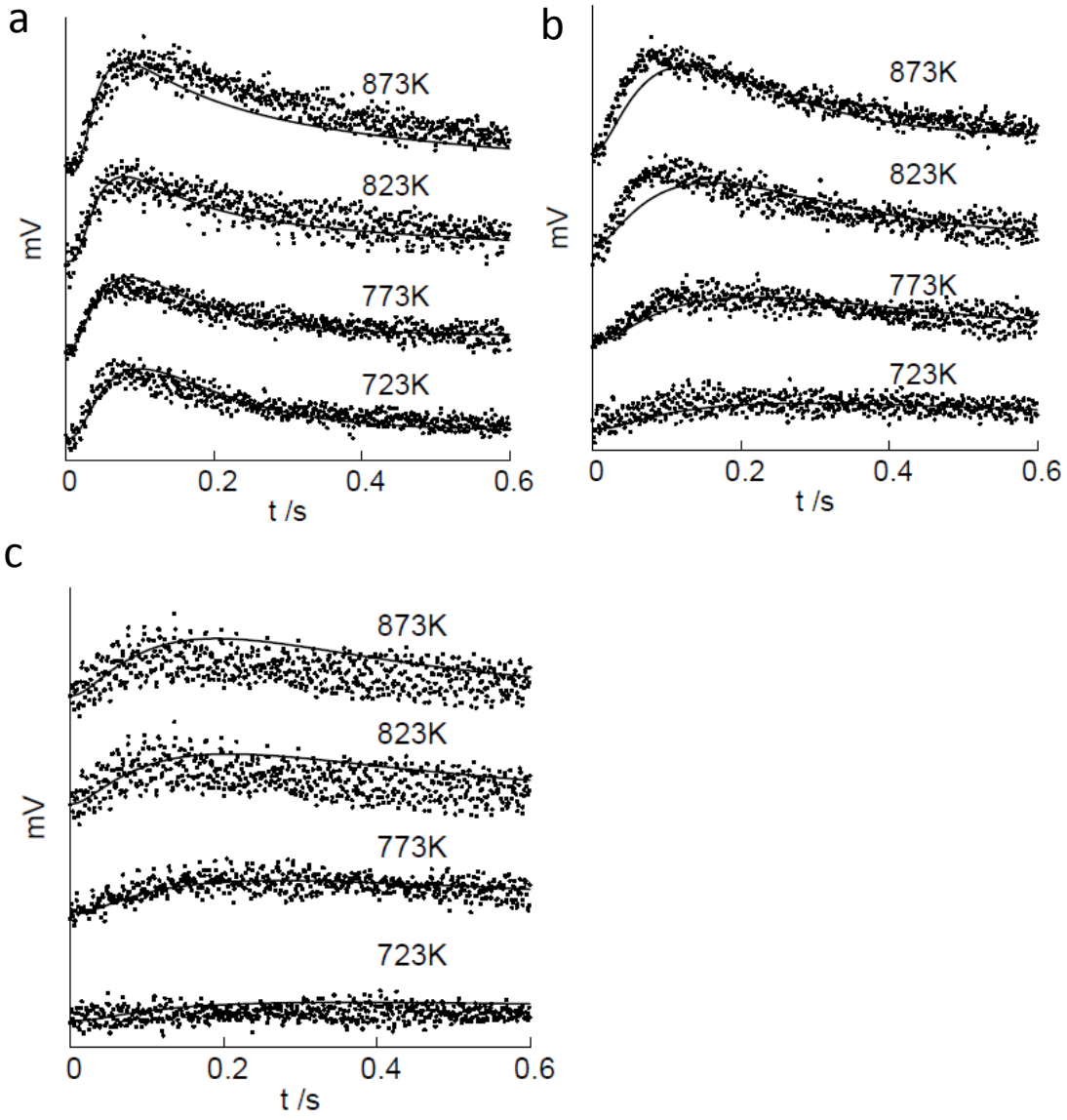

Fig. 5.4. TAP single pulse responses of CO_2 corresponding to feed: toluene at T=723 K – 873 K for (a) R_0=0.014-0.056 (b) R_0=0.279 (c) R_0=0.419. Full lines represent responses calculated by integration of Eq. 2.14-2.29 and with corresponding net production rates Eq. 5.15-5.30 and the parameter estimates given in Table 5.4.

In the elementary steps R6-R10, the carbon containing species accepts oxygen from the bulk of the catalyst to oxidize itself to $(C_6Z_{Cu,s}O_4)C$. The carbon containing species on the oxidized sites are activated for destruction of C atoms from the methyl group to form CO_2, see step R10. The rate coefficient of this step has a very high value and was not significantly estimated. Therefore a pseudo steady state was

assumed on $(C_6Z_{Cu,s}O_4)C$. The elementary steps R6-R10 are combined into one step, β. The rate coefficient at average temperature of step R6 and its activation energy are significantly estimated to be 202.5 kg mol^{-1} s^{-1} and 50.8 kJ mol^{-1}.

Oxygen diffuses from the bulk to the surface where it takes part in the destruction of the carbon containing ring. This occurs in several elementary steps, R11-R19. These steps are combined into two steps named γ and δ. The kinetic parameters of steps R11 and R14 were significantly estimated. The rate coefficient at average temperature of step R11 and step R14 are 5.5 kg mol^{-1} s^{-1} and 94.9 kg mol^{-1} s^{-1}) respectively. The activation energies of Step R11 and R14 are 72.6 kJ mol^{-1} and 86.4 kJ mol^{-1} respectively. The relative values of both the rate coefficient and of the activation energies indicate that the breakage of the aromatic ring takes place at a lower rate than the final removal of remaining C atoms. This also provides evidence of the slow removal of carbon containing species from the catalytic surface. A long and broad tail part of the CO_2 response also indicates the slow oxidation of the intermediates between $(C_6Z_{Cu,s}O_4)C$ and CO_2. A life time of 10 s for toluene on the catalytic surface was observed and reported in chapter 3.

During the reduction of the catalyst, viz. steps R1 – R19, reduced Cu sites, $Z_{Cu,s}$ are formed. These need to be regenerated. This process is complex and is described by Eq. R20 – R26 in Table 5.2. Dioxygen interacts with the catalyst at the ceria part of the Cu-Ce mixed oxide phase and the reduced Ce sites, $Z_{Ce,s}$, oxidizes into $Z_{Ce,s}O$, see elementary steps R20 and R21 in Table 5.2. Step ε which is a combination of the above mentioned steps explains the reoxidation of the Ce part of the $Ce_{1-x}Cu_xO_{2-x}$ mixed oxide solution. The rate coefficient of step R20 is significantly estimated was estimated to be 38.3 m^3 mol^{-1} s^{-1}. The activation energy of the reoxidation process could not be estimated significantly different from zero. The value of the rate coefficient and the activation energy for step R20 suggest a fast reoxidation of the Ce site. The time for reoxidation was calculated from the rate coefficient at a typical concentration of 12.75 mmol m^{-3} of

dioxygen and was found to be 2 s. Time-resolved operando X-ray absorption study of CuO–CeO_2/Al_2O_3 catalyst during oxidation of fully reduced catalyst showed a reoxidation time of 0.4 – 1.1 seconds [12].

The sticking coefficient of dioxygen on the Ce site was calculated in the similar way as was calculated for toluene. The sticking coefficient was found to be of the order of 10^{-5}. Literature suggests values of sticking coefficients of oxygen on clean metals and oxidized metal oxide surfaces, as low as 10^{-5} [35-37]. Sticking probabilities for oxygen of the order of 10^{-4} over the same catalyst were reported in atmospheric condition [13].

The oxidized Ce transfers the O atom to the reduced Cu part through the bulk. This is shown as step R22 in Table 5.2. Step R22 which is transfer of O from oxidized ceria to the bulk is a very fast process and the activation energy for the step cannot be estimated significantly different from zero at 95% probability level. The oxygen transport from bulk to surface for the reoxidation of reduced Cu part is shown in step R23. The rate coefficient for this process at average temperature was estimated significantly to be 202.5 kg mol^{-1} s^{-1}. According to the Einstein relation:

$$D_{O,b} = \frac{\bar{x}^2}{\bar{t}} \tag{5.32}$$

where $D_{O,b}$ is the diffusion coefficient of oxygen atoms from the bulk to the surface, $\bar{x}$ the average displacement of catalyst atoms in the lattice of the catalyst and $\bar{t}$ the time taken for the displacement which can be calculated from the rate coefficient of R23. Assuming an average displacement of 1 nm, the diffusivity of the oxygen atoms from the bulk to the surface was calculated to be 1.25 $\times 10^{-15}$ m^2 s^{-1}. This is in agreement with Sedmak et al. [38] where the diffusion coefficient of oxygen in a bulk $Cu_{0.1}Ce_{0.9}O_{2-y}$ crystallite lattice at 623 K was reported to be 10^{-15} m^2 s^{-1}.

The diffusion of oxygen from catalytic bulk to surface slows down as the catalyst reduces. Reaction steps that require oxygen transport from the bulk to the surface take place at a slower rate. The activation

energies for such steps increase linearly as the catalyst is reduced, according to the relation $E_a = E_a^0 + \alpha R^0$. The parameter α accounts for the linear dependence of activation energies of those steps with the degree of reduction of the catalyst, R^0. This parameter was estimated to be 52.5 kJ mol^{-1}. Steps that require oxygen transfer from the bulk to the surface are hence the slowest and rate determining steps in the model. For example the step with highest activation energy, that is R14, has an activation energy of 86.4 kJ mol^{-1} at fully oxidized state whereas 108.4 kJ mol^{-1} at $R^0 = 0.419$. This is reported to be caused by the increasing metal oxygen bond strength with increasing degree of reduction [39]. For example heats of oxygen adsorption over copper oxide vary from 40 to 80 kJ/mol O_2 at degree of reduction of the catalyst, R_C^0 ≤2% to 240 kJ/mol O_2 at $R_C^0 = 10\%$ [39].

5.8 Conclusions

Applying a transient technique provides experimental data for the description of reaction network and kinetic models that can adequately describe the processes occurring on the $CuO\text{-}CeO_2/Al_2O_3$ catalyst during toluene total oxidation, taking into account the adsorption and desorption of reactants and products over the Al_2O_3. Different initial states of the catalyst were investigated kinetically. Limiting the reaction network to the reduction and oxidation on the catalyst allows to obtain a kinetic model that describes adequately the experimental data. A single set of kinetic parameters can explain a broad range of temperatures and intial states of the catalyst. The kinetic parameters were estimated to be statistically significant and to have a sound physicochemical meaning. Among the different structure of active sites, a structure with four adjacent O atoms to Cu in the $Ce_{1-x}Cu_xO_{2-x}$ can adequately explain the experimental data. Toluene adsorbs and reacts to form water and carbon dioxide on the Cu^{2+} site, and dioxygen from the gas phase interacts and oxidizes the Ce^{3+}.

The $CuO\text{-}CeO_2/Al_2O_3$ catalyst shows a high rate of water formation in toluene during the reduction of the catalyst and a high

ability to restore its initial activity by O_2 activation and subsequent reoxidation of the catalyst.

The CO_2 formation occurs through three kinetically significant steps. The rate determining step in the whole process was found to be the destruction of the aromatic ring. The linear dependency of activation energies of the processes including diffusion of oxygen from the bulk to the surface on degree of reduction of the catalyst was calculated. Bulk to surface oxygen diffusion is found to be slower on reduced catalyst than on a preoxidized catalyst.

References

1 J.J. Spivey, Complete catalytic oxidation of volatile organics, Industrial & Engineering Chemistry Research, 26 (1987) 2165–2180.

2 L.F. Liotta, Catalytic oxidation of volatile organic compounds on supported noble metals, Applied Catalysis B: Environmental, 100 403-412.

3 E.M. Cordi, P.J. O'Neill, J.L. Falconer, Transient oxidation of volatile organic compounds on aCuO/Al2O3 catalyst, Applied Catalysis B: Environmental, 14 (1997) 23-36.

4 Christopher J. Heyes, James G. Irwin, Hilary A. Johnson, R.L. Moss, The catalytic oxidation of organic air pollutants part 1. Single metal oxide catalysts, Journal of Chemical Technology and Biotechnology, 32 (1982) 1025-1033.

5 H. Rajesh, U.S. Ozkan, Industrial and Engineering Chemistry research, 32 (1993) 1622-1630.

6 P.-O. Larsson, A. Andersson, Complete Oxidation of CO, Ethanol, and Ethyl Acetate over Copper Oxide Supported on Titania and Ceria Modified Titania, Journal of Catalysis, 179 (1998) 72-89.

7 P.-O. Larsson, A. Andersson, Oxides of copper, ceria promoted copper, manganese and copper manganese on Al_2O_3 for the combustion of CO, ethyl acetate and ethanol, Applied Catalysis B: Environmental, 24 (2000) 175-192.

8 C.-H. Wang, S.-S. Lin, C.-L. Chen, H.-S. Weng, Performance of the supported copper oxide catalysts for the catalytic incineration of aromatic hydrocarbons, Chemosphere, 64 (2006) 503-509.

9 V. Balcaen, H. Poelman, D. Poelman, G. B. Marin, Kinetic modeling of the total oxidation of propane over Cu- and Ce- based catalysts, Journal of Catalysis, 283 (2011) 75-88.

10 Unmesh Menon, Vladimir V. Galvita, Hilde Poelman, Vitaliy Bliznuk, Dirk Poelman, G.B. Marin, Nature of the active sites in $CuO\text{-}CeO_2/Al_2O_3$ for the total oxidation of toluene, Journal of Catalysis (Submitted), (2012).

11 G. Silversmit, H. Poelman, V. Balcaen, P.M. Heynderickx, M. Olea, S. Nikitenko, W. Bras, P.F. Smet, D. Poelman, R. De Gryse, M.-F. Reyniers, G.B. Marin, J. Phys. Chem. Solids., 70 (2009) 1274.

12 Konstantinos Alexopoulos, Mettu Anilkumar, Marie-Françoise Reyniers, Hilde Poelman, Sylvain Cristol, Veerle Balcaen, Philippe M. Heynderickx, Dirk Poelman, G.B. Marin, Time-resolved operando X-ray absorption study of $CuO–CeO_2/Al_2O_3$ catalyst during total oxidation of propane, Applied Catalysis B: Environmental, 97 (2010) 381–388.

13 P.M. Heynderickx, J.W. Thybaut, H. Poelman, D. Poelman, G.B. Marin, The total oxidation of propane over supported Cu and Ce oxides: A comparison of single and binary metal oxides, Journal of Catalysis, 272 (2010) 109-120.

14 A.-P. Jia, G.-S. Hu, L. Meng, Y.-L. Xie, J.-Q. Lu, M.-F. Luo, CO oxidation over $CuO/Ce_{1-x}Cu_xO_{2-\delta}$ and $Ce_{1-x}Cu_xO_{2-\delta}$ catalysts: Synergetic effects and kinetic study, Journal of Catalysis, 289 (2012) 199-209.

15 W. Shan, Z. Feng, Z. Li, J. Zhang, W. Shen, C. Li, Oxidative steam reforming of methanol on $Ce_{0.9}Cu_{0.1}O_Y$ catalysts prepared by deposition–precipitation, coprecipitation, and complexation–combustion methods, Journal of Catalysis, 228 (2004) 206-217.

16 G. Sedmak, S. Hocevar, J. Levec, Kinetics of selective CO oxidation in excess of H_2 over the nanostructured $Cu_{0.1}Ce_{0.9}O_{2-y}$ catalyst, Journal of Catalysis, 213 (2003) 135-150.

17 Z. Wu, M. Li, J. Howe, H.M. Meyer, S.H. Overbury, Probing Defect Sites on CeO_2 Nanocrystals with Well-Defined Surface Planes by Raman Spectroscopy and O_2 Adsorption, Langmuir, 26 (2010) 16595-16606.

18 X. Wang, J.A. Rodriguez, J.C. Hanson, D. Gamarra, A. Martinez-Arias, M. Fernandez-Garcia, Unusual Physical and Chemical Properties of Cu in $Ce_{1-x}Cu_xO_2$ Oxides, The Journal of Physical Chemistry B, 109 (2005) 19595-19603.

19 L. Dong, Y. Hu, M. Shen, T. Jin, J. Wang, W. Ding, Y. Chen, Dispersion Behaviors of Copper Oxide on the Mixed "CeO_2 + γ-Al_2O_3" Support, Chemistry of Materials, 13 (2001) 4227-4232.

20 V. Shapovalov, H. Metiu, Catalysis by doped oxides: CO oxidation by $Au_xCe_{1-x}O_2$, Journal of Catalysis, 245 (2007) 205-214.

21 J. Chen, Y. Zhan, J. Zhu, C. Chen, X. Lin, Q. Zheng, The synergetic mechanism between copper species and ceria in NO abatement over Cu/CeO_2 catalysts, Applied Catalysis A: General, 377 (2010) 121-127.

22 C. Doornkamp, V. Ponec, The universal character of the Mars and Van Krevelen mechanism, Journal of Molecular Catalysis A: Chemical, 162 (2000) 19-32.

23 Unmesh Menon, Vladimir V. Galvita, G.B. Marin, Reaction network for the total oxidation of toluene over CuO–CeO_2/Al_2O_3, Journal of Catalysis, 283 (2011) 1-9.

24 A.C. Gluhoi, N. Bogdanchikova, B.E. Nieuwenhuys, The effect of different types of additives on the catalytic activity of Au/Al_2O_3 in

propene total oxidation: transition metal oxides and ceria, Journal of Catalysis, 229 (2005) 154-162.

25 V. Balcaen, R. Roelant, H. Poelman, D. Poelman, G.B. Marin, TAP study on the active oxygen species in the total oxidation of propane over a $CuO–CeO_2/\gamma\text{-}Al_2O_3$ catalyst, Catalysis Today, 157 (2010) 49-54.

26 Sergiy O. Shekhtman, Gregory S. Yablonsky, John T. Gleaves, R.R. Fushimi, Thin-zone TAP reactor as a basis of "state-by-state transient screening", Chemical Engineering Science, 59 (2004) 5493-5500.

27 V. Galvita, H. Poelman, G. Rampelberg, B. De Schutter, C. Detavernier, G. Marin, Structural and Kinetic Study of the Reduction of $CuO–CeO_2/Al_2O_3$ by Time-Resolved X-ray Diffraction, Catalysis Letters, 142 (2012) 959-968.

28 T. Ioannides, X.E. Verykios, The Interaction of Benzene and Toluene with Rh Dispersed on SiO_2, Al_2O_3, and TiO_2 Carriers, Journal of Catalysis, 143 (1993) 175-186.

29 J.A. Gonzalez-Marcos, J.I. Alvarez-Uriarte, J.I. Gutierrez-Ortiz, A.T. Aguayo, J.R. Gonzalez-Velasco, Adsorption studies of different reagents on supported palladium catalysts, Applied Catalysis, 60 (1990) 1-12.

30 T.A. Gordymova, A.A. Budneva, A.A. Davydov, IR spectra of toluene adsorbed on $\gamma\text{-}Al_2O_3$, Reaction Kinetics and Catalysis Letters, 20 (1982) 113-117.

31 H.J. Freund, M.W. Roberts, Surface chemistry of carbon dioxide, Surface Science Reports, 25 (1996) 225-273.

32 R.I. Slioor, J.M. Kanervo, T.J. Keskitalo, A.O.I. Krause, Gas phase adsorption and desorption kinetics of toluene on Ni/γ-Al_2O_3, Applied Catalysis A: General, 344 (2008) 183-190.

33 A. Beuls, C. Swalus, M. Jacquemin, G. Heyen, A. Karelovic, P. Ruiz, Methanation of CO_2: Further insight into the mechanism over Rh/γ-Al_2O_3 catalyst, Applied Catalysis B: Environmental, 113–114 (2012) 2-10.

34 M. Boudart, Kinetics of chemical processes, Prentics-Hall, Inc, N.J.

35 J.L. Gland, B.A. Sexton, G.B. Fisher, Oxygen interactions with the Pt(111) surface, Surface Science, 95 (1980) 587-602.

36 M.A. Barteau, R.J. Madix, The adsorption of molecular oxygen species on Ag(110), Surface Science, 97 (1980) 101-110.

37 T. Siyama, Surface reactivity of oxide materials in oxidation-reduction environment, in: Surface and Near-Surface Chemistry of oxide materials, Materials Science Monographs, Elsevier, Amsterdam, 1988.

38 G. Sedmak, S. Hočevar, J. Levec, Transient kinetic model of CO oxidation over a nanostructured $Cu_{0.1}Ce_{0.9}O_{2-y}$ catalyst, Journal of Catalysis, 222 (2004) 87-99.

39 V.A. Sadykov, S.F. Tikhov, N.N. Bulgakov, A.P. Gerasev, Catalytic oxidation of CO on CuO_x revisited: Impact of the surface state on the apparent kinetic parameters, Catalysis Today, 144 (2009) 324-333.

Chapter 6
General conclusions

This PhD thesis is within the framework of the ongoing research activity on the elimination of volatile organic compounds (VOC) at the Laboratory for Chemical Technology, Ghent University. Total oxidation of toluene was investigated over metal oxide catalyst CuO-CeO_2/γ-Al_2O_3. By use of transient experiments, the reaction network and corresponding kinetics of the catalytic redox processes were established. The structure of the catalysts was investigated by use of high resolution transmission electron microscopy (HRTEM), selected area electron diffraction (SAED) electron energy loss spectroscopy (EELS), energy dispersive X-ray analysis (EDX), X-ray diffraction (XRD) and operando X-ray absorption spectroscopy (XAS).

The total oxidation of toluene was studied over a CuO–CeO_2/γ-Al_2O_3 catalyst in a Temporal Analysis of Products (TAP) setup in the temperature range 673–923 K in the presence and absence of dioxygen and at various degrees of reduction of the catalyst.

To obtain information about the participation of lattice and adsorbed oxygen in the reaction, the catalyst was pretreated with $^{16}O_2$ and was pulsed with a mixture of isotopically labeled oxygen $^{18}O_2$, toluene, and Ar and the product $C^{16}O_2$ and $C^{18}O_2$ monitored. Dioxygen ensures the reoxidation of the reduced catalyst according to the well-known Mars–van Krevelen mechanism. Weakly bound surface lattice oxygen atoms and adsorbed oxygen species, the lifetime of which is close to 1 s, are highly reactive and only found over a fully oxidized

catalyst and in the presence of dioxygen. The total oxidation rate significantly decreases over a mildly reduced catalyst.

Isotopic labeling experiments with C_6H_5–$^{13}CH_3$ and C_6H_5–CD_3 indicates that the reaction network of the catalytic total oxidation of toluene consists of the following sequence: adsorption of toluene on the catalyst surface; the simultaneous abstraction of H from the methyl and the phenyl group; abstraction of the carbon atom of the methyl group and finally, destruction of the aromatic ring. The carbon containing surface intermediates between toluene and CO_2 are slowly oxidized by the lattice oxygen atoms i.e., on a timescale of ~10 s. Water, however, is formed twice as fast.

The role of ceria in CuO-CeO_2/Al_2O_3 has been investigated. The catalytic activity for toluene total oxidation over a binary mixture of copper and cerium oxide supported on Al_2O_3 has been investigated in comparison to that of single metal oxide materials CuO/Al_2O_3 and CeO_2/Al_2O_3. Based upon structural characterization, the improved performance of the mixed oxide catalyst can be attributed to the formation of a solid solution $Ce_{1-x}Cu_xO_{2-x}$, i.e. with Cu^{2+} substitutionally incorporated into CeO_2, existing next to a bulk CuO phase. The average atomic ratio of Ce to Cu in this solid solution is 2:1, yielding an x-value of ~0.33. Temperature programmed reduction of the CuO-CeO_2/Al_2O_3 catalyst during operando XANES experiments indicates enhanced reduction of both Ce and Cu inside the solid solution. At the lowest reduction temperatures, ceria passes O to nearby copper to keep it oxidized. When all the readily available O^{2-} from Ce^{4+} are consumed, the dissolved Cu^{2+} reduces. At higher temperatures, the bulk CuO phase is reduced to Cu^0.

Enhanced activity in toluene total oxidation is due to the Cu^{2+} incorporation in the solid solution, which weakens the adjacent O bonds and is accompanied by O vacancies. Toluene is oxidized on the dissolved Cu^{2+} sites in the solid solution, while dioxygen is reduced at the Ce sites. The transfer of electrons and oxygen ions between Ce and Cu ensures the fast regeneration of available sites.

The reactions of the complete toluene oxidation cycle are given by the following equations:

$$Tol + Cu^{2+} \rightarrow Cu^{1+} + CO_2 + H_2O \quad \text{Eq. (6.1)}$$

$$Ce^{4+} + Cu^{1+} \rightarrow Ce^{3+} + Cu^{2+} \quad \text{Eq. (6.2)}$$

$$Ce^{3+} + 1/2O_2 \rightarrow Ce^{4+} \quad \text{Eq. (6.3)}$$

and/or

$$Ce^{3+} + H_2O/CO_2 \rightarrow Ce^{4+} + H_2/CO \quad \text{Eq. (6.4)}$$

Oxidation of the toluene and reduction of oxygen occur at different sites of the solid solution $Ce_{1-x}Cu_xO_{2-x}$ between which electrons and oxide ions are transferred. Oxidation of toluene occurs on Cu sites (Eq. 6.1), whereas Ce as CeO_2/Al_2O_3 shows no activity for reduction of toluene up to 773 K and only very low activity at 873 K. Reduction of oxygen on the other hand proceeds on Ce sites (Eq. 6.3).

Reduced Ce^{3+} can be re-oxidized by H_2O or CO_2 (Eq. 6.4). The addition of H_2O or CO_2 to the feed thus opens a new route for Ce re-oxidation, (Eq. 6.4). These re-oxidized sites can then act as oxygen supplier at the toluene oxidation site, i.e. for re-oxidation of nearby reduced Cu^{1+} (Eq. 6.2). Indeed, the addition of CeO_2 leads to a redox couple (Eq. 6.2), where Ce^{4+} can re-oxidize reduced Cu.

In contrast to CeO_2, reduced CuO/Al_2O_3 cannot be re-oxidized by H_2O or CO_2. The observed activity decrease of CuO/Al_2O_3 in the presence of water can be attributed to a competition between H_2O/CO_2 and dioxygen for the same active sites.

Applying a transient technique provides experimental data for description of reaction network and microkinetic models that can adequately describe the processes occurring on the $CuO\text{-}CeO_2/Al_2O_3$ during toluene total oxidation. Limiting the reaction network to the reduction and oxidation on the catalyst allow to obtain a microkinetic model describing adequately the experimental data with a single set of kinetic parameters over a temperature range, 723 K – 873 K, and degrees of reduction of the active phase, 0 – 40 %. The kinetic parameters were estimated to be statistically significant and to have a sound physicochemical meaning. Toluene adsorbs and reacts to form

water and carbon dioxide on the Cu^{2+} site, and dioxygen from the gas phase interacts and oxidizes the reduced Ce^{3+}. The structure of active site consisting of four simultaneously available oxygen atoms, $Z_{Cu,s}O_4$ was considered as the most appropriate structure. Each of the oxygen atoms adjacent to the Cu^{2+}, simultaneously react with adsorbed toluene. Along with the rate coefficients, the partial order of dioxygen was also significantly estimated. The linear dependence of activation energies of steps involving bulk oxygen atoms to the degree of reduction of the catalyst has also been modeled. The modeling results show a high rate of activation of the phenyl ring in toluene during the reduction of the catalyst and high ability to restore its initial activity by O_2 activation and subsequent re-oxidation of the catalyst.

Summarizing, this work has succeeded in better understanding the mechanism of action of the $CuO\text{-}CeO_2/\gamma\text{-}Al_2O_3$ in VOCs total oxidation. The results can be applied to optimize the industrial $CuO\text{-}CeO_2/Al_2O_3$ catalyst as well as an industrial reactor. For the design of the "ideal" catalyst for VOC oxidation, the $CuO\text{-}CeO_2/Al_2O_3$ catalyst should consist of nothing but solid solution $Ce_{1-x}Cu_xO_{2-x}$ at $T<873$ K, since the CuO phase will only participate in the reaction at $T>873$ K. The reason for the existence of these monocrystals is most likely a CuO overloading of the catalyst during synthesis. Indeed, CeO_2 can incorporate only a limited amount of Cu into its lattice and any excess will segregate during preparation into a separate bulk CuO phase with growing size as the loading increases.

At $T<873$ K, the CuO can be removed from the sample on the final step of catalyst preparation by treatment with nitric acid.

Appendix A

A.1: Crystallisation of CuO phase loaded onto alumina support

When loading CuO onto an alumina support, the CuO phase starts to show diffraction peaks from a loading of 5wt% on. Below this loading, CuO is present as amorphous or nanocrystalline material of size < 3nm (see figure A.1).

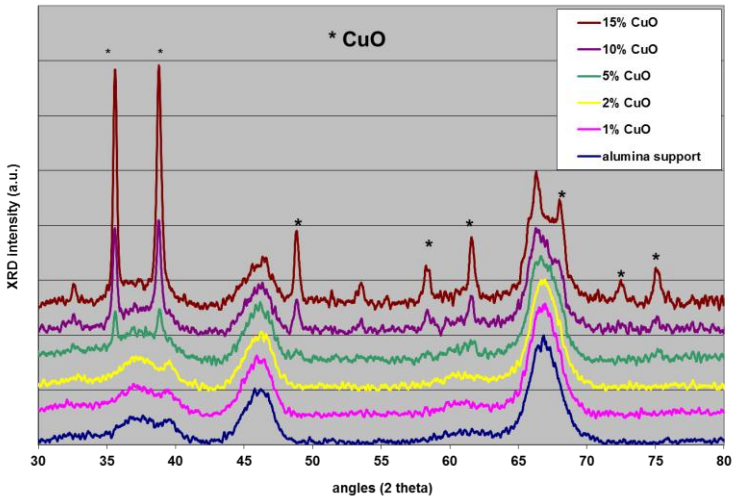

Figure A.1: XRD patterns for increasing loading of CuO on alumina.

A.2: In situ XANES spectra for $CuO\text{-}CeO_2/Al_2O_3$.

In situ XAS measurements were performed on the $CuO\text{-}CeO_2/Al_2O_3$ catalyst at the SAMBA beam line (synchrotron SOLEIL, Saint-Aubin, France). XANES spectra were measured in transmission at the Cu K edge (8979 eV) and the Ce L_{III} edge (5723 eV)

during H_2-TPR and isothermal re-oxidation experiments with CO_2 and water vapor at 923 K.

Figure A.2 displays the series of Cu K XANES spectra recorded during H_2-TPR, ramp rate 10K/min, with reference spectra for CuO, Cu_2O and Cu. Time resolution of the spectra is 10s.

A smooth and gradual evolution is present from CuO over Cu_2O towards Cu. The presence of an intermediate Cu^{1+} state can be deduced from the protruding shoulder in the edge of the spectra, at 8972 eV.

Figure A.3 displays the Ce L_{III} XANES spectra with 10s time resolution of the reduced $CuO\text{-}CeO_2/Al_2O_3$ catalyst during re-oxidation with water vapor at 923 K. Slight changes in first and second maximum after the edge indicate partial reoxidation of Ce^{3+}.

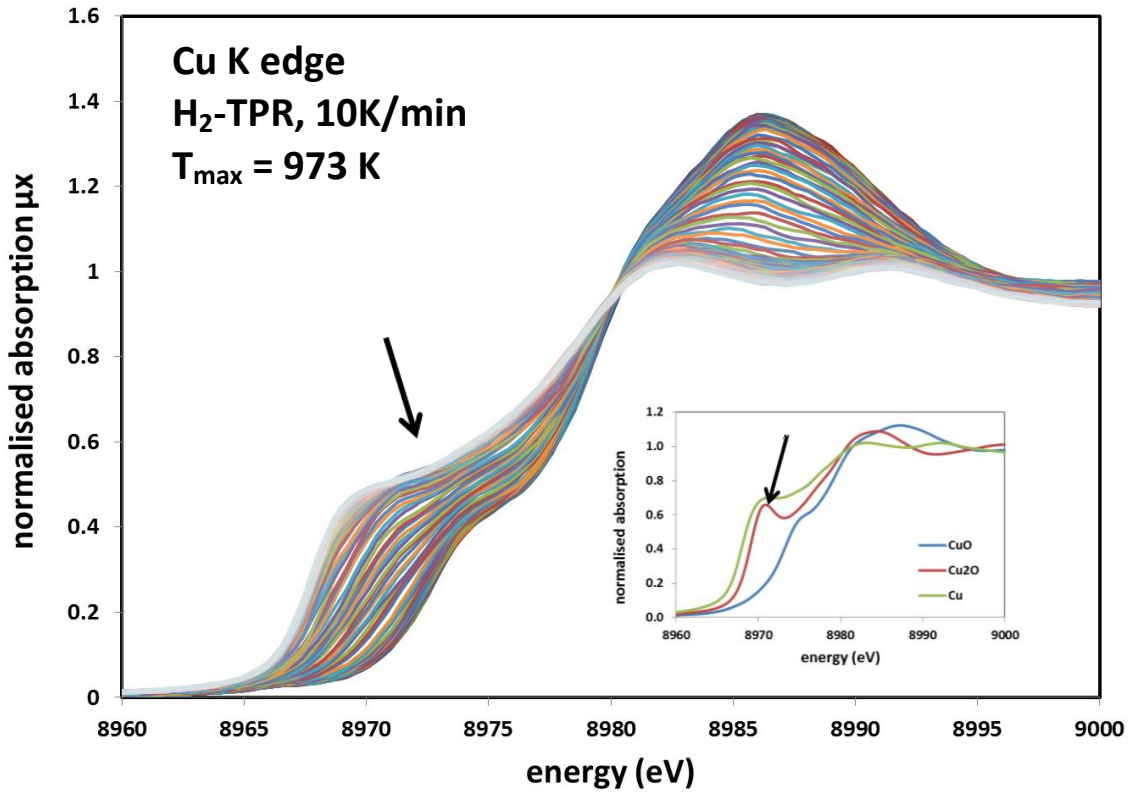

Figure A.2: XANES spectra recorded during H_2-TPR for $CuO\text{-}CeO_2/Al_2O_3$ at the Cu K edge, ramping rate 10K/min, maximum temperature 973 K, 10s/spectrum. Inset: XANES spectra of Cu references CuO, Cu_2O and Cu. Arrow indicates feature characteristic for the presence of Cu^{1+}.

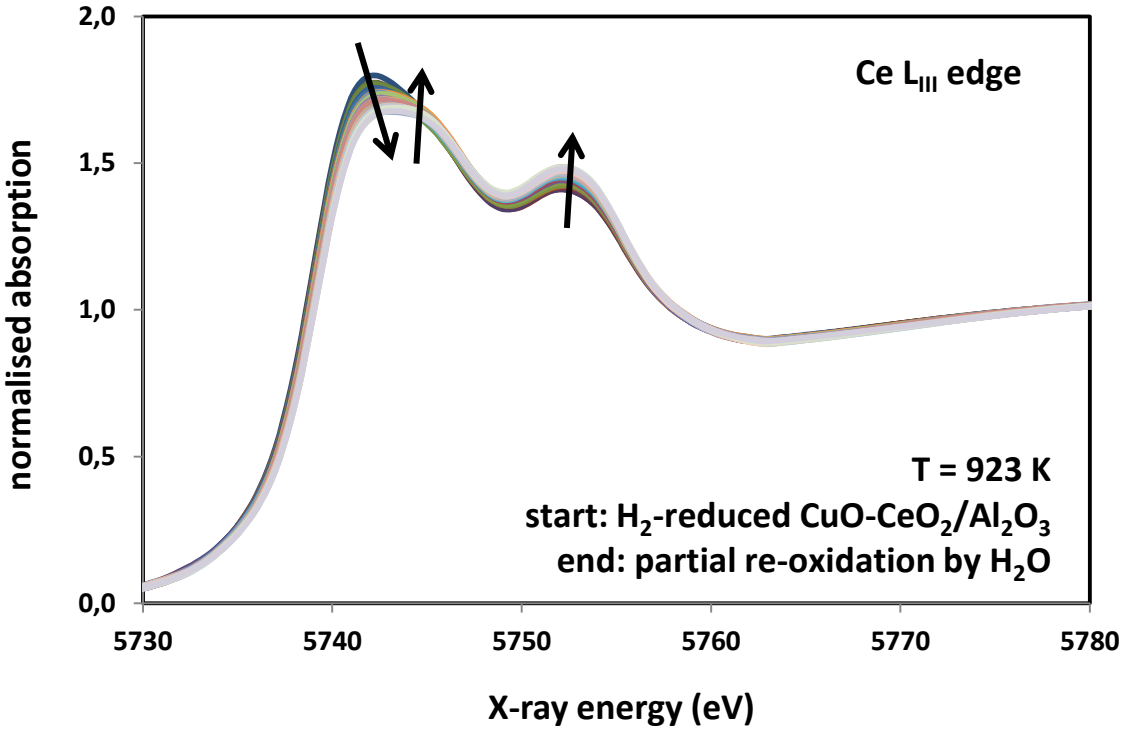

Figure A.3: XANES spectra during H_2O re-oxidation for reduced $CuO\text{-}CeO_2/Al_2O_3$ at the Ce L_{III} edge; T = 923 K, 10s/spectrum. Arrows indicate changes in XANES maxima during reoxidation.

Glossary

Activation energy:
A measure for the temperature dependence of the rate coefficient k=A exp(-Ea/RT) where E_a is the activation energy, A is the pre-exponential factor, R the universal gas constant, T the temperature.

Active sites:
Groups at the surface of a solid, responsible for their catalytic activity.

Adsorption:
Adhesion of atoms, ions or molecules from a gas, liquid, or dissolved solid to a surface.

Bulk oxygen species:
The oxygen species that is available in the bulk of the catalyst.

Catalysis:
Change in rate of a chemical reaction due to the participation of a substance called catalyst.

Catalyst:
A substance, usually used in small amounts relative to the reactants, that modifies and increases the rate of a reaction without being consumed in the process.

Catalyst oxidation:
The act of taking up oxygen by a catalyst from the gas phase resulting in an increase in oxidation state of the metals constituting the catalyst.

Catalyst reduction:
The act of losing oxygen from a catalyst resulting in a decrease in oxidation state of the metals constituting the catalyst.

Chemical kinetics:
Study of rates of chemical processes.

Conversion:
Measure of transformation of reactants into products during a chemical reaction.

Diffusion:
The movement of atoms or molecules from an area of higher concentration to an area of lower concentration.

Dispersion:
The fraction of atoms on the surface of a catalyst.

Elementary step:
A reaction representing an irreducible event at the molecular level.

Heterogeneous catalysis:
Catalysis where the phase of the catalyst differs from that of the reactant

Intermediate:
A component represented in a reaction network, but not in the net reaction.

Irreversible:
A reaction is irreversible if the rate of the reverse reaction can be neglected as compared to the rate of the forward reaction

Isothermal data:
A set of kinetic data which were all collected at the same reactor temperature.

Knudsen diffusion:
Low pressure diffusion through a porous bed, characterized by a diffusion coefficient independent of composition and pressure.

Mass Spectrometer:
Analytical technique with which several molecules are distinguished based on the mass-to-charge ratio of ionized components of these molecules.

Mars-van Krevelen mechanism:
Mechanism for a reaction on a catalyst surface in which some products leave the solid catalyst surface with one or more constituents of the catalyst lattice.

Objective function:
Function used during optimization problems which has to be minimized or maximized by choosing the best set of variables which determines the value of this function

Oxygen reservoir:
The oxygen species present in the bulk lattice of the catalyst.

Parameter estimation:
Process of estimating the parameters of a relation between independent and dependent variables as to describe a chemical reaction as good as possible.

Partial order of a reactant:
The index to which the concentration factor of a reactant is raised in the rate equation

Rate constant:
The constant of proportionality that doesnot depend on composition, in the expression for the rate of the reaction.

Rate determining step:
If, in a reaction sequence, consisting of *n* steps, *(n-1)* steps are reversible and if the rate of each one is very much larger in either direction than the rate of the nth step, the latter is said to be rate determining.

Reaction Mechanism:
Step by step sequence of elementary reactions by which overall chemical change occurs.

Reaction network:
A set of elementary steps.

Reaction rate:
The number of molecules of a component created by a chemical reaction per unit of time, volume of catalyst weight.

Redox:
The reduction-oxidation reactions in which oxidation state of atoms change.

Residence time:
Average time a particle spends in a particular system.

Reversible:
A reaction is reversible if the rates in the forward and reverse direction are of the same order of magnitude.

State-altering TAP-experiment:
A series of TAP pulse response experiments in which the reactant pulses cause a significant change of the catalyst.

State-defining TAP-experiment:
A series of TAP pulse response experiments in which the size of the reactant pulses is low enough to assume them to cause no significant change of the catalyst.

Steady state:
A system in a steady state has certain properties that are time independent.

Temporal analysis of products:
A transient kinetic experiment performed on a continuously evacuated microreactor loaded with a fixed catalyst bed, in which the response to a pulse of reactants is recorded.

Thin-zone-TAP-reactor:
A TAP-reactor packed with three zones, the middle one of which is much thinner than the outer ones. The middle zone is reactive (catalytic) while the outer zones are inert.

Transient experiments:
Experiments in which one or more state variables, i.e., pressure, temperature, concentration or flow rate are rapidly changed, investigating the response of a system to this change.

Yield:
The amount of products obtained in a chemical reaction.

List of publications

Peer-reviewed Publications

1. U. Menon, V. V. Galvita, G. B. Marin, Reaction network for the total oxidation of toluene over CuO–CeO_2/Al_2O_3, Journal of Catalysis 283 (2011) 1-9.
2. U. Menon, H. Poelman, V. Bliznuk, V. V. Galvita, D. Poelman, G. B. Marin, Nature of the active sites for the total oxidation of toluene over CuO-CeO_2/Al_2O_3, Journal of Catalysis 295 (2011) 91-103.
3. U. Menon, V. V. Galvita, D. Constales, G. B. Marin, Microkinetic modeling for toluene total oxidation over CuO–CeO_2/Al_2O_3 (to be submitted)

Conference contributions

Oral presentations

1. V. V. Galvita, U. Menon, H. Poelman, G. B. Marin; Microkinetics for toluene total oxidation over CuO-CeO_2/Al_2O_3; XX International Conference on Chemical Reactors (Chemreactor-20), 03-07 December 2012, Luxemburg, Luxemburg.
2. U. Menon, V. V. Galvita, H. Poelman, V. Bliznuk, G. B. Marin; Role of ceria in the total oxidation of toluene over CuO-CeO_2/Al_2O_3; Annual Meeting of American Institute of Chemical Engineers(AIChE) 2011, 15-22 October 2011, Minneapolis, United States of America.

3. U. Menon, V. V. Galvita, G. B. Marin; Reaction path analysis of the total oxidation of toluene over $CuO\text{-}CeO_2/Al_2O_3$: XIIth Netherlands Catalysis and Chemistry Conference; 28 Feb -02 March 2011; Noordwijkerhout, The Netherlands.
4. V. V. Galvita, U. Menon, G. B. Marin; Toluene total oxidation over $CuO\text{-}CeO_2/Al_2O_3$ catalyst : nature and role of oxygen species; Annual Meeting of American Institute of Chemical Engineers(AIChE) 2010, 07-12 November 2010, Salt Lake City, United States of America.

Poster presentations

1. V. V. Galvita, U. Menon, H. Poelman, G. B. Marin; Toluene total oxidation over $CuO\text{-}CeO_2/Al_2O_3$: reaction network and structural characterization; 15th International Congress on Catalysis 2012, 01-06 July 2012, Munich, Germany.
2. U. Menon, V. V. Galvita, G. B. Marin; TAP study of toluene total oxidation over $CuO\text{-}CeO_2/Al_2O_3$ catalyst; 12th FEA PhD symposium; 7 Dec, 2011; Ghent University, Belgium.
3. U. Menon, V. V. Galvita, G. B. Marin; Toluene total oxidation over $CuO\text{-}CeO_2/Al_2O_3$ catalyst: nature and role of oxygen species; M2dcR2 Methusalem Draft Management Committee; 28 June, 2010; Laboratory for Chemical Technology, Ghent University, Belgium.
4. V. V. Galvita, U. Menon, G. B. Marin; Reaction network and kinetics for the catalytic total oxidation of toluene over $CuO\text{-}CeO_2/Al_2O_3$; 4th IDECAT conference on Catalysis; 12-16 May 2010; Porquerolles, France.
5. U. Menon, V. V. Galvita, G. B. Marin; Study of role of the lattice oxygen of copper species during total oxidation of toluene in TAP reactor; XIth Netherlands Catalysis and Chemistry Conference; 01-03 March 2010; Noordwijkerhout, The Netherlands.